

Functional surfactants as energy valves in gradient structures of organic-inorganic perovskite structures

Von der Naturwissenschaftlichen Fakultät der
Gottfried Wilhelm Leibniz Universität Hannover

zur Erlangung des Grades
Doktorin der Naturwissenschaften (Dr. rer. nat.)

genehmigte Dissertation
von
Nicole Denise Fillafer, M. Sc.

2023

Referent: Prof. Dr. rer. nat. Sebastian Polarz
Korreferentin: Prof. Dr. rer. nat. Nadja-Carola Bigall
Tag der Promotion: 14.04.2023

Danksagung

Besonderer Dank gilt

Prof. Dr. **Sebastian Polarz** für deine langjährige Betreuung, das spannende, vielseitige Promotionsthema und dein Vertrauen in mich. Die konstruktive Zusammenarbeit und deine Unterstützung haben mich persönlich sehr vorangebracht und immer wieder angetrieben. Vielen Dank auch, dass du uns so viele AG Ausflüge, Weihnachtsfeiern und externen Retreats ermöglicht hast, welche ich immer als schöne Erinnerung behalten werde.

Prof. Dr. **Nadja Bigall** für die Übernahme des Zweitgutachtens und ihr sehr freundliches Entgegenkommen.

Prof. Dr. **Lukas Schmidt-Mende** für die Zusammenarbeit in Konstanz als Zweitbetreuer und für die Möglichkeit, auch nach dem Umzug nach Hannover in Konstanz PESA messen zu dürfen.

Dr. **Sonja Locmelis** für die Betreuung als Untergruppenleiterin in Hannover, dein Vertrauen in mich und die vielen Besprechungen und Gespräche.

Tobias Seewald und **Stefan Schupp** von der AG Schmidt-Mende in Konstanz danke ich für die Zusammenarbeit für die TAS und PESA Messungen.

Henning Kuper und Dr. **Yaşar Krysiak** danke ich vielmals für die Zusammenarbeit beim letzten Paper. Tut mir leid, für den Stress den ich gemacht habe, aber letztendlich ist das Ergebnis ja toll geworden!

Dr. **Andreas Schaate** für die Hilfe mit den XPS und XRD Messungen.

Dr. **Tom Kollek** und Prof. Dr. **Klaus Boldt** danke ich für die Erstellung des DFG-Drittmittelantrags, der die Finanzierung meiner Doktorarbeit möglich gemacht hat. Tom, dir besonderen Dank, für die Begeisterung und Unterstützung, die mich schon während meines Studiums zu einem riesen "Perowskit-Fan" gemacht hat. Ohne dich wäre meine wissenschaftliche Karriere vermutlich anders verlaufen!

Uli, Thomas, Sebastian, Sonja, Stephan und **Yaşar** danke ich für das Korrekturlesen meiner Doktorarbeit. Ohne euch wären vermutlich noch mehr "However"s im Text gelandet.

Brigitte und **Elana**, sowie **Claudia**, **Marc** und **Petra** die mir mit all den kleinen und größeren Problemen stets geholfen haben.

Vielen Dank der gesamten **AG Polarz**, seit Anfang an habe ich mich immer sehr wohl gefühlt und hatte eine super Zeit mit euch! Ob noch im “großen Büro” beim Kurve spielen, auf den (meist verkaterten) grandiosen Wanderungen in Unterwasser, bei der Fasnet oder beim Beachvolleyball spielen, es hat immer sehr viel Spaß gemacht! Ich bin froh, dass wir als Gruppe nach Hannover gekommen sind und auch in dieser schwierigen, seltsamen Zeit das Beste draus gemacht haben!

Meinen Laborpartnern **Hannah**, **Sebastian**, **Thomas**, **Marian** und **Sarah** für die tolle Zeit im Labor, die gute Musik, aber auch die wissenschaftlichen Diskussionen. Und sorry an Sebastian, für die Verkürzung seiner Lebenszeit um 1-2 Wochen aufgrund meines nicht-geschlossenen Abzugs.

Meinen StudentInnen **Jessi**, **Katja**, **Max**, **Adrian**, **Caro** und **Inez**, egal ob als BachelorantIn, PraktikantIn oder HiWi, ihr habt einen wesentlichen Teil zu meiner Doktorarbeit beigetragen. Vielen Dank, dass ihr die Begeisterung für Perowskit Nanopartikel mit mir geteilt habt! Ich habe viel gelernt in der Zusammenarbeit mit euch und hoffe, ich konnte euch auch ein bisschen auf euren Weg mitgeben.

Meinen Freunden, egal ob in Konstanz, Hannover oder von daheim. Ich bin froh, dass ich euch habe und ihr immer ein offenes Ohr hattet, wenn es mal nicht so gut lief. Vielen Dank für die unzähligen lustigen Abende, Ausflüge, Partys, Urlaube, Kochactions und Gespräche die immer eine schöne Ablenkung waren.

Vielen Dank an **Mama** und **Papa**, für eure Unterstützung, ohne euch wäre ich nicht die Person, die ich jetzt bin. Ich danke euch von ganzem Herzen, dass ihr immer an mich geglaubt habt, wenn ich es nicht konnte und mich wieder aufgebaut habt, wenn die Dinge nicht so gut liefen. Ohne euch wäre dieser Weg nicht möglich gewesen.

Auch meinen **Großeltern** danke ich von ganzem Herzen, ihr habt mich immer unterstützt und ward immer interessiert an meinem Studium (bzw. wolltet wissen, wie lang ich denn jetzt noch brauche).

Manu, einfach danke, für alles!!! Du begleitest mich nun seit über 3 Jahren, sogar bis nach Hannover, und ich bin so froh, dass du mir immer wieder den Rücken freigehalten hast, meine Hochs und Tiefs miterlebt hast und vor Allem, dass du immer an mich glaubst! Ich bin sehr stolz, dich an meiner Seite zu wissen und freue mich auf unseren gemeinsamen Weg!

Abstract

Hybrid perovskites are considered one of the most promising semiconductor materials of our time. Their ionic composition enables low-cost and simple production at low temperatures, making them a highly demanded semiconductor for photovoltaics, but also optoelectronic applications such as LEDs, lasers or photodiodes. Their hybrid nature enables the integration of organic cations, which brings a wide range of possible materials.

The classical perovskite structure permits the incorporation of small organic cations. If the given space in the structure is exceeded by the organic molecule, a layered crystalline phase with alternating arrangement of organic cations and inorganic 2D lead bromide layers is formed. This allows the use of a great variety of organic cations which become an integral part of the semiconducting material. Thus, molecules can be chosen that contribute to the functionality of the crystalline phase, for example, by using conductive conjugated π -systems. Energy transfer between the components of the layered phases becomes possible and extraordinary electronic and optical properties can result.

The aim of this thesis was the development of functional surfactants for the synthesis of hybrid lead halide perovskite particles with a special switchable feature. The switching was intended to introduce an energy valve into the phases, which could be switched by external stimuli (i.e. light or chemically). The obtained phases should be investigated for structural, optical and electronic properties, both before and after a switching of the ligands.

For this purpose, ligands based on photoswitchable azobenzene, redox-active ferrocene and conductive five-ring heterocycles were developed and their functionality was studied before and after incorporation into 2D layered hybrid perovskite phases. It was found that electronic exchange between the organic molecule and the perovskite framework is present in all the crystal phases obtained. Thus, the molecules are more than just a structural component of the phases, but contribute to the electronic properties.

The oxidation of ferrocene in particular made it possible to integrate a switchable energy valve. The decisive factor is the change in the energy of the molecular orbitals, which was achieved by the oxidation. Thus, the optical and electronic properties of the semiconductor could be greatly changed.

This work provides a comprehensive basis for the study of semiconducting particles with switchable ligands. Especially promising are redox-active hybrid perovskites, which emerge as a completely new class from these investigations.

Keywords: Perovskite, 2D materials, functional surfactants, ferrocene, azobenzene

Kurzfassung

Hybride Perowskite gelten als eine der vielversprechendsten Halbleitermaterialien unserer Zeit. Ihr ionischer Charakter ermöglicht eine günstige und einfache Herstellung bei niedrigen Temperaturen und macht sie somit zu einem gefragten Halbleiter für die Photovoltaik, aber auch für optoelektronische Anwendungen wie LEDs, Laser oder Photodioden. Ihre hybride Beschaffenheit ermöglicht die Integration von organischen Kationen, was eine breite Palette an Materialien ermöglicht.

In die klassische Perowskitstruktur lassen sich vor allem kleine Kationen einbauen. Wird der vorgegebene Platz in der Struktur von dem organischen Molekül überschritten entsteht eine geschichtete kristalline Phase mit abwechselnden Schichten organischer Kationen und 2D Bleibromid Schichten. Dies ermöglicht den Einsatz einer Vielzahl organischer Kationen, welche integraler Bestandteil der halbleitenden Struktur sind. So können Moleküle ausgewählt werden, welche zur Funktionalität der kristallinen Phase beitragen, bspw. durch konjugierte, leitfähige π -Systeme. Die Energieübertragung zwischen den Komponenten der geschichteten Phasen wird möglich, und es können außergewöhnliche elektronische und optische Eigenschaften resultieren.

Ziel dieser Arbeit war die Entwicklung funktioneller Tenside für die Synthese hybrider Bleihalogenid-Perowskit-Partikel mit einer speziellen schaltbaren Eigenschaft. Durch die Schaltung sollte ein Energieventil in die Phasen eingeführt werden, das durch externe Stimuli (z.B. Licht oder chemisch) geschaltet werden kann. Die erhaltenen Phasen sollten auf strukturelle, optische und elektronische Eigenschaften untersucht werden, sowohl vor als auch nach einem Wechsel der Liganden.

Zu diesem Zweck wurden Liganden auf der Basis von photoschaltbarem Azobenzol, redoxaktivem Ferrocen und leitfähigen Fünfring-Heterozyklen entwickelt und ihre Funktionalität vor und nach dem Einbau in 2D-Schichthybrid-Perowskitphasen untersucht. Es wurde festgestellt, dass in allen erhaltenen Kristallphasen ein elektronischer Austausch zwischen dem organischen Molekül und dem Perowskitgerüst stattfindet.

Insbesondere die Oxidation von Ferrocen ermöglichte es, ein schaltbares Energieventil zu integrieren. Entscheidend ist die Änderung der Energie der Molekülorbitale, die durch die Oxidation erreicht wurde. Dadurch konnten die optischen und elektronischen Eigenschaften des Halbleiters stark verändert werden.

Diese Arbeit liefert eine umfassende Grundlage für die Untersuchung von halbleitenden Partikeln mit schaltbaren Liganden. Besonders vielversprechend sind redoxaktive Hybrid-Perowskite, die sich als eine völlig neue Klasse herausstellen.

Stichworte: Perowskite, 2D Materialien, Funktionelle Grenzflächenadditive, Ferrocene, Azobenzol

Table of content

<i>Danksagung</i>	II
Abstract	V
Kurzfassung.....	VI
Table of content.....	VIII
1 Introduction	1
2 Theoretical Background	3
2.1 Hybrid lead halide perovskites.....	3
2.1.1 Structural diversity of hybrid perovskites.....	3
2.1.2 Low-dimensional layered hybrid perovskites.....	8
2.1.3 Diversity of layered hybrid perovskites.....	10
2.1.4 Applications of hybrid perovskites.....	14
2.2 Ligand systems.....	15
2.2.1 Azobenzene.....	15
2.2.2 Ferrocene.....	19
2.3 Preliminary Work	22
2.4 Analytical Methods	25
2.4.1 UV/Vis spectroscopy	25
2.4.2 Transient absorption spectroscopy	26
2.4.3 Photoluminescence spectroscopy.....	27
2.4.4 Photoelectron spectroscopy.....	28
2.4.5 Powder X-ray diffraction.....	28
2.4.6 Cyclic voltammetry.....	29
3 Challenges and Objectives	31
4 Results and Discussion.....	33
4.1 Azobenzene as functional surfactant.....	34
4.1.1 Synthesis and characterization of photoswitchable surfactants	35
4.1.2 Layered hybrid perovskites with photoswitchable surfactants.....	40

4.1.3	3D hybrid perovskites with surface coordinating azobenzene ligands ..	51
4.1.4	Ruddlesden-Popper phases with photoswitchable surfactants	61
4.2	Ferrocene as functional surfactant	65
4.2.1	Synthesis and characterization of redox-active surfactants	65
4.2.2	Crystal structure of ferrocene containing lead bromide phases	67
4.2.3	Electronic and optical properties	76
4.2.4	Redox-activity of ferrocene containing lead bromide phases	80
4.2.5	Ruddlesden-Popper phases with ferrocene-based ligands	90
4.3	Heterocycles as functional surfactant	96
4.3.1	2D layered hybrid perovskites with heterocycles	97
4.3.2	Halide variation in 2D layered hybrid perovskites with heterocycles ...	102
4.3.3	Ruddlesden-Popper phases with thiophen-based surfactants	106
5	Conclusion and Outlook	111
6	Experimental Section	118
6.1	Synthesis of functional ligands	118
6.2	Particle synthesis	126
6.2.1	Particles with AzoC _n Br	126
6.2.2	Particles with FcC _n Br	127
6.2.3	Particles with X-EABr	129
6.3	Methodology and analytical techniques	130
7	Literature	134
8	List of figures	147
9	List of tables	155
10	List of abbreviations	156
11	Appendix	159
	<i>Lebenslauf</i>	191
	Publication	192

1 Introduction

“A global shortage of these tiny, essential microelectronics that make so many things smart and connected - cars, homes, devices, cities - has come just as demand for these new necessities seems insatiable.”

IBM, J. Daly, 9th March 2021^[1]

What does the author refer to? At the beginning of the 21st century, we are in the middle of the semiconductor age. Being the heart of technological progress and innovations, they have never been more important to our daily lives. When scientists, historians and technologists were asked to rank the top innovations in human history since the wheel, only paper print, electricity and penicillin could beat the semiconductor.^[2] It is *the* indispensable component of microelectronics, from diodes and transistors to resistors and capacitors. Only the development of this technology made the digitalization of our age possible.

Semiconductors are ubiquitous and built into almost every electronic device we use. Every aspect of our daily lives, from data collection and search engines to healthcare, social networks and smart phones, depends on it.^[3] Hyperconnectivity between internet-based services enables access to numerous applications and has great potential to make people's lives easier and smarter.^[4] From smart wearables that monitor our daily habits, fitness and health, smart homes that control our energy efficiency, security and personal comfort (scheme at the right^[4]), to whole smart cities and industries, that optimize energy consumption and foresee challenges, they all require these small, microstructured semiconductor devices.

The increasing demand in recent years led to a shortage, which is noticeable in many industrial sectors and also in the increasing prices.^[5] High costs for silicon, the classic semiconductor for electronic components, but also photovoltaic applications, favor the development of cheaper alternatives. However, which semiconducting material combines low-cost production and high efficiencies and reliability at the same time? Scientists provide an answer to this question: hybrid perovskites.



The versatile class of hybrid lead halide perovskites includes semiconductors for numerous optical and electronic applications, such as solar cells,^[6] light emitting diodes (LEDs),^[7] lasers or field-effect transistors.^[8] A broadly adjustable bandgap enables their use in a wide variety of semiconductor technology applications. After more than a decade of intensive research, the materials have emerged as one of the most promising materials of the 21st century and are even about to be implemented in commercial applications.^[8]

The ease of the low temperature synthesis and the growing comprehension over shape-control and understanding of their properties make these materials of great interest to chemistry, physics and material research.^[9] Their hybrid character allows to tailor their properties as required for numerous applications. Compared to conventional semiconductors, the incorporation of organic cations simultaneously offers new possibilities to influence the optical and electronic properties. Large organic molecules can be either coordinated to the surface or even integrated into the semiconductors by inserting an ammonium head group, which is able to interact with the perovskite lattice. In the latter case, the so-called layered hybrid perovskites, 2D homologues of the classical perovskite structure, consisting of individual layers of lead halide octahedra, are formed.

Thus, organic functionalities e.g. with intrinsic conductivity through a π -conjugated system, photochromic molecules or polymerizable ligands are integrated into the hybrid materials, allowing an active control over their semiconducting features.^[10] This creates an electronic landscape of quantum wells in which the organic molecules interact with the inorganic phase. Charge carrier dynamics, excitation, and emissions depend strongly on the organic moiety.

If using organic molecules with extended functionality, such as reversible photoswitchability or organometallic molecules with easily accessible redox chemistry, it becomes achievable to manipulate the materials even after synthesis. This makes it possible to induce a change in the material by applying external stimuli.

Using hybrid perovskites as a versatile system, this work investigates the incorporation of functional organic and organometallic molecules into semiconductors and their influence on charge carrier dynamics, electronic and optical properties as a response to external stimuli. For this purpose, 2D layered hybrid perovskites serve as an ideal model system. The aim is to investigate whether certain properties can be influenced by the stimuli so that they can be switched on and off (e.g. as in field effect transistors).

2 Theoretical Background

2.1 Hybrid lead halide perovskites

2.1.1 Structural diversity of hybrid perovskites

Crystal structure of three dimensional (3D) perovskites

Compared to the original perovskite structure of CaTiO_3 , hybrid perovskites with the composition AMX_3 show one crucial difference: the possibility to incorporate organic ions.

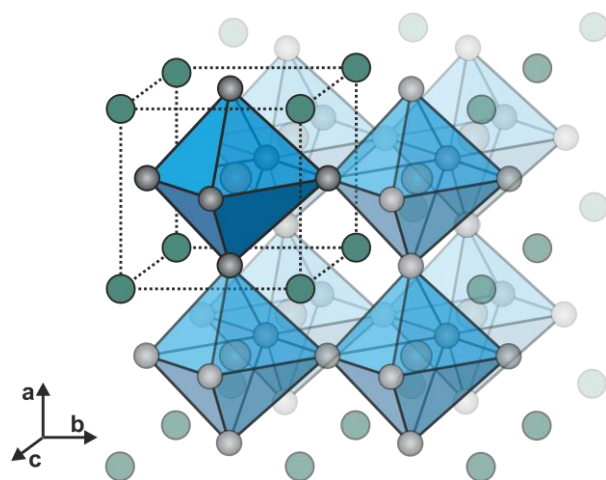


Figure 1 - Polyhedral representation of a cubic AMX_3 perovskite. (A^+ =green, M^{2+} =orange (center of octahedron), X^- =grey).

Thereby, at least one of the ions (A^+ , M^{2+} , X^-) is of organic nature. Typically, this is A^+ , while M^{2+} is a metal ion (e.g. Pb^{2+} , Sn^{2+}) and X^- is a halide ion (Cl^- , Br^- or I^-). The cubic structure of hybrid perovskites (shown in **Figure 1**) is build up by a network of corner-sharing MX_6 -octahedra, where the M^{2+} -cation is coordinated by six halide anions. The A^+ -cation is twelve-fold coordinated by halide anions, occupying the cuboctahedral gap of the network and balancing the charge of the MX_3 extended anion. The filling sizes of the

ions are decisive, which framework the set of the “A”, “M” and “X” ions adopt. This yields the Goldschmidt’s Tolerance Factor concept:

$$(R_A + R_M) = t\sqrt{2}(R_M + R_X)$$

with R_A , R_M and R_X as ionic radii of the corresponding ions.^[11–13] For most 3D perovskites, a value of $0.8 \leq t \leq 1.0$ is found empirically. The theory is based on the simplified assumption that all ions are treated as rigid spheres. For elementary ions this is mostly correct, but organic cations have a much more complex structure and pose a greater challenge. Therefore, it is assumed, that the molecule may rotate freely about its center of mass. Taking these assumptions into account, there are several, small organic cations that can be incorporated into the perovskite network.^[14] In addition to the sizes of the radii, the functional group that can interact with the anionic perovskite network is essential. On the one hand, it must compensate for charge, and on the other hand, it should contain a protonated cationic head group in order to be able to form hydrogen bonds with the anionic octahedra.^[12] Therefore, an ammonium group is well suited as head group for

organic cations. Calculations of more than 2500 amine-metal-anion permutations suggest the potential existence of more than 600 hybrid perovskites, which still remain undiscovered.^[15] In the case of lead iodide and bromide, formamidinium halide ($(\text{CH}(\text{NH}_2)_2\text{X}=\text{FAX})$) and methylammonium halide ($(\text{CH}_3\text{NH}_3\text{X}=\text{MAX})$) were found to be the most suitable components.^[12,16] Although the class of lead-halide perovskites has been known since the late 19th century^[17], a detailed structural characterization was published not before 1978 by Weber *et al.*^[18,19] Interestingly, the choice of halide in MAPbX_3 perovskites has a high impact on the crystal structure formed varying from tetragonal ($\text{X}=\text{I}$)^[20] to a cubic structure ($\text{X}=\text{Br}, \text{Cl}$)^[21,22] at ambient conditions. The composition mainly affects the electronic and optical properties, which will be discussed below.

Optical band gap of 3D perovskites

Not without reason, lead perovskites have been extensively studied in the last decade. Their optical and electronic properties stand out compared to other classical semiconductors.^[23] A simple, continuous anion exchange (Cl to I) allows easily tunable band gaps from UV to near-IR wavelengths, resulting in a wide color range, shown in

Figure 2.^[7,24–27] The exact halide composition can be adjusted before preparation, but also post-synthetically.^[28] The band gap engineering can be explained by the electronic band structure of the compounds. The electronic configuration of $\text{Pb}(\text{II})$ is $6s^26p^0$, while the halides have a configuration of np^6 ($n=3-5$ from

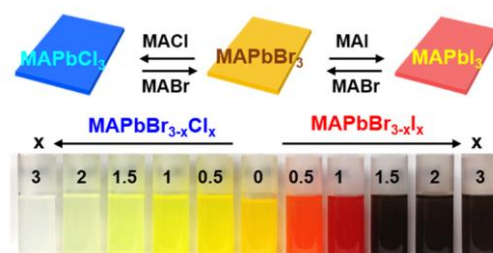


Figure 2 - MAPbX_3 perovskite materials with varying anions ($\text{X}=\text{Cl}, \text{Br}, \text{I}$). Taken from ref. [28].

Cl to I). The organic cation has no contribution to the electronic band structure and is therefore neglected. The conduction band (CB) consists of σ -antibonding Pb 6p and halide np orbitals. The valence band (VB) consists of σ -antibonding Pb 6s and halide np orbitals, which is dominated by the halide orbitals.^[29] Therefore, the energy of the valence band maximum (VBM) is strongly dependent on the halide, showing a downshift from iodine to chloride. The VBM and CBM both lie at the R point of the Brillouin zone, and hence the lead halide perovskites are direct semiconductors.^[29] It must be mentioned here that for MAPbI_3 the VBM and CBM are slightly shifted to R, as a result of the spin-orbit-coupling, as Pb and I are heavy elements.^[30]

Furthermore, theoretical calculations revealed that the band gap is strongly affected by the largest metal-halide-metal bond angle, that can be adjusted by the MX_6 octahedra tilting. This is mainly influenced by the size of the organic cation, which therefore has an indirect influence on the band gap.^[31,32] Thus, the choice of cation can have a major impact on the band gap. At the same time, the structural dynamics of the rotating organic cation strongly affects the optoelectronic properties of the 3D perovskite materials.^[33–35] It is suggested, that the “soft” nature of the hybrid perovskites is the core to their

exceptional optoelectronic properties. The interionic interactions allow molecular motions and ion migration on multiple timescales. These properties strongly deviate from the classic conception of charge transfer and optical absorption in a semiconductor, where ions are displaced only because of harmonic vibrations.^[36] For instance, the mobility and lifetime of charge carriers are increased at low temperatures in contrast to classical semiconductors.^[33] This is explained by the decreased dynamical motion of the MA cation at low temperatures. Its low symmetry and permanent dipole moment can result in a variety of orientations inside the crystal lattice. On cooling, the motion decreases and ordered domains form, also leading to changes in the geometry of the unit cell^[37] and furthermore is linked to its dielectric response^[38], ferroelectric behavior^[39,40] and the hysteresis of the I-V-curve.^[41,42] Selig *et al.* propose that H-bonding of the amine has a high impact on the rotation of the organic cation. The rotation varies with the size and polarizability of the anion (Cl, Br, I).^[43] They state that H-bonds preferably form with increasing polarizability, which increases with the size of the anion (from Cl to I). Consequently, the rotational motion decreases with increasing anion size. Interestingly, they find much slower rotation dynamics in mixed halide perovskites. This is due to symmetry breaking within the perovskite unit cell, in some cases even causing partial immobilization.^[43]

Defects in 3D perovskites

But not only the organic cation can move in these “soft” materials. The ion migration observed in hybrid perovskites often refers to the halide species.^[36,44,45] This effect is detrimental to the materials as it leads to unfavorable degradation.^[46] Based on these observations, the enormously increased stability of the lead bromides and chlorides, compared to the iodides can be explained. The activation energy for bromide migration is severely reduced in comparison to iodine. Despite this, the diffusion is much slower, presumably due to a lower entropic change during ion migration.^[47]

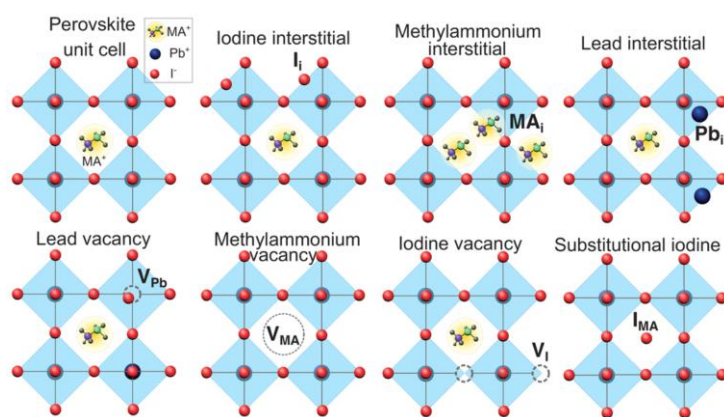


Figure 3 - Typical defects in MAPbI₃; taken from ref. [49].

However, it is believed that ion migration has not only disadvantages for the hybrid perovskites. The secret of the high-performance semiconductors lies in their high tolerance for defects *and/or* a low defect density due to self-healing. To date, scientists have not found an unambiguous answer to this extraordinary characteristic.^[48] Nevertheless,

it is clear that defects have little effect on optoelectronic properties compared to classical

semiconductors. The typical defects for MAPbX₃ perovskites are shown in **Figure 3**.^[49] The term "self-healing" refers to a material that is capable of autonomous repair of damage without external influences.^[50] In lead perovskites this effect is attributed to the A-cation, which migrates through the material. Investigations have shown, that FA⁺ heals best the bulk, Cs⁺ protects best the surface, as it is the least volatile and MA⁺ passivates the defects via CH₃NH₂ (mainly from photodissociation) binding to Pb²⁺.^[51] At the same time, very low defect densities are found in halide perovskites. Again, it must be pointed out that such low defect densities for classical semiconductors are otherwise obtained only with great effort and care.^[52]

Charge carrier dynamics and excitons

Recent studies demonstrate, that defects even seem to have a positive effect on charge carrier transport.^[49] Photogenerated charge carriers are trapped at defects, but the dominant part of the defects releases the free carriers after trapping. Active detrapping of carriers is the secret of the efficient charge transport. The defects preserve charge carriers from recombination. Therefore, the carrier's diffusion length is several times higher than the thickness of typical solar cells, which allows the collection of 99% of the charge carriers without significant losses.^[49] These properties, among others, make it an ideal reference system for direct semiconductors.

Understanding the dynamics of photoexcited charge carriers in lead perovskites is of fundamental importance for the optoelectronic properties of the semiconductor. Excitation above the band gap results in electron-hole pairs. Due to excess energy they are called "hot carriers". Through thermalization, namely by emitting optical phonons, the charge carrier relaxes down to the electronic band-edge.^[53] These charge carriers now either may be free charge carriers or excitons. Droseres *et al.* detected both excitons and free charge carriers at low excitation of MAPbBr₃. At high excitation, however, the free charge carriers convert to excitons due to their high density.^[54]

Here it is already evident, that the consideration of free charge carrier and exciton dynamics in hybrid perovskites proves to be very complex, as a wide variety of mechanisms are present, all contributing to the observed effects. For example, depending on the measurement method chosen, the charge carrier mobilities differ enormously.^[55] However, one highly intriguing aspect of lead perovskites should be highlighted here: the so-called photon recycling. By recombination of charge carriers a photon is emitted, which is however immediately absorbed by the material again.^[56] Upon repeated recycling charge carriers migrate over long distances.^[57] Recent findings show that exciton hopping (*via* Förster energy transfer) also contributes to the extremely high charge carrier mobilities.^[58] Furthermore, enormous differences between the bulk phase and nanocrystals are revealed, discussed in the following.

Nano- and microcrystals of 3D perovskites

Semiconducting nanocrystals (NCs) have been extensively studied because their fundamental optical and electronic properties change tremendously compared to the bulk phase.^[59–62] Hybrid perovskites in particular show very weak photoluminescence quantum yields (PLQY) if they are in bulk phase. As NCs, on the other hand, they exhibit extremely high PLQYs (up to 80%-100% for CsPbX₃) which is mostly attributed to the reduction of surface trap states passivated by surfactants on the surface.^[54] Today, they show great promises for the application in solar cells^[63], lasers^[64] or light emitting diodes (LEDs)^[65]. For the first time in 2011 Im *et al.* demonstrated the use of MAPbI₃ NCs in a TiO₂ matrix as potential sensitizer for photovoltaics.^[66] As recently as 2014, Schmidt *et al.* reported the synthesis of MAPbBr₃ NCs using medium-lengthed alkyl ligands as capping agents.^[67] Since then, extensive research has been conducted into the production of lead perovskite NCs.^[24,68–70] Typical approaches for the synthesis are ligand-assisted reprecipitation (LARP) or hot-injection techniques^[70,71]:

- The LARP method uses long-chain alkyl ligands, which inhibit crystal growth in a certain direction as they coordinate to the surface. Control over crystal size and shape is possible through the reaction temperature^[24,72] and the concentration of the ligand.^[69]
- In the hot injection method, the components are added as precursors to a hot solution to achieve rapid crystallization. Thus, monodisperse cubes in a size regime of 5-50 nm could be prepared by dissolving the starting salts (FAX and Pb(II) acetate) in octadecene and adding oleylammonium bromide (OLABr) in the presence of oleylamine (OA) at 130 °C.^[71] By using benzoyl-halides as halide source, even monodisperse MAPbX₃ particles could be obtained, which seems difficult with other methods.^[73]

The above-mentioned methods belong to the bottom-up approach, where molecular precursors are assumed. Top-down methods are much rarer, but are of interest for large-scale applications. Therefore, the ultrasonification of large crystals in solution^[74] and ball-milling^[75] were proposed as low cost and efficient synthesis of lead perovskite NCs.

A notable byproduct of many LARP synthesis were extremely thin nanoplatelets which exhibited quantum confinement effects.^[76] They showed drastically different properties, compared to their 3D related ones.^[77] To understand the formation of nanoplates, their optical and electric properties, low dimensional perovskites and their analogs are presented below.

2.1.2 Low-dimensional layered hybrid perovskites

Crystal structure of two-dimensional (2D) layered hybrid perovskites

Low dimensional perovskites are formed, when the small A-cation is substituted with a larger cation ($R-NH_3X$), exceeding the space given by the Goldschmidt-tolerance factor.^[12,14,78,79] The structure directing larger cation “cuts” the perovskite structure in a specific crystal direction, resulting in layered two-dimensional (2D) systems. **Figure 4** shows the three possible classes of layered hybrid perovskites (LHPs). Cutting in (100) direction (**Figure 4a**) layers of corner-sharing MX_6 -octahedra are formed, which are the most common layered hybrid perovskites (LHPs).^[11,77,79] If the small organic cation A is completely replaced by $R-NH_3X$, alternating layers of the organic ligands and the inorganic MX_6 octahedra are formed. With the incorporation of the small cation A, the structural properties of the 2D LHPs and the 3D perovskite are combined, and quasi-2D phases are obtained. These extraordinary crystal structures were named Ruddlesden-Popper phases (RPPs) after their discoverers and have the general formula $(R-NH_3)_2A_{n-1}M_nX_{3n+1}$ (with $n=2, 3, \dots$).^[80] Their crystal structure is shown in **Figure 5**.

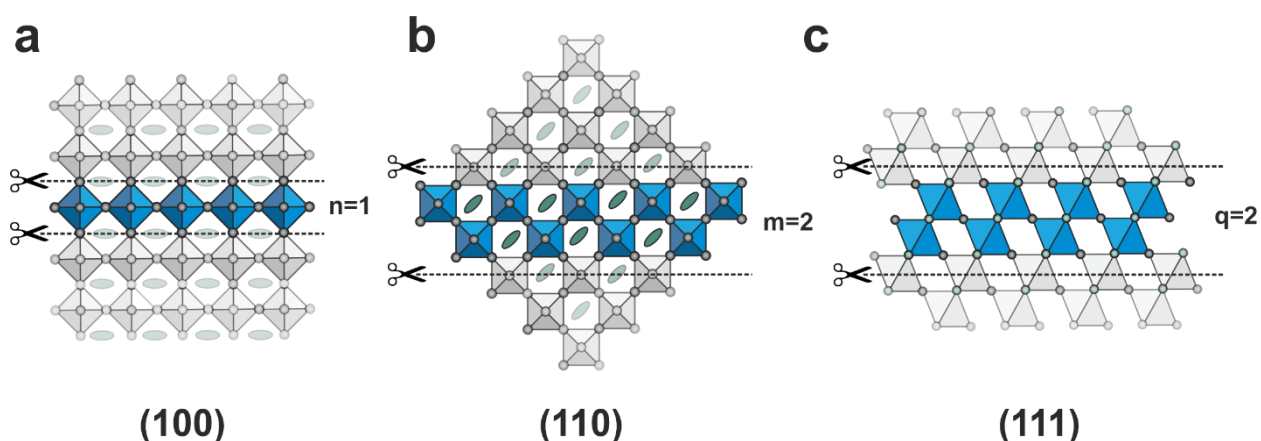


Figure 4 - Scheme of the layered perovskites structures, that can emerge through a cut of the perovskite structure in a certain crystal direction. a) layered perovskite in (100) direction with a layer thickness of $n=1$ having the general formula $(R-NH_3)_2A_{n-1}M_nX_{3n+1}$, b) layered perovskite structure in (110) crystal direction with a layer thickness of $m=2$ having the general formula $(R-NH_3)_2A_{m-1}M_mX_{3m+2}$ and c) layered perovskite structure in (111) crystal direction with a layer thickness of $q=2$ having the general formula $(R-NH_3)_2A_{q-1}M_qX_{3q+3}$.

When cutting in the (110) crystal direction one-dimensional (1D) chains of corner-sharing MX_6 octahedra are obtained. LHPs are obtained only from a layer thickness of $m \geq 2$ with the general formula $(R-NH_3)_2A_{m-1}M_mX_{3m+2}$ (see **Figure 4b**). There are considerably fewer known compounds for this more exotic structural class^[81–85] and to date no known quasi-2D phase with incorporated MAX. This is due to the organic cation $R-NH_3$, which needs to exhibit strong structure-directing properties. If the structure is sliced in the (111) crystal

direction zero-dimensional (0D) clusters with $q=1$ ^[86] or 2D layers with $q\geq 2$ having the general formula $(R-NH_3)_2A_{q-1}M_qX_{3q+3}$ are formed (see **Figure 4c**).

The selection of the large cation $R-NH_3$ is decisive for which structures can be obtained. Intramolecular interactions lead to strong templating effects and may influence the crystal structure tremendously.^[87]

Synthesis of colloidal perovskite nanoplatelets

As previously mentioned, the incidental synthesis of atomically thin nanoplatelets was observed in the LARP method for NC formation.^[76] In 2015, multiple groups reported the synthesis of colloidal perovskite crystals, which were reminiscent to the RPPs but dispersed in solution.^[69,76,88–90] RPPs are therefore stacked nanoplatelets with electronically decoupled inorganic layers. The structure-directing ligands are those used to inhibit crystal growth in LARP methods using medium- to long-chained ammonium alkyls. It seems that the colloidal platelets have the same range and composition with identical optical properties as the classical 2D LHPs.^[91,92] The platelets lateral extension may range from tenths of nanometers^[88–90] up to several micrometers^[91,93] without losing their quantum confinement.

Optical and electrical properties of LHPs

Using the LARP method, it was also obvious to achieve RPPs with layer thicknesses of $n\geq 2$. Sichert *et al.* observed decreasing quantum confinement with increasing MAX concentration.^[69] **Figure 5** shows why this effect is observed.

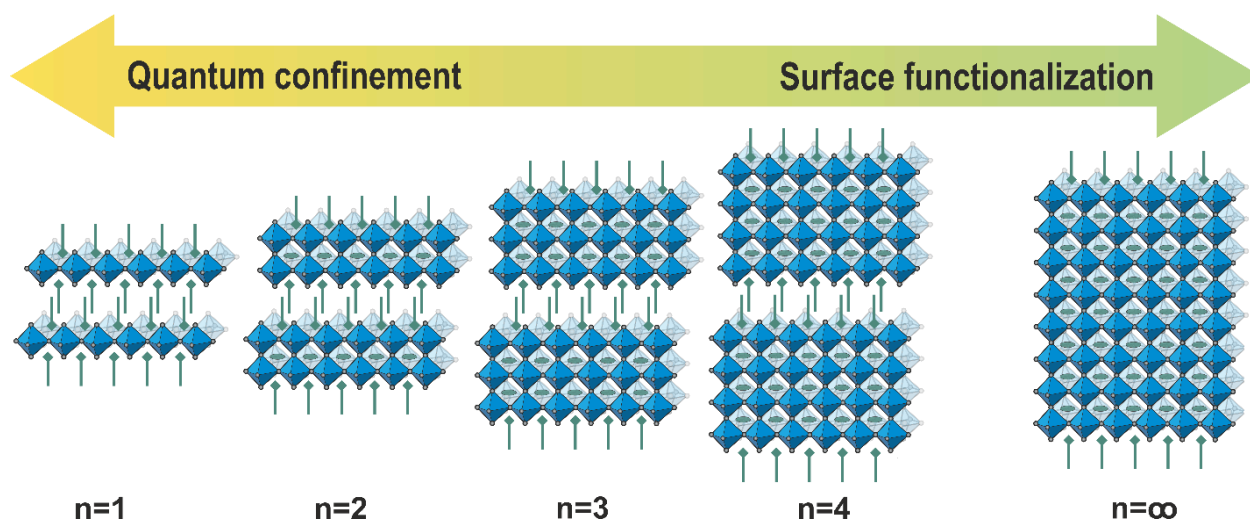


Figure 5 - LHPs of the Ruddlesden-Popper type with the general formula $(R-NH_3)_2A_{n-1}M_nX_{3n+1}$ with $n=1,2,3,4,\dots \infty$. The quantum confinement increases with decreasing layer thickness.

RPPs are formed by adding small cations that can be incorporated into the structure and large surface-coordinating cations that cut the structure ($R-NH_3X$). This means that the large organic cations have a structure-directing effect when they are incorporated into the crystal, but at low concentrations they can also “only” functionalize the surface.

Depending on the layer thickness, the band gap increases by up to 0.75 eV from the initial band gap (e.g. $E_{\text{gap}}=1.50$ eV for MAPbI_3 and $E_{\text{gap}}=2.35$ eV for $(\text{CH}_3(\text{CH}_2)_3\text{NH}_3)_2\text{PbI}_4$, $n=1$).^[77] The consequence of the vertical confinement to the octahedral network are decisively reduced electronic state dispersions. Below a certain size, the energy spectrum becomes discrete and the energy required to generate charge carriers is blue shifted. From a layer thickness of $n=5$, the quantum confinement no longer plays a role.

The LHPs also show increased stability compared to the hybrid 3D perovskites^[94,95], which makes them highly attractive for photovoltaics.^[96,97] Comparable light effective masses for electron and hole carriers with those of MAPbI_3 result in efficient solar cells. Since the layer thicknesses n differ greatly in their optoelectronic properties, a monodisperse layer thickness distribution is extremely important.^[88,89,91] However, until now it is difficult to synthesize monodisperse layer thicknesses, because mostly mixtures of the ($n=1,2,3,4\dots$) layer thicknesses are obtained using the LARP method.

In addition to quantum confinement, the layers are also dielectrically confined by the surrounding organic cations. The alkylammonium chains form a barrier layer between the semiconducting lead halide layers. The relative permittivity (dielectric constant) decreases drastically at the interface and the electric field generated by a charge extends into the lower dielectric constant medium, where it is screened less effectively.^[98] This effect induces excitonic absorption of the inorganic layer.^[99] The small dielectric constant of the barrier layer makes the Coulomb interaction between the electron and hole stronger, therefore, large exciton binding energies are found for the LHPs.^[100,101] The length of the alkyl chain has a negligible effect, as the optical properties do not alter, regardless of the Pb-Pb distance between two separate inorganic layers.^[102]

Alkylammonium cations (R-NH_3^+) are very useful for the synthesis of NCs and LHPs as they inhibit crystal growth in one direction. Nevertheless, they have an insulating effect on the semiconducting phase perpendicular to the layers. For this purpose, more functional surfactants can be introduced to the perovskite network. Organic molecules such as chromophores, photoswitches or conductive ones may interact with the semiconducting layers to achieve a synergetic combination.^[10,103]

2.1.3 Diversity of layered hybrid perovskites

Influence of the organic cation

LHPs can be functionalized to a much higher degree than their 3D relatives, due to the significantly larger number of molecules that can be incorporated.^[84,104–106] The inorganic perovskite layer, which consists of corner-sharing metal-halide octahedra, provides a specific area for the coordinating organic cation. The cross-sectional area of the organic cation must fit within the interstitial space between four terminal halide ions of four adjacent MX_6 octahedra.^[12] Increasing the cross-sectional area of the organic cation will

influence the orientation of the cations inside the lattice and affects the largest metal-halide-metal bond angle. The reduction of the optimal bond angle of 180° alters the band gap, which increases continuously.^[104] The connecting head group also plays a major role here. Usually, at least one methylene group should be present between the functional organic molecule and the head group to stabilize the 2D layered structure.^[107] A methyl ammonium group ($-\text{CH}_2\text{NH}_3$) may lead to more strain than an ethyl ammonium group ($-(\text{CH}_2)_2\text{NH}_3$) and therefore a smaller metal-halide-metal bond angle and consequently a higher band gap.^[107]

Another aspect of hybrid materials is evident at low temperatures. Upon cooling a phase transition may occur which is associated with the melting temperature of the organic cations. This can also lead to changes in the band gap.^[102] The optical and electronic properties are also highly dependent on the type of cation incorporated, as the relative permittivity changes tremendously compared to alkyl ligands.

Dielectric confinement in LHPs

As previously mentioned, the dielectric confinement plays an important role for the band gap and excitons. Replacing alkyl groups with a conjugated, aromatic cation, e.g. phenylethyl ammonium (PEA) the dielectric constant of the organic layer changes enormously. The Coulombic screening of excitons increases and the exciton binding energy decreases (e.g. from 320 meV in $(\text{C}_{10}\text{H}_{21}\text{NH}_3)_2\text{PbI}_4$ compared to 220 meV in $(\text{PEA})_2\text{PbI}_4$).^[108] By intercalating certain organic molecules between the ligands, it is even possible to increase the electrostatic screening and lower the exciton binding energy.^[109] At the same time, the electronic band gap decreases with the dielectric confinement.^[110] A further possibility to influence the band gap arises here through mixed cation systems. By using cations with differing dielectric constants, the band gap could be tuned.^[111] This approach could be beneficial, as cations can favorably interact with different surfaces.

Quantum-well structure in LHPs

Conjugated organic moieties (e.g. aromatic or thiophene derivatives)^[108,112] often result in heterojunctions, where the cation is an integral part of the energetic landscape. Thereby two different quantum-well (QW) electronic structures are observed: Type I QW, where both, electrons and holes are located on one species and type II QW, where (photo)excited charge carriers may be separated.

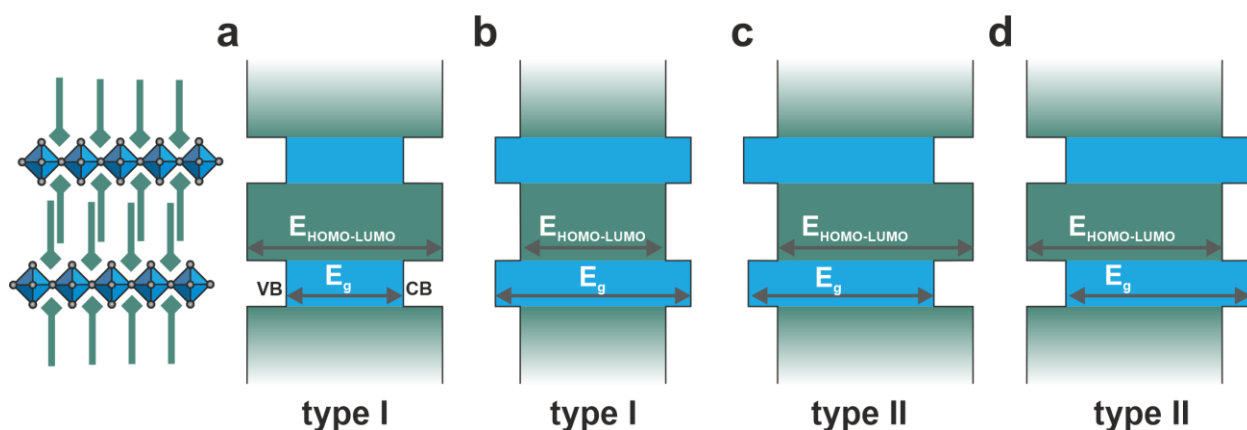


Figure 6 - Type I and Type II quantum-well (QW) electronic structures based on the energy alignment of the valence band maximum (VBM), conduction band minimum (CBM), highest occupied (HOMO) and lowest unoccupied molecular orbitals (LUMO) in hybrid LHPs. a)+b) Type I QW with one component (blue = inorganic MX_6 octahedra, green = organic cation) serving as quantum well. c)+d) Type II QW with a step-like arrangement allowing charge carrier separation.

What matters here, is the energy alignment of the valence band maximum (VBM), conduction band minimum (CBM), highest occupied (HOMO) and lowest unoccupied molecular orbital (LUMO).^[112] **Figure 6** demonstrates the possible alignments. Many LHPs exhibit the type I heterojunction^[105,113], however type II heterojunctions were reported as well.^[112,114]

The VBM and CBM are mainly affected by the inorganic metal-halide layers as only the p and s orbitals of the metal respectively the halide contribute to the density of states.^[29] Here, similarly, the band gap can be adjusted by continuous halide substitution.^[11,14,107]

Functional organic molecules

Through customization of the conjugated organic molecule, e.g. by substitution at the aromatic rings, it is possible to influence the energy alignment actively.^[115] Consequently, the optical properties of the materials are affected. Radiative recombination, namely photoluminescence may only occur, when the (photo)excited charge carriers are located on one species, thus in type I QWs.^[115] The radiative species can either be the inorganic semiconducting layer^[112] or the organic cation itself.^[116] It can therefore be assumed that charge carriers can be transferred between the organic and inorganic components of the

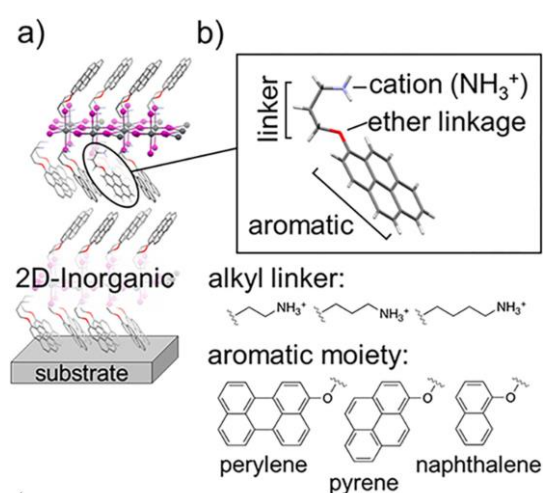


Figure 7 - a) Crystal structure of the $n=1$ LHP for $(\text{R-NH}_3)_2\text{PbI}_4$ and b) the used functional cations. Taken from ref. [117].

LHPs. This simultaneously leads to increased conductivity perpendicular to the layers compared to aliphatic cations.^[117] Passarelli *et al.* were able to significantly improve out-of-plane conductivity by using extended aromatic systems (perylene, pyrene, naphthalene). By ether linkage they attached an alkyl linker with ammonium head group to the molecules, shown in **Figure 7**. Depending on the orientation of the cations to each other the conductivity increased (edge-face better than edge-edge).^[117] Similar to aromatic systems, thiophene derivatives were used to improve the conductivity.^[112,115,118] Besides the aromatic molecules and chromophores, photoswitchable cations, namely azobenzene were also incorporated into the structure.^[119,120] These are distinguished by a change in conformation from a *trans* isomer to a *cis* isomer. A detailed consideration of azobenzenes follows in **chapter 2.2.1**. Furthermore, organic cations with polymerizable groups were integrated.^[121,122] Subsequent polymerization improved the stability of the material against external influences, as well as the rigidity leading to reduced phonons and consequently suppressed electron-phonon coupling.^[122] With this approach it might be able to separate charges, where one charge carrier is transported in the inorganic and one in the organic layer.^[11] Another interesting aspect is the use of chiral molecules. The intrinsically chiral materials are suitable for emitting or detecting polarized light.^[123,124] This makes them highly interesting materials for spintronic devices.

Photoluminescence and excitons in LHPs

Considering photoluminescence (PL) and excitons, LHPs show special features. Excitons can be classified in two categories: Wannier excitons which have small exciton binding energies (<100 meV), typically found in inorganic semiconductors and Frenkel excitons which have large exciton binding energies (~500 meV), found in organic semi-conductors.^[14] Due to their hybrid character both, Frenkel^[125,126] and Wannier^[102,108,127] are found in LHPs. Since they fall between the regimes they can have properties of both types.

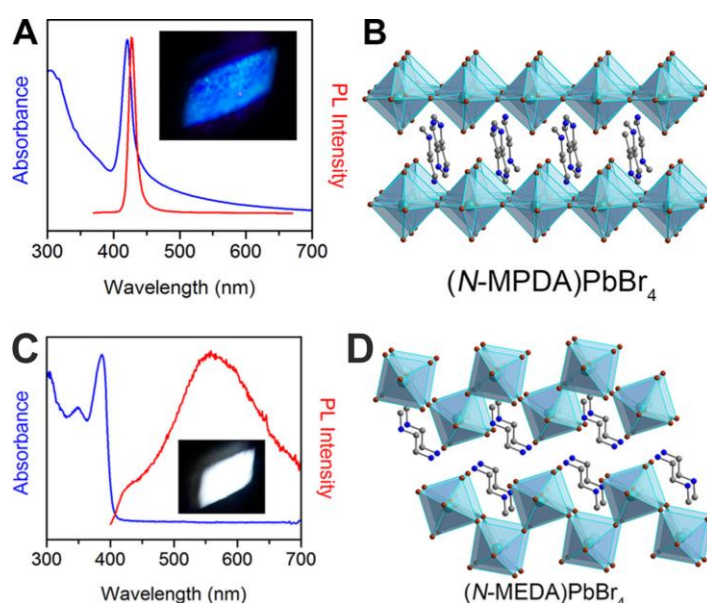


Figure 8 - a) Absorption and emission spectra with photograph and b) crystal structure of (n-MPDA)PbBr₄. c) absorption and emission spectra with photograph and d) crystal structure of (N-MEDA)PbBr₄. Taken from ref. [132].

The emission color of LHPs ranges over the whole visible spectrum from purple^[128], to blue^[85], green^[129], red^[130] and even near-IR^[131], depending on their composition and the organic cation used.^[132] This is due to narrow emission near the band edge, which is classically observed for direct semiconductors. Exemplary, a blue emitting (100) LHP is shown in **Figure 8a+b**. Even more exciting is the white light emission (a continuous emission from 400 to 700 nm) typically (110) LHPs exhibit.^[83–85,87,133] Most of the reports implicate exciton self-trapping as the dominant emission mechanism for the broadband PL in LHPs. Excitons are localized in a single unit cell due to a strong exciton-phonon-coupling and are trapped by their own lattice deformation.^[134] Therefore, self-trapped excitons can be considered as “excited-state” defects, as they create transient, light-induced lattice deformations. Self-trapped excitonic PL has a broad Stokes shift several times higher than the exciton binding energy, which causes the emission of white light. **Figure 8c+d** shows a white-light emitting LHP found by Smith *et al.* which exhibits a (110) structure type. Again the “softness” of the network set up the conditions for this extraordinary feature.^[135]

2.1.4 Applications of hybrid perovskites

The exceptional properties of hybrid metal-halide perovskites make them highly interesting low-cost materials in numerous applications (**Figure 9**).^[9] Here, only the most important of these applications will be mentioned for an overview. Probably the most famous application is, of course, solar cells for sustainable energy generation.^[6,53,136] Enormous research in the last 10 years in the field of photovoltaics achieved efficiencies of 25.7 % in 2021 for single-junction cells (comparatively 3.8 % in 2011).^[137] High absorption coefficients in the complete visible range enable the production of ultrathin

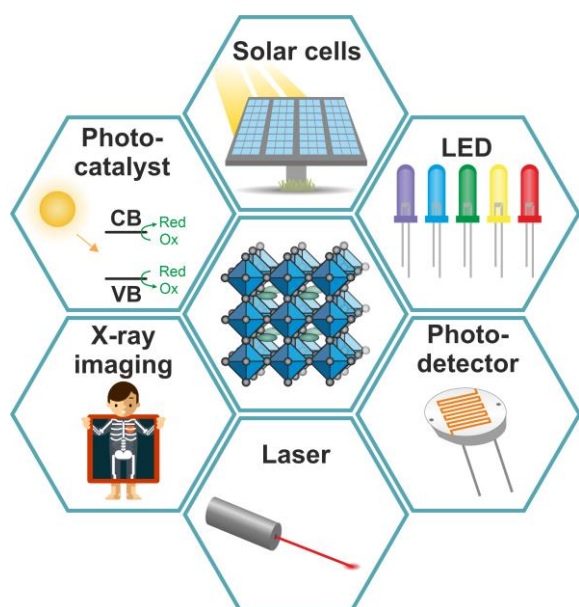


Figure 9 – Various applications of hybrid perovskites.

devices with films around 500 nm.^[138] Unfortunately, the classic 3D perovskites (e.g. MAPbI₃), which are commonly used for solar cells, are not very stable against environmental influences. Therefore, device architecture and synthesis methods were optimized to obtain higher stabilities. One approach to increase the stability is the use of nanostructured perovskite materials.^[139] Despite their increased stability, 2D perovskites in combination with 3D perovskites depict a further option.^[140] It has even been possible to produce high-efficient, pure RPP solar cells.^[141,142]

The second promising area of application are light emitting diodes (LEDs).^[143,144] High PLQYs and narrow emission spectra make them perfect candidates for low-cost and easy processable materials for LEDs.^[68,143] The high defect tolerance is also beneficial for this application.^[145] Due to their low stability, however, they must be protected from the environment, which can be done, for example, by embedding them in a polymer matrix.^[146] Therefore, for the sake of simplicity, all-inorganic CsPbX₃ are often used for LEDs.^[24,147]

Furthermore, stimulated emission (SE) is observed in halide perovskite NCs, which makes them a promising gain media for lasing.^[64] Both hybrid MAPbX₃ NCs and all-inorganic CsPbX₃ NCs, which were close-packed to thin films, demonstrated robust SE under femtosecond or nanosecond pulsed excitation.^[148,149] In order to achieve laser radiation by electrical pumping, the unfavorable organic ligands used for surface passivation still need to be replaced.^[149,150]

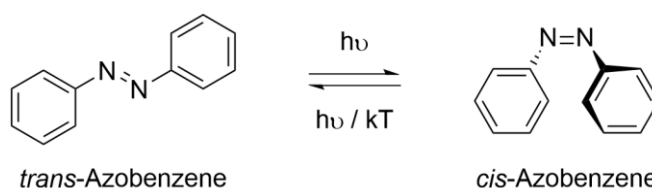
Hybrid perovskites may as well be used for photodetectors and field-effect-transistors owing to their strong optical absorption and ultralong carrier diffusion lengths.^[151,152] Due to a lower defect density 2D LHPs were considered as photoactive media for photodetectors, also because of their large surface area to volume ratio.^[153] Applications beyond the named include photocatalysis^[143], memory devices, X-ray detectors, Li-ion batteries, gas sensors or piezoelectric energy generators.^[154]

2.2 Ligand systems

2.2.1 Azobenzene

The unique photochemistry of azobenzene

The azobenzene molecule is characterized by its unique photochemistry and a simple isomerization upon photoexcitation. The photochrome, which by definition reversibly changes its color by light induction,



Scheme 1 - Photoisomerisation mechanism of azobenzene.

is composed of two phenyl rings bridged by an azo linkage (-N=N-; see **Scheme 1**, left).^[155] The extended aromatic structure gives rise to its strong optical absorption and the related optical properties.^[156] Typically, they are classified into three subclasses, shown in **Figure 10**: (a) (unsubstituted) azobenzene, (b) aminoazobenzene and (c) pseudo-stilbenes.^[157] The term *azobenzene* (or *azo*) refers only to the unsubstituted parent molecule, though it is now frequently used to describe the entire class of substituted azo molecules. The unsubstituted azobenzene molecule (a) especially

absorbs in the UV. The class of aminoazobenzene (b) is substituted with an electron donating group in ortho- or para-position (typically an amino-group, $-NH_2$), which shifts absorption features into the blue region. Lastly, the class of pseudo-stilbenes (c) is characterized by a strongly asymmetric electron distribution due to substitution in 4 and 4' positions with an electron-donating and an electron-withdrawing group. Furthermore, this causes a broad absorption in the visible.^[156] The dipole of pseudo-stilbene can be oriented in an electric field with a significant non-linear response.^[158]

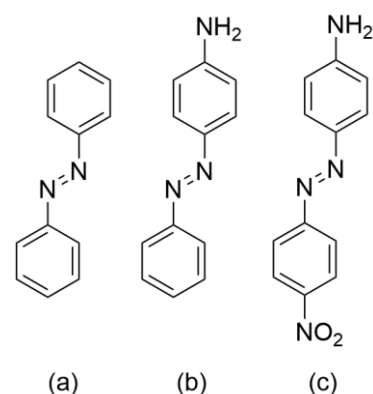
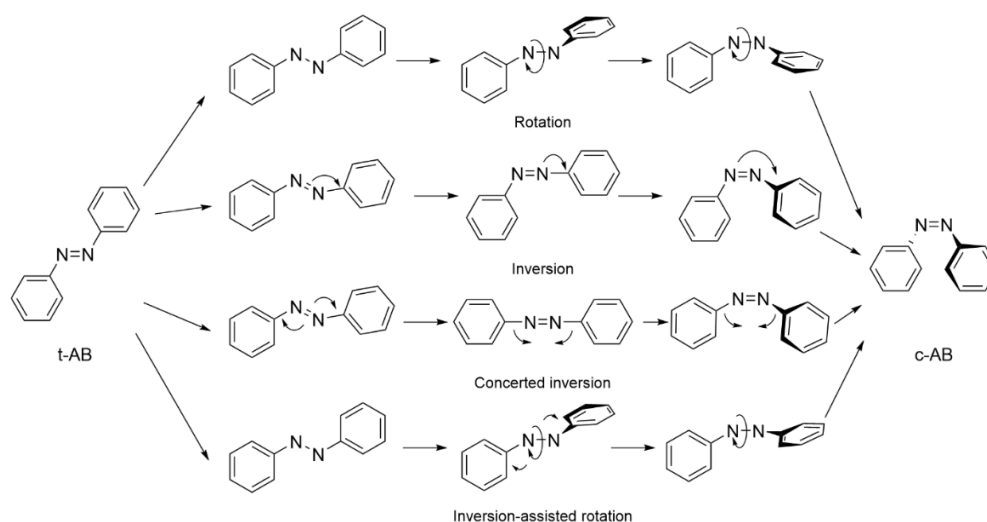


Figure 10 - Subclasses of azobenzene (a) azobenzene, (b) aminoazobenzene and (c) pseudostilbene.

It is known that substituents strongly influence the absorption spectra of azobenzene derivatives, which can be red-shifted in particular.^[159] At the same time, they also influence the photoisomerization from *trans* to *cis* isomer (see **Scheme 1**), both electronically and sterically.^[160] A fully reversible, efficient and fast photoisomerization occurs upon absorption of a photon of a certain wavelength, forcing the movement of the phenyl rings about the azo bond from the *trans* to the *cis* state.^[156] Isomerization occurs predominantly by excitation of the $S_2 \leftarrow S_0$ electronic state (a π to π^* transition), with a small contribution from the direct excitation through the symmetry forbidden $S_1 \leftarrow S_0$ (n to π^*) transition.^[161,162] Reverse isomerization occurs as well by absorption of a photon (typically in the blue region) or thermally, since *trans* is the thermodynamically more stable isomer.^[163,164] Therefore, the *trans* isomer is more dominant at high temperatures.

The switching behavior of azobenzene is well described in the gas phase^[165] and in organic solvents.^[166] Nevertheless, there are four mechanisms that are proposed for the isomerization, shown in **Scheme 2**.



Scheme 2 - Proposed mechanism for the photoisomerization of azobenzene.

The rotational pathway allows free rotation about the ruptured N=N π -bond, with a fixed N-N-C bond angle of 120° . For the inversion, the N=N-C angle increases to 180° and a transition state with one sp hybridized azo-nitrogen atom results. The concerted inversion involves a linear transition state with increased bond angles to 180° . Inversion-assisted rotation occurs under large changes in the C-N=N dihedral angle and a smaller change in the N=N-C angle, simultaneously. Experimental observations are often explained by several isomerization pathways.^[162] During the isomerization, not only the molecules geometry changes from planar for *trans*^[163] to non-planar for *cis*^[167], but also the dipole moment changes tremendously from $\mu_{trans} = 0.0$ D to $\mu_{cis} = 3.0$ D due to redistribution of charges.^[168]

Since isomerization is an equilibrium, a photostationary state is observed for each system. This state is unique for each azobenzene derivative, as it strongly depends on the quantum yields of the isomerization processes (Φ_{trans} , Φ_{cis}) but also on the thermal relaxation constant (k).^[156] Therefore, the lifetime of the photostationary state varies from a couple of seconds to several days and weeks, depending on how stable the *cis*-isomer is.^[169]

Several methods can be used to determine as to when the photostationary state has been reached. UV/Vis absorption spectra are often recorded because the *cis*-isomer absorbs more strongly in the blue range but more weakly in the UV-range.^[170]

Figure 11 exemplarily shows the change of the UV/Vis spectra during the isomerization by irradiation.^[171] In addition to the optical absorption spectroscopy, ¹H-NMR can be used as well.^[172] This takes advantage of the fact, that the chemical environment of the hydrogen atoms changes, what can be distinguished in NMR. The chemical shift of the aromatic H atoms is thereby shifted to smaller values from *trans* to *cis* isomer.

Azobenzene in smart materials

With so-called “smart” materials it is possible to modify their physical or chemical properties upon application of an external stimuli. Since azobenzene is easy chemically accessible, it is present in numerous smart materials that are switchable by light.^[162,173] It is used in polymers^[174], soft matter^[175], photonics^[176], sensors and actuators^[177] and molecular electronics^[178].

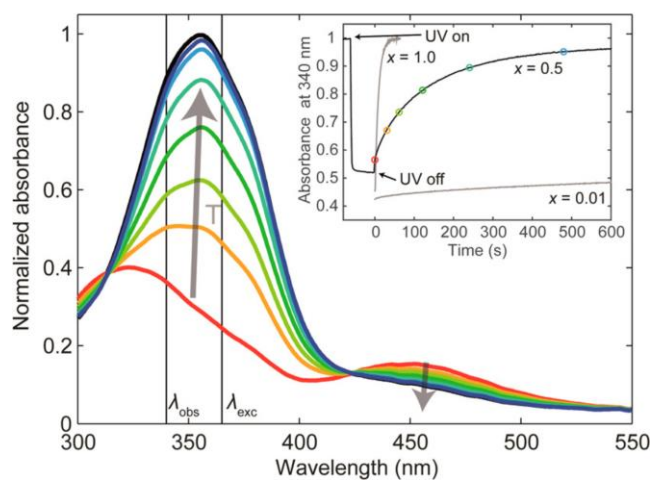


Figure 11 - UV/Vis absorption spectra of the thermally induced isomerisation from *cis* (red) to *trans* (purple) isomer. Taken from ref. [171].

Due to the reversible change in geometry from *trans* to *cis*, materials can be altered mechanically, but also electronically. For example, polymers can be elongated or contracted by optical excitation.^[174] Also in liquid crystals a phase transformation can take place due to the photoinduced isomerization.^[179] This property is also exploited for drug-delivery processes. Irradiation of macromolecular amphiphiles containing azobenzene can generate self-assembled host-guest structures (i.e., vesicles) to take up and release drugs reversibly.^[180]

When using azobenzene in molecular electronics, a distinction is made between single molecule and ensemble molecule junctions.^[178] In single molecule junctions a sole azobenzene derivative is trapped between two electrodes. Thus, it was possible to determine the conductance of a single azobenzene molecule in the *trans* and in the *cis* conformation. Kim *et al.* demonstrated, that the *cis* isomer is more conductive than the *trans* isomer.^[181] This trend is also observed in self-assembled monolayers (SAMs) on a (111) Au surface. The resistance of the ensemble molecule junction decreases 30 times upon photoisomerization.^[182] The incorporation and subsequent isomerization of azobenzene in a polyaniline film also increases its conductivity.^[183]

Azobenzene and semiconductors

Since, on the one hand, the conductivity of the azobenzene system can be modified by the photoswitching and, on the other hand, an electronically active chromophore is present, the combination of azobenzene and semiconductors appears to be fascinating. Azobenzene is often used for coating e.g. for photoactive surface patterning^[184], data storage devices, molecular motors or switches.^[162] Interestingly, most studies use polymers^[185], silica or gold surfaces^[184] as substrate, but semiconductors are rarely used. Is there a reason for this? Already in 2001, azobenzene was incorporated into LHPs by Era *et al.*^[119] They observed the incorporation of the azo ligand into the LHP structure and the controlled orientation of azobenzene between CdBr₄-layers. However, they treated the azobenzene as an ordinary chromophore and did not exploit the photoswitchable properties. Later, Sasai *et al.* demonstrated the incorporation of azobenzene in a

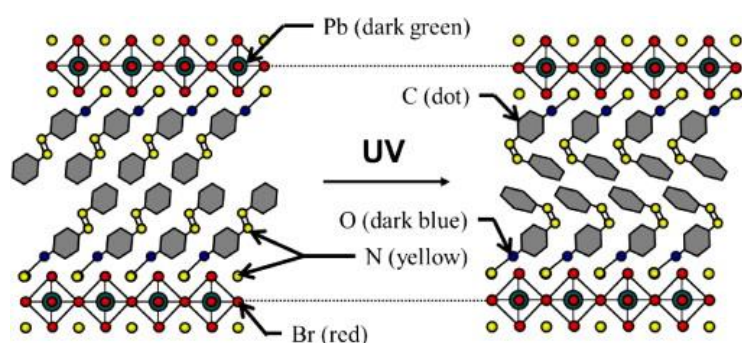


Figure 12 - Schematic model structure of azo based LHPs before (left) and after (right) UV irradiation according to Sasai *et al.*^[120]

lead-based LHP with subsequent photoisomerization (see **Figure 12**).^[120] Their observations are based on the change in absorption of the materials due to UV irradiation. In fact, they observe an abnormal photoisomerization, i.e. an increased probability for an $n-\pi^*$ phototransition.

However, they have no explanation for this. Further, structural changes, as well as stress or strains of the crystals due to the tilting of the molecule were not considered.

In 2018 Torres *et al.* calculated the photoswitching behavior of azobenzene on TiO₂, a wide-band gap semiconductor.^[186] Their simulations showed an ultrafast charge carrier transfer from the excited azobenzene to the TiO₂. The transfer causes a transient oxidation of the chromophore and suppresses the photoinduced isomerization.

It now remains to be clarified why photoisomerization is either amplified or prohibited by a semiconductor, and what this depends on.

2.2.2 Ferrocene

Ferrocene as versatile redox-switch

Shortly after the discovery of ferrocene (Fc) in 1951, its unique structural features, as the first sandwich compound ever discovered, were characterized by Woodward *et al.*^[187]

They suggested two parallel cyclopentadienyl (cp) rings sandwiching an iron (II) cation (see **Figure 13**, left). The great stability of the compound against high

temperatures, air and all common organic solvents is attributed to its aromatic character.^[188,189] The organometallic nature of the molecule also makes it ideal for reversible redox reactions, since the Fe²⁺ cation easily oxidizes to Fe³⁺ and vice versa (**Figure 13**).^[190] Soon the Fc/Fc⁺ couple became iconic in electrochemistry, mainly for the fast and kinetically uncomplicated self-exchange reaction and its solvent independence for the redox reaction. In cyclic voltammetry a half-wave potential around 0.4 V (versus Saturated Calomel Electrode (SCE)) marks a (electro)chemically reversible single-electron oxidation.^[191] The exact value depends on the solvent, because the solvent molecules interact differently with the positively charged central iron. Through the introduction of substituents the redox potentials may as well be shifted.^[192] The cp-ring of the structure allows electrophilic reactions at the ferrocene itself leading to numerous Fc derivatives.^[189] Alternatively, there is also a large family of substituted cp ligands that generate Fc by treatment with Fe²⁺ salts.^[193] Thus, simple electron donating groups like methyl or *tert*-butyl units shift the redox potential significantly.^[192]

As well, biferrocenes are of interest, which are two Fc-units connected via two bridged cp-rings. Due to the two iron cores, single electron oxidation creates mixed valent systems (Fe²⁺/Fe³⁺). Mössbauer spectroscopy revealed both, localized and delocalized valency, depending on the counter anion and cp substituents.^[194]

Unlike photochromes (like azobenzene), the structure of Fc changes only marginally (a slight elongation of the Fe-C bonding distances) upon oxidation. And yet the electronic

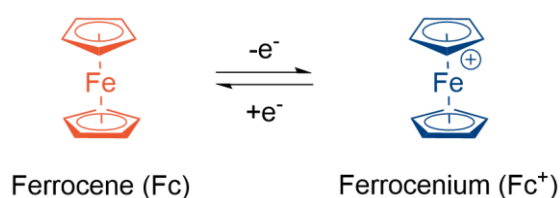


Figure 13 - Redox reaction of the ferrocene (Fc) / ferrocenium (Fc⁺) couple.

system changes enormously and so do the absorption bands, luminescence properties and many other physical properties, as magnetism, catalytic activity or relative permittivity.^[190,195–197]

Ferrocene in materials chemistry

Ferrocene has been used in a wide variety of materials and applications. For example, they are used in surfactants, surface-active molecules that form superstructures (e.g. micelles, vesicles, liquid crystals) in solution.^[198,199] By incorporating Fc, such structures can be made not only redox active, but also magnetic, for example. Application of a magnetic field can alter the aggregation behavior of such compounds.^[196] For example, a phase transformation can be achieved for liquid crystals via multiple stimuli (oxidation and application of a magnetic field).^[199,200]

Another very popular application of Fc is the use in polymers. It is either part of the main polymer backbone or integrated in the sidechains.^[189] Numerous Fc-based materials may find use in biomedicine, batteries, membrane fuel cells, sensors, aerospace materials, self-healing materials or electrocatalysis.^[201,202] Staff *et al.* demonstrated a nanocapsule based on a block copolymer containing Fc, where oxidation leads to swelling and release of a loaded dye.^[203] Thus, the polymer becomes hydrophilic after oxidation, which is also exploited in surface coatings to alter wettability.^[204]

It also becomes interesting when the redox activity is exploited for electronic and optical applications. For example, they are excellent for cathodic battery materials due to their air stability and fast electrochemical kinetics.^[205] The incorporation of Fc in metal organic frameworks (MOF) is a further benefit, since MOFs usually have localized electronic states.^[206] Mohammad-Pour *et al.* observed charge transfer due to self-exchanges (hopping processes) between oxidized and non-oxidized Fc units in the material, shown in **Figure 14**. In this way, an artificial conductivity can be created.^[207]

Besides electronic transfer for conductivity, Fc is a crucial element for excited state quenching of radiative states.^[195] In the reduced form (Fc), excited states of e.g. emitting dyes can be quenched via a photoinduced electron or energy transfer (PET).^[208,209] Whether an electron or energy is transferred depends on the excited species.^[195] A fast transfer prevents radiative recombination and the PL is quantitatively quenched. In contrast,

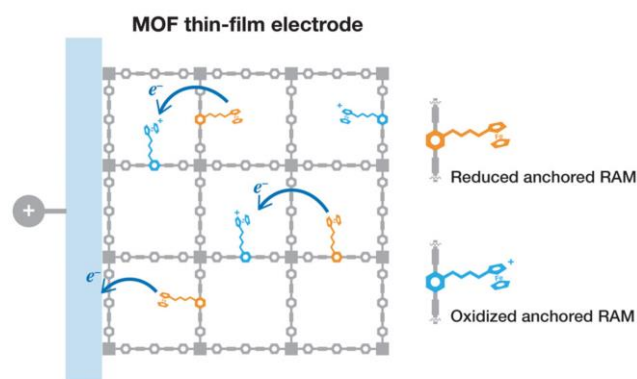


Figure 14 – MOF thin-film electrode containing redox active mediators (=RAM; Fc) enabling fast redox conductivity via hopping. Taken from ref. [207].

Fc^+ does not quench the excited states, so radiative emission can be turned on and off by controlling the oxidation state of Fc .^[195] The question that now arises: What happens when Ferrocene is combined with semiconductors?

Ferrocene and semiconductors

In some publications, Fc has been used to quench excited states of semiconductors, especially nanoparticles like CdSe or CdS .^[204-207] On the one hand, the distance of the Fc moiety is significant for the PET, since the length of the spacer determines the quenching degree of the system.^[211] On the other hand, chemical oxidation and reduction of the Fc ligands allows reversible on and off switching of the PL.^[212]

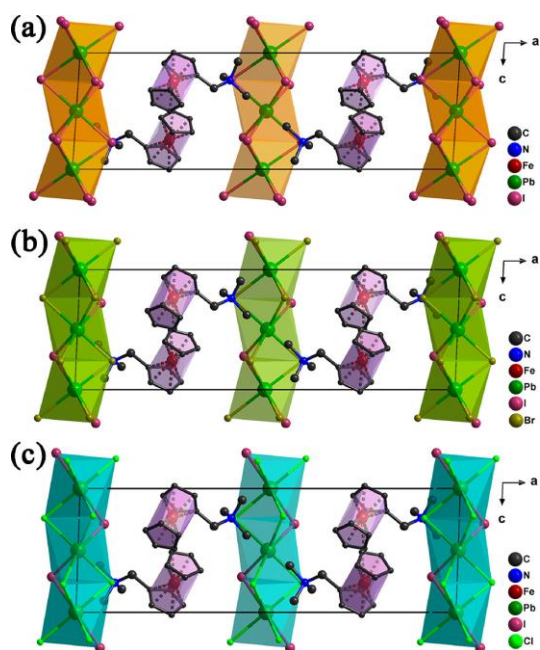


Figure 15 - Crystal structure of ferrocene containing 1D perovskites of a) $(\text{FMTMA})\text{PbI}_3$ b) $(\text{FMTMA})\text{PbBr}_2\text{I}$ and c) $(\text{FMTMA})\text{PbCl}_2\text{I}$. Taken from ref. [205].

Regarding Fc in combination with perovskite materials, only few publications exist up to date. With inorganic perovskite particles (CsPbBr_3) it was possible to proof photocatalytic properties of the perovskite particles by reducing Fc^+ to Fc . As well, PL quenching was observed when Fc was present.^[213] Interestingly, Fc can also be used as recovery shuttle for defects in hybrid perovskites.^[214] In both cases, however, no direct connection was established between the two compounds (e.g. with a linking headgroup).

In 2020 Zhang *et al.* were the first to present a Fc containing, semiconducting perovskite phase, shown in **Figure 15**. They used (ferrocenylmethyl) trimethylammonium (FMTMA) salts for the integration of the organometal into the lead halide network. They obtained face-sharing octahedra with varying halide composition (Cl, Br, I), which showed extraordinary piezoelectric properties. The anionic chains aligned along the b axis, resulting in a polar structure, that gives rise to the piezoelectricity. Via halide exchange they could even improve the piezoelectricity due to structural distortions.^[215] However, they did not investigate emission properties nor did they exploit the redox activity of the compound.

2.3 Preliminary Work

Prior to this work, a glycol-based precursor synthesis was established by Tom Kolk for the synthesis of hybrid perovskite nanoparticles with the composition $\text{CH}_3\text{NH}_3\text{PbI}_3$ (MAPbI_3) and $\text{CH}_3\text{NH}_3\text{PbBr}_3$ (MAPbBr_3).^[118,216–218] Triethylene glycol (TEG) serves as solvent for the starting materials $\text{CH}_3\text{NH}_3\text{X}$ and PbX_2 ($\text{X} = \text{Br}, \text{I}$), which can then be reacted in various synthetic pathways. Both single-source precursor are solid at room temperature, thus their crystal structure could be determined via single crystal X-ray diffraction.^[216,218] **Figure 16a** shows the crystal structure of the crystallized precursor with bromine having a composition of $(\text{TEG})_2(\text{CH}_3\text{NH}_3)\text{PbBr}_3$. The structure consists of 1D chains of face-sharing lead-bromide octahedra forming a hexagonal packing, analog to the CsNiBr_3 crystal structure.^[219]

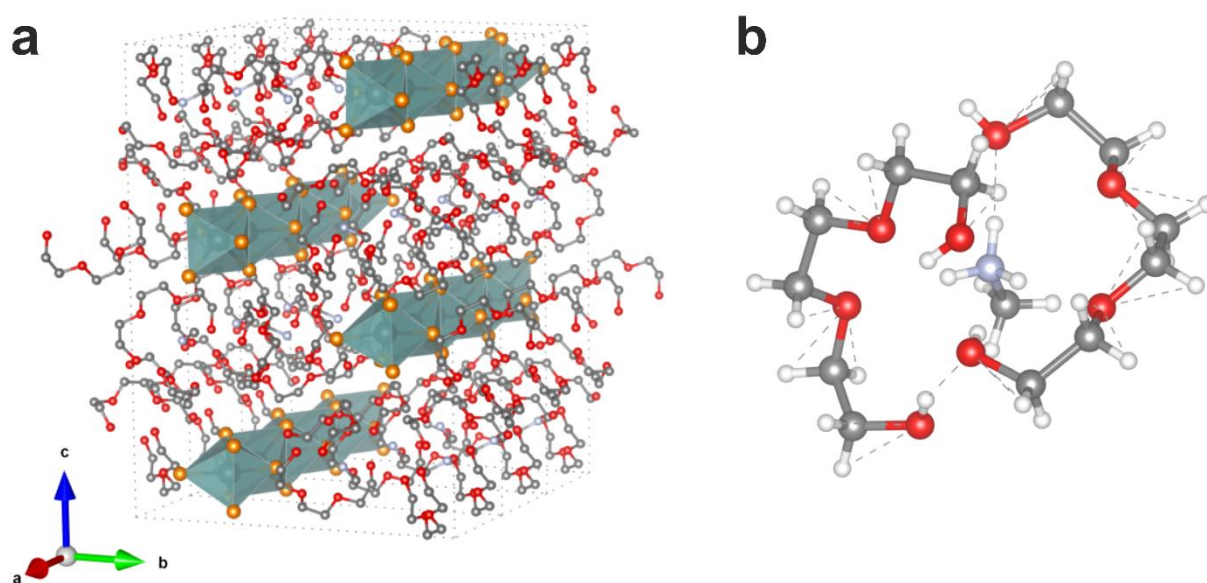


Figure 16 - a) Crystal structure of $(\text{TEG})_2(\text{CH}_3\text{NH}_3)\text{PbBr}_3$ (structure can be found at CCSD, number 1538521). Hydrogen atoms have been removed for clarity. b) Two TEG molecules chelating the MA^+ cation.

The distinctive feature of the precursor lies in the TEG molecules located in the space between the inorganic lead-bromide chains. Two of the uncharged molecules are able to chelate the methylammonium cation (see **Figure 16b**), which allows controlled conversion. The crystal structure of $\text{MAPbI}_3(\text{TEG})_2$ is reminiscent to the shown above and can be found in T. Kolk *et al.*^[216] Both precursor phases are solid at room temperature ($T_{\text{mp}}(\text{Br}) = \sim 35\text{-}40\text{ }^\circ\text{C}$ and $T_{\text{mp}}(\text{I}) = \sim 70\text{ }^\circ\text{C}$). In the melted state short chains of $[\text{PbBr}_3]_n$ are assumed to be randomly distributed in the solution.

Since 2015 a couple of techniques were developed for the conversion of the precursor to obtain micro- to nanosized perovskite particles. Thus, the precursor can either be converted via inverse temperature crystallization^[217,218] or a classical antisolvent synthesis.^[118,216] Both approaches will be discussed separately.

Antisolvent synthesis

The transformation of solid $\text{MAPbI}_3(\text{TEG})_2$ into MAPbI_3 could be initiated via a crystal-to-crystal reaction. Differential solubility is the key for the transformation. Using a suitable antisolvent, usually dichloromethane (CH_2Cl_2 ; DCM), the soluble TEG molecules are removed from the precursor phase, retaining the insoluble MAPbI_3 . This approach leads to porous particles, which unfortunately could not be further characterized (concerning their porosity) due to the low stability of the crystal phase and the porous structure.^[216] Precipitation in DCM of the diluted precursor solution (typically 0.1 M) gave poorly defined NPs with the composition MAPbI_3 . Adding a crystallization inhibitor to the antisolvent, the long-chain dodecylammonium iodide ($\text{C}_{12}\text{H}_{25}\text{NH}_3\text{I}$; DAI), enabled shape control, so that small cubic particles were obtained. When increasing the concentration of DAI plate-like particles were obtained, which formed RPPs. They exhibited quantum confinement effects as the dimensionality was restricted by the crystallization inhibitor.^[216] The conversion of the $\text{MAPbBr}_3(\text{TEG})_2$ precursor was also investigated as part of a bachelor thesis. Here, the same effect was achieved by using a crystallization inhibitor (dodecylammonium bromide = $\text{C}_{12}\text{H}_{25}\text{NH}_3\text{Br}$; DABr).^[220] In the scope of a Master thesis it was found that, depending on the solubility of the capping agent in the antisolvent, a dynamic exchange of ligands takes place at the surface of the growing particles. If there is low solubility, coordination of the ligands to the surface is preferred and particularly defined, large particles are formed. If the solubility is high, small particles are more likely to be formed, since the structures can dissolve and reform during particle growth. Therefore, the solubility, but also the concentration of the ligand in the antisolvent is crucial for the particles shape. For example, by changing the temperature, increased or decreased solubility can be achieved and the shape of the particles can be influenced.

The NPs obtained with DAI resulted in electrically insulating surfaces that hinders electronical communication between the particles. Therefore, it was obvious to develop a more functional crystallization inhibitor. A thiophene derivative with methylammonium headgroup and a hexyl chain (shown in **Figure 17a**) significantly improved the conductivity between the particles.^[118]

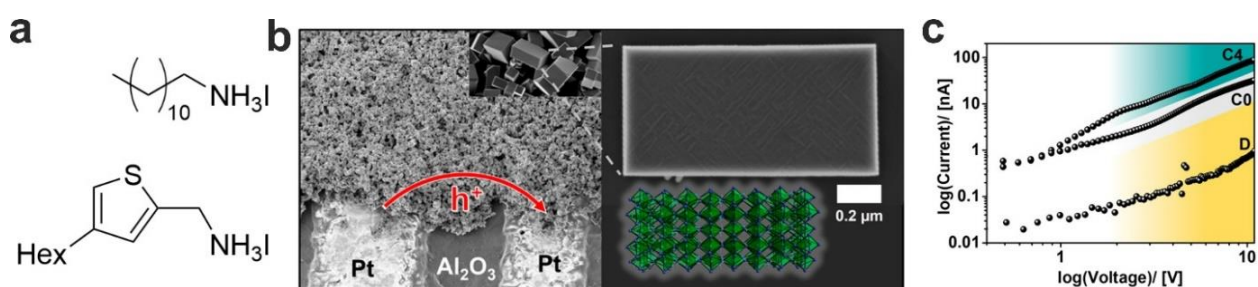


Figure 17 - a) chemical structure of DAI (top) and the thiophene derivative, b) micrometersized MAPbI_3 particles applied on a sensor, c) conductivity measurements of MAPbI_3 with surface functionalized particles (D = DAI, C0+C4 = thiophene capper with low (C0) and high (C4) concentration)

Since the solubility of the new capping agent is comparatively lower, micrometer-sized particles are obtained, seen in **Figure 17b**. The functionalized particles were then used in a photodetector device to investigate charge carrier transport between the particles. The particles indeed show reduced conductivity compared to the alkyl-functionalized particles (see **Figure 17c**).^[118] Further investigations with these particles revealed, that the capping agent enables surface passivation.^[221]

Inverse temperature crystallization

Hybrid perovskites show the unusual phenomenon of retrograde solubility and therefore the inverse temperature crystallization, usually applied for large single crystal growth.^[222] For this thesis this mechanism will not be exploited, but for the sake of completeness the results will be mentioned here.

The phenomenon of inverse temperature crystallization was likewise observed for the $\text{MAPbX}_3(\text{TEG})_2$ precursor phases. In a microwave assisted synthesis, hollow MAPbI_3 particles in the micrometer range were obtained, shown in **Figure 18a**.^[217] In an aerosol-assisted crystallization, the $\text{MAPbBr}_3(\text{TEG})_2$ precursor

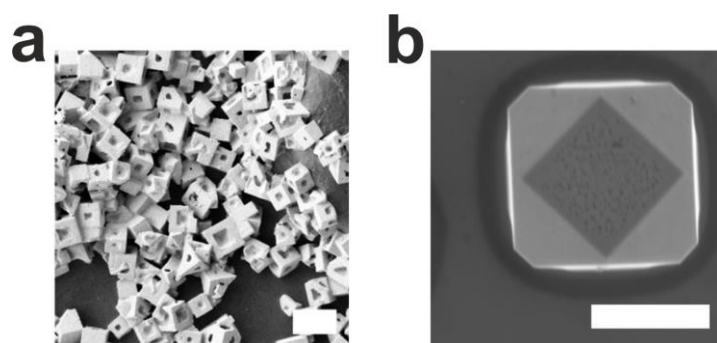


Figure 18 - Crystals obtained via a) a microwave assisted (scalebar = 5 μm) and b) aerosol assisted (scalebar = 1 μm) inverse temperature crystallization.

yielded micrometer-sized particles with unusual shape, as seen in **Figure 18b**. Observation of the photoluminescence revealed crystal-facet dependent lifetime of the photo-generated charge carriers.^[221] Further insights into the surface chemistry of the particles revealed the facet-dependent photoluminescence properties. A higher defect density in the (110)-facet of the crystals leads to faster radiative recombination and therefore shorter lifetimes.^[223]

2.4 Analytical Methods

2.4.1 UV/Vis spectroscopy

The absorption of photons in the UV to visible spectral range is one of the most important properties for semiconductor materials and conjugated molecules. The UV/Vis absorption spectroscopy probes the light absorption of a sample in the range of typically 300-1200 nm (depending on the experimental setup). Thereby, the excitation source is a visible and IR light emitter, usually a tungsten lamp, and a source for UV-light, a deuterium lamp. For absorption measurements, samples may be liquid (in a solution or dispersion) or thin films on a substrate. The easiest way to measure absorption is the transmission-mode, where excitation light passes the sample. Then, the intensity I_1 after transmission is compared to the incident intensity I_0 .^[224]

Absorption occurs when electromagnetic waves initiate the excitation of electrons from their ground state to a higher level. This can either be absorption bands, as observed in molecules with discrete molecular orbitals or quantum confined semiconductors with discrete energy levels. In bulk semiconductors, however, an absorption edge is present where photons can be continuously absorbed above a certain energy. This energy is given by the band gap, i.e. the distance between valence band maximum (VBM) and conduction band minimum (CBM). The energy of a photon is given by the equation:

$$E_{\text{gap}} = \frac{h \cdot c}{\lambda} \quad (1)$$

When measuring in transmission, two major issues have to be considered. First, scattering of light or reflection reduce I_1 , which is therefore not only a function of the light absorbed. Baseline measurements (with empty cuvettes or cuvettes, filled with only solvent) can help to reduce measurement errors. However, strongly scattering samples are measured in an integration sphere, which is covered with a white reflective coating. Small holes provide the entrance and exit of light for detection. The light is scattered multiple times by the reflective coating, which allows a homogeneous light distribution. Second issue is the over- or underestimation due to the thickness of thin films. If the film is in the order of the used wavelength, interference effects may occur.^[224] To overcome the above issues, Paul Kubelka and Franz Munk developed a theory for the reliable measurement of thin films.^[225] The thin films are measured in reflection in an integration sphere. The determination of the band gap is then determined with:

$$F = \frac{K}{S} = \frac{(1-R_{\infty})^2}{2R_{\infty}} \quad (2)$$

With: F = Kubelka-Munk factor
 K = light absorption coefficient
 S = scattering coefficient
 R_{∞} = reflectance of an infinitely thick layer

The thickness of the layer is negligible since $K \cdot S^{-1}$ is assumed to be constant. When plotting the Kubelka-Munk function F^α ($\alpha = 0.5$ for direct semiconductors) against the energy of photons (in eV), the intersection of the inflectional tangent with the approximated function $F^\alpha = 0$ indicates the energy of the band gap.^[226]

A further method for the estimation of the band gap is the Tauc-method, which corresponds to the absorption spectra of the sample. However, since this method was not used in the thesis, it will not be discussed in detail here.

It must be mentioned here that simplifications are made in both methods, so the band gap can only be estimated approximately. When they are applied to semiconductors which show absorption below their band gap E_g , further caution is required.^[227] This can be the case when a dye is applied to the surface or integrated into a semiconductor. Therefore, the absorption/reflectance of the dye must not be mistaken for the band gap.

2.4.2 Transient absorption spectroscopy

A powerful technique for the time-dependent dynamics in semiconductors is the transient absorption spectroscopy (TAS). In particular, with TAS it is possible to monitor charge transfer processes and exciton dynamics on the femtosecond scale. The pump-probe technique uses two fs laser pulses (commonly a titanium:sapphire (Ti:Sa) laser) with a defined temporal offset in order to probe ultrafast dynamics. Typically, excitation pulses last 100 fs with a wavelength between 670 nm and 1070 nm. Using a pulse compressor, the duration of the pulse can be reduced on timescales below 10 fs. The wavelength can be altered using an optical amplifier which generates two photons with adjustable energy ratio, or a second harmonics generator (SHG) can be used to double or triple the energy of the photons. **Figure 19a** shows the schematic experimental setup for TAS measurements.

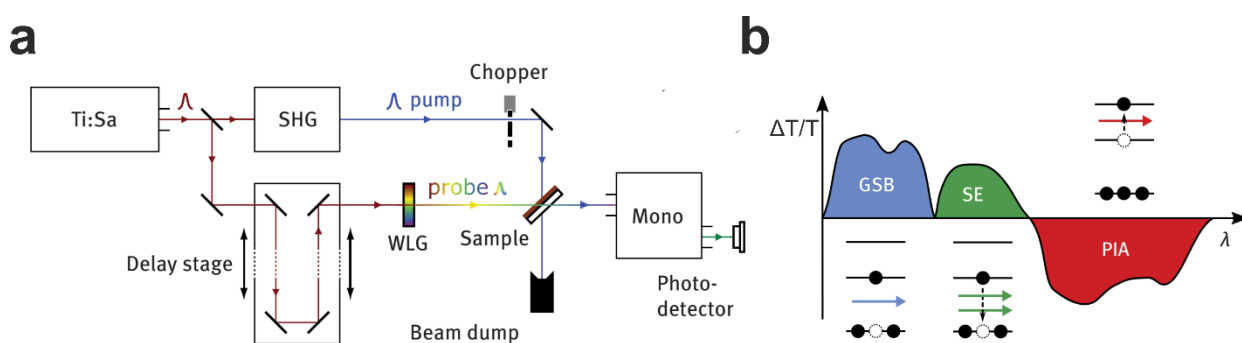


Figure 19 - a) Schematic experimental setup for transient absorption spectroscopy experiments. b) Example for the most common TA signals, which are *ground-state bleach* (GSB), *stimulated emission* (SE) and *photoinduced absorption* (PIA). Figures taken from ref. [224].

The excitation pulse is first split by a beam splitter, which defines the pump and probe light paths. The pump beam is then guided through a SHG (in this example) to create blue light. It is then focused on the sample with a preceding mechanical chopper (typically

with a frequency of 1 kHz). The probe beam is guided through a delay stage, where the light travels through aligned mirrors and is held there for a defined duration. The adjustment of the mirrors allows to control the duration and length of the path, and therefore the time delay between pump and probe. The probe beam is further guided through a white light generator for the creation of a continuous broadband pulse. This allows to measure the absorption of the sample across the whole UV/Vis spectrum after excitation with a defined pulse. The differential transmission signal $\Delta T/T$ for the cases with and without pump pulse are then determined.^[224]

With the above demonstrated setup it is possible to measure solid thin films and liquid samples, such as solutions or dispersions of NPs. The obtained TA signals then depend on the process observed. The most common observed processes are shown in **Figure 19b**. A *ground-state bleach* (GSB) originates from the reduction of available ground-states due to the pump pulse, which excites charge carriers in a chromophore or semiconductor for a certain time. The bleach can be a good hint for the lifetime of charge carriers or excited states and can easily be determined by comparing to the initial absorption measurement without excitation. A *stimulated emission* (SE) is always red-shifted to the GSB and resembles the steady-state photoluminescence spectrum. After excitation of the material by the pump pulse, radiative recombination can occur. The emitted photons are detected as well, leading to a positive net differential transmission. Further, *photoinduced absorption* (PIA) can be detected. Charge carriers in excited states can absorb light and be transferred to even higher states.^[224]

The interpretation of TA spectra often proves to be very difficult, since several signals can overlap. For chromophore-semiconductor systems in particular, very complex charge carrier dynamics are observed. Nevertheless, the method gives significant results about the communication of two electronically independent systems.

2.4.3 Photoluminescence spectroscopy

The photoluminescence (PL) spectroscopy is an efficient tool to further characterize the optical and electrical properties of semiconductors or chromophores. Samples can be measured as solid thin films or liquid in solution or dispersion. The measurement is performed by exciting the sample with a defined wavelength. The excitation source may be a white-light emitting lamp (usually an Xe-lamp) with a monochromator, or a laser (diode) with a single wavelength. Photons with sufficiently high energy are absorbed by the emitting medium and can induce radiative recombination. Emitted photons are detected in a 90° angle to the excitation source.^[228] For dispersed or solid samples, filters are often used to eliminate the scattered excitation wavelength. The emitted wavelength gives information about the emitting species in the material.

In addition to steady state measurements, time-resolved PL spectroscopy gives insights in time-dependent radiative dynamics. Therefore, a pulsed excitation source (a laser or a

fast, pulsed diode) is needed. PL decays can then be recorded at a specific wavelength, giving information about the lifetime of excited states.^[224] This technique is a good complement to TA measurements, as it provides information about radiative recombination.

2.4.4 Photoelectron spectroscopy

Photoelectron spectroscopy (PES) is based on the photoelectric effect, the interaction of photons with solid matter. Photons with a sufficiently high energy or frequency, respectively, are able to dislodge electrons from their bonds in atoms, valence bands or conduction bands. The electrons thus extracted are called photoelectrons and provide a large amount of information about the observed material. Which type of electrons is examined depends mainly on the wavelength used. PES is divided into the fields UV photoelectron spectroscopy (UPS), angle resolved photoelectron spectroscopy (ARPES) and X-ray photoelectron spectroscopy (XPS). UPS provides information about the electronical properties of a material, such as Fermi level, valence band (VB) or highest occupied molecular orbitals (HOMO). With ARPES it is possible to determine band structures of semiconductors.^[229] Since XPS uses photons with higher energy, electrons can be removed from the atomic cores, which carry information about the elemental composition of the solid sample. For this thesis, especially the oxidation state of iron is of interest. With XPS it is, for example, possible to distinguish between Fe²⁺ and Fe³⁺.

Furthermore, in this thesis a facilitated method of PES is used, PES on air (PESA). Usually photoelectron spectroscopy is measured in ultra-high vacuum, but in PESA a simplified measurement setup is used, which allows to determine the energy of the VB maximum of semiconductors and HOMOs of chromophores.

2.4.5 Powder X-ray diffraction

Powder X-ray diffraction (PXRD) is a method for qualitative and quantitative crystal phase determination of fine crystalline solid samples. A powdered sample is irradiated with a characteristic X-ray radiation, typically from a Cu source with $\lambda = 1.5406 \text{ \AA}$ (Cu-K α) or a Mo source with $\lambda = 0.70926 \text{ \AA}$ (Mo-K α). A major part of the photons passes through the crystal unhindered. However, some are reflected from the crystal. These photons are diffracted and show constructive interference, when the Bragg's law is valid, which is given by:

$$n\lambda = 2d \sin \Theta \quad (3)$$

With: n = diffraction order
 d = lattice plane distance
 Θ = glancing angle

Bragg diffraction is observed when a periodic arrangement of scattering objects i.e. electron density of atoms, is given. As a result of the Bragg condition, constructive interference only occurs when the path difference $2d \sin \Theta$ is an integer multiple of the wavelength λ . Every angle Θ can then be assigned to a specific lattice plane d_{hkl} . The lattices planes are defined by the Miller indices (hkl), a definite designation of crystal faces or planes in the crystal lattice. The constructively reflecting crystal planes are characteristic for the present crystal system of a sample. Thus, not only can PXRD identify the crystal system of the sample, but the intensity and shape of the reflections can also be used to determine properties such as size or anisotropy of the sample. The full-width half-maximum (FWHM) of a reflection correlates with the size of the crystals, described with the Debye-Scherrer equation:

$$L = \frac{K \cdot \lambda}{\Delta(2\theta) \cdot \cos \theta} \quad (4)$$

With: L = expansion of the crystal perpendicular to the lattice plane
 $\Delta(2\theta)$ = FWHM
 K = Scherrer shape factor

This permits the identification of crystallite sizes of the observed sample. Diffraction patterns may further be refined using the Rietveld method. Initially developed as a tool for structure refinement it is now widely used for quantitative phase analysis (e.g. when a phase mixture of crystals is present) or the measurement of stress and strain in the crystals. Such information is mainly obtained from the shape of the reflections.

Furthermore, the ratio between the reflections gives hint to the orientation of the crystals on a substrate. If the particles are elongated in one crystal direction, there are many lattice planes perpendicular to this direction at which diffraction may occur. The intensity of the corresponding reflection increases, compared to the others.

2.4.6 Cyclic voltammetry

Cyclic voltammetry (CV) is a versatile technique for studying electron transfer processes in redox-active species. In inorganic and organic chemistry, the kinetic of electron transfer processes provide information about the electrochemical properties of the material. CV is increasingly used to study potential-dependent interface reactions such as adsorption processes, electrocrystallization phenomena, and charge transfer reactions at semiconductor electrodes. A typical setup consists of three electrodes which are placed in a suitable electrolyte, seen in **Figure 20a**.

Redox processes proceed at the working electrode (WE) which in the example shown above is a solid film of the sample on a suitable substrate. An initial potential is applied to this electrode, which is changed linearly. The WE potential always refers to a non-

polarized reference electrode (RE), typically an Ag/AgCl or saturated calomel electrode (SCE). The current to build up the voltage, which corresponds to the electrochemical processes, is provided with the help of the counter electrode (CE). All electrodes are connected to a potentiostat, which allows to regulate the applied voltage. To guarantee conductivity, salts are added to the solvent, which are inert with the species under investigation.^[230] **Figure 20b** shows a typical cyclic voltammogram of a reversible single electron process with $E_{\text{ox/red}}$ the oxidation/reduction potential and a half-wave potential $E_{1/2}$. The half-wave potential provides information about the present species.

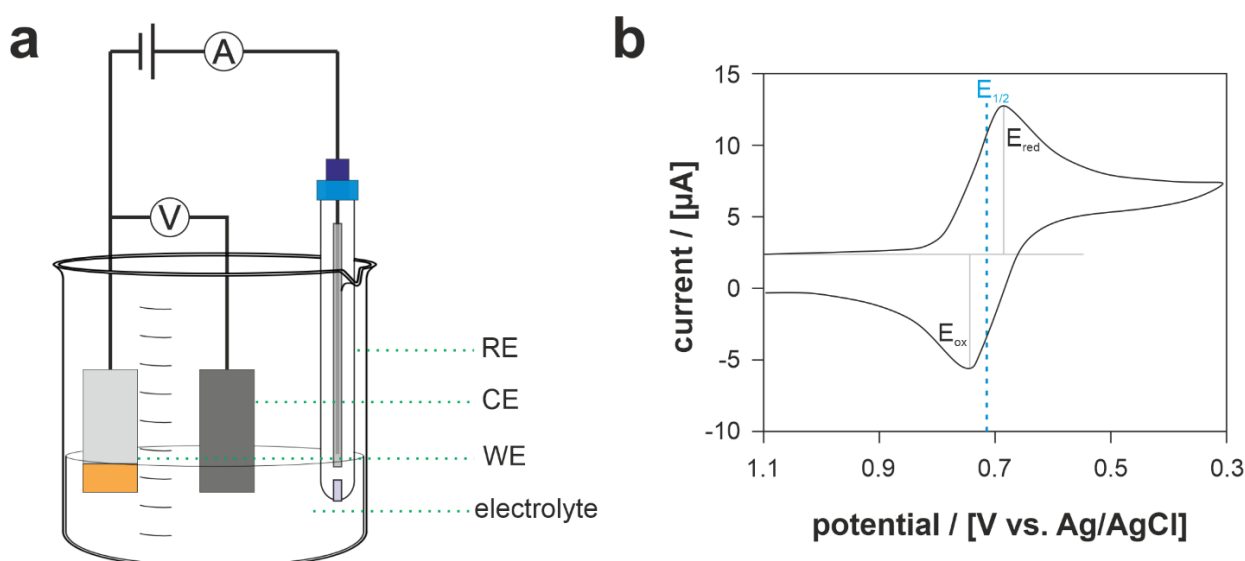


Figure 20 - a) Setup of a typical CV measurement with a reference electrode (RE), a counter electrode (CE) and the working electrode (WE) which are placed in an electrolyte. b) Current signal of a reversible single electron process.

For the measurement of solid samples, the substrate used for the WE should be inert to electrochemical reactions. In the case of hybrid perovskites, the electrolyte also plays a major role. The polar material dissolves in most electrolytes, as aqueous or polar solvents are usually used. Hasan *et al.* were the first to present a suitable electrolyte for the electrochemical characterization of hybrid perovskites ($\text{CH}_3\text{NH}_3\text{PbI}_3$).^[231] An electrolyte based on hydrofluoroether (HFE), which is normally used in lithium-ion batteries, has proven to be very suitable.

3 Challenges and Objectives

Hybrid lead halide perovskites proved to be a suitable candidate for intrinsic functionalization of semiconductors. Due to their ionic character and high structural flexibility, organic cations with ammonium unit can be incorporated with an ease.^[10] Thus, periodically arranged layered materials can be obtained, which have alternating layers of inorganic lead halide sublattices and organic molecules as an integral part of the structure. This sets them apart from other semiconductors, which can only be functionalized on the surface. If the organic part is given a special feature, highly functional materials can be obtained. Understanding the interactions and the synergistic cooperation of the organic and inorganic part of the structure is still the most important question to be solved. Would it be possible to **actively influence the energy transfers** between the two components?

This purpose requires a component that can respond to external stimuli, for instance, which can be enabled with organic switchable molecules. Schematically, this can be described as a kind of energy valve, as shown in **Figure 21**.

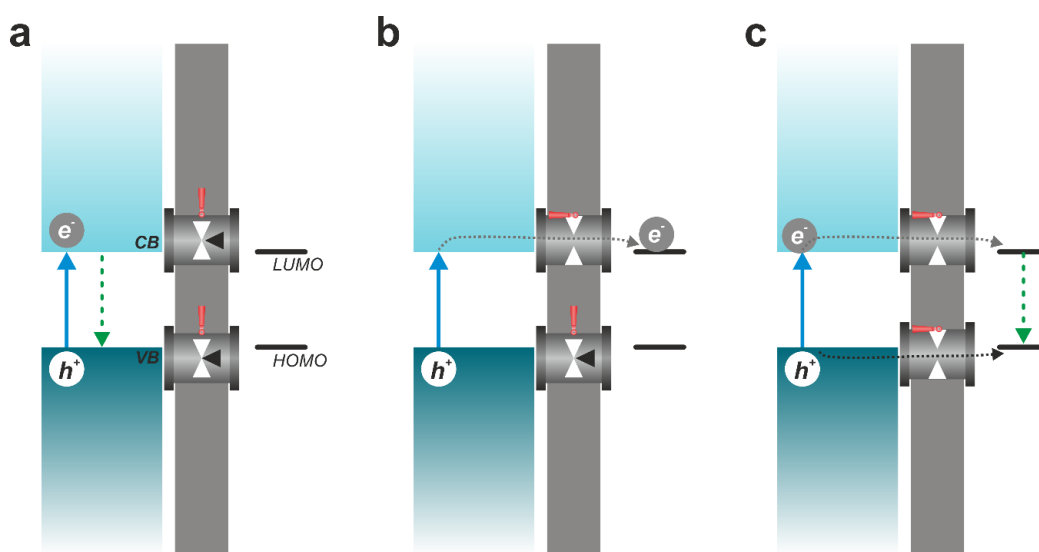


Figure 21 – Schematic representation of the architecture of the energy levels in layered hybrid perovskite with functional organic molecules. Different scenarios for energy transfers from the perovskite phase to the functional molecule: a) no energy transfer due to closed valves, b) partial energy transfer with one valve opened and c) full energy transfer from the perovskite to the organic moiety due to both valves opened. Note that the energy levels are not to be considered quantitatively.

Three different scenarios are possible: a) the transfer of both charge carriers (holes = h^+ and electrons = e^-) is not allowed. Recombination (radiative or non-radiative) of the excited charge carriers takes place in the excited species. b) Only one charge carrier is transferred and separated. Recombination is not possible for any component. And c) both charge carriers are transferred and recombination occurs in the non-excited species.

In this thesis, the main focus is on layered hybrid perovskites and Ruddlesden-Popper phases with functional surfactants, tailored to the materials and possessing a certain switchability to implement the above mentioned energy valves. Various functional organic molecules are used for this purpose, which are both conductive and switchable. These are tailored via organic synthesis routes to be incorporated as an integral component in layered hybrid perovskites. After incorporation, it should be examined whether their functionality is available and whether or how the charge carrier dynamics behave. For the synthesis of hybrid perovskites, an antisolvent synthesis based on the precipitation of a liquid precursor solution has proven suitable for functionalized nano- to micrometer sized particles.^[118,216,232]

In the first part of the thesis, **photoswitchable azobenzene ligands** will be developed, that allow a simple and fast isomerization around the azo-bond from the *trans*- to the *cis*-conformation by irradiation with UV light. Isomerization ensures modification of the energetic landscape after incorporation of the ligands. As a conjugated π -system, azobenzene is conductive and might also interact electronically with the semiconducting layers. Therefore, the head group length is varied to understand possible distance-dependent energy dynamics between the two components. The photoswitchability of the integrated ligands will be verified and, if present, possible energy dynamics in the photoswitched state will be investigated. In addition, pure surface effects of the photoswitching will be investigated on functionalized 3D perovskite particles.

The second part of the thesis will deal with **redox-active ferrocene ligands** that can be modified by a simple electronic oxidation of the iron central atom ($\text{Fe}^{2+} \rightarrow \text{Fe}^{3+}$). Since ferrocene also exhibit a conjugated π -system, electronic transfers are expected. The length of the head group of the ligands will be varied in order to investigate whether a distance-dependent energy exchange exists. Furthermore, the redox activity of the incorporated ferrocene ligands will be examined. Since oxidation affects the electronic system of the ferrocene derivative, a change in electronic dynamics in the crystalline material is expected. For this purpose, the redox activity of the incorporated ligands must be verified. Two approaches will be investigated here: electrochemical oxidation, by applying a voltage, and purely chemical oxidation by using a suitable oxidant. Thus, the materials will be examined for possible energy transfers, before and after oxidation.

In the third part of the thesis, **heterocyclic conductive ligands** are embraced in which the heteroatom is varied (furan (= O), thiophene (= S) and selenophene (= Se)). Although these ligands cannot be modified by an external stimulus, they provide valuable information about the interplay between organic ligands and inorganic crystal phase. The ligands used have a similar molecular structure and differ only in the heteroatom, thus, the crystal phases formed are comparable. Varying the heteroatom changes the aromaticity of the ligands and can lead to improved or worsened energy transfer. Again, possible energy transfers will be investigated in relation to the ligand used.

4 Results and Discussion

This chapter outlines the synthesis and characterization of tailor-made surfactants for the functionalization of semiconducting hybrid perovskite materials in form of particles in the micrometer range. The main focus in this work is on switchable molecules such as azobenzene (**photoswitchable**) and ferrocene (**redox-switchable**), which show an electronic change due to external stimuli, but also **conductive** ligands based on five-ring heterocycles with varying heteroatom. Hybrid perovskites serve as a model system for the investigation of possible effects such as directional charge transfer or recombination dependent on the electronic state of the molecules. Due to the π -conjugation of the organic molecules, charge carriers are allowed to migrate between the organic and inorganic part of the structure.

Crystals of 2D and 3D hybrid perovskites are used for the investigations. Both show semiconducting properties but mainly distinguish due to their periodical crystal structure. 2D layered hybrid perovskites (LHPs) are characterized by a periodic arrangement of layers of organic integrated ligands and inorganic semiconducting lead halide layers. 3D hybrid perovskites, on the other hand, can only be functionalized with organic ligands on the surface of the crystal phase. Exploiting the high surface of micrometer sized particles, these systems are highly suitable for investigating the impact of the organic ligands on the semiconducting properties of the perovskites.

In each case, a series of ligands is synthesized to investigate possible interactions with the perovskite phase and the impact of external stimuli to the compound. Variations include changing the length of the head group (azobenzene and ferrocene) and changing the aromatic system (heterocycles). Both can have influences on the charge transport between the π -conjugated system and the semiconducting lead bromide phase.

The first part of the chapter deals with surfactants based on azobenzene and their photoswitchability in LHPs. Here, 2D perovskites with integrated surfactant as well as 3D perovskite particles with functionalized surface were prepared. A specially developed combination of UV/Vis and $^1\text{H-NMR}$ is used to investigate the photoswitching properties of the free molecules and the molecules on the functionalized particles. Photoswitchability was observed for surface-positioned azobenzene surfactants, which was actually enhanced by the coordination with the semiconductor compared to the free ligand. In contrast to literature,^[120] however, the photoswitchability of integrated ligands was suppressed by steric hindrances. Most of the data represented in this sub-chapter was published in: *“Interfacial Charge Transfer Processes in 2D and 3D Semiconducting Hybrid Perovskites: Azobenzene as Photoswitchable Ligand”*^[233]

The second part of this chapter deals with surfactants based on the redox-switchable ferrocene. A systematic series of surfactants reveals the structure directing properties of

ferrocene and the importance of the length of the head group. Besides LHPs, more exotic lead bromide crystal phases are obtained, which is revealed by 3D electron diffraction. With the obtained phases, the redox activity of the incorporated ferrocene can be demonstrated. Chemical and electrochemical oxidation lead to the oxidized state of the material, which shows extraordinary properties due to the change of the electronic system. Most of the data represented in this sub-chapter was published in “*Design of Active Defects: 3D Electron Diffraction revealed novel Organometallic Hybrid Bromide Semiconductor Phases containing Ferrocene as Redox Switches*”^[234]

Finally, conductive heterocyclic based surfactants, namely furan, thiophene and selenophene were synthesized for integration into LHPs. Within the scope of an internship and a bachelor thesis 2D perovskites as well as quasi-2D phases (Ruddlesden-Popper phases = RPPs) were prepared and characterized. By changing the heteroatom (O, S, Se) in the five-membered ring, the properties (such as aromaticity) of the heterocycle can be altered and thus the electro-optical properties of the LHPs can be changed.

4.1 Azobenzene as functional surfactant

The molecular switch azobenzene is mainly characterized by its conformational change from *trans* to *cis* upon irradiation with UV-light (see **chapter 2.2.1**). The switchability of these molecules is often exploited to design surfaces and interfaces as desired.^[162] The advantage of azobenzene is that the photoswitching process is fully reversible, by irradiating blue light or heat treatment. Since the conformational change generates a dipole moment ($\mu_{trans} = 0.0$ D to $\mu_{cis} = 3.0$ D) in the molecule and a changed absorption behavior (due to symmetry-forbidden transitions), azobenzene is highly interesting for optical applications. Furthermore, the conformational change leads to a significant change in the length of the molecule, resulting in distorted materials.^[174]

When integrating chromophores such as azobenzene into LHPs, the conjugated π -system is expected to interact with the semiconducting phase electronically.^[112,115,117] Charge carrier dynamics between organic and inorganic structures are known to be highly distance dependent, since a hopping process occurs between the two components. In order to adjust the distance of the chromophore to the semiconducting phase, the head group can be adapted, which consists of a terminal ammonium group, coordinating to the perovskite phase and an alkyl chain as spacer in between. Therefore, four ligands with varying spacer length between the azobenzene and the head group are synthesized to investigate possible distance-dependent charge transfer processes. The obtained phases are further irradiated with UV-light to analyze their geometrical and optical behavior upon the conformational change.

4.1.1 Synthesis and characterization of photoswitchable surfactants

In order to provide different distances between the azo group and the semiconducting perovskite phases, four different ligands are synthesized, shown in **Figure 22**. To ensure coordination of the ligands to the perovskite phase, a head group ($-\text{NH}_3\text{Br}$) with spacers of different lengths (methyl = C_1 , ethyl = C_2 , butyl = C_4 , dodecyl = C_{12}) is attached to the azobenzenes (Azo). The synthesis strategy of the short chained AzoC_1 (= 1-(4-(phenyldiazenyl) phenyl)methyl-1-ammonium bromide) and AzoC_2 (= 2-(4-(phenyldiazenyl)phenyl)ethyl-1-ammonium bromide) ligands was previously developed as part of a master's thesis.^[232] These are obtained by azo coupling of nitrosobenzene and a Fmoc-protected diamine in acidic medium (a detailed synthesis strategy is found in **chapter 6.1**).

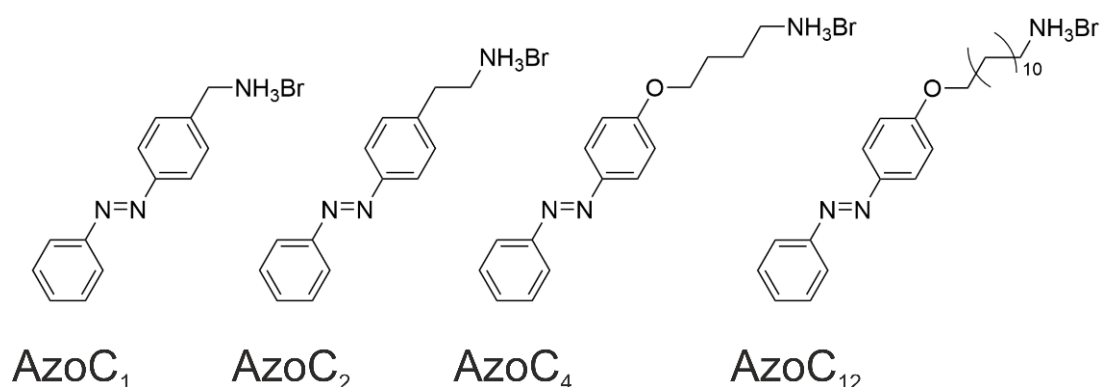


Figure 22 - Systematic series of azobenzene derivatives for the synthesis of hybrid perovskites.

The medium to long chained derivatives AzoC_4 (= 4-(4-(phenyldiazenyl)phenoxy)butyl-1-ammonium bromide) and AzoC_{12} (= 12-(4-(phenyl-diazenyl)phenoxy)dodecyl-1-ammonium bromide) are prepared via a Williamson ether synthesis starting from 4-phenylazophenol. The exact experimental details are provided in **chapter 6.1**. The ligands are characterized by molecular spectroscopy using NMR (^1H and ^{13}C) and electron spray ionization mass spectrometry (ESI-MS), as shown in **Figure A1-Figure A4**. The obtained spectra confirm the successful synthesis of the desired ligands.

To understand the photoswitching process of the ligands, their photoswitchability is examined in solution. Thus, the dynamics of the photoswitching process can be studied in absence of a semiconductor and can be compared to subsequent photoswitching experiments when integrated into the LHPs. In a typical experiment, a solution of AzoC_n ($n=1,2,4,12$) in purified water with the concentration 1.0×10^{-5} M is irradiated with 313 nm to force the isomerization. Irradiation of the compounds causes the switching from the ground state, the *trans*-isomer to the excited state, the *cis*-isomer (see **Figure 23a**).

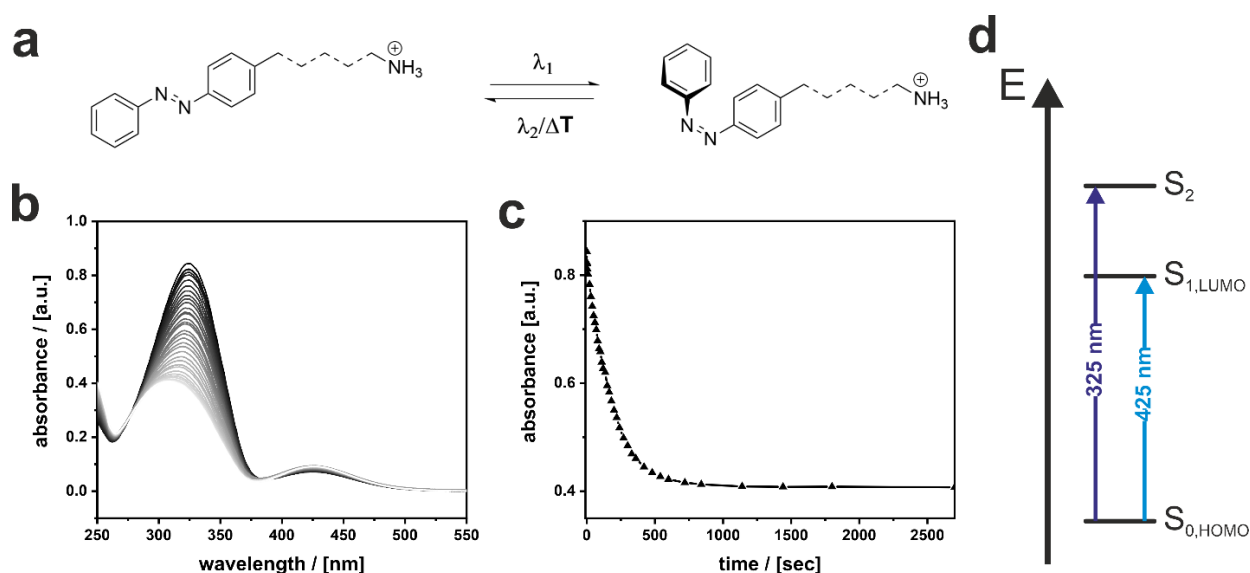


Figure 23 – a) Scheme of the photoswitching reaction the azobenzene ligands, when irradiating with UV-light (λ_1) a conformational change from *trans*- to *cis*-conformation occurs. Blue light (λ_2) or heat (ΔT) cause the reverse reaction, b) UV/Vis kinetic measurement of AzoC₂ in purified H₂O. The solution was irradiated with 313 nm, black: beginning of the reaction, light-grey: ending of the reaction, c) absorption at 325 nm during a time period of 2600 sec. d) Energy scheme of azobenzene with the singlets S₀ (HOMO), S₁ (LUMO) and S₂ and possible transitions, responsible for the absorption bands at 425 nm and 325 nm in b).

Immediately after the irradiation, the UV/Vis absorption of the solution is measured. For simplicity, **Figure 23b+c** only shows the results of the photoswitching experiment with AzoC₂. All other ligands are found in **Figure A5**.

Figure 23b shows a typical UV/Vis kinetic measurement of an AzoC₂ solution in water. In the ground state (black) two absorption features at 425 nm (2.92 eV) and at 325 nm (3.81 eV), respectively, mark the symmetry forbidden $n \rightarrow \pi^*$ transition ($S_0 \rightarrow S_1 \triangleq$ HOMO-LUMO transition) and the symmetry allowed $\pi \rightarrow \pi^*$ transition ($S_0 \rightarrow S_2$). **Figure 23d** shows the arrangement of the molecular orbitals S₀, S₁ and S₂ and the possible transitions. Excitation of the $S_0 \rightarrow S_2$ transition with irradiation at 313 nm (3.96 eV) causes the photoinduced isomerization from *trans*- to *cis*-isomer.^[162] The $S_0 \rightarrow S_2$ transition is much more pronounced for the *trans*-isomer, which can be seen by the decreasing intensity in the region from 275 nm to 375 nm during the irradiation. Strikingly, the maximum of this transition shifts to smaller wavelengths to 309 nm for the *cis*-isomer. This is due to a subtle shift in the relative energies of the molecular orbitals of azobenzene.^[156] At the same time, the absorption of the $S_0 \rightarrow S_1$ transition between 400 nm and 450 nm increases with continuous irradiation. This can be explained with the conformational change and associated symmetry breaking, which makes the $S_0 \rightarrow S_1$ transition more likely for the *cis*-isomer.

In **Figure 23c**, the maximum absorbance of the $S_0 \rightarrow S_2$ transition between 325 nm and 309 nm is plotted versus the time of irradiation. The photostationary state is reached, as soon as the slope of the curve approaches 0. For AzoC₂ in water this is after approximately 1200 seconds (~20 minutes). The behavior of AzoC₁ and AzoC₄ is comparable to that shown here, AzoC₁₂, however, shows a clearly decelerated photoswitching (see **Figure A5f**). Here, the photostationary state is reached only after 4800 seconds (~80 minutes). Presumably, this is attributed to the much longer alkyl chain, which may form a local non-polar environment around the azobenzene, destabilizing a polar transition state.^[235] Therefore, the thermal relaxation reaction responsible for the *cis* to *trans*-isomerization (which competes with the photoinduced *trans* to *cis*-isomerization) is suppressed and the photostationary state is reached much later. Therefore, a higher fraction of photoswitched molecules is expected for AzoC₁₂ than for the other ligands.

For the quantitative evaluation of the photostationary state, a method must be applied in which the *trans* and *cis*-isomer can be clearly distinguished. Therefore, ¹H-NMR of the ligands is measured in the photostationary state, since the chemical environment of the aromatic hydrogen atoms changes significantly with the isomerization. **Figure 24a** shows the relevant region between 8.2 ppm and 6.8 ppm of the ¹H-NMR of AzoC₂ in MeOD before (top) and after irradiation (bottom) with 313 nm for 4 hours. A triplet at 7.95 ppm and a multiplet between 7.6 ppm and 7.5 ppm are assigned to the *trans*-isomer. After irradiation a multiplet between 7.4 ppm and 7.2 ppm and another multiplet at 6.9 ppm arise (marked in grey), which can be assigned to the *cis*-isomer. Before irradiation (upper ¹H-NMR spectrum), a small amount of *cis*-isomer is already found in the sample, indicating that photoswitching has already occurred.

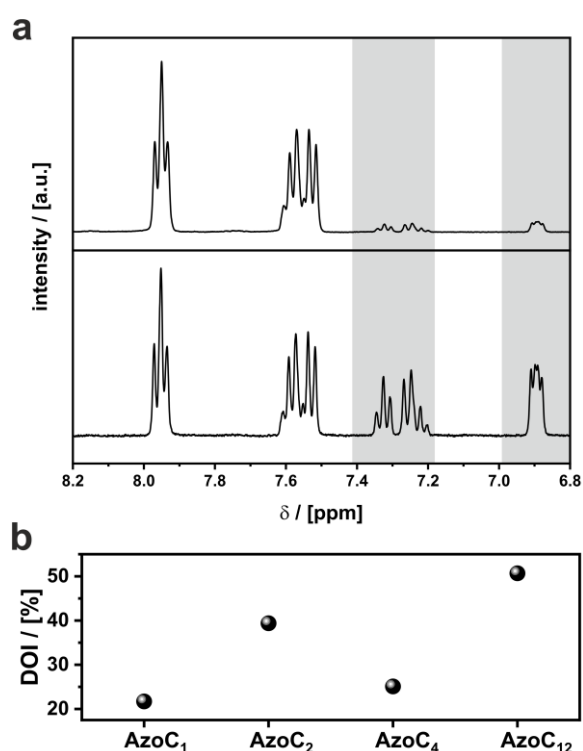


Figure 24 – a) ¹H-NMR of AzoC₂ in MeOD before (top) and after (bottom) irradiation at 313 nm for 4 h. b) DOI of AzoC_n determined from ¹H-NMR.

This may have occurred, for example, due to solar irradiation or some other UV light source. By integration of the multiplets, a degree of isomerization (DOI) can be determined. For AzoC₂ a DOI of 39.4% is determined. **Figure 24b** illustrates the DOIs for all ligands, which are also investigated by ¹H-NMR (see **Figure A6**). As already evident from the

UV/Vis kinetic measurements, the highest DOI is found for AzoC₁₂, which is attributed to the fact that the back reaction is suppressed by the long chain.^[235] Interestingly, AzoC₄ shows a lower DOI than AzoC₂, which is presumably due to the ether linkage, since the photoinduced isomerization is strongly influenced by the substituents.^[156]

Up to now, photoswitchability has been shown for all ligands prepared, allowing a DOI from 22 % to 51 % depending on the length of the spacer and the linkage of the head group. In order to classify the geometrical changes of the ligands, the structure of the free ligands was calculated and the isomers were compared.

DFT calculations of the ligands revealed the geometrical properties and spatial dimensions of the ligands. **Figure 25** shows the DFT calculated *trans*- (a) and *cis*-isomer (b) of AzoC₂. DFT calculated structures of the other ligands are provided in **Figure A7**.

Table 1 - DFT calculated distances from the ammonium head group (-NH₃⁺) to the terminal carbon group (C₄) of the azobenzene moiety.

	AzoC ₁	AzoC ₂	AzoC ₄	AzoC ₁₂
<i>d_{trans}</i>	11.1 Å	12.7 Å	16.4 Å	26.6 Å
<i>d_{cis}</i>	8.9 Å	10.0 Å	12.9 Å	22.6 Å
Δd	2.2 Å	2.7 Å	3.5 Å	4.0 Å

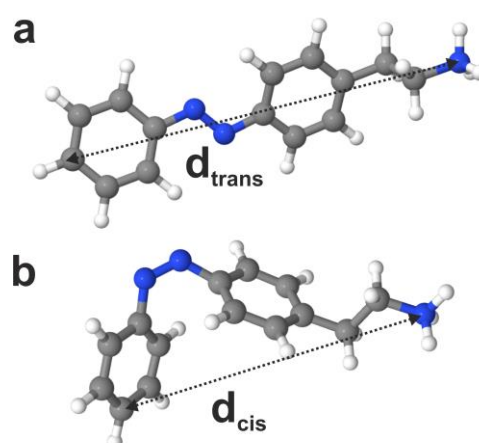


Figure 25 - DFT calculated structure of AzoC₂ in a) *trans* conformation and b) *cis* conformation.

Table 1 lists the distances between the terminal nitrogen atom of the ammonium head group and the carbon atom of the aromatic ring in para position to the azo-bond found for the *trans*- and *cis*-isomers of the ligands. Interestingly, the change of the distance (Δd) between the headgroup and the opposite carbon of the azobenzene ring increases with increasing spacer length of the ligand. This is attributed to the increased flexibility of the alkyl chain, which is significantly higher for twelve methylene groups.

When integrating the azobenzene ligands into the semiconductors, it is inevitable to determine the relative energies of the molecular orbitals of the azobenzene derivatives with respect to the semiconductor. For further investigations of possible charge or energy transfers the exact position of the relative energy levels is important. To identify the relative energy of the HOMO (S₀), photoelectron spectroscopy on air (PESA) is measured as dried film of the azobenzene ligand on a glass substrate. In combination with UV/Vis spectroscopy the remaining molecular orbitals (S₁ and S₂) can be sorted energetically.

Table 2 summarizes the resulting energies. PESA measurements of the ligands are given in **Figure A8**.

Table 2 – Relative energy of molecular orbitals of the azobenzene ligands determined and calculated using PESAs and UV/Vis measurement.

	AzoC₁	AzoC₂	AzoOC₄	AzoOC₁₂
S₀ (HOMO)	-5.37 eV	-5.46 eV	-5.40 eV	-5.36 eV
S₁ (LUMO)	-2.46 eV	-2.55 eV	-2.48 eV	-2.08 eV
S₂	-1.50 eV	-1.65 eV	-1.78 eV	-1.51 eV

Since charge carrier dynamics often appear in the form of radiative recombination, the emissive properties of the free ligands are investigated. To understand possible transfers between the semiconductor and the azobenzene, fluorescence spectra of the ligands were recorded, shown in **Figure A9**. Even though azobenzene shows only low fluorescence quantum yield, a signal is found for all ligands. Upon irradiation at 405 nm, a signal around 500 nm is found for all ligands. The fluorescence is attributed to radiative recombination from the S₁→S₀ state, thus a HOMO-LUMO transition.^[236] The slight red-shift is attributed to a typical Stokes-shift.

4.1.2 Layered hybrid perovskites with photoswitchable surfactants

Only a few LHPs based on azobenzene surfactants and lead halides are known from literature.^[119,120] Two techniques were applied to gather the crystal phases. Era *et al.* used a Langmuir-Blodgett technique, where the amphiphilic azobenzene salts formed a monolayer at the interface of an aqueous solution. With the addition of PbBr₂ they were able to isolate a single layer of the n=1 LHP.^[119] However they treated the azobenzene as an 'ordinary' chromophore and did not investigate photoswitchable properties of the single layered material. Sasai *et al.* used a classical antisolvent synthesis, where they dissolved the starting materials in dimethyl formamide (DMF), PbBr₂ and the azobenzene salt in a ratio of 1:2, as precursor solution. By adding it to an antisolvent, namely acetone, they obtained flat particles with a composition (azo-salt)₂PbBr₄, which complies to a n=1 LHP.^[120] The photoswitching properties of the particles were investigated using a combination of UV/Vis absorption and PL spectroscopy.

They stated an improved photoswitchability of the integrated ligands, however they could not explain the observed results. Furthermore, they did not investigate any structural changes or changes in layer periodicity due to the photoswitching event. Here it would have to be assumed that the basal distance between two n=1 layers decreases due to isomerization. Whether the chromophore is electronically connected (meaning charge carrier transfers or hopping processes) to the PbBr₄-layers is not addressed as well. Therefore, the following questions arise:

- Can the ligands (AzoC₁, AzoC₂, AzoC₄ and AzoC₁₂) presented above be **incorporated as integral components** in LHPs?
- What happens when the integrated ligands are **isomerized by irradiation**?
- Does **mechanical distortion** of the crystals occur?
- And is it possible that **charge carriers are transferred**?

In order to obtain LHPs from the photoswitchable azobenzene surfactants, the starting materials are dissolved in a suitable solvent to form a liquid precursor solution. The crystal phases can then be precipitated via an antisolvent process, yielding particles in the micrometer range. For the antisolvent process, a precursor based on triethylene glycol (TEG) was established in the group (see **chapter 2.3**). Thus, the starting materials were dissolved in TEG with a ratio of AzoC_n:PbBr₂ = 2:1 (n=1,2,4,12) and precipitated in dichloromethane (DCM). Surprisingly, crystalline precipitates are formed only for AzoC₂, AzoC₄ and AzoC₁₂. AzoC₁ cannot be integrated into the LHPs. Considering the structure of AzoC₁ the methylene spacer between the ammonium head group and the azobenzene does not provide enough space for a structured arrangement of the organic molecules between the PbBr₄-layers. For the incorporation of the ligands into LHPs, there must be

an interlayer arrangement of the ligands. Presumably, the planar molecules are too rigid for intercalation, which is why no LHP can form with AzoC₁.

A first hint that 2D LHPs have formed comes from the scanning electron microscopy (SEM) images, taken from the particles, shown in **Figure 26a-c**. Flat particles are obtained, which show a lateral extension of several micrometers and a thickness in the nanometer range. It is noticeable that, the longer the head group, the less pronounced the individual particles. This is probably due to stacking defects of the layered crystal phase. If the chain becomes longer, its degree of freedom increases and thus also the possible arrangements between the lead bromide layers. For simplification the phases are named 2D-AzoC_n in the following.

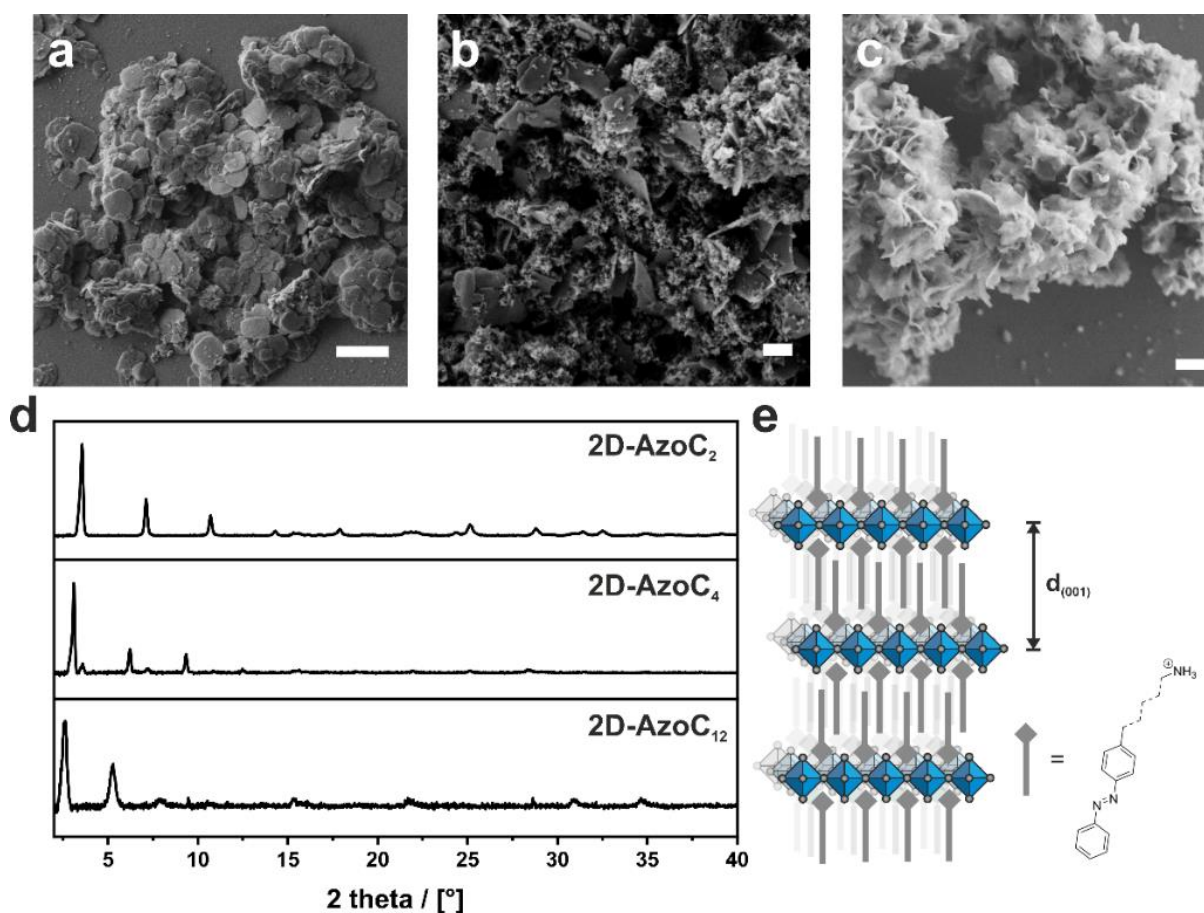


Figure 26 –SEM images of a) 2D-AzoC₂ b) 2D-AzoC₄ and c) 2D-AzoC₁₂ with scalebar = 1 μm . d) PXRD patterns of the obtained precipitates. e) Scheme of the resulting 2D LHPs.

Possible stacking disorders can be detected when considering the crystallinity and the lamellar periodic structure of the particles. The crystal structure of the resulting particles is determined with powder X-ray diffraction (PXRD), shown in **Figure 26d**. The diffraction patterns show a typical alignment of the reflections for an $n=1$ LHP.^[77] The first intensive reflection marks the (001) lattice plane of the layered structure and indicates the basal distance between two PbBr₄-layers. A crystal structure as shown in **Figure 26e** is

assumed, similar to other literature known 2D LHPs.^[119,120] Layer thicknesses of $d_{(001)} = 2.48$ nm for 2D-AzoC₂, $d_{(001)} = 2.85$ nm for 2D-AzoC₄ and $d_{(001)} = 3.40$ nm for 2D-AzoC₁₂ are found, respectively. The basal distances were further confirmed using small angle X-ray scattering (SAXS), which are shown in **Figure A10**. In **Table 3** the basal distances determined with PXRD and SAXS are summarized.

Table 3 - Basal distances of 2D-AzoC_n ($n = 2, 4, 12$) phases determined with PXRD and SAXS.

	2D-AzoC₂	2D-AzoC₄	2D-AzoC₁₂
$d_{(001),PXRD}$	2.48 nm	2.85 nm / 2.46 nm	3.40 nm
$d_{(001),SAXS}$	2.47 nm	2.82 nm / 2.42 nm	3.10 nm

Two things are striking regarding the found distances of the LHPs. First, a relatively large discrepancy is found between the layer spacing determined in SAXS and that determined in PXRD for 2D-AzoC₁₂ ($\Delta d_{(001)} = 0.30$ nm). Very broad reflections are found in both methods, suggesting low crystallinity of the lamellar stacking order. This is probably due to a large degree of stacking disorder. The high degree of freedom of the dodecyl-chain (AzoC₁₂) leads to various possible arrangements of the chain. Therefore, the soft character of the organic layers leads to a high degree of defects in the stacking and therefore a broad distribution of reflections is found in X-ray scattering methods. Second striking point is that two reflections are found for 2D-AzoC₄. Since both reflections are sharp, there are probably two different crystal phases. This can on one hand be due to contamination of the sample with other ammonium salts, that form LHPs as well. On the other hand, regarding the distances this could as well be the *cis*-isomer. However, this would be surprising, since ¹H-NMR measurements confirm the high conformational purity of the ligand before the synthesis of the LHPs (see **Figure A3a**). It is also possible for the ligand to arrange itself in various ways, so that no superordinate lamellar layered structure can develop. In this case however, a broad reflex is more likely to be expected, since different layer thicknesses are more likely to be statistically distributed in the material. So far it is not evident why a second reflex is obtained, but this can be investigated in future electron diffraction measurements on individual particles.

To understand possible photoswitching effects in the LHPs, the next step is to synthesize a material in which there is an intrinsically high proportion of *cis*-isomers. In the optimal case, a material with exclusively *cis*-isomers is obtained. Thus, it is verified, that both isomers can be incorporated into the LHPs and possible intermediate stages can be investigated.

Therefore, the precursor can be irradiated with 313 nm to induce photoswitching before particle synthesis. Since 2D-AzoC₂ showed the best crystallinity and clearest results this phase was chosen to prove the integration of *cis*-azobenzene. Since it is important to know the DOI before precipitation, ¹H-NMR of the precursor is measured using a capillary with benzene. Thus, an exact ratio between *trans*- and *cis*-isomer can be determined. **Figure 27a** shows the ¹H-NMR measurements of the precursor solution during the irradiation.

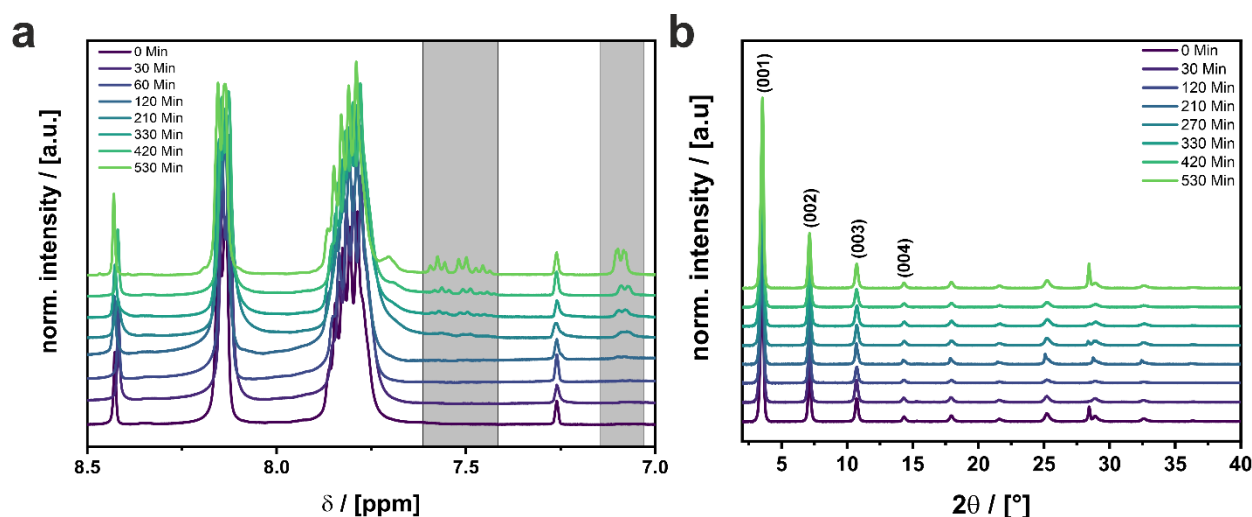


Figure 27 - a) ¹H-NMR of the precursor during the irradiation with 313 nm measured with a capillary with benzene. The DOI after 530 minutes is 9.9 %. b) PXRD patterns of the resulting particles after irradiation with 313 nm of the precursor.

Peaks at 7.8 ppm and 8.2 ppm are attributed to the *trans*-isomer. Before irradiation, only signals from the *trans*-isomer are found. With continuous irradiation at 313 nm, peaks at 7.5 ppm and 7.15 ppm reveal the presence of the *cis*-isomer. The signals are found not before 210 minutes, which might be due to the relatively high concentration of the precursor. In typical irradiation experiments, the concentration of the ligand is approximately at 10⁻⁵ M, which is low, compared to the precursor solution at 0.1 M. However, after 530 minutes (8.8 h) of irradiation a DOI of 9.9 % is achieved, which should affect the crystal formation. Simultaneously to the ¹H-NMR measurement, a part of the precursor is precipitated in DCM. The particles yielded show no significant differences in shape or size (see **Figure A11**). The crystallinity and phase of the particles was determined with PXRD, shown in **Figure 27b**. Two scenarios are possible, regarding the formation of LHPs. Either, the basal distance decreases with increasing percentage of *cis*-conformation, when both ligands are incorporated into the structure. Or, the *cis*-isomer forms a separate crystal phase, resulting in a second reflection at higher 2 θ angles. Considering the PXRD patterns with increasing content of *cis*-isomer, no significant changes are found in the basal distance, given by the (001) reflection. This could be due

to the bent structure of the organic molecule, which cannot be integrated into the LHPs due to its steric nature. This would mean, that it was not possible to obtain a LHP with

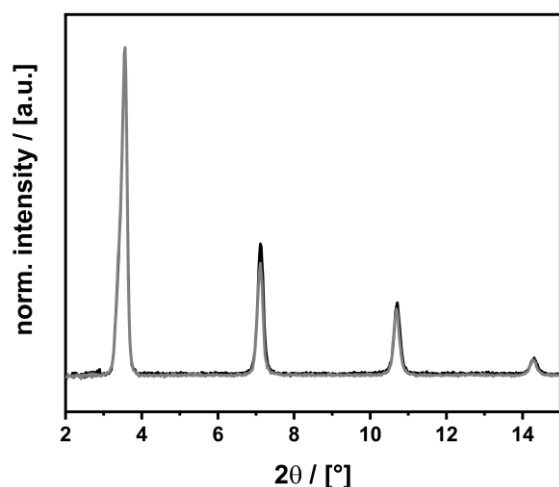


Figure 28 - PXR D of 2D-AzoC₂ before (black) and after (grey) 6 hours of irradiation at 313 nm.

solely *cis*-AzoC₂. To verify this, the initial material is irradiated with 313 nm as solid film on a glass substrate. Since the inorganic PbBr₄ layers have already formed, only the distance between these should change upon irradiation of the organic azobenzene ligands. However, after six hours of irradiation, no significant changes of the (001) reflection is determined (see **Figure 28**). If the irradiation causes photoswitching and therefore conformational change of the azobenzene molecule, a smaller distance would be expected. Here, again a larger angle of 2 θ would mark the successful photoswitch between the perovskite sheets.

Since **no method** (irradiation before and after precipitation) yielded a **different crystal phase** the question is, what happens during irradiation of the initial material with integrated *trans*-ligand?

Sasai *et al.* claim to observe photoswitching of the integrated azobenzene ligands. They support their statement on optical absorption measurements.^[120] Therefore, to understand the present mechanisms in our systems, the particles were characterized in terms of their optical absorption during the irradiation.

Similar to the photoswitching experiments with the dissolved azobenzene ligands (**Figure 23**), the particles can be dispersed and irradiated with 313 nm. **Figure 29a** shows the UV/Vis absorption spectrum of the dispersed particles with the crystal phase 2D-AzoC₂. Initially a broad absorption band at 328 nm and a sharper absorption band at 409 nm are found. The broad absorption band is attributed to the AzoC₂ (see **Figure 23b**), the sharp one is attributed to the excitonic absorption band of the [PbBr₄]-layers. Absorption at approximately 410 nm (3.1 eV) is well known for LHPs based on PbBr₄ layers.^[132] The maxima of the absorption of the dispersed particles is then evaluated over the time of irradiation with 313 nm. As expected the absorption at 328 nm decreases over the period of the irradiation, since the proportion of *trans*-azobenzene in the material decreases. However, the absorption at 409 nm decreases as well. Presumably, the dispersion is destabilized by the conformational

change of the azobenzene ligands at the surface. As the polarity of the surface changes, destabilization occurs in the dispersant and the particles sink down. To determine the photostationary state, the absorbance at 328 nm is thus referenced to the absorbance at 409 nm, since the concentration of [PbBr₄]-layers should not change due to irradiation. **Figure 29b** shows the referenced absorbance at 328 nm over a period of 1200 sec (2 h).

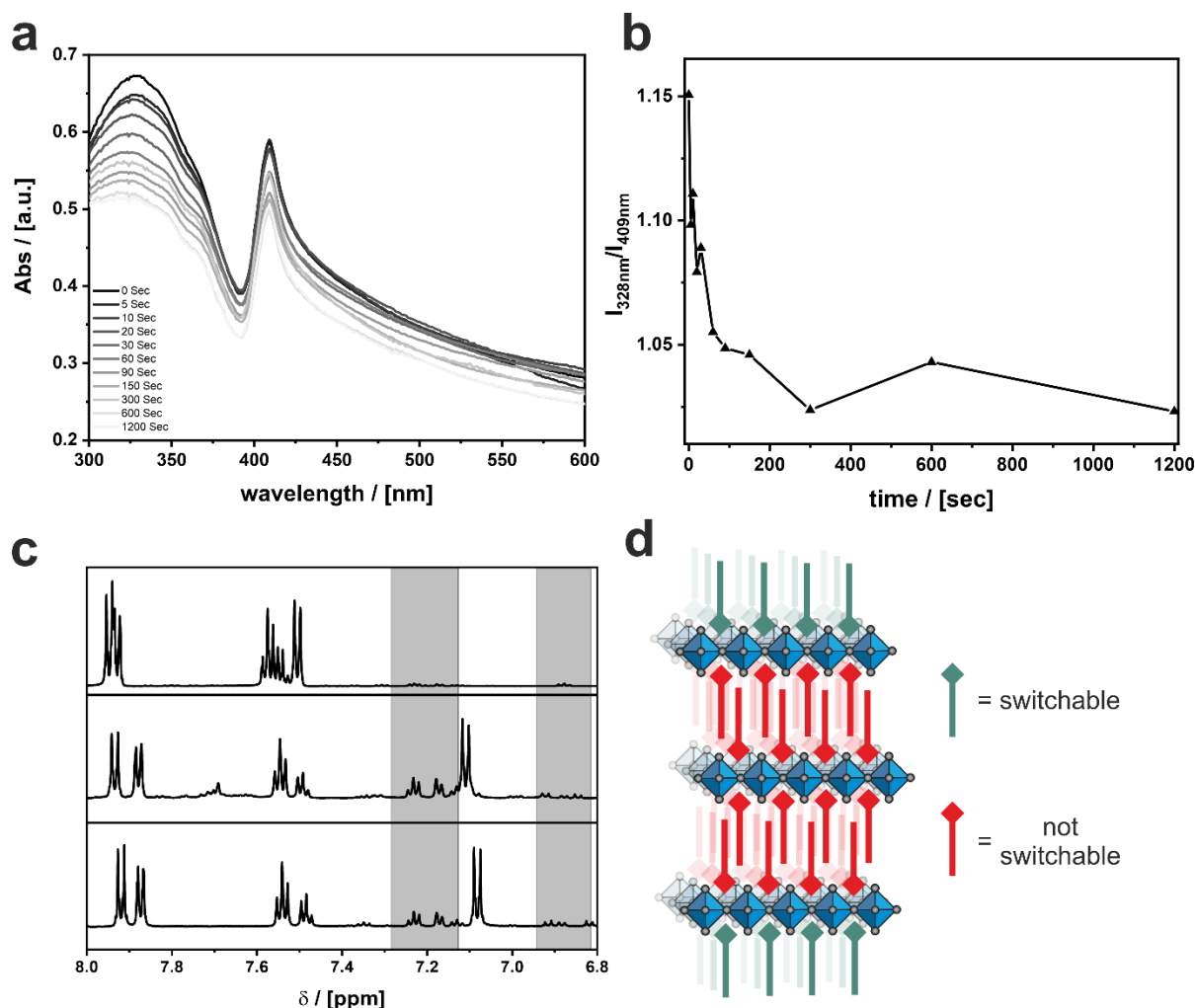


Figure 29 – a) UV/Vis absorption measurement of dispersed particles of 2D-AzoC₂ during the irradiation with 313 nm. b) Intensity of absorbance maximum of AzoC₂ (328 nm) referenced to the absorption of the PbBr₄ layers (409 nm). c) ¹H-NMR of 2D-AzoC₂ (top), 2D-AzoC₄ (middle) and 2D-AzoC₁₂ (bottom) after irradiation dissolved in MeOD. DOI is 2.5 %, 12.3 % and 7.8 % respectively. d) Schematic representation of the crystal phase during irradiation at 313 nm.

The photostationary state is reached after approximately 300 seconds. This is significantly earlier than for the free ligand in solution (see **Figure 23c**). For 2D-AzoC₄ and 2D-AzoC₁₂ the same effects are observed upon irradiation (see **Figure A12**).

It is concluded that the **photoswitching** of the azobenzene ligands is indeed **possible**. However, the photostationary state is reached much **earlier** than for the **free ligands**.

Two effects may be the reason for this observation. Either the photoswitching event is much faster, or only a small fraction of the ligands is available for photoswitching. For a quantitative analysis, the particles are dissolved in MeOD after irradiation for 1200 seconds and $^1\text{H-NMR}$ is measured. Since PbBr_2 is insoluble in MeOD, the inorganic phase can be separated from the solution and only the azobenzene ligand is detected. **Figure 29c** shows the relevant region from 8.0 ppm to 6.8 ppm of the $^1\text{H-NMR}$ spectrum of the dissolved particles. Signals at 7.2 ppm and 6.9 ppm can be assigned to the *cis*-isomer, highlighted in grey. The DOI is determined by the ratio between the integrated signals of the *trans*- and *cis*-isomer. For 2D-AzoC₂ a very low DOI of 2.5 % is found. 2D-AzoC₄ and 2D-AzoC₁₂ show slightly higher DOIs with 12.3 % and 7.8 %. In all cases, the DOI is significantly smaller than for the free ligands (see **Figure 24b**).

Since the layer thickness does not change significantly and a very low DOI is found after the irradiation of the LHPs, it is assumed that the azobenzene ligands between the layers are not available for photoswitching (see **Figure 29d**). However, a small fraction of the ligands which are located at the surface show a photoinduced conformational change, which is verified with $^1\text{H-NMR}$ and UV/Vis spectroscopy. It can be concluded, that no structural changes are induced by the irradiation between the $[\text{PbBr}_4]$ -layers, contrary to Sasai *et al.* stated in their publication.^[120]

Although it is not possible to exploit the photoswitchability of the azobenzene *within* the layered structure, the chromophore can still serve as an **electronic component** of the LHPs.

Charge carrier dynamics like electron or hole hopping are possible and need to be verified for the present phases. To identify presumptive electronic processes, the quantum well structure of the phases must be identified (compare **Figure 6**). Therefore, the relative energies of the valence band maximum (VBM) and the conduction band minimum (CBM) are determined. The combination of UV/Vis absorption spectroscopy and PESA already yielded the relative energies of the azobenzene ligands (see **Table 2**). This method is also applicable on the 2D-LHPs, revealing the relative energy of the VBM from PESA and the CBM from the band gap E_g ($E_{\text{CBM}}=E_{\text{VBM}}+E_g$), shown in **Figure 30** and summarized in **Table 4**. For the determination of E_g UV/Vis reflectance spectroscopy is performed. A Kubelka-Munk analysis then yields the energy of the band gap E_g .

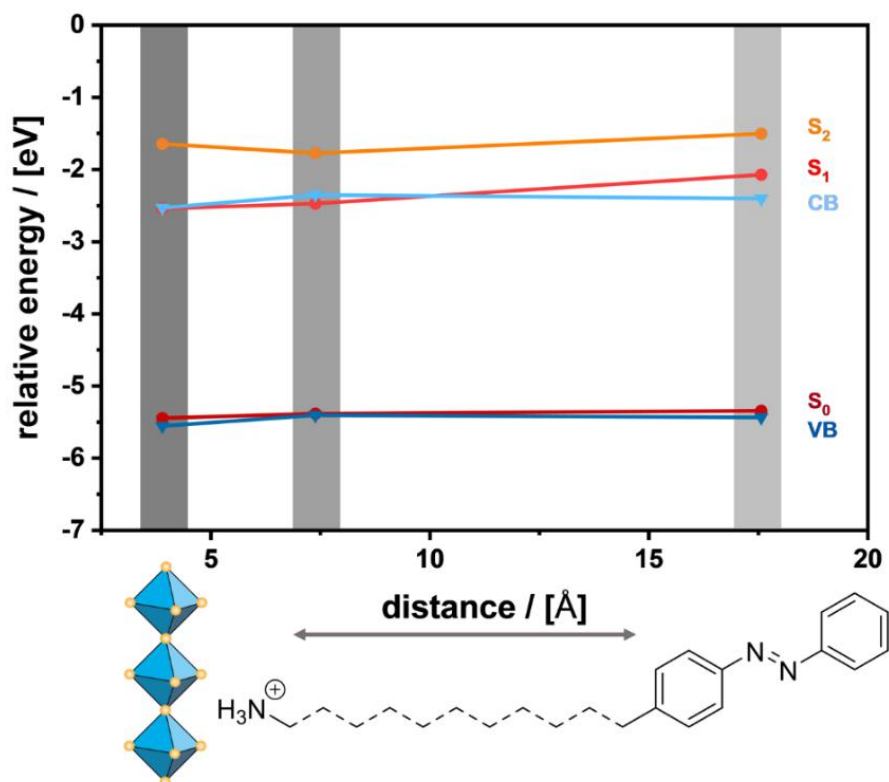


Figure 30 – Energy level diagram of 2D-AzoC₂, 2D-AzoOC₄ and 2D-AzoOC₁₂ in dependency to the distance between the perovskite layer and the azobenzene moiety. UV/Vis and PESA measurements are provided in **Figure A13**.

Table 4 - Summary of relative energies of the VBM and CVM, determined with a combination of UV/Vis reflection with Kubelka-Munk analysis and PESA of all 2D LHPs with AzoC_n. Spectra are found in **Figure A13**.

	2D-AzoC₂	2D-AzoC₄	2D-AzoC₁₂
VBM (PESA)	-5.57 eV	-5.42 eV	-5.52 eV
CBM	-2.54 eV	-2.36 eV	-2.48 eV
E_g (UV/Vis)	3.03 eV	3.06 eV	3.04 eV

Since possible interactions (charge carrier or energy transfer) are highly distance dependent, the relative energies are plotted against the length of the spacer between the head group and the azobenzene moiety of the ligands. Interestingly, the relative energies are comparable for all ligands. Both VBM and S₀, the highest occupied states of the two components, and CBM and S₁, the lowest unoccupied states, are relatively at the same energetic levels. This situation makes electronic hopping processes between the inorganic and the organic component very likely. Therefore, only the distance has an

influence on the dynamics occurring in the phases. In this context, PL spectra of the LHPs give additional information about radiative recombination and therefore also the charge carrier dynamics. It is well known from literature, that the PL of LHPs with integrated chromophore is dependent on the energy level alignment,^[112] since charge carriers can migrate from one species to the other. **Figure 31** shows the PL spectra of the LHPs excited below the bandgap at 350 nm. Regarding the UV/Vis spectra of the dispersed particles (see **Figure 29a** and **Figure A12a+c**), a wavelength of 350 nm is sufficient to excite both, the azobenzene and the semiconducting perovskite phase.

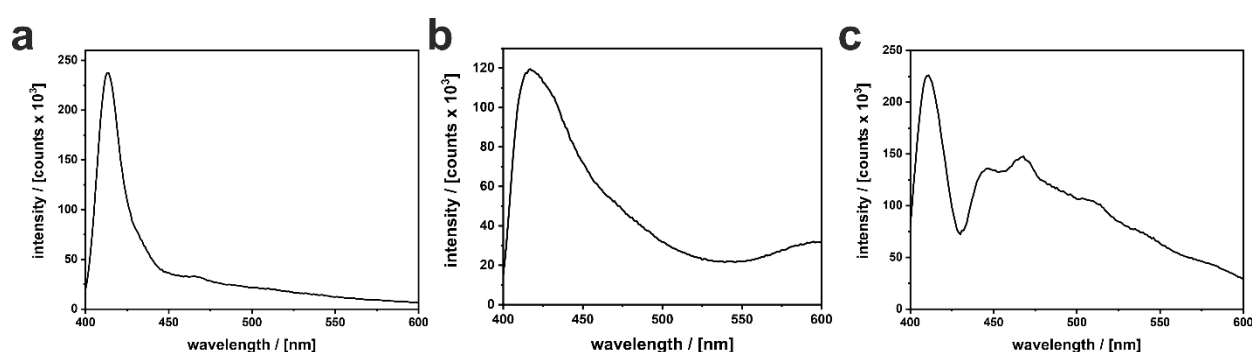


Figure 31 – PL spectra of a) 2D-AzoC₂, b) 2D-AzoC₄ and c) 2D-AzoC₁₂ excited with an Xe-lamp at 350 nm.

A local maximum at approximately 410 nm is found for all phases, which is attributed to a radiative recombination near the band edges of excitons in the semiconducting phase. Surprisingly, 2D-AzoC₁₂ shows an additional emission between 450 nm and 550 nm, which indicates the fluorescence of the integrated azobenzene moiety (see **Figure A9d**). 2D-AzoC₂ and 2D-AzoC₄ do not show this feature. This observation can be explained as follows. The ligands in 2D-AzoC₂ and 2D-AzoC₄ provide only a small distance between the [PbBr₄]-layers and the azobenzene moiety. Here, a charge carrier or energy transfer occurs from the azobenzene to the perovskite phase, presumably through a hopping process, thus no PL of the ligand can be detected. For 2D-AzoC₁₂ however, the distance between the azobenzene moiety and the [PbBr₄]-layers is increased, therefore the excited charge carriers from the azobenzene cannot or can only partially migrate to the VBM/CBM.

To summarize, it can be stated that the integration of **three out of four** of the synthesized azobenzene ligands in between the layers of a 2D perovskite is possible.

AzoC₁ could not be integrated due to a too short spacer length between the head group and the azobenzene moiety. However, the elongation of the spacer by one methylene unit already leads to the incorporation of the ligands. An ordered arrangement between the perovskite sheets can therefore only be achieved from a certain chain length and thus from a certain flexibility of the ligands. The spacer length is further responsible for the crystallinity of the yielded particles, confirmed with PXRD. 2D-AzoC₂ showed the highest crystallinity, since the chain has the lowest degrees of freedom and the arrangement of the ligands is clear. Thus, for high crystallinity of LHPs, the flexibility of the incorporated ligands is of great importance. This must not be too low, otherwise the incorporation will be prevented, but also not too high, otherwise stacking faults will occur. Irradiating the 2D-LHPs revealed, that only surface bound ligands are available to a conformational change, the integrated ligands are sterically hindered. As well, irradiating of the precursor did not result in an LHP with integrated *cis*-isomer, which is presumably due to the steric hindrance of the tilted structure of the azobenzene moiety.

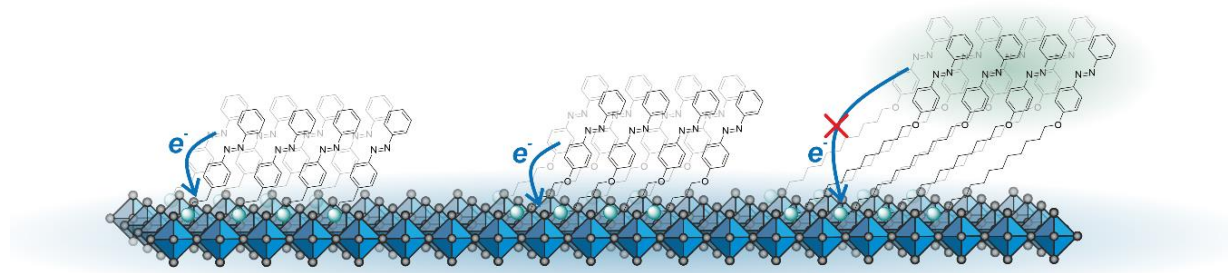


Figure 32 - Schematic overview of the observed PL in LHPs based on azobenzene ligands. The excited state of the ligand is quenched by an electron (or energy) transfer to the PbBr₄ layers, when the spacer length is short (AzoC₂ and AzoC₄). A long spacer suppresses the quenching event and emission of the azobenzene is observed (AzoC₁₂).

As for the electronic structure of the quantum wells, charge carrier transfers are possible for all LHPs, since the band edges of the VBM and CBM lie favorably to the MOs of the azobenzene ligands. However, in 2D-AzoC₁₂ no or only a partial transfer is possible, which is confirmed by the PL spectra. Emission of the azobenzene is suppressed due to a charge transfer, when the chain between the chromophore and the [PbBr₄]-layers is small (2D-AzoC₂ and 2D-AzoC₄). However, if the interstitial space is increased (2D-AzoC₁₂) the ligand emits as well. **Figure 32** shows a schematic overview of the PL observed.

The intensive study of the LHPs with photoswitchable ligands revealed that observation of **optical data alone** may lead to **erroneous conclusions** about the photoswitchability of the integrated ligands.

Conclusively, a distinction must be made between surface-bound and integrated azobenzene ligands. The extent to which electron transfer between the organic and inorganic species plays a role in photoswitching is yet unclear. To study surface effects solely, a system is needed in which the azobenzene coordinates only at the surface. The coordinating ligands have a much higher degree of freedom at the surface, which should facilitate the conformational change. If this is possible, it can be assumed that the photoswitching in LHPs is suppressed only due to steric effects.

4.1.3 3D hybrid perovskites with surface coordinating azobenzene ligands

3D hybrid perovskites, unlike LHPs, contain only the small cation MABr in their structure. This means that ligands can only be located on the surface of the particles. In order to verify the photoswitching of azobenzene ligands on the surface, the ligands are used to synthesize hybrid perovskites with 3D crystal structure. Since 3D hybrid perovskites are direct semiconductors, possible electron or charge transfer can be observed, similar to LHPs. Therefore, a mixture of a small cation, in this case methylammonium bromide ($\text{CH}_3\text{NH}_3\text{Br} = \text{MABr}$) and an azobenzene ligand are used for the synthesis of hybrid perovskite nanoparticles (NPs). All components are dissolved in TEG as a precursor solution, which is then precipitated in DCM at room temperature (for details see **chapter 6.2.1**). All precursors yield orange precipitates which were investigated with SEM, shown in **Figure 33**. The precipitate consists of cubic shaped particles with sizes between 100 nm and 300 nm.

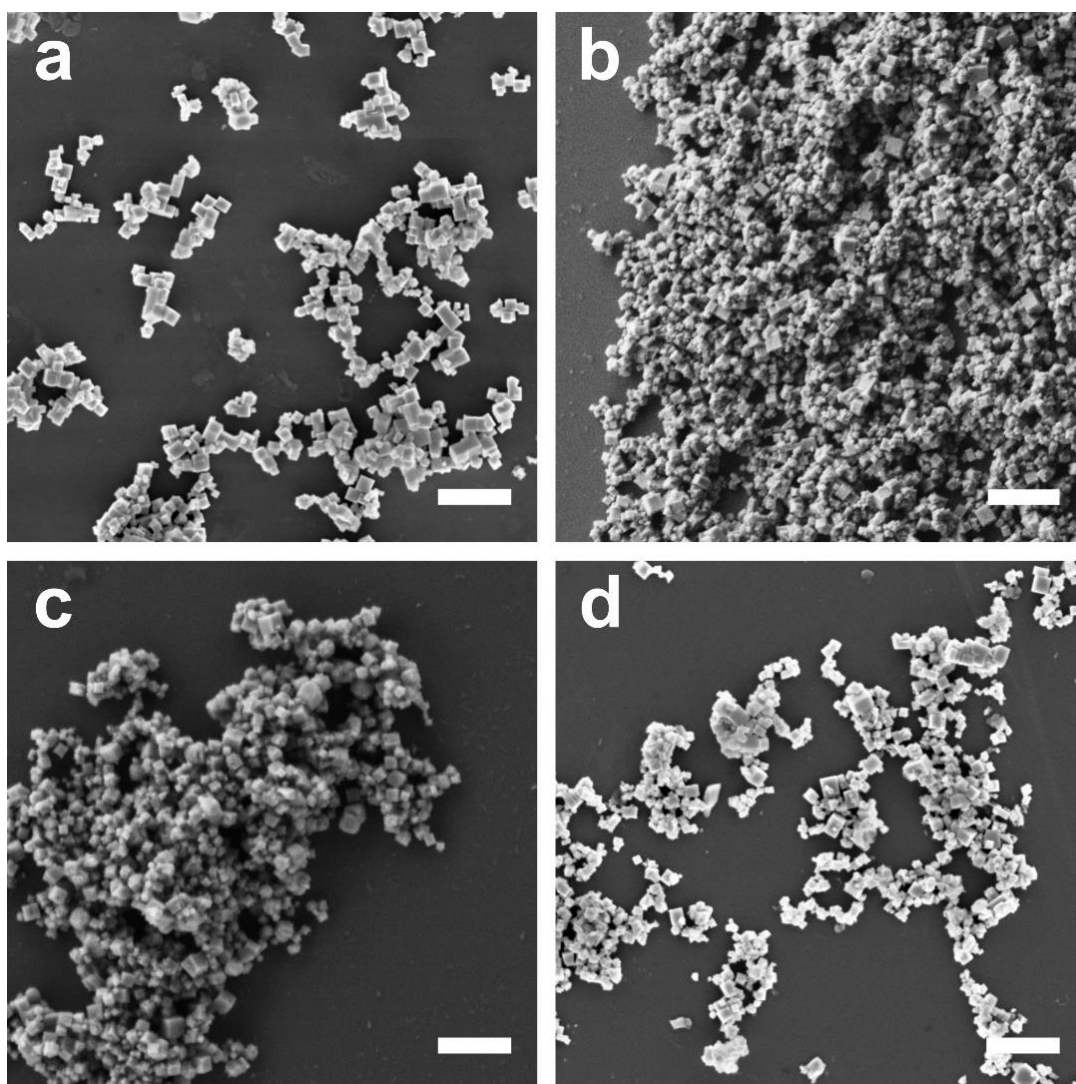


Figure 33 - SEM images of MAPbBr_3 NPs from the antisolvent synthesis with a) AzoC_1 , b) AzoC_2 , c) AzoC_4 and d) AzoC_{12} . Scalebar = 1 μm .

The cubic shape of the particles is a first hint, that the 3D perovskite $(\text{CH}_3\text{NH}_3)\text{PbBr}_3$ (MAPbBr_3) is obtained. For simplicity, the precipitates are denoted as 3D-AzoC_n ($n=1,2,4,12$) from now on. The PXRD measurement of 3D-AzoC_2 , shown in **Figure 34a** demonstrates the presence of phase-pure MAPbBr_3 particles. This is also confirmed by the PXRD patterns for the other particles, shown in **Figure A14**.

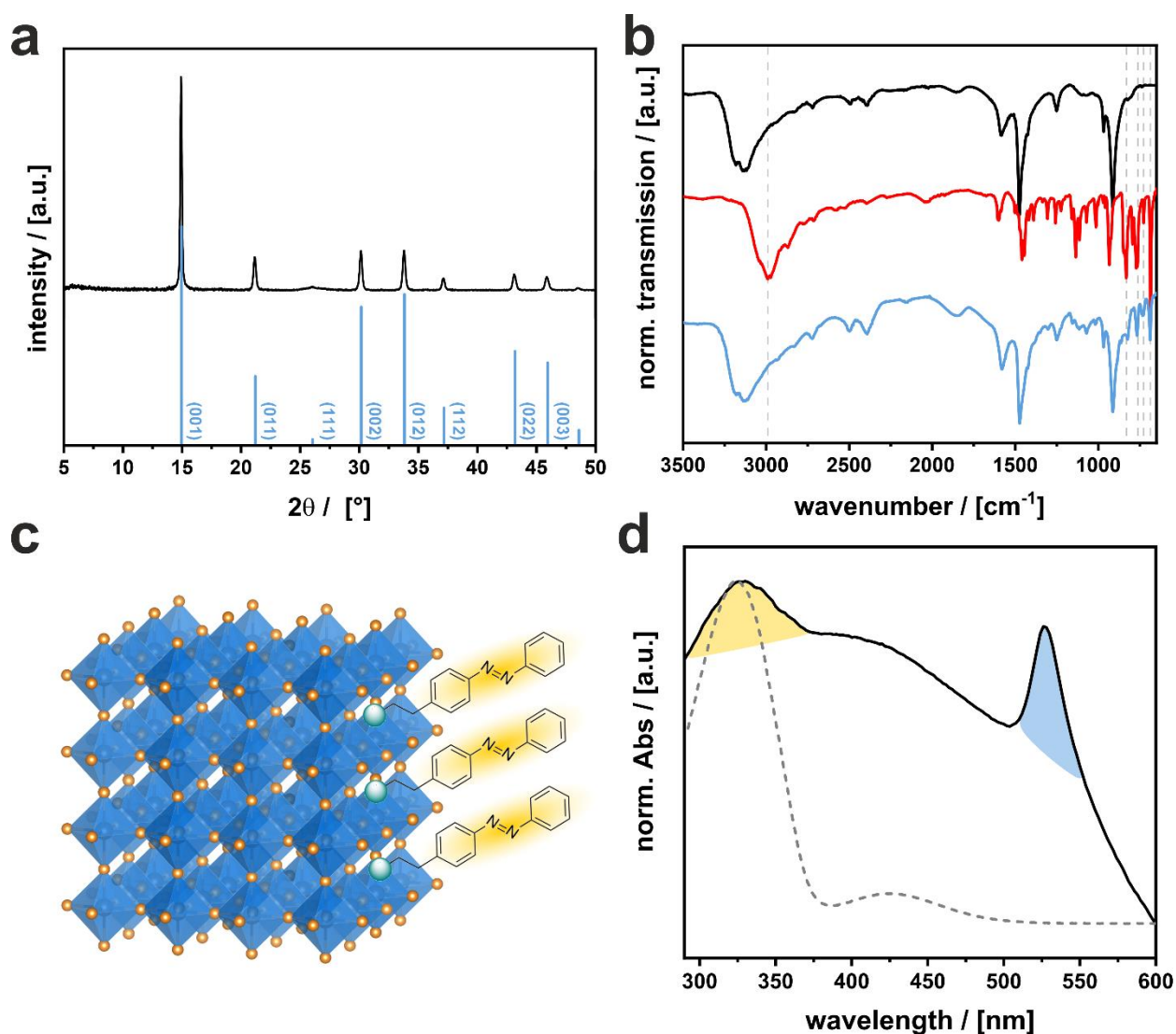


Figure 34 - a) PXRD measurements of 3D-AzoC_2 (black) with reference taken from ^[237]. b) Fourier transform infrared (FT-IR) spectra of non-functionalized MAPbBr_3 phase (black), AzoC_2 (red) and 3D-AzoC_2 (blue). Wavenumbers at 2991 cm^{-1} , 832 cm^{-1} , 765 cm^{-1} , 727 cm^{-1} and 685 cm^{-1} are highlighted in grey as significant vibrations for the azobenzene. c) Schematic representation of surface functionalized 3D-AzoC_2 and d) normalized UV/Vis absorption spectrum of 3D-AzoC_2 dispersed in toluene (black) and AzoC_2 in H_2O (grey, dashed). Signals of azobenzene (yellow) and MAPbBr_3 (blue) are highlighted.

To verify that the ligands really coordinate to the surface of the particles, a combination of Fourier-transform infrared (FT-IR) spectroscopy and UV/Vis absorption spectroscopy is applied. **Figure 34b** depicts the FT-IR spectra of pure unfunctionalized MAPbBr₃ particles (black), the solid ligand AzoC₂ (red) and 3D-AzOC₂ (blue). As reference for non-functionalized MAPbBr₃, particles were synthesized without any surface-coordinating ligand (see **chapter 6.2.1**). Spectra of the other particles are provided in **Figure A15**. A significant signal at 2991 cm⁻¹ is attributed to the N-H-stretching bond vibration of the ammonium head-group, which vanishes completely for 3D-AzoC₂. Such vibration is known to vanish, if the amine is coordinated to the surface of the particle.^[238] Furthermore, signals at 832 cm⁻¹, 765 cm⁻¹, 727 cm⁻¹ and 685 cm⁻¹ can be associated with the aromatic vibrations of the azobenzene moiety and are also found for 3D-AzoC₂. In addition, UV/Vis absorption spectroscopy is recorded for the characterization of the optical properties, shown in **Figure 34d** (3D-AzoC₂) and **Figure A15** (3D-AzoC₁, 3D-AzoC₄, 3D-AzoC₁₂). Since the azobenzene-ligands cannot be dissolved in toluene any detected absorption comes from the dispersed, functionalized particles. Two absorption bands at 328 nm and 526 nm are found for the dispersed particles of 3D-AzoC₂. The sharp absorption band at 526 nm is assigned to the excitonic bandgap of the perovskite particles.^[67] The broader absorption band at 328 nm is assigned to the AzoC₂ ligand, which is shaded in yellow. Note that the absorption spectrum of AzoC₂ is recorded in H₂O (**Figure 23b**), which is why the maximum is slightly shifted. However, from IR and UV/Vis absorption spectroscopy it can be assumed that the ligands coordinate to the surface of the particles (see **Figure 34c**) and not only form a solid mixture with the perovskite phase.

Concluding, the 3D-AzoC_n (n=1,2,4,12) are perfectly suited for the observation of **photoswitching** effects on the **surface** of a semiconductor. Furthermore, the variation of the spacer length between the azobenzene moiety and the semiconductor allows the investigation of **distance dependent effects**, such as energy or electron migration through a hopping process. The **steric constraints** compared to the 2D LHPs are expected to be much **lower** for the 3D phases.

Regarding literature, different scenarios can be expected for the photoswitchability of the ligands at the surface of the semiconducting MAPbBr₃ particles. On the one hand, a very fast charge transfer from azobenzene to the conduction band of TiO₂ (a wide-band gap semiconductor) was simulated by Rego *et al.* After the transfer, they observed a strong vibronic relaxation that excites the N-N-stretching mode. They stated, that due to this effect no conformational change can occur at the surface of TiO₂.^[186] On the other hand, an improved *trans* to *cis*-isomerization of the azobenzene ligands was observed by Saeed *et al.* They used CdTe quantum dots for their observations.^[239] The two semiconductors differ mainly in their band structure, which may be a reason for the different behavior of

the azobenzene at their surface. Therefore, the quantitative arrangement of the bands for MAPbBr₃ and the azobenzene ligands is determined below.

To reveal the band structure of the 3D-AzoC_n phases, similar to 2D-AzoC_n, UV/Vis reflectance spectroscopy is performed in combination with PESA. The resulting spectra are given in **Figure A16** and combined in **Figure 35**. Determination of the relative energies of the VBM, CBM and the band gap E_g are summarized in **Table 5**.

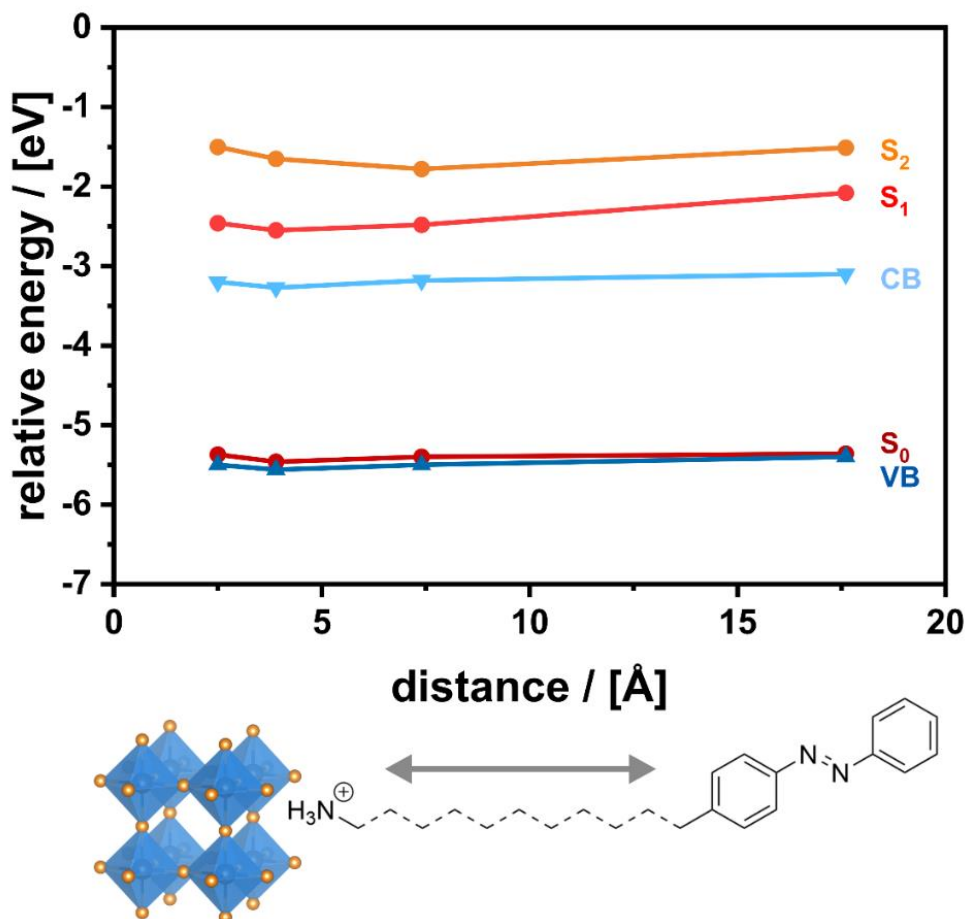


Figure 35 – Energy level diagram of 3D-AzoC₁, 3D-AzoC₂, 3D-AzoOC₄ and 3D-AzoOC₁₂ in dependency to the distance between the perovskite phase and the azobenzene moiety. UV/Vis and PESA measurements are provided in **Figure A16**.

Table 5 – Summary of relative energies of the VBM and CBM, determined with a combination of UV/Vis reflection with Kubelka-Munk analysis and PESA of all functionalized particles. Spectra are found in **Figure A16**.

	3D-AzoC₁	3D-AzoC₂	3D-AzoC₄	3D-AzoC₁₂
VBM (PESA)	-5.50 eV	-5.56 eV	-5.50 eV	-5.40 eV
CBM	-3.20 eV	-3.27 eV	-3.18 eV	-3.10 eV
E_g (UV/Vis)	2.30 eV	2.29 eV	2.32 eV	2.30 eV

As seen in **Figure 35**, the relative energies of the band edges of all particles are comparable, thus only the distance between the perovskite phase MAPbBr₃ and the azobenzene moiety plays a role in the possible charge carrier dynamics. The VBM is energetically similar to the ground state S₀ of azobenzene, which allows charge transfer of excited holes. Furthermore, the CBM lies favorable between the S₀ and S₁ states of the azobenzene, allowing the transfer of excited electrons from the azobenzene to the perovskite. Therefore, it is concluded, that electronical communication between the two components would be possible. How this affects the photoswitching properties of the coordinated ligands is considered in the following.

To evaluate the availability of the photoswitching of the azobenzene ligands at the surface, the particles were dispersed and subsequently irradiated with 313 nm. Again, the optical UV/Vis absorption is recorded, to verify the photoswitching of the ligands, similar to the LHP. Subsequent dissolving in MeOD and ¹H-NMR measurements revealed the DOI of the ligands. **Figure 36** shows the results representative for 3D-AzoC₂.

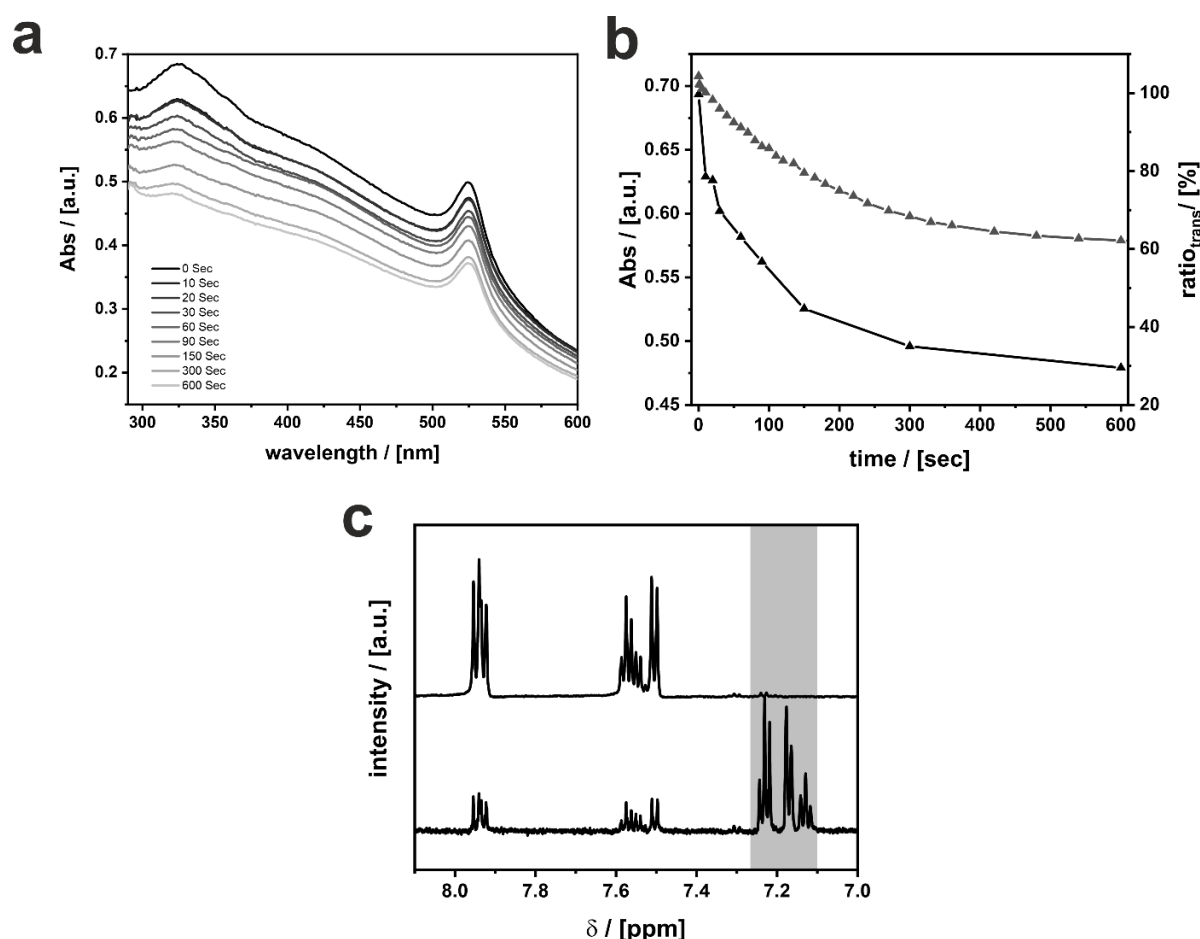


Figure 36 - a) UV/Vis absorption spectra of 3D-AzoC₂ during the irradiation at 313 nm. b) Absorption maximum at 328 nm of AzoC₂ at the surface of MAPbBr₃ particles (black) and in solution (grey; compare **Figure 23c**) c) ¹H-NMR spectra of dissolved 3D-AzoC₂ before (top) and after irradiation at 313 nm for 600 sec (bottom).

Before the irradiation (black), two absorption bands at 328 nm and 526 nm are found which refer to the AzoC₂ ligand and the perovskite phase. **Figure A17** show the UV/Vis absorption kinetics for 3D-AzoC₁, 3D-AzoC₄ and 3D-AzoC₁₂, where similar absorption bands are found, which is why only 3D-AzoC₂ is discussed here. Upon irradiation, the absorption decreases throughout the observed range, which is attributed to two different effects. The particles show slow sedimentation in the earth's gravitational field, even without irradiation (see **Figure A18**). However, it is observed that irradiation accelerates this process. Upon irradiation, the dipole moment of azobenzene changes from 0 Debye for the *trans*-isomer to 3 Debye for the *cis*-isomer.^[240] Thus, the polarity of the particles surface is affected by the conformational change. Due to the decreased polarity, particles tend to precipitate, which was also observed for other systems.^[241]

To exclude precipitation effects, the signal at 328 nm was referenced to the signal of the excitonic absorption band at 526 nm, to determine the photostationary state (see **Figure 36b**). After reaching the photostationary state, the particles are dissolved in MeOD. In ¹H-NMR, the soluble components (AzoC₂ and MABr) can then be detected and the DOI determined by integrating the signals, shown in **Figure 36c** (and **Figure A17**). MABr does not show signals in the significant region, which is why it can be neglected. Interestingly, the DOI is significantly increased for the ligands attached to the surface of

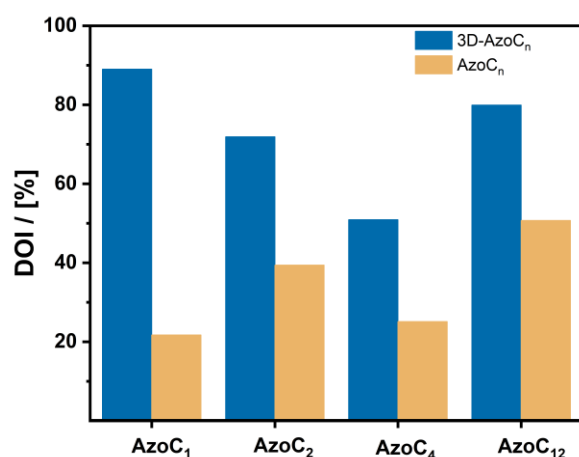


Figure 37 - DOI of the azobenzene ligands attached to the MAPbBr₃ particles (blue) and in solution (orange).

the particles (**Figure 37**), compared to the free ligands in solution. The photoswitching in azobenzene occurs by photonic excitation of the S₀→S₂ transfer. Coordination of the ligands to the semiconductor somehow enhances this transfer, which results in an improved photoswitching. A possible explanation for the enhanced photoswitchability is an energy or electron transfer, presumably a hopping process from the semiconductor to the ligand. The irradiation at 313 nm (3.96 eV) is sufficient to excite the MAPbBr₃, which has a continuous band gap at 2.3 eV.^[29] Thus, the excited

semiconductor can transfer energy to the azobenzene moiety which undergoes a conformational change.

To observe possible energy or electron transfers between the semiconductor and the azobenzene ligands, time-dependent measurements are required. PL signals of the particles reveal an emission at approximately 530 nm, which is attributed to the excitonic recombination near the band edges (see **Figure A19**). In comparison to NPs synthesized

with alkyl ligands, the emission of the particles is enormously reduced (see **Figure 38**, photographs). Unfortunately, quantitative measurements were not possible, since no integration sphere was available for the measuring setup. However, quenching of excited radiative states is a first hint, that the ligand has an influence on the electronic dynamics of the semiconductor. In time-resolved PL spectroscopy, it is possible to observe the lifetime of excited radiative states. **Figure 38** shows the lifetimes of the radiative states at 530 nm of the surface functionalized particles.

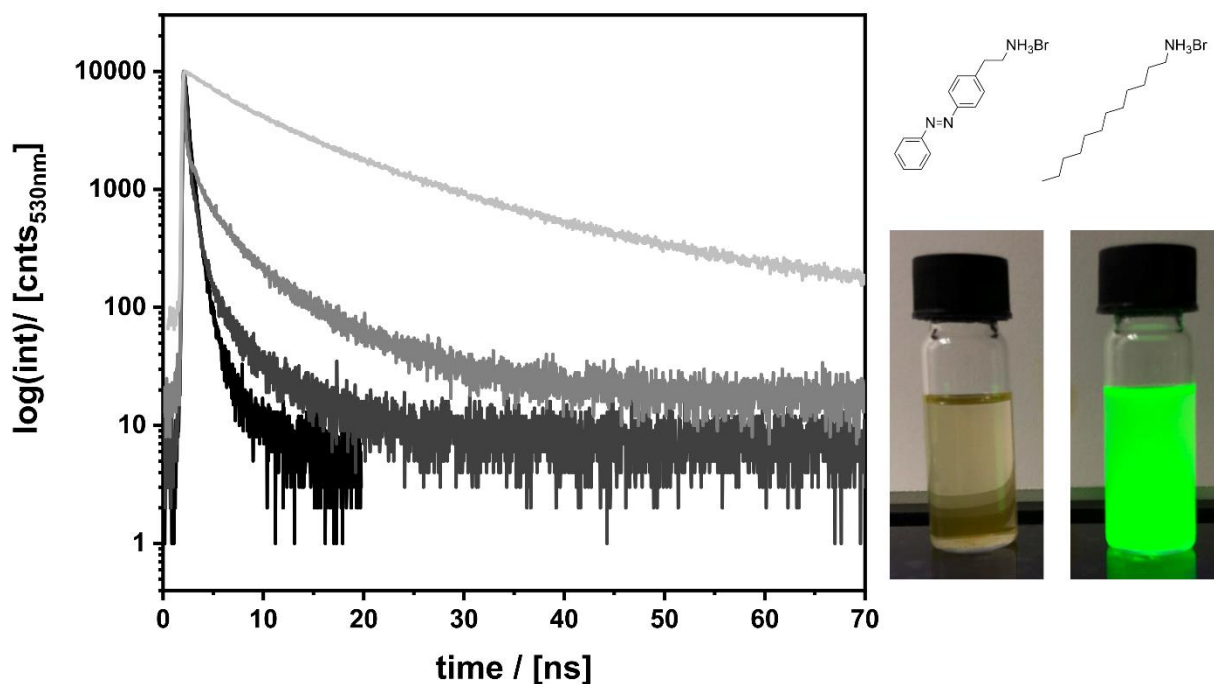


Figure 38 – Time-resolved PL decay of dispersed particles in toluene of 3D-AzoC₁ (black), 3D-AzoC₂ (dark-grey), 3D-AzoC₄ (grey) and 3D-AzoC₁₂ (light-grey). Radiative recombination at 530 nm of the semiconductor phase is observed. Photographs of dispersed particles under UV-irradiation with AzoC₂ (left) and dodecylammonium bromide (DABr) at the surface.

Since various charge carrier dynamics like (surface) defects or photo-recycling influence the PL signal, no (bi)exponential fit could be found.^[56,242] However, the lifetime of the excited radiative states of the particles increases with increasing spacer length between the azobenzene moiety and the MAPbBr₃ phase. This is attributed to the altered distance between the semiconducting phase and the dye.

Short distances, as in AzoC₁ or AzoC₂, enable **fast transfer** of excited charge carriers, which greatly shortens lifetimes. A **larger spacing**, as in AzoC₄ or AzoC₁₂, **increases** the lifetimes significantly, since the hopping process becomes less likely.

As mentioned before, there are many influences on the radiative recombination, so the result is verified with transient absorption spectroscopy (TAS). The following measurements are the result of a cooperation with Tobias Seewald from the AG Schmidt-Mende from the University of Konstanz. TAS is a very versatile technique to observe rapid charge carrier dynamics (see **chapter 2.4.2**) in chromophore-semiconductor systems. It is observed how the absorption behavior of the particles change after excitation, allowing conclusions to be drawn about the length and nature of the excited state. Therefore, the particles are applied to a glass substrate and measured as a solid film. Then, the particles are excited at 398 nm with a laser pulse and the absorption spectra are recorded. The resulting TA spectra are shown in **Figure 39**. Measurements of 3D-AzoC₄ failed due to a low stability of the particles and were unfortunately not repeated.

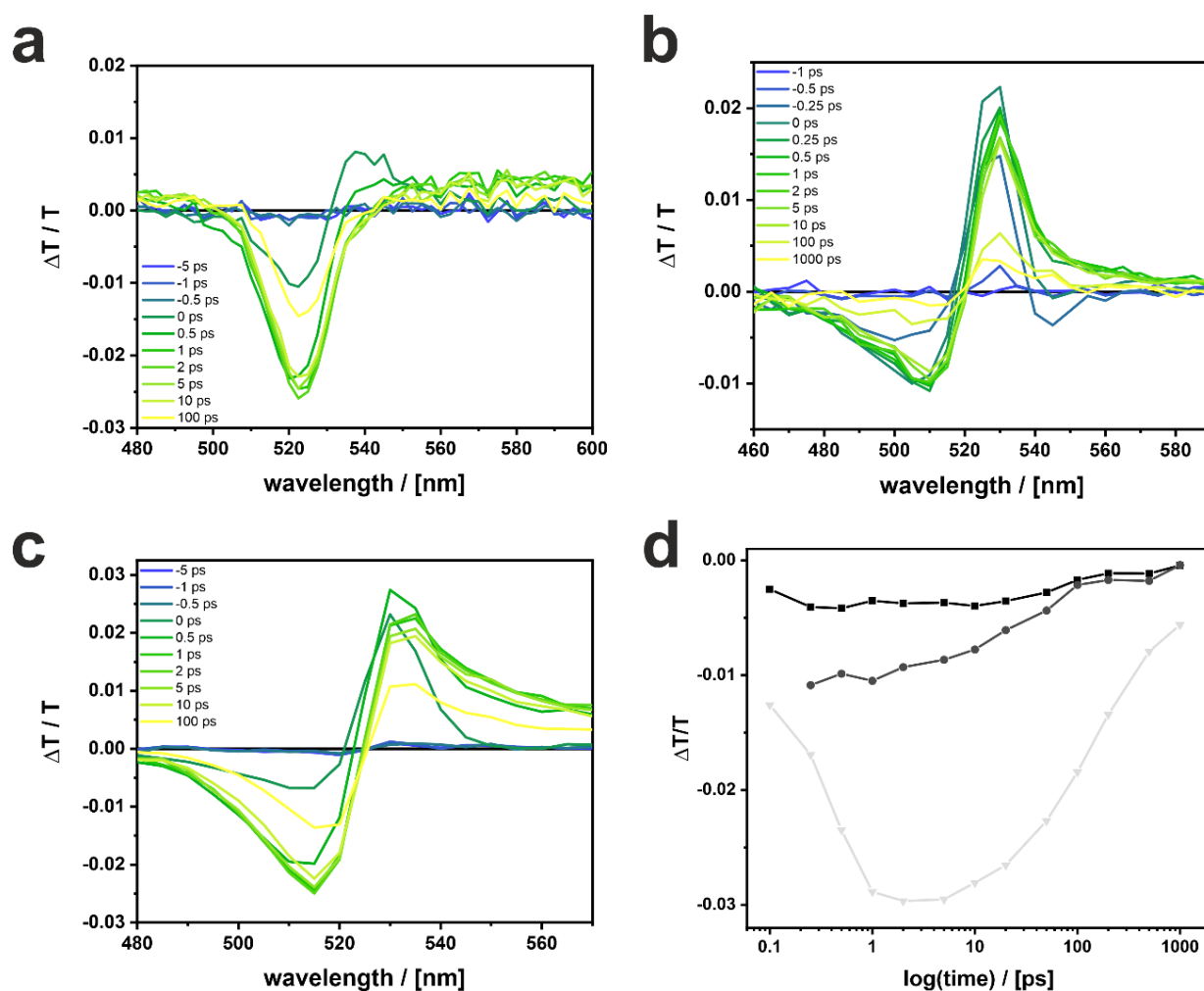


Figure 39 – TA spectra with excitation at 398 nm of a) 3D-AzoC₁, b) 3D-AzoC₂ and c) 3D-AzoC₁₂. d) Decay of the ground-state bleach after the excitation at 398 nm for 3D-AzoC₁ (at 533.5 nm, in black), 3D-AzoC₂ (at 500 nm, in dark grey) and 3D-AzoC₁₂ (at 515 nm, in light grey).

TA spectra are measured in the range between 480 nm and 570 nm, where the band gap of the semiconducting MAPbBr₃ phase can be observed, which is identified as the radiative species. A typical ground-state bleach red-shifted to the band gap is observed for all particles ($\Delta T/T$ positive, between 520 nm and 550 nm), as the absorption at the band gap decreases due to the excited states. A negative $\Delta T/T$ signal (between 500 nm and 520 nm) is attributed to a change of the refractive index, which is caused by a change of the band gap.^[243] Time-dependent observations of the ground-state bleach at 522.5 nm (3D-AzoC₁), 500 nm (3D-AzoC₂) and 515 nm (3D-Azo₁₂) reveal longer lifetimes for an increasing spacer length. Typically, the ground-state bleach is accelerated when the recombination of the excited carriers is faster, e.g. due to trap states at the surface, most probably Pb²⁺ ions.^[244,245]

Here, however, a fast charge carrier transfer from the excited semiconductor phase to the dye is proposed. A short spacer length is responsible for a **very fast recombination** of the charge carriers.

The extension of the spacer leads to a longer ground-state bleach. Similarly, the transfer is responsible for obtaining higher DOIs for surface-bound ligands. The performance of the photoswitching is therefore improved by the excited semiconductor.

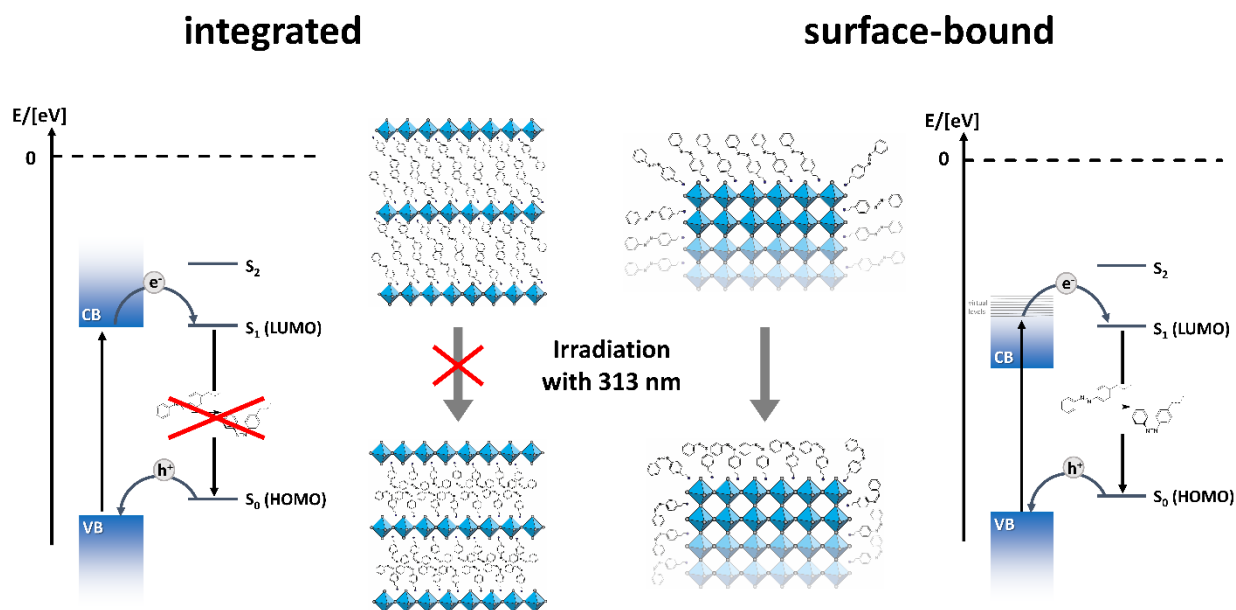


Figure 40 – Schematically overview of the photoinduced isomerization of the synthesized azobenzene ligands between the perovskite layers (left, 2D phase) and on the surface of hybrid perovskite particles (right, 3D phase). When integrated into the semiconductor phase, no photoswitching is available due to steric hindrance. However, surface bound ligands show an improved photoswitching reaction due to a charge carrier transfer from the perovskite to the ligands.

In conclusion azobenzene based surfactants are suitable for the synthesis of surface functionalized NPs of the phase MAPbBr₃. The photoswitching process of the surface bound ligands is possible and even improved by the connection to the semiconductor. Electron hopping is proposed to be responsible for the improved photoswitching. It is revealed, that the distance between the dye and the semiconductor particles is highly responsible for the time-scale of the hopping process. **Figure 40** best summarizes the results of this chapter. The integration of the ligands into LHPs limits their degree of freedom to such an extent that photoswitching is no longer possible (**Figure 40**, left). Only in the case of surface bound ligands a conformational change can be induced by irradiation. This effect is even amplified, if the ligands are attached to the 3D phase MAPbBr₃. Thus, charge carrier transfer is possible, which improves the photoswitching process (**Figure 40**, right).

Therefore, azobenzene in its ground state (*trans*-isomer) is highly suitable as functional ligand for the synthesis of hybrid perovskites, both, the 2D phases with layered character and the 3D phases with functionalized surface. However, with the photoinduced conformational change the optical or electronical properties of the material cannot be altered. Therefore, no energy valve or similar is possible as previously expected.

4.1.4 Ruddlesden-Popper phases with photoswitchable surfactants

Besides LHPs and 3D hybrid perovskites, Ruddlesden-Popper phases (RPPs) with variable layer thicknesses should as well be possible (compare **Figure 5**), using azobenzene based surfactants. These materials are characterized by a modified band gap due to quantum confinement, which allows the energy levels to be adjusted. In the scope of a Bachelor thesis, different attempts were made to produce RPPs with the surfactant AzoC₂. For this purpose, AzoC₂ and MABr have to be integrated in a certain ratio, with the formula (AzoC₂)₂(MA)_{n-1}Pb_nBr₃₊₁ (with n=1,2,3,4, ...).

First, varying proportions of AzoC₂ (0.3 eq, 0.5 eq, 0.7 eq) are added to the commonly used precursor with a ratio of PbBr₂:MABr = 1:1.3 for the antisolvent process at room temperature. Experimental details are given in **chapter 6.2.1**. By varying the proportion of the large cation, layer thicknesses should form with a composition of n>1. **Figure 41a-c** show SEM images of the resulting precipitates. With high equivalents (0.7 eq, 0.5 eq) of AzoC₂, a mixture of small cubic particles and larger flat particles are obtained. With a small ratio of AzoC₂ only cubic particles are obtained.

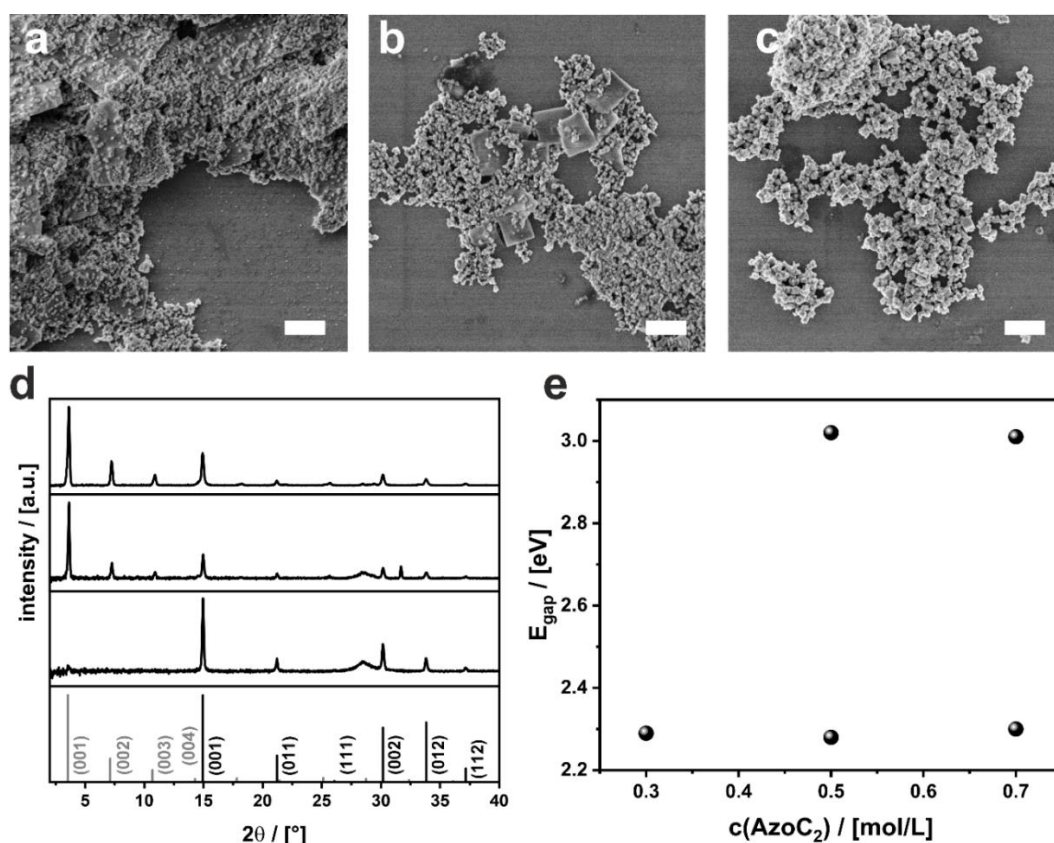


Figure 41 – SEM images of precipitates with a) 0.7 eq AzoC₂, b) 0.5 eq AzoC₂ and c) 0.3 eq AzoC₂. Scalebar = 1 μm d) PXR patterns of the precipitates with 0.7 eq AzoC₂ (top), 0.5 eq AzoC₂ (middle) and 0.3 eq AzoC₂ (bottom). e) Overview of the found band gaps determined with UV/Vis reflectance spectroscopy using the Kubelka-Munk analysis (see **Figure A20**).

For simplicity the particles will be named $\text{RPP}^{\text{RT}_{\text{eq}}}\text{-AzoC}_2$ from here on. Regarding the PXRD patterns two phases can be identified for $\text{RPP}^{\text{RT}_{0.7}}\text{-AzoC}_2$ and $\text{RPP}^{\text{RT}_{0.5}}\text{-AzoC}_2$. The precipitate consists of a mixed phase of 2D-AzoC₂ and 3D-AzoC₂ as the reference pattern show (**Figure 41d**, bars at the bottom). According to SEM and PXRD, the crystal structure of RPPs does not seem to be present, but rather the formation of the n=1 2D LHP and the 3D phase MAPbBr₃ is observed. UV/Vis reflectance spectroscopy reveals the band gap of the precipitates (see **Figure 41e** and **Figure A20**). For particles with a high AzoC₂ content, two band gaps at 2.3 eV and 3.1 eV can be determined. This also suggests that a mixture of the two phases is obtained.

The question now arises as to how the observed phase separation occurs. Considering the growth mechanism of RPPs in the antisolvent process, the solubility of the large cation plays a major role.^[232] The solubility of the ligand can be adjusted by the temperature of the antisolvent. Thus, precipitation is carried out at room temperature, -10 °C and -20 °C with 0.5 eq of AzoC₂. PXRD patterns again indicate the precipitation of the layered 2D LHP with n=1 and the 3D phase MAPbBr₃ for all temperatures, demonstrated in **Figure 42a**. It is striking that with decreasing temperature the proportion of 3D phase increases, as can be seen in the (001) reflection at $2\theta \approx 15^\circ$ and the (002) reflection at $2\theta \approx 30^\circ$ (gray background). By lowering the temperature, the formation of the 3D phase is thermodynamically favored.^[246] However, no additional phase is found for the precipitates.

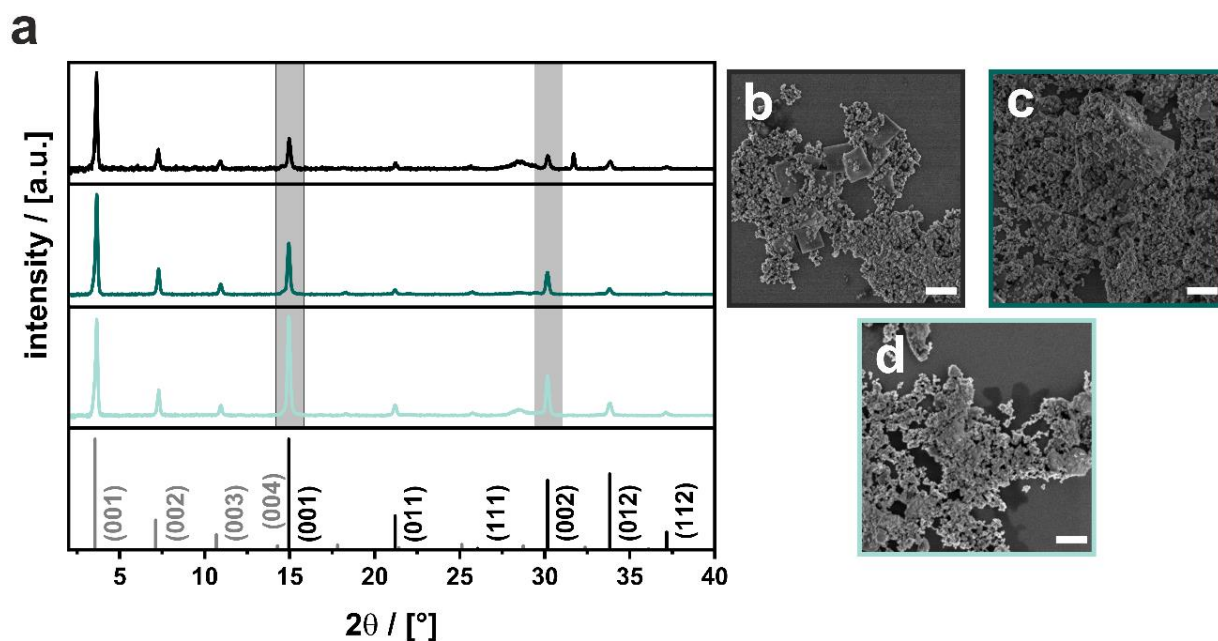


Figure 42 - a) PXRD patterns of $\text{RPP}^{\text{RT}_{0.5}}\text{-AzoC}_2$ (top, black), $\text{RPP}^{-10^\circ\text{C}_{0.5}}\text{-AzoC}_2$ (middle, dark green) and $\text{RPP}^{-20^\circ\text{C}_{0.5}}\text{-AzoC}_2$ (bottom, light blue). SEM images of b) $\text{RPP}^{\text{RT}_{0.5}}\text{-AzoC}_2$, c) $\text{RPP}^{-10^\circ\text{C}_{0.5}}\text{-AzoC}_2$ and d) $\text{RPP}^{-20^\circ\text{C}_{0.5}}\text{-AzoC}_2$.

Figure 42b-d show the SEM images of the obtained particles. Since no change in size or shape is observed, it is concluded, that temperature has no influence on the formation of the particles.

Further investigations of the optical properties of the particles reveal, that again only two band gaps are found for the precipitates. **Figure 43a** summarizes the band gaps determined from UV/Vis reflectance spectroscopy with subsequent Kubelka-Munk analysis (see **Figure A21**). Here, in addition to the absorption properties, the emission was also determined (see **Figure 43b**).

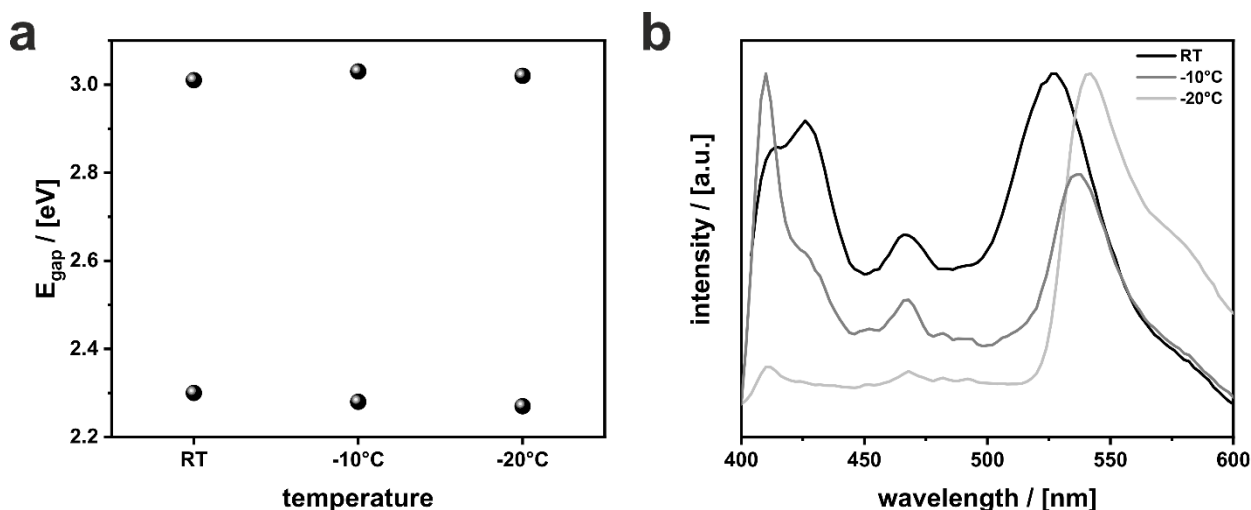


Figure 43 - a) Overview of the band gaps for the particles obtained at varying temperature. Determination occurs with UV/Vis reflection spectroscopy with subsequent Kubelka-Munk analysis (see **Figure A21**). b) PL spectra of the dispersed particles in toluene which were synthesized at varying temperatures. Excitation occurred with an Xe-lamp at 380 nm.

When excited at 380 nm, three emission peaks between 410 nm and 425 nm, at 465 nm and at ~530 nm are obtained for $\text{RPP}^{\text{RT}}_{0.5}\text{-AzoC}_2$ and $\text{RPP}^{-10^\circ\text{C}}_{0.5}\text{-AzoC}_2$. For $\text{RPP}^{-20^\circ\text{C}}_{0.5}\text{-AzoC}_2$ only one emission peak at 543 nm is found. Emission at approximately 530 nm is attributed to radiative recombination of the excited states near the band edges of the 3D phase MAPbBr_3 . Emission between 410 nm and 425 nm is attributed to the radiative recombination of the excited states near the band edges of the LHP 2D-AzoC_2 , with $n=1$. However, an emission peak at 465 nm does not occur for the two mentioned phases. Since the band gap for RPPs ($n>1$) is larger compared to the 2D LHP with $n=1$, it is possible that the observed emission can be assigned to a layer thickness with $n>1$. Since the emission of the particles raises the question whether RPPs with $n>1$ are present in the material, an explanation for the observed signals must be found.

RPPs consist of a periodic array of independent layers. The incorporation of MABr should add more $[\text{PbBr}_4]$ -layers so that a larger layer spacing can be found in the PXRD. Since PXRD strongly depends on periodicity, many layers of the same thickness must follow

each other to detect a periodic arrangement. However, if there are only occasional thicker layers in the particles, they may not be detected in the PXRD.

Optical measurements are not dependent on the periodicity of the layered structure. Therefore, UV/Vis reflectance spectroscopy and PL spectroscopy allow the determination of all band gaps present in the material. For the materials investigated above, UV/Vis spectroscopy reveals two distinct band gaps, while emission spectra yield three. Since charge carrier transfers (by tunneling or hopping) between layers are possible, the PL signals can be falsified.^[247] This means that generated charge carriers are transferred to layers with the smallest band gap, where they then recombine radiatively.^[248] This can quickly lead to the false conclusion that a high number of thicker layers ($n > 1$) with smaller bandgaps are present. Therefore, it is assumed that only a very small fraction of thicker layers with $n > 1$ are present in the particles, that are responsible for the observed emission properties.

Other approaches (e.g., increasing or decreasing the AzoC₂ concentration the precursor, irradiation of the precursor before conversion, change of precursor solvent or antisolvent, respectively) also failed to achieve RPPs. Presumably, this is due to very strong interactions of the ligands with each other, so that no MABr can be incorporated after the formation of an $n=1$ layer. Due to the extended conjugated system, it is possible that π -interactions arise between the ligands. Since the AzoC₂ is poorly soluble in non-polar solvents, the interactions are probably too strong to dissolve ligands from the interface. Consequently, MABr does not intercalate between the layers and therefore forms only the 3D phase MAPbBr₃.

In summary, it is very **difficult** to **obtain RPPs** with AzoC₂. However, initial results show that it should be quite possible. Further approaches and investigations need to be made here.

4.2 Ferrocene as functional surfactant

In addition to molecular photoswitches such as azobenzene, there is a further class of molecules that can actively be influenced by an external stimulus. Organometallic complexes mostly contain a redox-active metal center, such as iron(II) in ferrocene (Fc). Fc and its derivatives are characterized by a unique and reliable redox chemistry, which is provided by a simple one-electron process. Due to the reliability of the process, Fc is popularly used as a standard in electrochemistry.^[189] Surfaces of non-conductive materials can be made conductive by functionalization with Fc, for instance.^[207] Thus, they find application in various materials such as electrocatalysis, membrane fuel cells or batteries.^[201,202]

The chemistry behind Fc, which has now been established for over 70 years, allows the synthesis of a wide variety of derivatives. This enables to prepare also cationic surfactant-like derivatives, making them suitable for the synthesis and functionalization of hybrid perovskites. However, so far there is only one known lead halide crystal phase containing ferrocene. Zhang *et al.* observed the formation of one-dimensional (1D) face-sharing lead halide octahedra, when integrating (ferrocenylmethyl)trimethylammonium iodide, a commercially available Fc derivative. They describe semiconducting properties and observe extraordinary piezoelectricity.^[215] Surprisingly, however, they do not exploit the redox activity of the ligand.

Hence, it has already been shown that the incorporation of Fc into hybrid perovskites is beneficial to the material.^[215] The following questions arise from these observations:

- Is it possible to prepare 2D layered hybrid perovskites (LHPs) with a **chemically adapted** Fc ligand? How should the chemical structure be adapted to achieve this?
- Are there **electronic interactions** between the ligands and the semiconducting lead halide phases?
- Is it possible to influence the phases optically and electronically by **oxidation**?

4.2.1 Synthesis and characterization of redox-active surfactants

For the investigation of redox-active hybrid perovskites five novel Fc derivatives are synthesized. Their chemical structure is shown in **Figure 44**. Starting from ferrocenyl carboxylic acid, head groups with different spacer lengths (alkyl chain) are attached to the Fc via ester coupling. A detailed synthesis protocol can be found in **chapter 6.1**. Different lengths of the head group provide the investigation of distance dependent interactions and structure-directing properties of the ligands. For simplicity, the ligands will be named FcC_n (n=2,3,4,5,6) from now on. The ligands are characterized with ¹H-NMR, ¹³C-NMR and ESI-MS (see **Figure A22+Figure A23** and **chapter 6.1**).

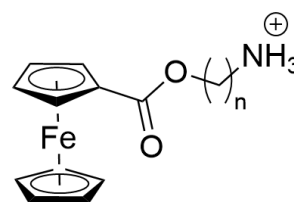


Figure 44 - Chemical structure of Fc ligands with n=2,3,4,5,6

Infrared (IR) transmission spectroscopy confirmed the successful synthesis of the ligands (see **Figure A24**).

To investigate and understand possible interactions with the semiconducting lead halide phases, the ligands are analyzed for their absorption in the UV/Vis region before and after oxidation. **Figure 45a** shows the UV/Vis absorption spectrum of FcC_2Br before oxidation. Absorption bands at 446 nm (2.78 eV), 359 nm (3.55 eV) and 311 nm (3.98 eV) are present. The absorption band at 446 nm is attributed to the

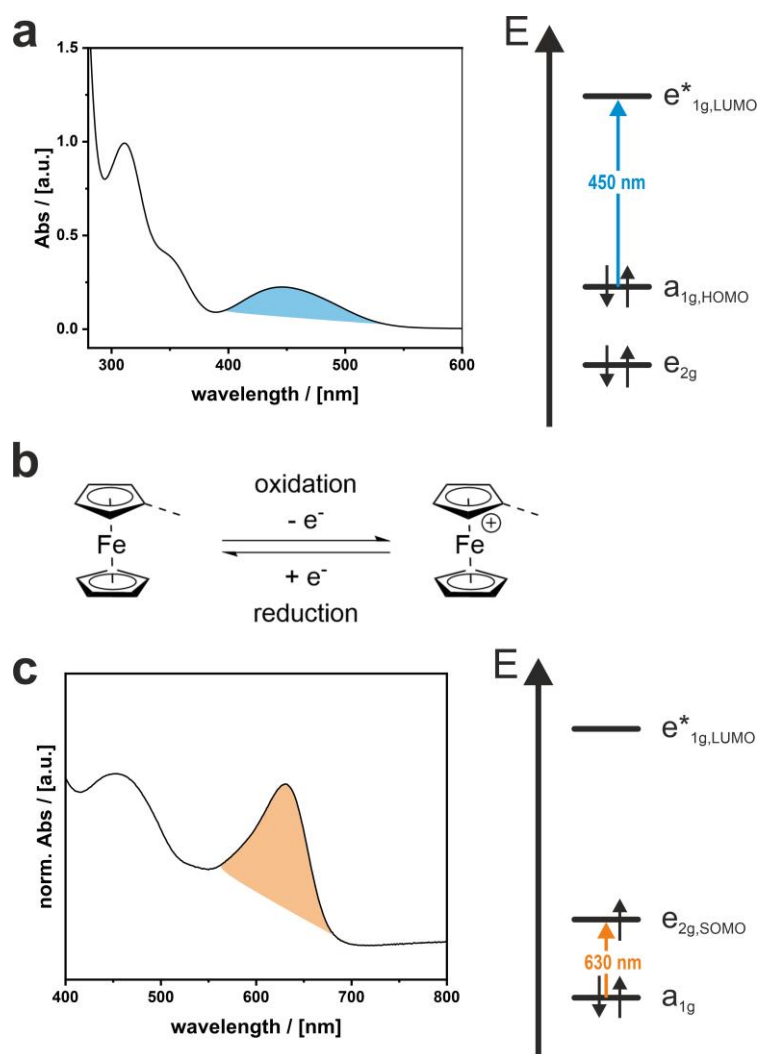


Figure 45 – a) UV/Vis spectrum of FcC_2Br in H_2O with energy scheme of the MO alignment. The HOMO-LUMO transition at ~ 450 nm occurs from the a_{1g} MO to the e^*_{1g} MO. b) Schematic representation of the oxidation/reduction process of Fc derivatives and c) UV/Vis spectrum of FcC_2Br in H_2O after oxidation with $\text{Ce}(\text{SO}_4)_2$. A new absorption band is found which is attributed to a transition from a deeper lying MO into the emerging SOMO e_{2g} , which now lies above the initial HOMO a_{1g} .

present. The absorption band at 446 nm is attributed to the HOMO-LUMO transition from the bonding molecular orbital (MO) a_{1g} to the antibonding MO e^*_{1g} . Oxidation with a suitable oxidizing agent (here $\text{Ce}(\text{SO}_4)_2$) oxidizes the iron core from Fe^{2+} to Fe^{3+} (see **Figure 45b**). Oxidation affects the MO e_{2g} which is now a single occupied molecular orbital (SOMO) and lies above the initial HOMO a_{1g} . Thus, the electronic structure of Fc is altered by the oxidation.^[249] An absorption band at 631 nm (1.97 eV) is found after the oxidation of FcC_2Br (see **Figure 45c**). The absorption is attributed to a transition from a deeper lying MO into the emerging SOMO e_{2g} . Due to oxidation, the solution thus changes its color from originally orange to green/blue. For simplicity, only FcC_2Br is shown here, however, other ligands behave similar and the spectra can be found in **Figure A25-Figure A28**.

4.2.2 Crystal structure of ferrocene containing lead bromide phases

After complete molecular characterization, the Fc ligands are used to synthesize hybrid perovskites in the form of crystalline particles in the micrometer range. For this purpose, a precursor solution is prepared, which is precipitated in an antisolvent. Since only a small amount of the Fc ligands are soluble in triethylene glycol (TEG), dimethylformamide (DMF) is used as a solvent for the FcC_nBr ligands ($n=2,3,4,5,6$) and PbBr_2 . The exact synthesis protocol of the particle synthesis is given in **chapter 6.2.2**. From all antisolvent processes, a precipitate can be separated. A first indication of a successful particle synthesis is given by SEM images of the precipitates, which show particulate systems, shown in **Figure 46**.

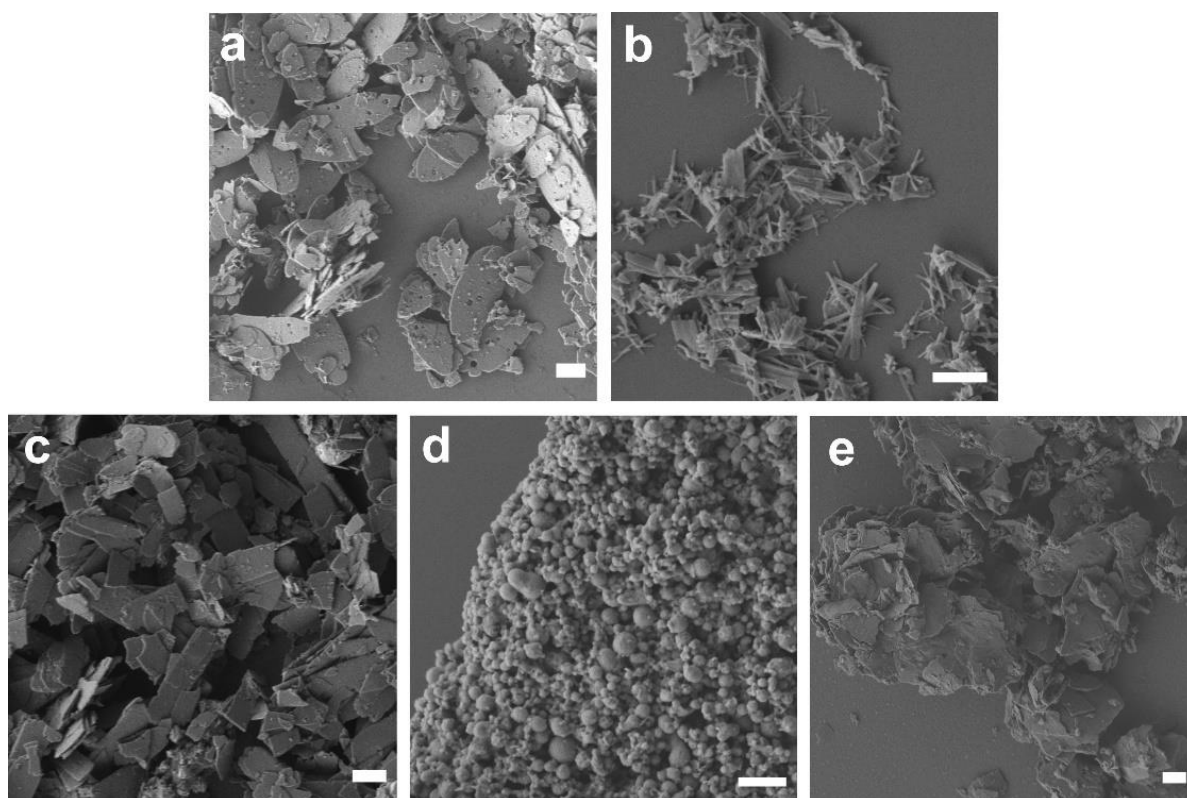


Figure 46 – SEM images of precipitations with PbBr_2 and a) FcC_2Br , b) FcC_3Br , c) FcC_4Br , d) FcC_5Br and e) FcC_6Br . Scalebar = 1 μm .

The largest resulting particles from the antisolvent process are lateral in the micrometer range and nanosized in thickness (see **Figure 46**). The particles obtained with FcC_2Br have an oval, flat shape, indicating a layered character of the crystal structure. Needle-shaped particles are obtained with the FcC_3Br ligand. Their length is in the micrometer range, but they are much narrower, i.e. previously the particles with FcC_2Br . Particles formed with the FcC_4Br ligand have a flat shape and are elongated in one direction. Interestingly, with FcC_5Br the particles get very round and shapeless. With FcC_6Br , on the other hand, very large flat particles are obtained, suggesting a layered character of the obtained crystal structure.

Thus, it can be shown that it is possible to crystallize a solid phase with all ligands, although they already show significant differences in their particles shape and size. Larger structures form with FcC₂Br, FcC₄Br and FcC₆Br, indicating enhanced crystal growth of the resulting particles. The round shape of the particles with FcC₅Br suggests that there is no good crystallinity of the phase. This can be due to the inability of the ligand to be well incorporated into the phase because of its steric nature. To verify this, the crystal phase of the particles must be determined. For the determination of the crystal phase and crystallinity, PXRD measurements are obtained, shown in **Figure 47** and **Figure A29**.

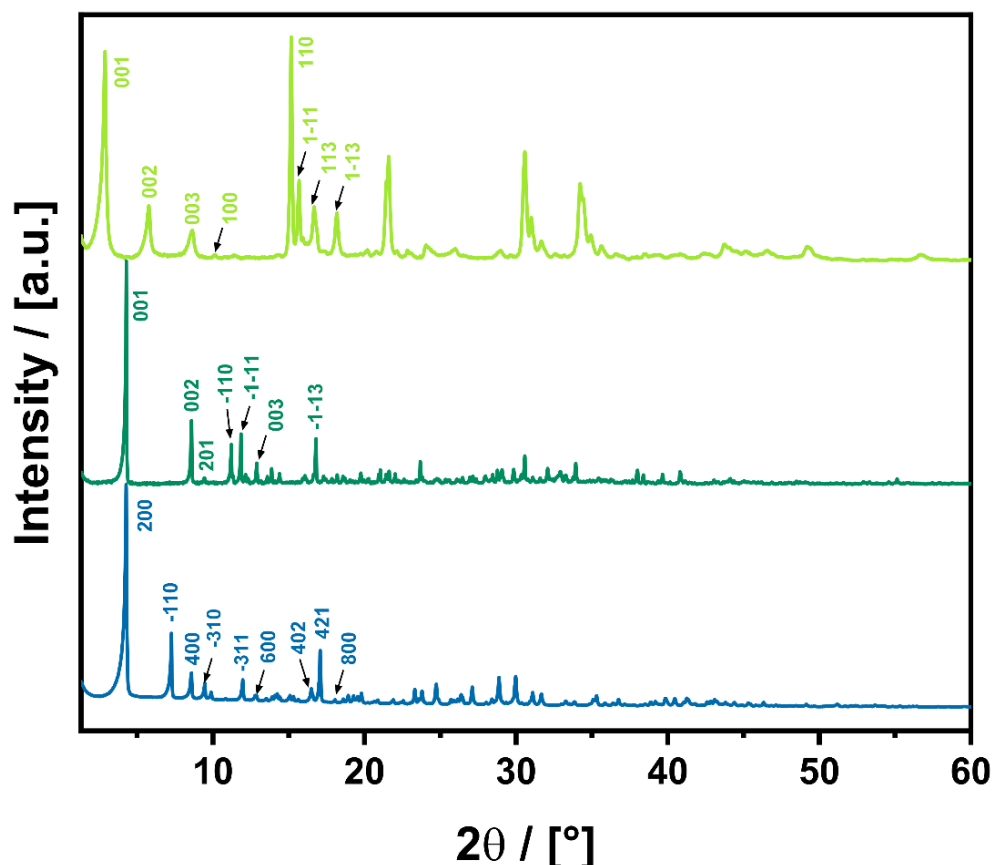


Figure 47 – Experimental PXRD patterns of precipitation products with PbBr₂ and FcC₂Br (bottom, blue), FcC₄Br (middle, dark green) and FcC₆Br (top, light green). Reflections were indicated based on the crystal structure analysis, which will be described later.

It is striking that FcC₃Br and FcC₄Br, as well as FcC₅Br and FcC₆Br show very similar diffraction patterns (see **Figure A29**). This can be attributed to a very similar crystal structure of the inorganic lead bromide framework. The arrangement of the lead and bromide ions is very similar, but the Fc ligands arrange themselves slightly differently, due to the changed spacer length of the head group. Therefore, distortions occur, which are represented by modified diffraction patterns. The lowered crystallinity for crystal phases with FcC₃Br and FcC₅Br can be attributed to comparatively poorer packing of the ligands between the lead bromide frameworks. These phases will not be considered for

future studies, as structure elucidation is significantly more difficult due to the lower crystallinity. In addition, it can be assumed that a very similar crystal structure can be expected.

The first intensive reflections ((001) and (200) respectively) confirm the formation of layered structures, since they can be assigned to the basal distance. Regarding the diffraction patterns of the crystalline phases, only the particles with FcC_6Br can be assigned to a typical LHP with a layer thickness of $n=1$.^[77] However, the other diffraction patterns are too complex for an unambiguous characterization of the crystal structures solely from PXRD.

One possibility for structure elucidation is the preparation of (large) single crystals, which can be measured by single crystal X-ray diffraction (SCXRD). Discrete point diffractions which are obtained from a single crystal can be used to determine the exact crystal structure. When attempting to produce single crystals (e.g. via slow evaporation of the solvent^[215]), large single crystals are obtained, which, however, do not correspond to the phases obtained via the antisolvent process. Investigation of the single crystals with SCXRD gives a novel phase with the composition $\text{Fe}(\text{C}_3\text{H}_7\text{NO})_6\text{Pb}_2\text{Br}_6$. The crystal structure is shown in **Figure 48a**, crystal data is given in **Table 16** and fractional coordinates in **Table 17** (see appendix). SCXRD analysis reveals a structure in which Fe^{2+} is coordinated octahedrally by six DMF ligands, best seen in **Figure 48b**. The charge of the cationic complex is balanced by 1D chains of anionic lead bromide pyramids, which are connected at their edges and form a zig-zag like chain.

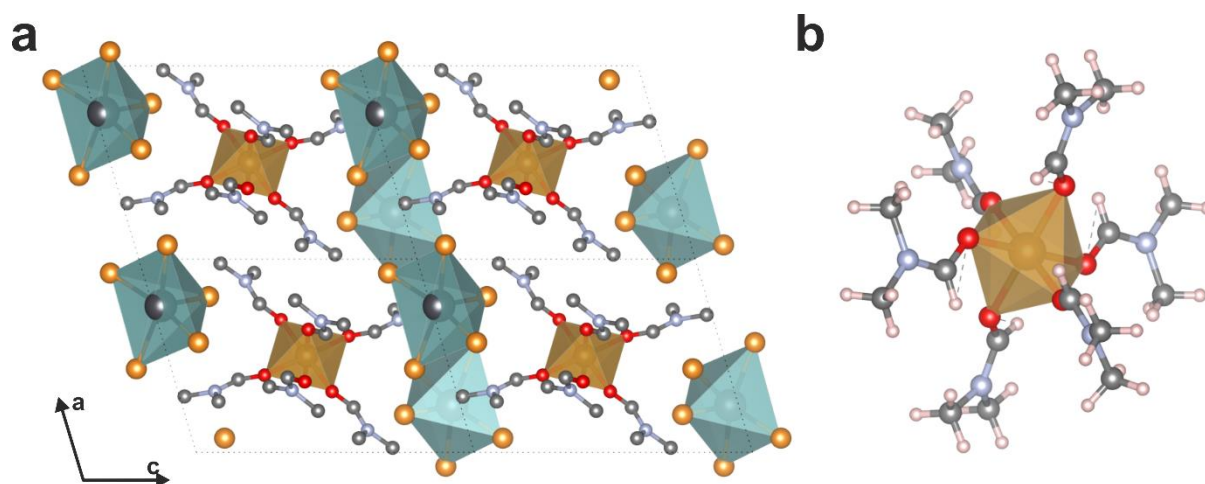


Figure 48 – a) Crystal structure of $\text{Fe}(\text{C}_3\text{H}_7\text{NO})_6\text{Pb}_2\text{Br}_6$ viewed from the b-direction. Hydrogen atoms were removed for clarity. b) Fe^{2+} cation which is coordinated octahedrally by six dimethylformamide ($\text{C}_3\text{H}_7\text{NO} = \text{DMF}$) solvent molecules. In solution, a ligand exchange takes place due to an excess of DMF.

In the precursor solution there is an excess of DMF, thus, a slow ligand exchange occurs, so that large crystals precipitate after about 7 to 10 days. Ligand exchange presumably

occurs from about 5-6 hours after dissolution of the starting materials, as indicated by a color change from orange to brown. Unfortunately, UV/Vis spectra do not show any change of the absorption of the precursor solution, so it can only be judged by eye. For precipitation of particles in the antisolvent process, the precursor solution was therefore always prepared fresh and reacted immediately after dissolution of the substances.

Since preparation of single crystals is not possible due to the above-mentioned effect, another technique is applied for crystal structure analysis. The recently developed technique of 3D electron diffraction (3D ED) exploits the diffraction of electrons at crystals in the beam of a transmission electron microscope (TEM). Thus, it is now possible to solve crystal structures from small crystals down to the nanoscale.^[250–252] The dynamic scattering at single crystals even allows the detection of hydrogen atoms and a precise structure refinement.^[253,254] However, beam-sensitive materials are still difficult to measure because they can decompose in the electron beam.

Using 3D ED, the prepared crystals with FcC_2Br and FcC_4Br can be structurally elucidated and refined. However, the precipitate with FcC_6Br is unfortunately too beam sensitive and decomposes after a short exposure in the electron beam. Since the PXRD pattern indicates that it is an LHP, a structural model is calculated. All structural determinations were made by Yaşar Krysiak. More details of the structure determination can be found in the publication and will not be discussed in detail here.^[234] The composition for the phases are $(\text{C}_{13}\text{H}_{16}\text{FeNO}_2)\text{PbBr}_3$ (= $(\text{FcC}_2)\text{PbBr}_3$), $(\text{C}_{15}\text{H}_{20}\text{FeNO}_2)_4\text{Pb}_3\text{Br}_{10}$ (= $(\text{FcC}_4)_4\text{Pb}_3\text{Br}_{10}$) and $(\text{C}_{17}\text{H}_{24}\text{FeNO}_2)_2\text{PbBr}_4$ (= $(\text{FcC}_6)_2\text{PbBr}_4$), respectively. The crystal structures are shown in **Figure 49-Figure 51**, the crystal data of the phases is represented in **Table 6**. In the following, the novel crystal structures are discussed and how the Fc ligands influence the formation of the crystal phases.

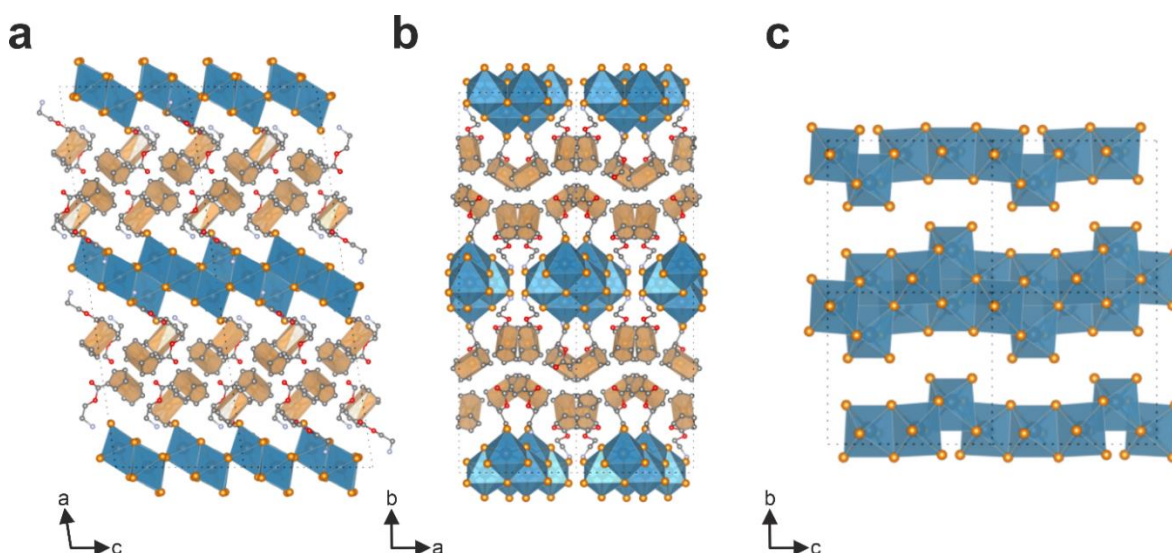


Figure 49 – Crystal structure of $(\text{FcC}_2)\text{PbBr}_3$ viewed from the a) b-direction, b) c-direction and c) a-direction (without Fc ligands). Hydrogen atoms are removed for clarity.

Probably the most exotic structure is formed by the ligand FcC_2Br with lead bromide. A 1D “ribbon” structure with edge-sharing octahedra, which form polymeric $[\text{PbBr}_3]^-$ -chains (**Figure 49a+c**) has not yet been observed in literature. The ribbon is reminiscent of the well-known $(\text{NH}_4)\text{CdCl}_3$ structure type,^[255] which also contains edge-sharing octahedra. Four octahedra are connected to form a tetramer via their edges, similar to the $(\text{NH}_4)\text{CdCl}_3$ type, best seen in **Figure 49b**. A staggered arrangement of the tetramers leads to a zig-zag like structure of the $[\text{PbBr}_3]^-$ -ribbons, which extend along the c-axis (see **Figure 49c**). This unusual structure is attributed to the Fc ligands, which possess a strong structure-directing character. Two adjacent Fc moieties are arranged perpendicular to each other, which is very similar to the arrangement in the crystalline structure of non-functionalized solid Fc.^[256] The arrangement of the Fc moieties thus also strongly influences the arrangement and extension of the chain.

When considering the position of the Fc ligands, a distinction is made between two configurations of the ethyl ammonium head group. On the one hand the ammonium group coordinates the ribbons from above (N_1 ; see **Figure A30**), on the other hand it extends deeper in between two $[\text{PbBr}_3]^-$ -ribbons (N_2). This is best seen in **Figure 49b**: a pair of two Fc-units that appear to overlap here coordinate the lead bromide phase either above the ribbon or between two ribbons. The head group N_1 is furthermore connected to the ester group of an adjacent ligand by hydrogen bonding ($\text{N}_1\text{-H-O}_3$). The head group N_2 is only coordinated to the $[\text{PbBr}_3]^-$ -ribbons. Since the crystal structure of lead bromide phases is strongly dependent on the formation of hydrogen bonds,^[96] this competing hydrogen bond formation influences the crystal structure. The hydrogen bond formed between the head group N_1 and the O_3 of the ester group therefore competes with this interaction and a very exotic inorganic framework is observed (see **Figure A30**).

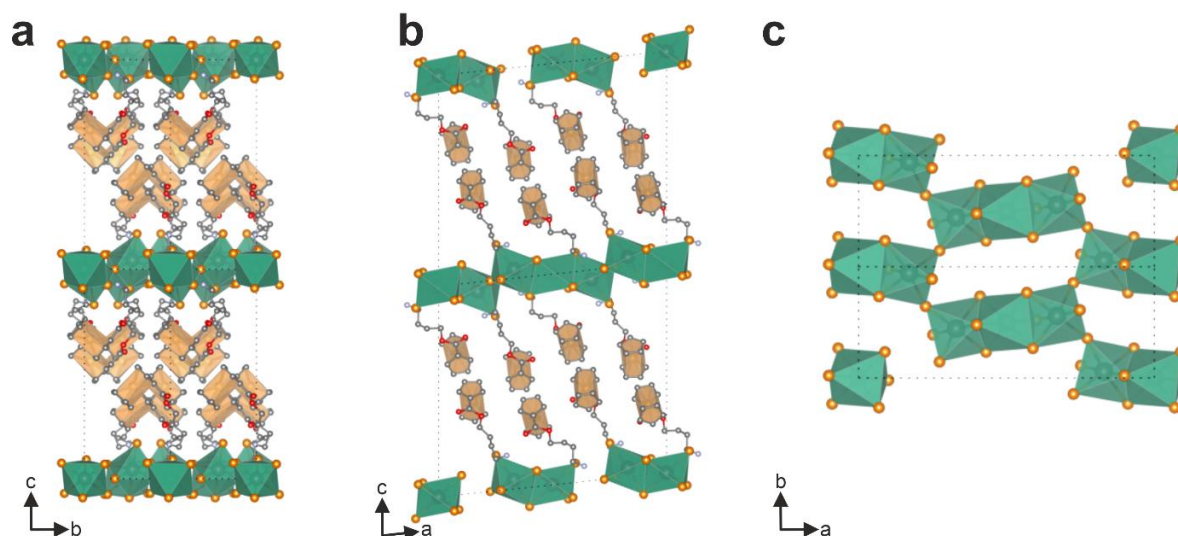


Figure 50 – Crystal structure of $(\text{FcC}_4)_4\text{Pb}_3\text{Br}_{10}$ viewed from the a) a-direction, b) b-direction and c) c-direction (without Fc ligands). Hydrogen atoms are removed for clarity.

Extending the head group to FcC_4Br (or FcC_3Br) results in a layered structure, analogous with the structure of $\text{Cs}_4\text{Mg}_3\text{F}_{10}$.^[257] The inorganic lead bromide sheets of $(\text{FcC}_4)_4\text{Pb}_3\text{Br}_{10}$ contain trimers of face-sharing octahedra linked through bridging bromides to adjacent trimers (see **Figure 50c**). The same inorganic sublattice was observed before, containing phenyltrimethylammonium bromide $(\text{C}_6\text{H}_5\text{N}(\text{CH}_3)_3\text{Br})$ ^[258] and trimethylsulfonium bromide $(\text{CH}_3)_3\text{SBr}$ ^[259] as templating organic cation. Compared to these structures, the connecting Pb-Br-Pb bridge of the trimers are more tilted with an angle of $157.70(8)^\circ$. This is attributed to the increased distortion of the lattice due to the strong templating properties of the Fc ligand. Considering the position of the Fc ligands, the packing appears to be less complex than for $(\text{FcC}_2)\text{PbBr}_3$.

Here, the packing of the ligands plays a crucial role for the structure formed. Two different configurations of the head group of the FcC_4Br ligand can be distinguished. The Fc moieties are also perpendicular to a ligand of the next layer (best seen in **Figure 50a**). For FcC_2Br , coordination always takes place to the nearest ligand along its “own” ribbon. In one configuration, the alkyl spacer is extended to its full length. Here the Fc unit is farther away from the lead bromide phase. In the other configuration, the alkyl chain folds slightly, which is due to a hydrogen bond between the ester group and an ammonium head group of the adjacent Fc ligand (best seen in **Figure 50b**). However, the longer chain allows more degrees of freedom in the structure, which is why the inorganic framework extends in two dimensions (a and b) and a stronger layered character is achieved.

To compare the observed structures, a parameter for the packing density of Fc ligands is defined as the distance between two iron atoms ($d_{\text{Fe-Fe}}$, see **Table 6**). In comparison to $(\text{FcC}_2)\text{PbBr}_3$ ($d_{\text{Fe-Fe}} = 6.35 \text{ \AA}$), the Fc moieties are closer together for $(\text{FcC}_4)_4\text{Pb}_3\text{Br}_{10}$

($d_{\text{Fe-Fe}} = 6.24 \text{ \AA}$), which is attributed to the more flexible chain and therefore a higher degree of freedom of the ligands. The packing of the metalorganic component of the structure is therefore more efficient, when the length of the head group is extended by one (FcC_3Br) or two (FcC_4Br) methylene groups.

If the alkyl spacer between the ammonium head group and the Fc unit is extended even further, the crystal phase of the particles changes again. For the ligands FcC_5Br and FcC_6Br , an LHP results, so that these phases can now be assigned to a true perovskite phase of the Ruddlesden-Popper type. With this assumption, a possible crystal structure can be calculated by approximations and converged to the experimental PXRD via Rietveld refinement. A detailed description of the calculation can be found in the publication.^[234]

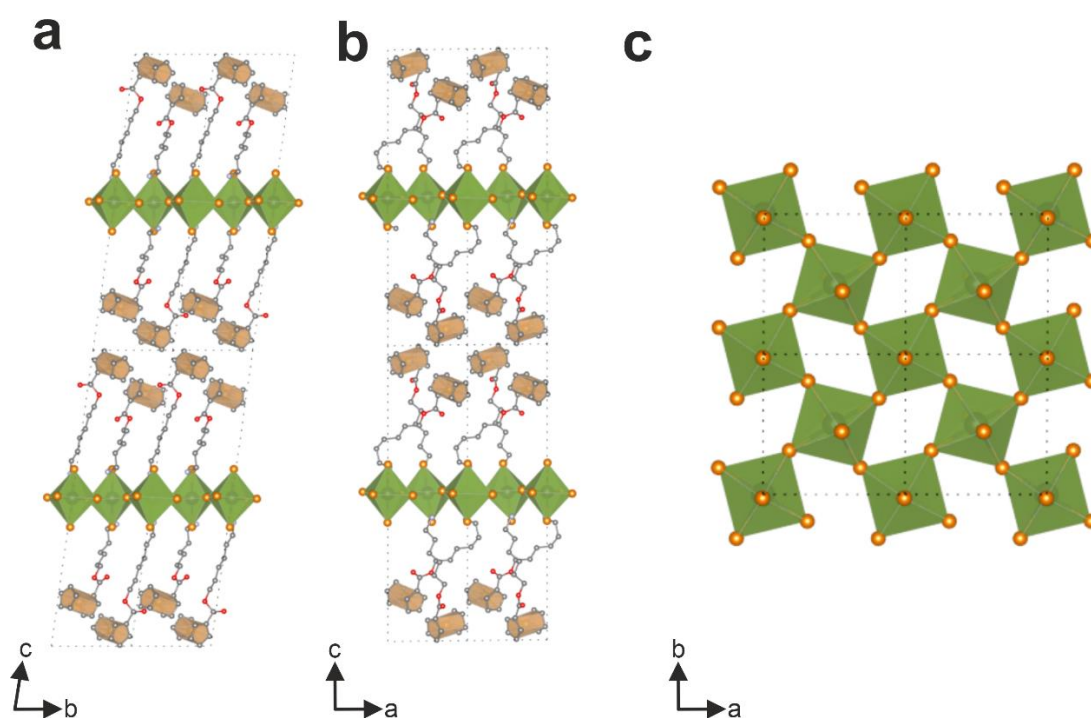


Figure 51 – Crystal structure of $(\text{FcC}_6)_2\text{PbBr}_4$ viewed from the a) a-direction, b) b-direction and c) c-direction (without Fc ligands). Hydrogen atoms are removed for clarity.

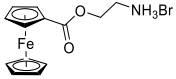
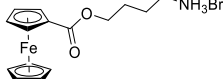
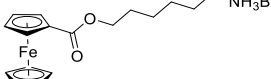
For the ligand FcC_6Br , a typical LHP with the composition $(\text{FcC}_6)_2\text{PbBr}_4$ is obtained, as the diffraction pattern already suggests. The inorganic lattice consists of distorted corner-sharing octahedra (see **Figure 51c**). A similar arrangement of the Fc-dumbbells is observed, with the ligands slightly closer together with $d_{\text{Fe-Fe}} = 6.14 \text{ \AA}$. This results in an oblique, folded position of the chain of every second ligand between the $[\text{PbBr}_4]$ -layers (see **Figure 51b**). In addition, the longer alkyl chain now prevents the formation of hydrogen bonds between the ammonium head group and the carboxyl group, which results in a less densely packed structure.

From crystal structure analysis, it is clear that both the **functionality** and the length of the **head group** have strong effects on the inorganic framework of the resulting lead bromide phase.

Based on these studies, it can be stated that the chemical structure of the ligands, especially the nature of the head group, plays a major role in the formation of new crystal phases. Especially the formation of hydrogen bonds is essential for hybrid perovskites,^[105] which is why competing groups such as the ester group can have a major influence. At the same time, the flexibility of the head group determines how well the ligands can be packed. Due to these many requirements that must be fulfilled, a true LHP can only be obtained from a chain length of 6 methylene groups.

However, similar to azobenzene, the functionality of the ligand, in this case Fc, also has an influence as these also adopt a preferred arrangement, namely perpendicular to each other. Apart from weak Van-der-Waals interactions, observed in alkyl-based perovskites, stronger π -interactions (e.g. π -stacking) are present in these conjugated systems.

Table 6 - Crystal structure data determined for precipitates with FcC_nBr and $PbBr_2$. Crystal structures for $n=2,4$ were determined with 3D ED. Crystal structure of $n=6$ was modelled using DFT calculations.

	(FcC₂)PbBr₃	(FcC₄)₄Pb₃Br₁₀	(FcC₆)₂PbBr₄
precursor salt			
empirical formula	(C ₁₃ H ₁₆ FeNO ₂)PbBr ₃	(C ₁₅ H ₂₀ FeNO ₂) ₄ Pb ₃ Br ₁₀	(C ₁₇ H ₂₄ FeNO ₂) ₂ PbBr ₄
formula weight (g/mol)	721.03	2630.44	1187.88
crystal system	Monoclinic	Monoclinic	Triclinic
space group	<i>C2/c</i>	<i>P2₁/a</i>	<i>P-1</i>
Z	16	2	2
<i>a</i> [Å]	41.6677(13)	22.3384(10)	8.287(5)
<i>b</i> [Å]	12.7153(4)	8.43444(19)	8.284(4)
<i>c</i> [Å]	14.0140(4)	20.6965(7)	31.09(3)
<i>V</i> [Å ³]	7333.9(4)	3877.3(2)	2113(3)
α, β, γ [°]	90, 98.9741(11), 90	90, 96.109(3), 90	81.97(16), 90.62(9), 89.83(5)
ρ [g/cm ³]	2.61	2.25	1.86
d_{Fe-Fe} [Å]	6.35(5) ^{a)}	6.24(5) ^{a)}	6.14(4)
E_{gap} [eV]	3.51 ^{b)}	3.27 ^{b)}	3.06 ^{b)}

^{a)} For the structure determination at 97 K.

^{b)} Energy of the band gap was determined by reflectance spectroscopy with a Kubelka-Munk plot provide in **Figure A31**.

4.2.3 Electronic and optical properties

In order to be able to make statements about a possible electron or energy transfer between the Fc ligands and the semiconducting lead halide phases, the quantum well structure must be elucidated. For this, the determination of the band gap and the relative energies of the VBM and CBM is essential. The semiconducting properties of hybrid perovskites and their structural relatives depend strongly on the connectivity of the lead halide octahedra. It is well known from literature, that the band gap follows the trend “corner sharing < edge sharing < face sharing”.^[87,96] To determine the relative energies of the VBM and the CBM of the phases, a combination of UV/Vis reflectance spectroscopy with subsequent Kubelka-Munk analysis (see **Figure A31**) and PESA is recorded (see **Figure A32**). **Figure 52a** shows the band gap alignment of the relative energy levels of the VBM and CBM of the crystal phases with the FcC_nBr ligands ($n=2,3,4,5,6$).

For $(\text{FcC}_2)\text{PbBr}_3$, which is composed of edge-sharing octahedra (best seen in **Figure 49c**), the largest band gap is found with 3.51 eV. For the phases $(\text{FcC}_3)_4\text{Pb}_3\text{Br}_{10}$ and $(\text{FcC}_4)_4\text{Pb}_3\text{Br}_{10}$, band gaps of 3.32 eV and 3.27 eV are found, respectively, which is in good agreement with the literature.^[259] Interestingly, these phases with a mixture of face and corner sharing octahedra (best seen in **Figure 50c**) have a smaller band gap than the edge sharing $(\text{FcC}_2)\text{PbBr}_3$. As expected, the obtained Ruddlesden-Popper phases $(\text{FcC}_5)_2\text{PbBr}_4$ and $(\text{FcC}_6)_2\text{PbBr}_4$, containing only corner sharing octahedra (**Figure 51c**) show the smallest bandgaps with 3.11 eV and 3.06 eV, respectively. These values are in good agreement with the literature as well.^[260] Regarding the energy level alignment shown in **Figure 52a**, the energies of the VBM of the materials remain almost constant, while the energy of the CBM varies with the band gap.

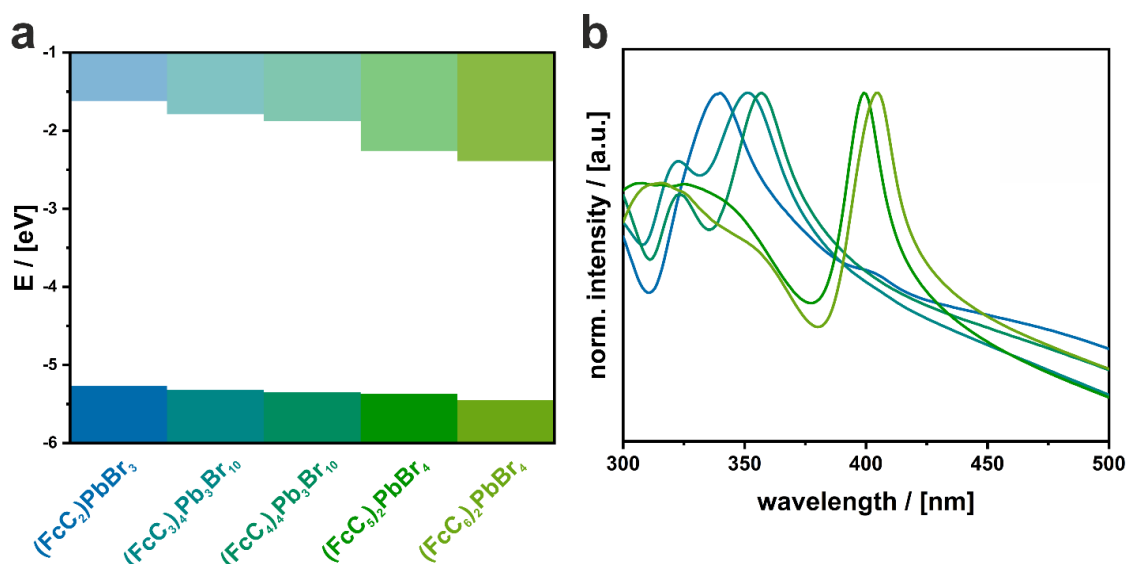


Figure 52 - a) Energy level alignment of the obtained particles with FcC_nBr ($n=2,3,4,5,6$). UV/Vis reflectance spectroscopy with Kubelka-Munk analysis and PESA measurements are provided in **Figure A31** and **Figure A32**. b) UV/Vis absorption spectra of the particles dispersed in toluene. The color coding corresponds to that from a).

Besides UV/Vis reflectance spectroscopy it is also possible to study the absorption behavior of the particles in dispersion, shown in **Figure 52b**. For this purpose, the particles are dispersed in toluene, which is suitable as dispersant on the one hand because of its non-polar properties and on the other hand because of the poor solubility of the ligands in it. This prevents the decomposition or dissolution of the particles. At the same time, it does not absorb in the relevant UV/Vis region. The absorption of Fc can barely be detected, since Fc has a very low extinction coefficient.^[192] Only a slight shoulder in the region between 450 nm and 500 nm is found, which represents the HOMO→LUMO transition (compare **Figure 45a**).

A near-band-edge absorption of the inorganic phase with strong resonance peaks is found for all compounds. The absorption maximum, but also the width of the absorption peaks provide information about the excitons and their binding energy. The peaks of the excitonic resonance are clearly separated from the continuous absorption, suggesting strongly bound excitons. Excitonic bandgaps for (FcC₂)PbBr₃ showing a maximum at 337 nm, for (FcC₃)₄Pb₃Br₁₀ and (FcC₄)₄Pb₃Br₁₀ with maxima at 351 nm and 357 nm and for (FcC₅)₂PbBr₄ and (FcC₆)₂PbBr₄ with maxima at 399 nm and 405 nm are found. Interestingly, (FcC₃)₄Pb₃Br₁₀ and (FcC₄)₄Pb₃Br₁₀ show a blue shifted maximum at 323 nm which is attributed to material defects in the structure.^[259]

It is noticeable that the peaks become narrower and sharper with a longer head group of the Fc ligand. Based on the peak shape, conclusions can be drawn about the exciton binding energy. Mainly two effects define the excitonic binding energy in low-dimensional organic-inorganic materials: the quantum confinement and the dielectric confinement. Since the spatial dimension of the inorganic framework increases with elongated head group, the quantum confinement of generated charge carrier decreases. From the ribbons of (FcC₂)PbBr₃, over the perovskite-like (FcC₄)₄Pb₃Br₁₀ to the layered Ruddlesden-Popper type (FcC₆)₂PbBr₄, the exciton binding energy shrinks and the peak shape becomes narrower. On the other hand, the Fc ligands also define the dielectric environment and influence the screening of the Coulombic attraction between the exciton's hole and electron. The length of the head group plays a crucial role for the proximity to the inorganic phase and thus also the influence of the dielectric constant of the organometallic molecules. The closer the Fc ligands are to the inorganic phase, the stronger the confinement of the excitons and the broader the peak.

It is found that the ligands not only have a **strong structure-directing** effect on the phases, but also have an extraordinarily **large** influence on the **excitonic absorption**.

Based on the excitonic absorption and the direct band character of the phases, intense luminescence in a broad range could be expected.^[132] The PL can be strongly red-shifted to the band gap and also very broad, so that white light is emitted.^[83,84] White-light emitting occurs, when the excitons are strongly bound and self-trapped due to phonon-exciton coupling (see **chapter 2.1.3**). However, no PL signal can be detected for the crystalline phases with FcC_nBr ($n=2,3,4,5$), only for $(\text{FcC}_6)_2\text{PbBr}_4$ (see **Figure A33**) a signal is observed. A weak emission at 416 nm (2.98 eV) of $(\text{FcC}_6)_2\text{PbBr}_4$ shows a slight Stokes shift compared to the band gap (3.06 eV) and is attributed to the radiative recombination of excitons near the band edges.

Now the following questions arise for the novel lead bromide phases:

- How does the PL quenching occur?
- What is the arrangement of electronic energy levels (quantum well type)?

The answer to the quenching mechanism lies in the nature of ligands. Ferrocene is well-known for quenching luminescent states efficiently by photoinduced electron transfer (PET).^[195] Through a hopping process or similar, excited charge carriers migrate to the Fc and luminescence is suppressed. Thereby, PET is strongly distance dependent,^[211] which is why PL can only be detected for the longest spacer of FcC_6Br .

The suppression of PL is a first hint, that the ligands and the semiconducting phases are connected electronically. A quantum well-like arrangement of energy levels of the organic and inorganic compounds is expected, where charge carriers can hop between the energy levels. For this purpose, the energy level alignment of the Fc ligands is determined using a combination of UV/Vis absorption spectroscopy and PESA (see **Figure A25-Figure A28** and **Figure A34**). Since the relative energies of the VBM and CBM are already detected (see **Figure 45**), the energy levels are directly compared to each other.

Figure 53 shows the quantum-well structures found for the VBM/CBM and the HOMO/LUMO of the materials (with FcC_n , $n=2,4,6$). Independent from the headgroup length, relative energies of HOMO and LUMO of the Fc ligands remain almost constant. The head group does not contribute to the conjugated π -system, which is responsible for the energy of the MOs. $(\text{FcC}_2)\text{PbBr}_3$ is a classical type II quantum well, where the relative energies show a staggered arrangement. This is also the case for the other two phases, but here the energy difference between VBM and HOMO is only marginal with 0.04 eV for $(\text{FcC}_4)_4\text{Pb}_3\text{Br}_{10}$ and 0.03 eV for $(\text{FcC}_6)_2\text{PbBr}_4$. The lowest energy state for holes and electrons is thereby on different species of the structure, which allows charge separation and therefore quenching of excited luminescent states in the semiconductor.

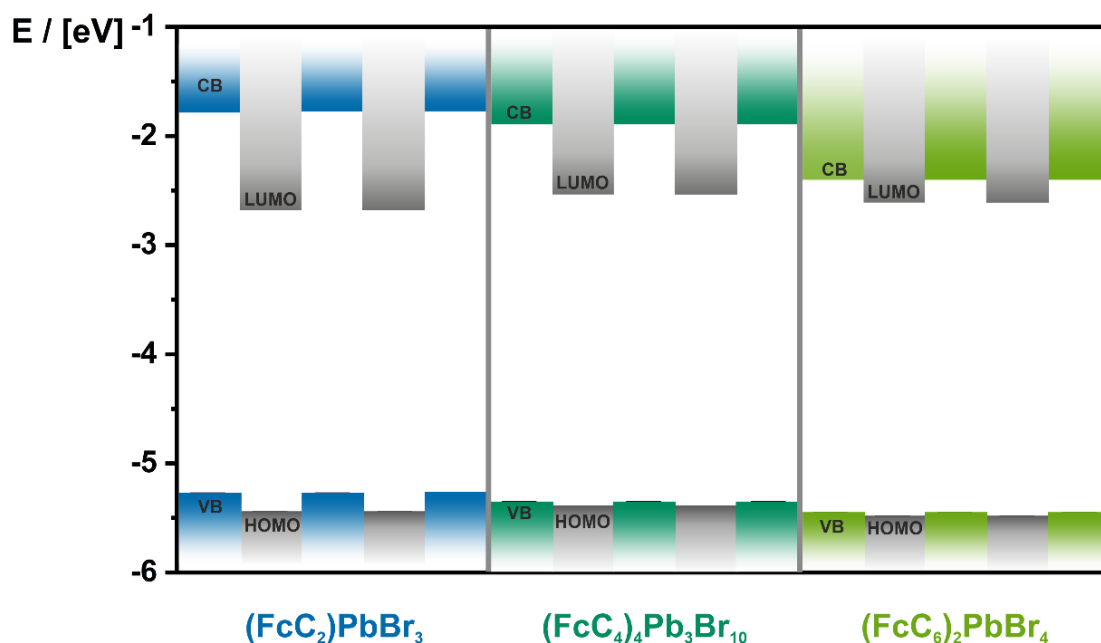


Figure 53 - Quantum well structures of the obtained materials for $(\text{FcC}_2)\text{PbBr}_3$, $(\text{FcC}_4)_4\text{Pb}_3\text{Br}_{10}$ and $(\text{FcC}_6)_2\text{PbBr}_4$ (left to right). VBM, CBM, HOMO and LUMO levels were calculated using a combination of UV/Vis reflectance spectroscopy and PESA.

In summary, the Fc ligands not only have a structure-directing effect on the novel phases, they are also **electronically part** of the semiconducting material. Due to the arrangement of relative energy levels, **charge transfer** between the inorganic and organic parts of the structure is possible.

Upon excitation of the semiconducting part, they react with an energy or electron transfer, which suppresses the excitonic luminescence. The conditions for an energy transfer are therefore given.

4.2.4 Redox-activity of ferrocene containing lead bromide phases

After the complete crystallographic and electrooptical characterization of the obtained materials, it is obvious that the ligands have a strong influence on the semiconducting lead bromide phases. The incorporation of Fc should now allow oxidation of the integrated ligands within the crystalline particles.

Therefore, the following points should be clarified:

- Is it possible to oxidize the integrated Fc ligands?
- How does oxidation influence the energy transfers in the material?
- Does oxidation affect the PL properties of the material?

In the following chapter, the oxidation of a selected phase ((FcC₂)PbBr₃) is performed and possible changes in the electronic processes are investigated.

Ferrocenium (Fc⁺), the oxidized species, does not quench excited luminescent states and shows a color-change due to the rearrangement of MOs (compare **Figure 45**).^[195,249] Rearrangement of MOs will also affect the quantum well structure and can have influence on the optoelectronic properties of the material. Therefore, the redox-activity of the Fc inside the structures has to be proven and persistent oxidation must be achieved to observe the optical properties.

To investigate the redox-activity of Fc in combination with a semiconductor, different methods can be adopted: electrochemical oxidation by applying a voltage or chemical oxidation with a suitable oxidant. Both approaches are investigated for (FcC₂)PbBr₃. Since (FcC₂)PbBr₃ turns out to be the most stable phase against external influences, only this material is used for the observation of the redox-activity and possible effects on the semiconductor. At the same time, the distance between the Fc ligand and the inorganic lead bromide phase is smallest, which is why the greatest effect on the energy transfer is expected for (FcC₂)PbBr₃.

To investigate the electrochemical properties and electron processes in a material, cyclic voltammograms (CV) are recorded for (FcC₂)PbBr₃. Therefore, a suitable electrolyte must first be identified. The electrolyte may not dissolve the material but has to be sufficiently conductive for CV measurements. Typically, aqueous or acetonitrile-based electrolytes are used to measure electrochemical properties from solid films e.g. MOFs.^[207,261] Preliminary tests showed that (FcC₂)PbBr₃ dissolves in all common electrolytes, as perovskite materials are known to be highly soluble in polar solvents. Hasan *et al.* were the first to present a suitable electrolyte for the electrochemical characterization of hybrid perovskites (CH₃NH₃PbI₃).^[231] An electrolyte based on hydrofluoroether (HFE), which is normally used in lithium-ion batteries, has proven to be very suitable for (FcC₂)PbBr₃ as well.

For the CV measurement, a conductive substrate is required to provide current flow at the electrodes. Therefore, the particles shown in **Figure 46a** are deposited on a conductive indium tin oxide (ITO) substrate. Then, CV measurements (see **Figure 54a**) are recorded using an Ag/AgCl reference electrode, a platinum counter electrode and the coated ITO substrate as working electrode (for a detailed measurement protocol see **chapter 6.3**). The measurement setup is also shown in **Figure 20a**.

Bare ITO is measured to exclude the possibility of electrochemical processes taking place on the substrate (**Figure 54a**, light blue). For $(\text{FcC}_2)\text{PbBr}_3$ redox peaks centered at 0.45 V are found, indicating that the Fc molecules inside the crystalline structure are electrochemically addressable. The signal of the oxidation at 0.65 V as well as the signal of the reduction at 0.24 V show no asymmetries, which indicates a simple electron transfer between the electrolyte and ferrocene.^[261]

To verify whether the material is reversibly oxidizable and reducible, 10 cycles of the CV measurement were carried out (see **Figure A35a**). The shape of the CV curve obtained remains the same, but the current applied increased over the period of the measurement (see **Figure A35b**). The increase of the current can be explained by different mechanisms. On the one hand, the application of a voltage can result in degradation of the presented material. On the other hand, the material consists of micrometer-sized particles, which may realign on the substrate due to the voltage and present a higher surface area.

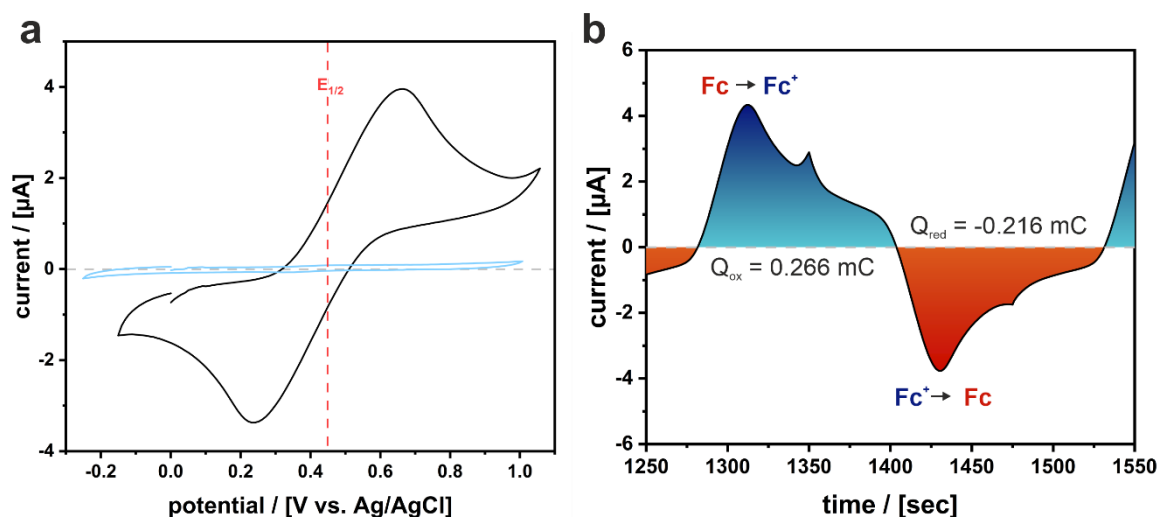


Figure 54 - a) Cyclic voltammogram (CV) of $(\text{FcC}_2)\text{PbBr}_3$ (black) on ITO (lightblue) at scan speed of 10 mV/sec in 0.1 M LiTFSI in HFE:DEC=(97:3). (b) Current vs. time for sixth cycle (10 cycles see **Figure A35**).

By integrating the current signal over time, the charge consumed can be determined, shown in **Figure 54b**. Indeed, a higher charge is consumed during oxidation, than during

reduction. PXRD measurements confirm decomposition of the material due to the repeated CV measurement (see **Figure A35c**). Additional reflexes, that can be assigned to PbBr_2 and the free ligand FcC_2Br are found after 10 cycles. It was experimentally not possible to electrochemically treat the materials under inert gas, therefore, it cannot be excluded that degradation occurs during the measurement due to atmospheric oxygen.

Since the ligands are now known to be electrochemically addressable, it is possible to oxidize $(\text{FcC}_2)\text{PbBr}_3$ persistently. By applying a voltage at 0.65 V for 1800 sec, the oxidation of the FcC_2Br ligands incorporated into the hybrid material occurs (see **Figure A36a**). Only small changes in the PXRD pattern and in SEM images are observed, indicating that the particles are stable during the oxidation process (see **Figure A36b-d**). With the oxidized material, it is possible to investigate the optical properties with Fc^+ integrated. Therefore, UV/Vis reflectance spectroscopy and PL measurements are recorded on the substrate, shown in **Figure 55**.

As already evident, the color of the material changes after the oxidation (see photographs, **Figure 55a**). This observation is confirmed in the reflectance spectrum in **Figure 55a**. In the range between 400 nm and 500 nm the reflection increases, whereas it decreases between 600 nm and 650 nm, which is attributed to the emergence of Fc^+ (also see **Figure 45c**).

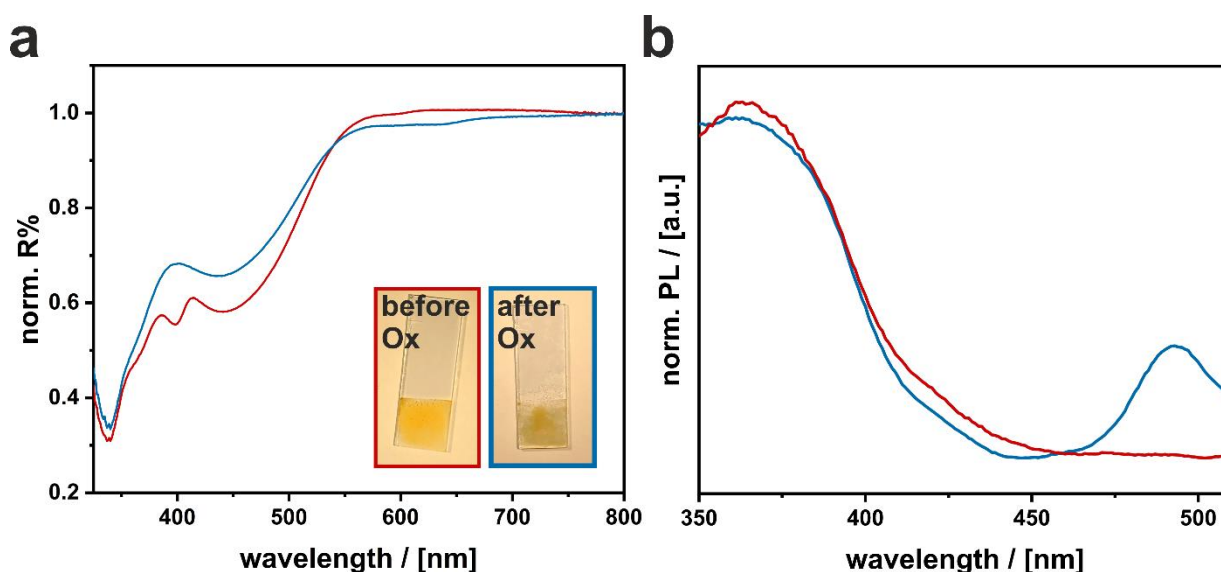


Figure 55 - a) Normalized UV/Vis reflectance spectra of the particles before (red) and after (blue) oxidation. Inset: Photographs of the ITO substrates coated with $(\text{FcC}_2)\text{PbBr}_3$. b) PL spectra of $(\text{FcC}_2)\text{PbBr}_3$ on ITO before (red) and after (blue) oxidation with emission maximum at 494 nm. Excitation at 310 nm with an Xe-lamp.

Beside the absorption, luminescent properties of the oxidized material change as well. In contrast to the initial $(\text{FcC}_2)\text{PbBr}_3$, the electrochemically oxidized material shows a weak emission at 494 nm (**Figure 55b**, blue) upon excitation at 310 nm (4.00 eV). An emission

signal between 350 nm and 400 nm is attributed to the ITO substrate, which can as well be found for the bare ITO (see **Figure A37b**). The emission at 494 nm can be attributed to the oxidized Fc⁺ ligand, which, in contrast to Fc, shows a weak emission at approximately 500 nm. However, the excitation spectrum of Fc⁺ suggests that the emission cannot be stimulated at 310 nm (emission and excitation spectra see **Figure A37a**). Radiative recombination is thus not possible by direct photonic excitation at this wavelength, but proceeds in a detoured way.

With the excitation wavelength used, nevertheless, it is possible to excite the semiconducting [PbBr₃]⁻-ribbons.

Excited electron-hole pairs can presumably **migrate** from the semiconductor's bands to the MOs of the Fc⁺ ligands, where they **recombine radiatively**.

A detailed explanation of the mechanism follows after investigation of the chemical oxidation of the particles.

The electrochemical approach (CV) is suitable to prove the redox-activity of the system, however only a small amount of the sample is affected by the oxidation. To control the oxidation ratio is rather difficult because of the poor connection of the particles to the electrode. Therefore, chemical oxidation of dispersed (FcC₂)PbBr₃ particles in a solvent (CHCl₃) with a suitable oxidant (iron(II) perchlorate = Fe(ClO₄)₃) is attempted. For this purpose, different equivalents (eq; 0.1, 0.2, 0.5, 1.0, 2.0) of oxidant are added to the dispersed particles. A detailed experimental description is provided in **chapter 6.3**.

In order to verify that the particles phase and shape remain stable during the oxidation, SEM images are taken, shown in **Figure 56**. The shape of the particles is preserved up to 1.0 eq of oxidant. At the surface, small holes are visible with increasing oxidant concentration, indicating a partial degradation of the particles. At high concentrations, however, they lose their shape and form long needles. The ions of the oxidant can presumably intercalate into the structure, destroying the morphology of the particles. The oxidant enters the structure through a tunnel provided by the Fc molecules (see **Figure 49b**). As counter anions (ClO₄)⁻ are attached to the surface by the oxidation, they split the particles into long needles. However, phase and composition remain unaltered, proofed by PXRD and EDX shown in **Figure A38**.

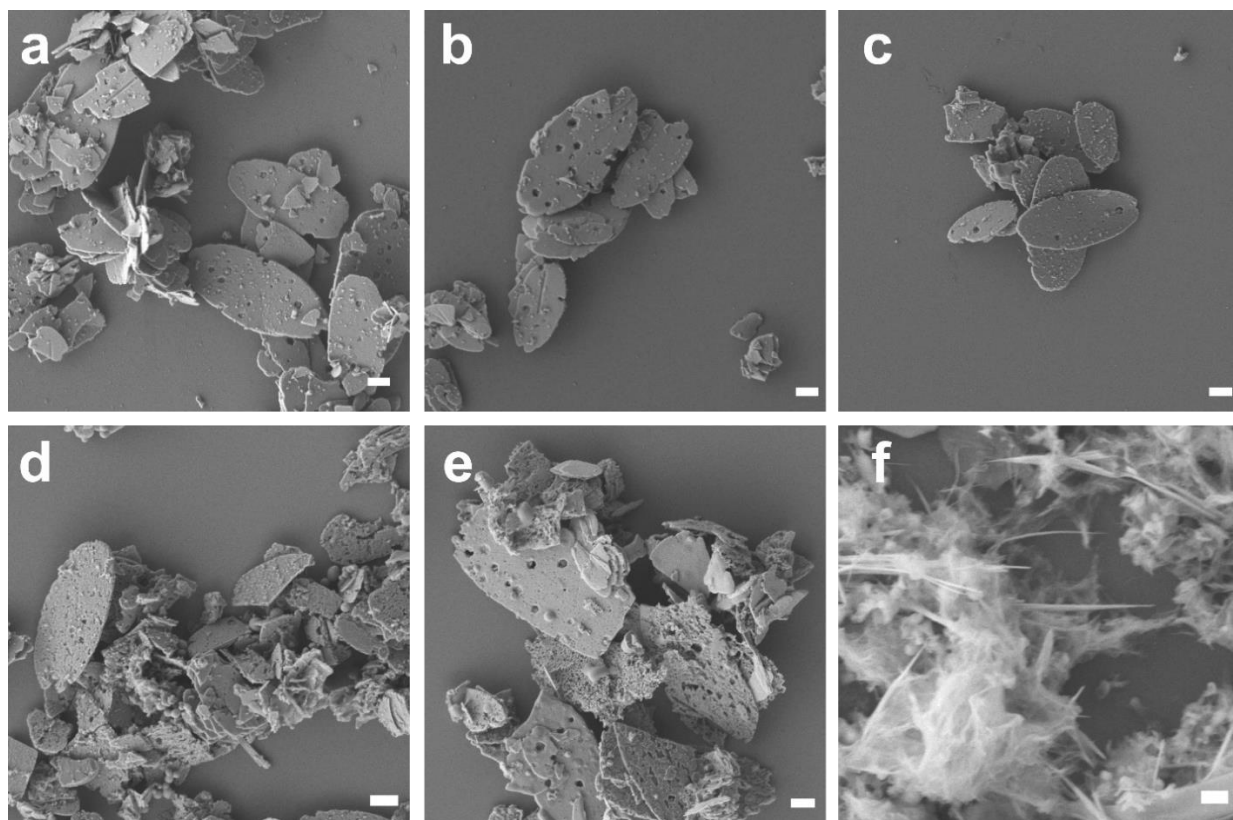


Figure 56 - SEM images of the particles a) before oxidation and after oxidation with b) 0.1 eq c) 0.2 eq, d) 0.5 eq, e) 1.0 eq and f) 2.0 eq of the oxidant. a)-e) Scalebar = 1 μm , f) Scalebar = 2 μm .

After the stability of the particles has been verified, they can be examined more closely for their degree of oxidation. In order to determine a degree of oxidation, the content of Fc^+ is investigated using X-ray photoelectron spectroscopy (XPS). With XPS the content of Fe^{2+} (Fc) and Fe^{3+} (Fc^+) can be determined and thus a degree of oxidation of the Fc ligands is revealed. A signal at 710 eV can be assigned to Fe^{3+} and a signal at 704 eV can be assigned to Fe^{2+} , shown in **Figure A39**. The integration of the signals gives the amount of the species included. The evaluation of the spectra is given in **Table 7**.

With chemical oxidation it is possible to adjust the degree of oxidation from **10.8 % with 0.1 eq** oxidant up to up to **63.3 % with 2.0 eq** of the oxidant.

In the following, the electronic and optical properties that depend on the degree of oxidation are investigated.

Table 7 - Content of Fe^{3+} of the particles after oxidation.

$[\text{Fe}(\text{ClO}_4)_3]$	0.0 eq	0.1 eq	0.2 eq	0.5 eq	1.0 eq	2.0 eq
Fe^{3+}-content	0 %	10.8 %	18.2 %	46.4 %	57.8 %	63.3 %

A color change of the dispersed particles is visible due to the oxidation, which is best seen when the particles are dried on a glass substrate, shown in **Figure 57a**. This is attributed to the oxidized Fc ligands, which have another absorption band in the red region, giving the material a greenish appearance. Furthermore, it is observed that in dispersion the particles tend to sink to the ground with an increasing amount of oxidant. The dispersibility of the particles is lowered, due to a change in polarity and an additional charge at the surface (ClO_4^- counter anion) caused by oxidation. In a non-polar solvent this results in the destabilization of the dispersed particles. This is also evident in film formation during the drying process, since a continuous film can no longer be produced because the particles repel each other during the drying process (compare **Figure 57a**, 0 % and 63.3 %). After the visual observations, the optical absorption and the emission properties of the dispersed particles are investigated, shown in **Figure 57b+c**.

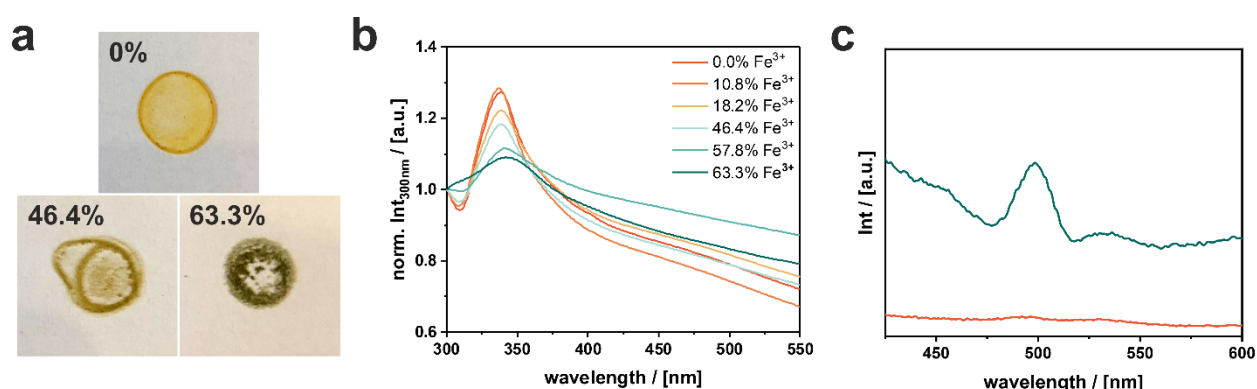


Figure 57 - a) Photographs of glass substrates with a film of dried particles. b) UV/Vis absorption spectra of the dispersed particles in toluene with varying Fe^{3+} content. The color coding of the varying Fe^{3+} contents is used for further diagrams and is no longer specified there. c) PL emission spectra of dispersed particles with 0.0 % (orange) and 63.3 % (green) Fe^{3+} with excitation at 310 nm.

UV/Vis absorption spectra reveal that the oxidation has impact on the excitonic absorption maximum of the excitons in the inorganic semiconducting ribbons at 337 nm. The excitonic peak for the oxidized species is broadened, which can be explained by the change of the dielectric environment.^[259] The anions that accumulate as a result of oxidation create a polar double layer at the surface, which leads to a change in the polarization of the ligands. Therefore, the inorganic phase and the excitons become even more confined as the relative permittivity of the ligand is altered. The increased absorption above 450 nm is attributed to the emergence of Fc^+ , which absorbs at 630 nm (see **Figure 45c**). At the same time, similar to the observation that was made for electrochemical oxidation (see **Figure 55b**), emission at 494 nm upon excitation at 310 nm can be found, which is attributed to the Fc^+ ligands.

To investigate the influence of the oxidation to the band gap of the material, UV/Vis reflection spectroscopy with subsequent Kubelka-Munk analysis is performed. **Figure 58a** shows the evaluated spectra exemplary for particles with Fe^{3+} content of 0 %, 10.8 % and 63.3 %. Other spectra are found in **Figure A40**.

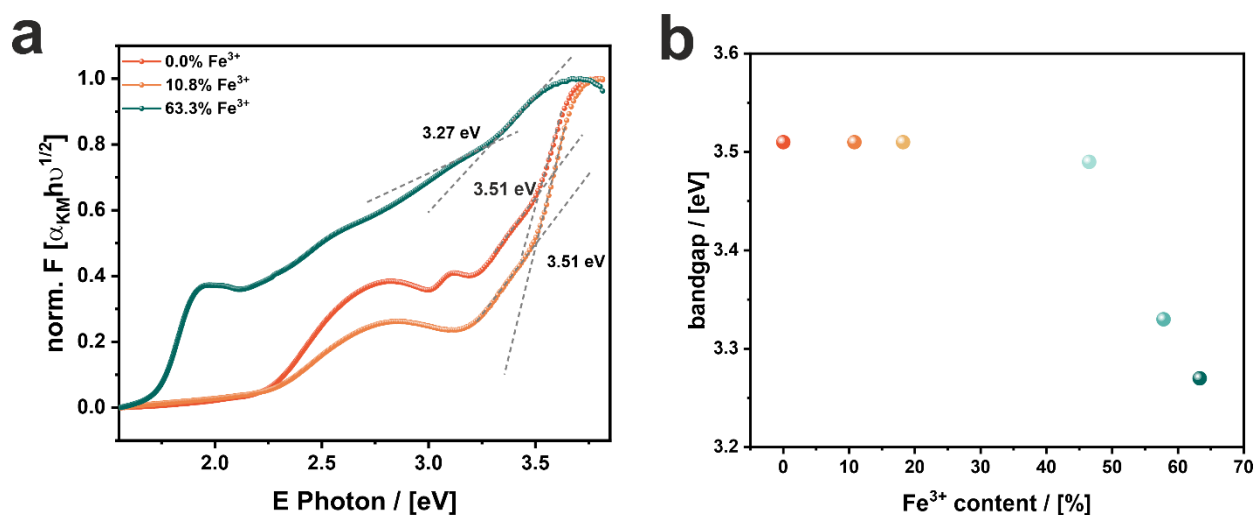


Figure 58- a) Normed Kubelka-Munk plots of the (oxidized) particles with evaluation of the band gap. Two linear regression lines are fitted to the slope and the baseline. b) Band gap vs. Fe^{3+} content in the particles determined with XPS.

Indeed, a change in the optical reflectance spectrum is observed when the oxidation degree is varied. A high oxidation degree (63.3 % Fe^{3+}) results in a signal at about 2.0 eV (620 nm), which is attributed to the emergence of Fc^+ in the particles. The observed color change can as well be attributed to that signal. The broad signal at 2.75 eV (450 nm) decreases due to the oxidation, which is attributed to the decreasing Fc content in the material. However, the band gap at 3.51 eV of the semiconducting $[\text{PbBr}_3]$ -ribbons is altered as well. It is evaluated by fitting two linear regression lines to the slope and the baseline of the spectrum and determining the intersection of the lines. Interestingly, the evaluation results in a narrowing of the band gap from 3.51 eV to 3.27 eV for the highest oxidation degree (see **Figure 58b**).

The evaluation of all Kubelka-Munk plots suggests that above a content of about 50 %, the **electronic situation** of the semiconductor seems to change **tremendously**.

To find an explanation for this, the electronic states must be considered. A change in the electronic situation of a semiconductor and the narrowing of its band gap is usually observed for heavily doped semiconductors, where discrete states of doping atoms inside

the band gap evolve an independent band, which can overlap with the VBM or CBM.^[262-264] However, in this case, an abrupt change above a critical concentration of Fc⁺ ligands is observed. Therefore, the observed effect must be attributed to the Fc ligands.

From literature it is known, that oxidized Fc⁺ and unoxidized Fc species can interact intramolecularly with each other.^[207,261] That means, that they can oxidize/reduce each other, creating a kind of electron flow in the material without external influence. The ligands appear to exhibit a cooperative effect through oxidation. At low degrees of oxidation, the phase shows an emission of the incorporated Fc⁺ ligands, which can be considered as the creation of a defect state. Would it be possible that, similar to heavily doped semiconductors, a defect band is created at high oxidation degrees?

For the observation of electron hopping processes, computational calculations of the structure were performed in cooperation with Henning Kuper from the AK Becker from the Leibniz University of Hannover. For a detailed description of the method used refer to the publication.^[234]

For simplicity, only the surface area of (FcC₂)PbBr₃ is calculated, which corresponds to a Helmholtz layer model. Thus, four Fc ligands are represented at the surface, shown in **Figure 59a**. Oxidation then is simulated by addition of one or two ClO₄⁻ anions (**Figure 59b+c**), same counter anion as for the experimental chemical oxidation. Note that the representation shows two or four anions, which are symmetrically equivalent. Therefore, the simulations cover a degree of oxidation of 25 % which represents a low degree of oxidation and 50 % which represents a turning point from which cooperative effects are expected.

It is expected that the electron spin of the Fe sites changes, since Fe³⁺ has a spin of ½. Thus, spin density calculations make the visualization of the location of the spins possible (blue isosurfaces, **Figure 59b+c**). It is apparent that already in the case of one ClO₄⁻ anion, the spin is not localized on a single Fe site, but delocalized on adjacent Fe sites. When a second ClO₄⁻ anion is added to the model, the delocalization is almost uniformly distributed over the Fe centers. It is assumed, that the delocalized charge and spin density in the oxidized state could correspond to a significant electron transfer for an electron from the Fe²⁺ site to the Fe³⁺ site. Electron hopping can be explained using the Marcus model, as well explained in the publication.^[234]

The calculations show, that oxidation indeed induces a **cooperative effect** between the ligands. Delocalized spin density of the iron centers indicates an **electron hopping** process.

Thus, a type of electronic band is created between the Fc ligands that contributes to the electronic structure of the hybrid material. If the relative energies of the oxidized materials

are now considered, electronic processes result which explain the observed change in the band gap and the luminescence well. Excitation from the emerged band results in the narrowing of the band gap from 3.51 eV to 3.27 eV (transition see **Figure 59c**).

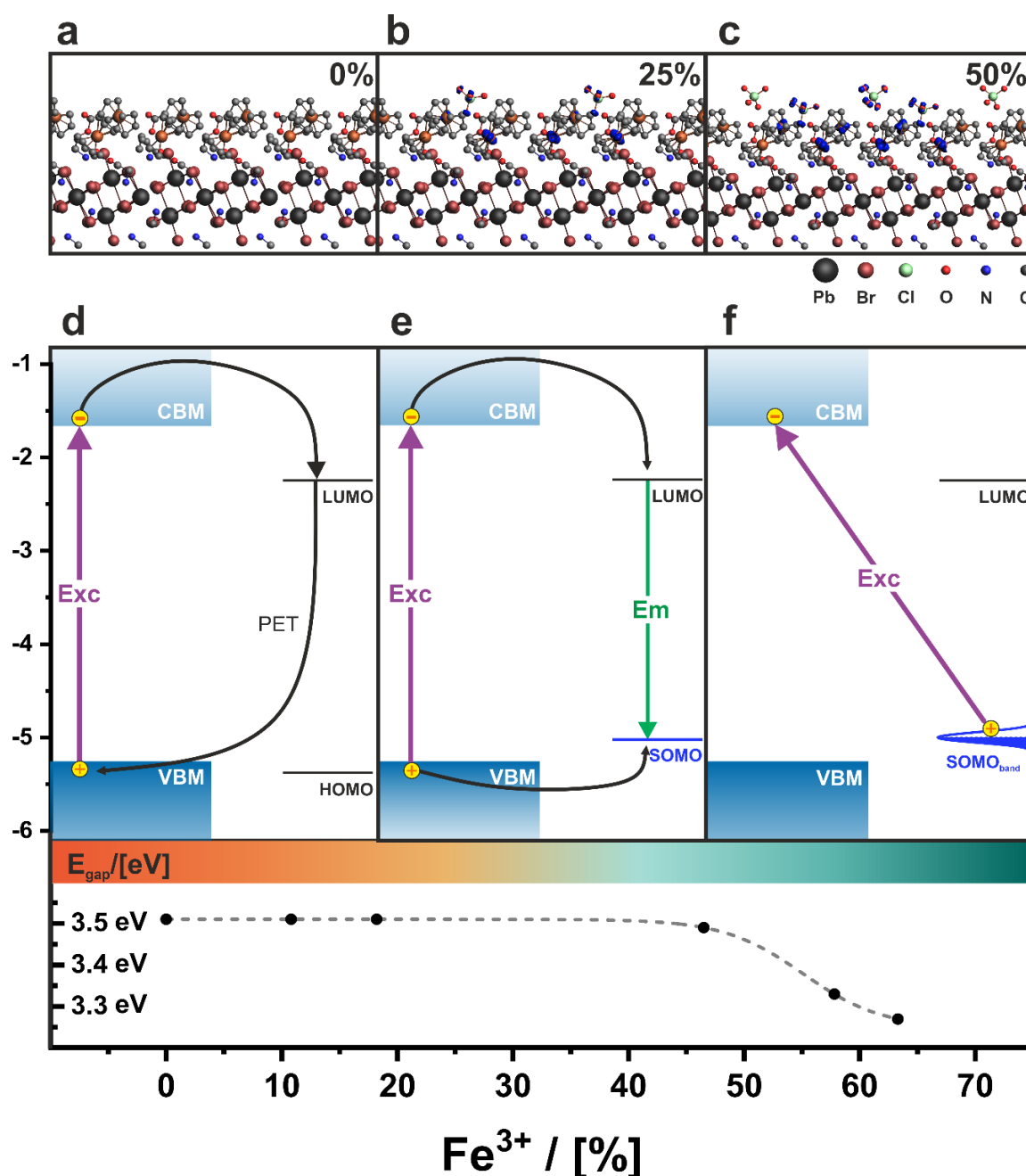


Figure 59 - Representation of the *ab initio* calculations using the BAND code for a) the intrinsic $(\text{FcC}_2)\text{PbBr}_3$, b) with 25% of the ligands oxidized with $(\text{ClO}_4)^-$, c) with 50% of the ligands oxidized with $(\text{ClO}_4)^-$. The location of the unpaired paramagnetic spin was calculated and made visible with spin density calculations (blue isosurface). Hydrogen atoms were removed for clarity; Experimentally determined band structure of $(\text{FcC}_2)\text{PbBr}_3$ d) in the intrinsic state showing why PET occurs upon excitation (Exc) at 310 nm, e) after the oxidation with $(\text{ClO}_4)^-$ at low oxidation degrees, where radiative recombination/emission (Em) occurs due to the new energy alignment of the single occupied molecular orbital (SOMO) and f) at high oxidation degrees with the emergence of the new SOMO_{band}.

The arrangement of the relative energy levels and possible transitions are shown in **Figure 59d-e**. In the ground state (d) PET occurs due to a staggered arrangement of the VBM/CBM and the HOMO/LUMO levels. Both, the HOMO and the LUMO lie below the VBM and the CBM, respectively, which allows excited electrons to migrate to the LUMO, but holes may not migrate to the HOMO. Thus, recombination does not occur by radiation, but presumably by the excitation of phonons.

Oxidation changes the electronic situation depending on the degree of oxidation. Due to the oxidation, a SOMO evolves, which lies above the VBM. The altered arrangement now allows the migration of excited holes and electrons from the semiconductor to the Fc^+ ligands. The excited charge carriers are therefore no longer separated and are collected in one species. At low degrees of oxidation (e) this results in the emission of the Fc^+ ligands at 494 nm. At high degrees of oxidation (f), electron hopping between oxidized Fc^+ and non-oxidized Fc ligands occurs. Due to a cooperative effect, an electronic band emerges from which excitation into the CBM is observed.

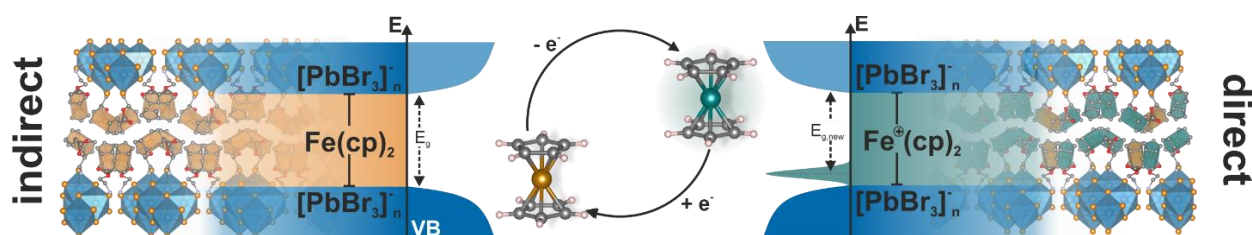


Figure 60 - Schematic overview of the observed effects in $(\text{FcC}_2)\text{PbBr}_3$. In the ground state, no radiative recombination is observed, similar to an indirect semiconductor. When oxidized, however, radiative recombination is possible.

Figure 60 best summarizes the effects of oxidation observed in the novel hybrid phase $(\text{FcC}_2)\text{PbBr}_3$. Before oxidation, electron transfer from the semiconducting phase to the organometallic Fc ligand occurs, therefore no radiative recombination is observed. This behavior is similar to classical indirect semiconductors like silicon. However, oxidation allows radiative recombination, since the quantum well structure alters due to a rearrangement of the MOs of the Fc ligands. Furthermore, a new defect-like band emerges, due to cooperative effects between the oxidized and unoxidized Fc ligands.

4.2.5 Ruddlesden-Popper phases with ferrocene-based ligands

Besides single-layered materials (LHPs, $n=1$), multilayered perovskites, i.e. RPPs ($n=2,3,4,5$), can also be produced thanks to the incorporation of MABr. This allows the band gap to be varied and the electronic band structure to be adjusted. By changing the quantum well structure, other electronic processes can be observed if required.

Crystal structure analysis revealed, that FcC_6Br in combination with PbBr_2 form a typical LHP. A general formula of the composition of multilayered RPPs is formulated with $(\text{FcC}_6)_2(\text{MA})_{n-1}\text{Pb}_n\text{Br}_{3n+1}$ for $n=1,2,3,4,5$. Since it proved difficult to obtain RPPs with azobenzene-based ligands, this will now be tested with FcC_6Br , in combination with MABr and PbBr_2 . This part of the chapter is a preliminary set of results that will provide the basis for future studies.

For the synthesis of RPPs, DMF precursors with defined concentrations of the cations are prepared and precipitated in an antisolvent (toluene). For experimental details see **chapter 6.2.2**. **Table 8** lists the ratio of the salts used for the precursors. The precipitations obtained from these precursors are called $\text{RPP}_{[\text{MABr}]}$ from now on, referring to the ratio of MABr in the precursor.

Table 8 - Ratios of the precursors used for the formation of RPPs.

Sample name:	$\text{RPP}_{0.5}$	$\text{RPP}_{1.0}$	$\text{RPP}_{2.0}$
ratio (MABr : FcC_6Br : PbBr_2)	(0.5:2:2)	(1:2:2)	(2:2:3)

Different layer thicknesses show an altered quantum confinement, resulting in different absorption maxima (see **Figure 5**). Compared to the absorption of a single $[\text{PbBr}_4]^{2-}$ layer, the absorption of thicker layers with $n>1$ is red-shifted.^[77] Therefore, kinetic UV/Vis absorption measurements are a versatile method to observe the formation of RPPs during the synthesis. Using an immersion probe, UV/Vis absorption spectra can be recorded directly in the reaction vessel. **Figure 61a** shows the records of the precipitation of $\text{RPP}_{0.5}$ with a baseline measurement in yellow and the final measurement after 35 minutes in red. The temporal sequence of the measurement is from black to white. In the beginning of the measurement an absorption peak at 325 nm (3.81 eV) is visible, which decreases very fast. This signal is attributed to the free FcC_6Br ligand in solution (see **Figure A28a**). The rapid decrease of the signal indicates that ligands are incorporated into the nascent hybrid RPPs shortly after addition of the precursor into the antisolvent. In the end of the measurement, two absorption peaks at 402 nm (3.08 eV) and 434 nm (2.86 eV) are found. An absorption at 402 nm is attributed to the $n=1$ layer thickness of the LHPs (compare **Figure 52b**). An absorption peak at 434 nm is attributed to a layer thickness with $n=2$. **Figure 61b** depicts the normed absorption at 402 nm (blue) and 434 nm (green)

over the period of the measurement. At first, the absorption at 402 nm decreases but increases rapidly again after 120 seconds. Since the ligand FcC_6Br also absorbs at 402 nm, the absorption first decreases as the free ligand in solution is depleted by incorporation into LHPs. Then the absorption of the $n=1$ layer takes over and a rapid increase is observed which is finished after 500 seconds. From this point on, the absorption is almost constant. At the same time, the absorption at 434 nm increases as well but much slower than the absorption at 402 nm. After about 900 seconds, there is a bend in the curve and the increase is even slower than before, but steady.

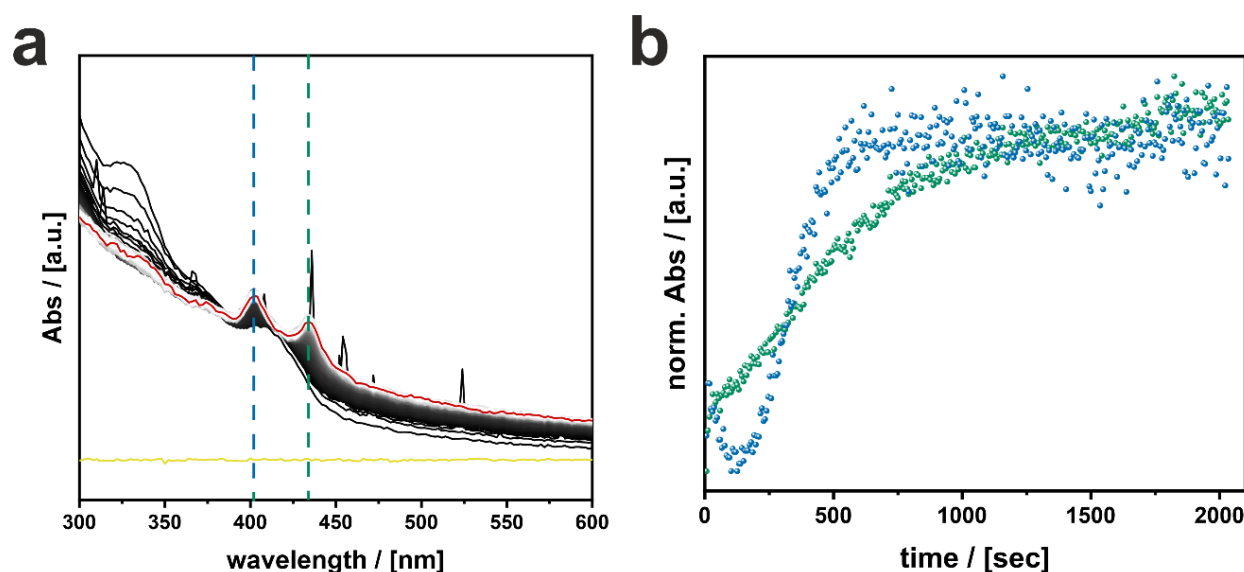


Figure 61 - a) UV/Vis absorption spectra recorded during the reaction of $\text{RPP}_{0.5}$ in DCM. Baseline before addition of the precursor = yellow, final measurement = red. Temporal sequence of the spectra is from black to white. b) Normed absorption at 402 nm (blue) and 434 nm (green) over the timescale of 2100 sec.

The results of the UV/Vis kinetic measurements for $\text{RPP}_{0.5}$ suggest, that RPPs are indeed possible for FcC_6Br . However, the formation of $n=1$ layers seems to be preferred, compared to the $n=2$ layers. The single layer $n=1$ is the thermodynamically most stable phase, therefore, it is preferably formed.^[246] Since the ligand is slightly soluble in toluene, a dynamic growth mechanism is possible and MABr is integrated after the formation of $n=1$ layers and thicker layers (i.e. $n=2$) are formed.^[232]

The investigation of the UV/Vis absorption spectra of the dried and redispersed particles (see **Figure A41**) shows, that with increasing MABr concentration also thicker layers of $n=3$ with an absorption maximum at 456 nm (2.72 eV) and $n=4$ with an absorption maximum at 492 nm (2.52 eV) are achieved. For $\text{RPP}_{2.0}$ even a continuous band edge at 530 nm (2.30 eV) is found, which can be assigned to the layer thickness $n \geq 5$. In addition to the RPPs, a reference sample was prepared consisting of only surface functionalized MAPbBr_3 particles (see **Figure A42**). This serves as a reference 3D phase for all phases

with $n \geq 5$. With a band gap of 2.29 eV, this agrees well with the results found for the RPPs. All results are summarized in **Table 10**. However, none of the used precursors results in a phase pure RPP with a defined periodicity of layer thickness, which is also observed in literature for antisolvent processes.^[67]

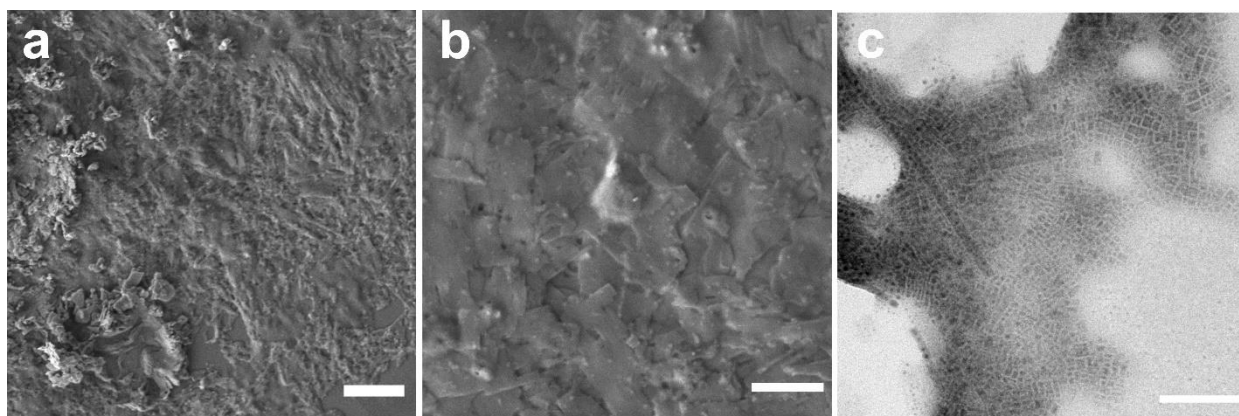
This finding is also evident from PXRD measurements shown in **Figure A43**. A first reflex at small angles marks the basal distance of the layered structures. Based on the $n=1$ layer, the layer distances for $n > 1$ can be approximately calculated by adding the height of one unit cell of the MAPbBr_3 structure ($\sim 5.9 \text{ \AA}$). The calculated values are listed in **Table 9**.

Table 9 - Calculated layer thicknesses for $(\text{FcC}_6)_2(\text{MA})_{n-1}\text{Pb}_n\text{Br}_{3n+1}$.

Layer thickness n	1	2	3	4	5
distance d	30.6 Å	36.5 Å	42.4 Å	48.3 Å	54.2 Å
angle 2θ	2.89°	2.42°	2.08°	1.83°	1.63°

With a basal distance of 32.9 Å (2.68°) for $\text{RPP}_{0.5}$ a superposition of $n=1$ and $n=2$ is found. $\text{RPP}_{1.0}$ and $\text{RPP}_{2.0}$ behave similarly with basal distances of 37.1 Å (2.38°) and 42.8 Å (2.06°), respectively. It is assumed, that the layers with different thicknesses stack on top of each other in a disorderly manner. Therefore, a basal distance is found, which is the average of the existing distances.

Besides their crystalline structure, the shape and size of the particles are investigated with electron microscopy, shown in **Figure 62**. Very large, layered structures are observed for $\text{RPP}_{0.5}$ and $\text{RPP}_{1.0}$ with no defined shape. A side effect of the drying of the particles is that the layered particles align parallel to the substrate and thus overlap each other. Therefore, no defined interfaces are detected in the SEM. The particles with the highest concentration of MABr, $\text{RPP}_{2.0}$, are even too small to be observed in the SEM, which is why transmission electron microscopy (TEM) is used. The particles show a cubic and plate-like shape in a size regime of 5 nm to 25 nm. Surprisingly, the smallest particles form with the thickest layered structure. Presumably, the growth direction of the particles is influenced both by the MABr and the FcC_6Br concentration. At high FcC_6Br and low MABr concentration, growth direction is preferably parallel to the layers. A large number of large cations cover the surface of the emerging particles, therefore, the small crystals preferably grow lateral. At low FcC_6Br and high MABr concentration, growth direction is preferably vertical to the layers, since a smaller amount of large cations cover the surface. Thus, it is assumed that FcC_6Br acts like a classical crystallization inhibitor in c -direction, similar to alkyl ligands.^[216]



MABr-concentration

Figure 62 - SEM images of a) RPP_{0.5} with scalebar = 1 μm and b) RPP_{1.0} with scalebar = 2 μm and TEM images of c) RPP_{2.0} with scalebar = 100 nm.

Due to the changed crystalline structure and the larger layer thicknesses, a change in the luminescent properties is to be expected as well. Investigations of the LHP (FcC₆)₂PbBr₄ with the layer thickness $n=1$ have already shown a weak emission for the inorganic phase at 416 nm (2.98 eV). Therefore, the RPPs are examined for their emission properties, represented in **Figure 63a**. The emission maxima found are listed with the absorption maxima already determined in **Table 10**.

In comparison to the UV/Vis absorption maxima, PL emission is slightly red-shifted, which is attributed to a classical Stokes shift. Analogous to UV/Vis absorption spectra, multiple emission maxima are found for RPP_{0.5} (blue). An emission maximum at 423 nm (2.93 eV) is attributed to the $n=1$ layer, an emission maximum at 450 nm (2.76 eV) is attributed to a $n=2$ layer and a shoulder at 477 nm (2.60 eV) is attributed to a $n=3$ layer. RPP_{1.0} (dark green) shows only one broad emission maximum at 478 nm (2.59 eV) which is attributed to a $n=3$ layer and RPP_{2.0} (light green) shows as well only one emission maximum at 505 nm (2.45 eV) which is attributed to the $n=4$ layer. Due to the mixed crystalline phases, one could expect multiple emission peaks. However, here again the effect of exciton migration to the phase of the smallest band gap (i.e. thickest layer thickness) is observed.^[248] Thus radiative recombination occurs preferentially when the excited charge carriers have reached the phase with the lowest band gap, meaning, that they are collected there and recombine. By considering the arrangement of the relative energy levels, this effect can be well explained.

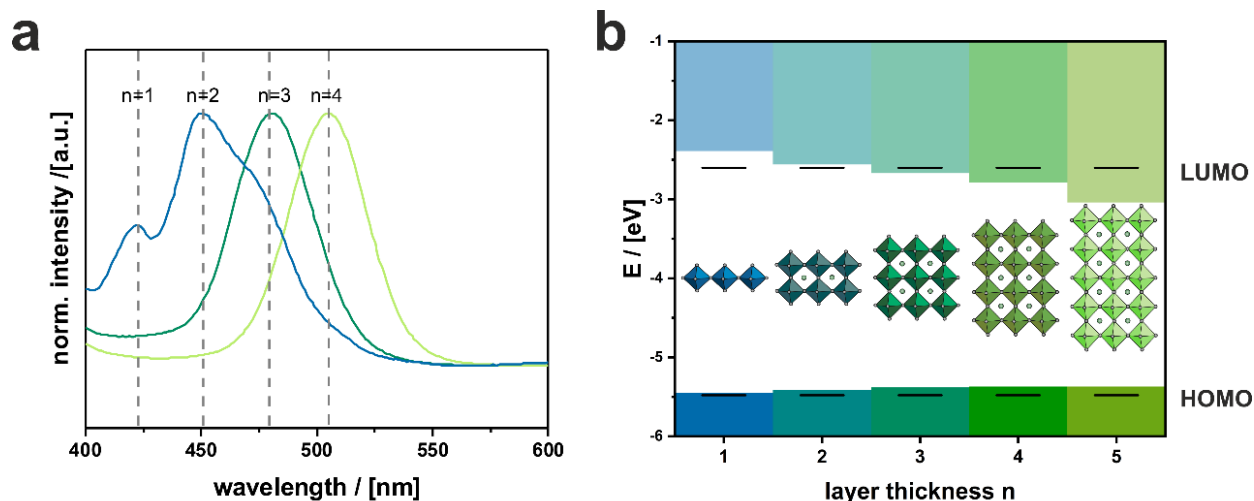


Figure 63 - a) Normed PL spectra of RPP_{0.5} (blue), RPP_{1.0} (dark green) and RPP_{2.0} (light green) with excitation at 310 nm. b) Band gap alignment of the RPPs based on UV/Vis absorption measurements and PESA measurements shown in **Figure A44a-c**. HOMO and LUMO levels of FcC₆Br are calculated from PESA measurements shown in **Figure A44d** and UV/Vis absorption measurement shown in **Figure A28a**.

Table 10 - Band gap found from UV/Vis and PL for varying layer thicknesses.

band gap E_g	$n=1$	$n=2$	$n=3$	$n=4$	$n \leq 5$
UV/Vis	402 nm (3.08 eV)	436 nm (2.84 eV)	456 nm (2.72 eV)	492 nm (2.52 eV)	529 nm (2.34 eV)
PL	416 nm (2.98 eV)	450 nm (2.76 eV)	478 nm (2.59 eV)	505 nm (2.45 eV)	525 nm (2.36 eV)

For the investigation of the quantum-well structure, the alignment of the bands is determined using PESA, shown in **Figure A44**, in combination with the band gaps determined from UV/Vis absorption spectroscopy listed in **Table 10**. It should be noted that this is an approximation, since the exact band gap can only be defined by means of Kubelka-Munk evaluation. However, this approach is sufficient to observe a trend and explain the observed emission.

Figure 63 clearly shows the change of the CBM and thus the reduction of the band gap with increasing layer thicknesses. The VBM, determined from PESA, is nearly constant. The step-like arrangement of the energy levels of the bands shows well why the migration of excited charge carriers to the structures with the smallest band gap occurs. Excited electrons can flow in the CBs into the energetically lower state of the thickest layers. For the holes, there seems to be only a small barrier between the VBs, which is why they also migrate. Radiative recombination then occurs in the thickest layer present in the material.

Regarding the position of the MOs of FcC₆Br, an interesting trend emerges. For layer thicknesses with $n=1,2$ a step-like arrangement results and thus a quantum-well type II. From $n\geq 3$, however, VBM and CBM lie within the HOMO-LUMO gap, hence a quantum-well type I is obtained (compare **Figure 6**). Accordingly, other electronic properties related to the Fc ligand are expected for phase-pure RPPs with film thicknesses of $n\geq 3$.

In summary, FcC₆Br allows the preparation of RPPs with all layer thicknesses known from the literature.^[77]

These materials seem to be quite interesting since **different quantum well structures** are obtained depending on the layer thickness. The energy and electron transfer could behave differently for the different layers.

Since it has not yet been possible to obtain phase-pure RPPs, energy and electron transfer processes cannot be studied. However, the preliminary results are very promising and should be followed up in the future.

4.3 Heterocycles as functional surfactant

Preliminary work already demonstrated increased conductivity between surface functionalized $(\text{CH}_3\text{NH}_3)\text{PbI}_3$ particles, when using a thiophene based surfactant (see **chapter 2.3**).^[118,221] However, the derivative used in this approach could not be integrated into the perovskite phase due to the short methylammonium head group, which plays a major role for the integration into LHPs. The relatively rigid head group allows little room for the arrangement of functional groups between the perovskite layers.

For the investigation of RPPs on the base of thiophene derivatives, the length of the head group is increased by a further methylene group. The longer ethylene ammonium head group $(\text{CH}_2\text{CH}_2\text{NH}_3^+)$ ensures enough space for the integration and the arrangement between the perovskite sheets. Beside thiophene (S), the ligand is systematically studied by variation the heteroatom from the smaller oxygen (O) to the larger selenium (Se) and the resulting phases are examined for the following properties:

- How does the heteroatom influence the structure and electronic situation of LHPs?
- Is the synthesis of RPPs with heterocycles possible and how is the quantum well type affected by the varying layer thicknesses?
- Is a continuous halide exchange possible and does it affect the electronical and optical properties of the LHPs?

The idea is that the frontier orbitals of the heteroatoms alter the conjugated π -system, so different molecular orbital (MO) energies are expected. Given the similar steric very similar crystalline phases are expected, with only slight differences. Thus, electronic processes of different ligands can be studied at isostructural crystal phases.

For band gap engineering, the synthesis of RPPs is investigated, as well as the influence of the halide anion. Both, lead bromide $([\text{PbBr}_4]^{2-})$ and lead iodide $([\text{PbI}_4]^{2-})$ layered perovskites and their halide mixtures should be adopted for the incorporation of the thiophene derivative. The change in the composition should provide varying quantum-well structures and thus altered electronic processes in the materials.

This chapter will help to better understand the interaction between ligands and a layered perovskite phase. Since the three chosen ligands are structurally very similar, only little influence of the structure on the electrooptical processes is expected.

4.3.1 2D layered hybrid perovskites with heterocycles

To provide surfactants based on five-ring heterocycles, three derivatives with an ethyl ammonium head group and a varying heteroatom (O, S, Se) are synthesized, shown in **Figure 64**. Here, the LHPs based on lead bromide (PbBr_2) are investigated, which is why the bromide-based ammonium salts are produced. 2-thiophene ethylammonium bromide (S-EABr) and 2-furane ethylammonium bromide (O-EABr) are provided by the acidification with HBr of the commercially available amine derivatives (see **chapter 6.1**).

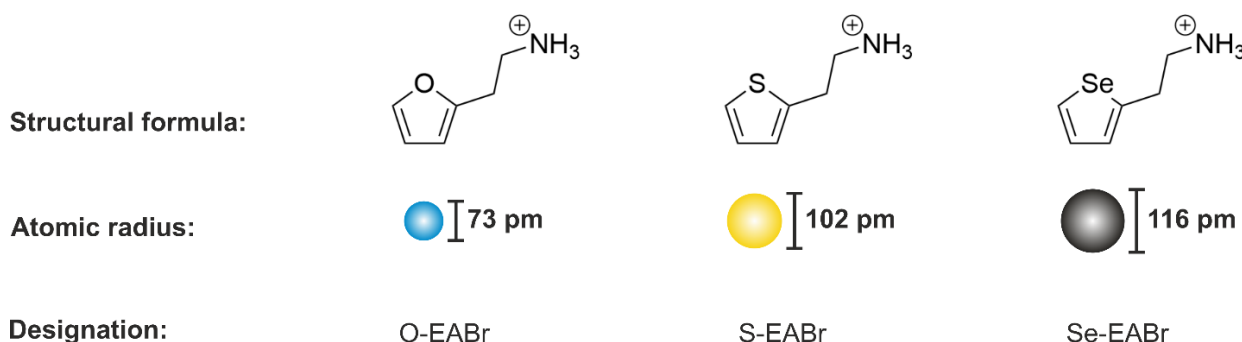


Figure 64 - Structural formula and designation of the three surfactants based on heterocycles with varying hetero atom. Atomic radii of the heteroatoms suggest that there is little change in the size of the functional group.

Since selenophene derivatives are rarer and only few compounds are commercially available 2-selenophene ethylammonium bromide (Se-EABr) is synthesized via a three-step synthesis, described in **chapter 6.1**. Since up to the present time unexplained partial decomposition of the molecule occurs in the last step of the synthesis, this also influences the synthesis of the LHPs. All ligands were characterized using $^1\text{H-NMR}$ spectroscopy (see **chapter 6.1**). Since O-EABr and S-EABr are commercially available, no further examinations were performed.

For the synthesis of the 2D LHPs, PbBr_2 and the appropriate heterocycle (ratio = 1:2) are dissolved in dimethylformamide (DMF) and converted in an antisolvent-process. The detailed experimental procedure is described in **chapter 6.2.3**. The obtained phases will be named 2D-X-EABr (with X = O, S, Se) in the following.

A combination of PXRD and SEM confirms the preservation of LHPs with a general formula $(\text{X-EA})_2\text{PbBr}_4$, shown in **Figure 65**. The arrangement of reflections of the precipitated particles of 2D-O-EABr (top) and 2D-S-EABr (middle) suggests a typical diffraction pattern for $n=1$ LHPs.^[77] The first reflection of the (001)-lattice plane is marked in color and gives the basal distance between the $[\text{PbBr}_4]$ -layers, which is 15.5 Å ($2\theta = 5.70^\circ$) for 2D-O-EABr and 15.8 Å ($2\theta = 5.60^\circ$) for 2D-S-EABr. The latter is already known in literature and agrees well with the values found here.^[265] However, for 2D-Se-EABr (bottom) a very poor crystallinity and stacking order is found for the resulting

particles, even after purification (purification process see **chapter 6.3**). Only the first reflection (marked in grey) and the succeeding higher orders can be detected, suggesting a layered structure with $n=1$ layer thickness as well. Here, the basal distance is 15.9 \AA ($2\theta = 5.56^\circ$). The tendency of the increasing basal distance from O-EABr to Se-EABr correlates with the atomic radius of the heteroatom. Although the heterocycles are very similar in terms of their chemical structure, the choice of heteroatom therefore has major influence on the basal distance and crystallinity of the LHPs. The size and shape of the particles give an indication of the integrability of the ligands into the LHPs.

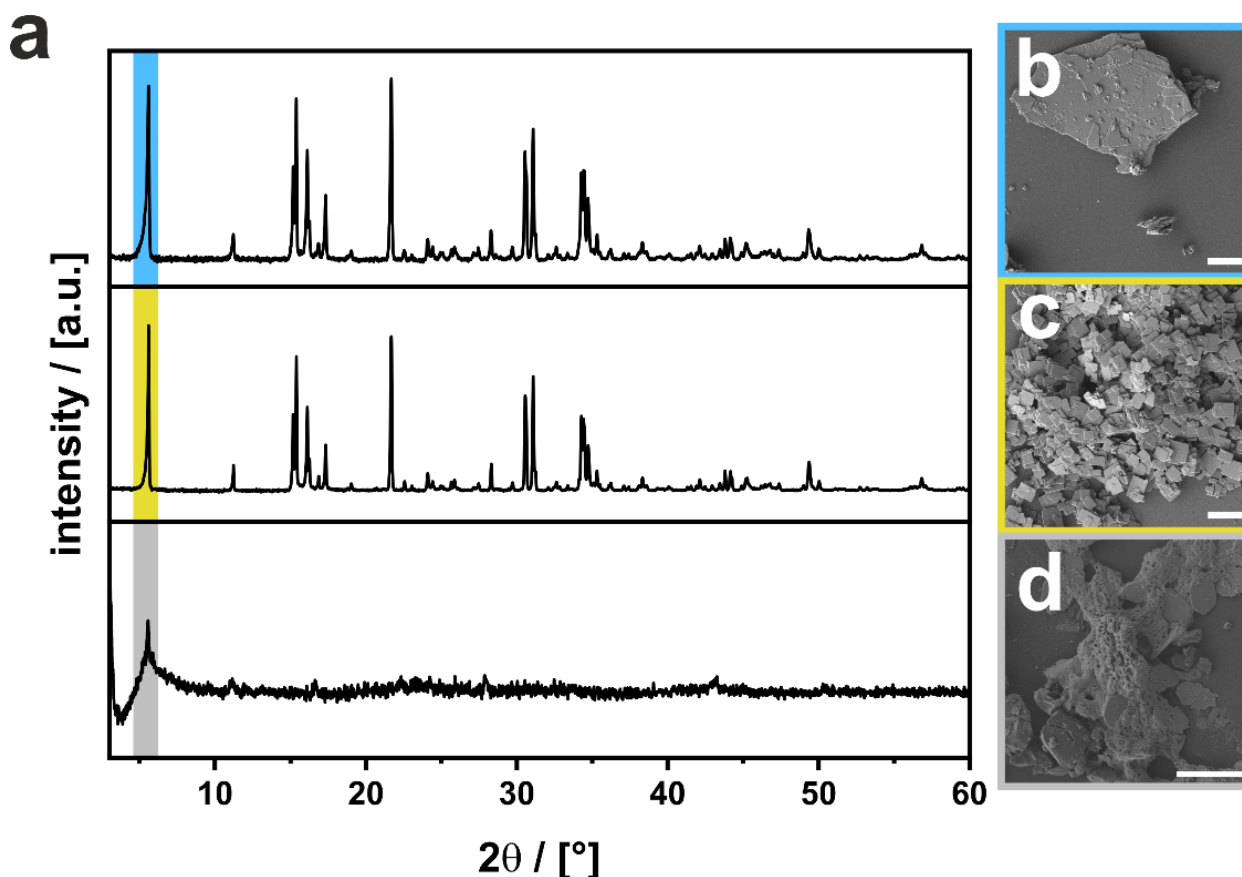


Figure 65 - a) PXRDs of 2D-O-EABr (top), 2D-S-EABr (middle) and 2D-Se-EABr (bottom). The basal distance of the $n=1$ LHP is colored. SEM images of b) 2D-O-EABr, c) 2D-S-EABr and d) 2D-Se-EABr with scalebar = $5 \mu\text{m}$.

Observation in the SEM reveals flat particles with layered character, confirming the preservation of LHPs. However, the particles appear very distinct for the different heterocycles. O-EABr yields very large particles up to $25 \mu\text{m}$ with an undefined shape (see **Figure 65b**). It seems as if several particles overlap and form these undefined structures. With S-EABr flat particles with defined rectangular morphology are obtained. They are much smaller than 2D-O-EABr and range from $1 \mu\text{m}$ to $3 \mu\text{m}$ (see **Figure 65c**). The situation changes again for Se-EABr and particles of about $2 \mu\text{m}$ with an ill-defined shape are obtained (see **Figure 65d**). In addition, a lot of (presumably organic) impurity

is found around the particles, which is a result to decomposition during the final synthesis step of the ligand. EDX measurements confirm the presence of an $n=1$ LHP, but a large fraction of organic decomposition products is also detected (see **Figure A45** and **Table 19**).

Although the chemical structure of the ligands based on the three heterocycles furane, thiophene and selenophene differs only slightly, the particle formation behaves very differently. All three ligands are incorporated in between the layers, but different particle morphologies and sizes indicate crucial differences in the formation mechanism of the particles. Very large planar particles for O-EABr indicate decelerated crystal growth in the z -direction of the particles. However, the growth takes place preferentially in the lateral direction, which is why large particles are obtained. This could indicate that the organic layer is poorly able to pack because the ligands are unfavorably aligned with each other. For S-EABr, on the other hand, very defined crystalline particles are obtained, which indicates a uniform growth. Smaller particles suggest improved nucleation compared to O-EABr. In contrast, the stacking order seems to be significantly improved for 2D-S-EABr, which is best seen at the full-width half-maximum (FWHM) of the first reflection of the (001)-lattice plane. A FWHM of 0.09° is found for 2D-S-EABr and a FWHM of 0.15° is found for 2D-O-EABr. A broader reflection indicates larger stacking disorders for 2D-O-EABr. Therefore, it is assumed, that the organic layer of 2D-S-EABr can be arranged more efficiently.

It is yet not possible to make a clear conclusion about 2D-Se-EABr, because too many organic impurities are present. The size of the particles is in the range of the 2D-S-EABr particles, but the morphology is less pronounced in comparison.

However, it is indeed possible to **integrate Se-EABr** into the LHPs, which is a promising first step towards the **comparative study** of the integration of the three heterocycles

Based on the crystallographic investigation, very similar optoelectronic properties are expected, since the inorganic layers are present in all phases. Differences are attributed to the ligands solely. Therefore, a combination of UV/Vis absorption spectroscopy and PESA is applied. The evaluation of the spectra gives the energy level alignment and the quantum-well type, with E_{HOMO} or E_{VBM} from PESA measurements and E_{LUMO} or E_{CBM} from UV/Vis absorption spectra (see **Figure A46-Figure A49**). The results are summarized in **Figure 66**.

The relative energy of the VBM of the three LHPs increases minimally by 0.1 eV from 2D-O-EABr to 2D-Se-EABr. Since the band gap is about 3.02 eV for all layered materials, the energy of the CBM behaves identical. This value is in good agreement with

literature.^[265] The energy of the HOMO of the heterocycles is the same for all ligands and is about -5.6 eV. The relative energy level of the LUMO, on the other hand, strongly increases from O-EABr to Se-EABr for the conjugated ligands, which is attributed to the heteroatom. The heterocycles from furan to selenophene have a decreasing aromaticity, which is due to a lower overlap of the frontier molecular orbitals. While the 2p electrons of oxygen in furan have a good overlap with the 2p electrons of carbon, the overlap with the 3p electrons of sulfur and the diffuse 4p electrons of selenium becomes worse.^[266] Accordingly, decreasing aromaticity also affects the arrangement of molecular orbitals and increases the HOMO-LUMO gap.

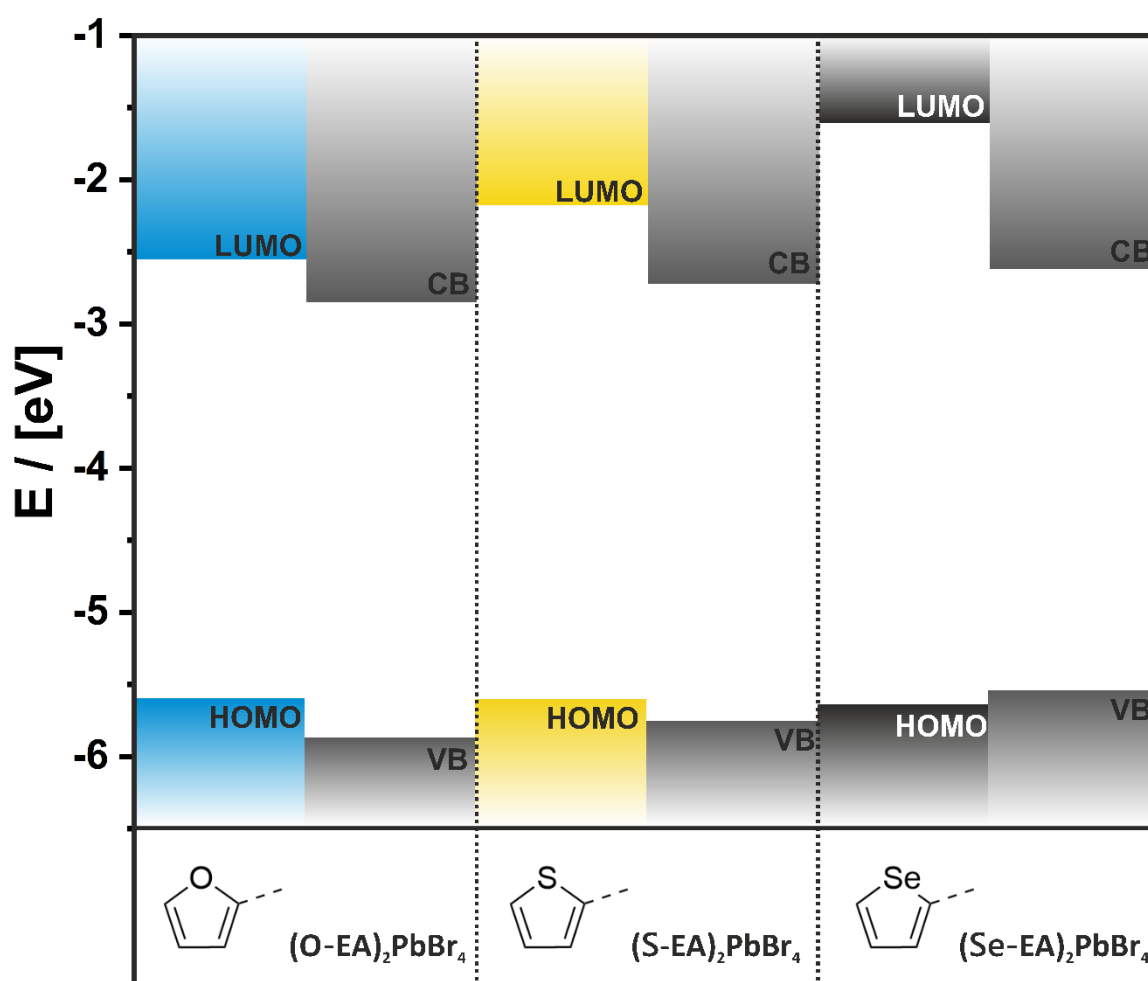


Figure 66 - Alignment of energy levels of 2D-O-EABr (left, blue), 2D-S-EABr (middle, yellow) and 2D-Se-EABr (right, black) determined from UV/Vis absorption spectroscopy and PESA given in **Figure A46-Figure A49**.

The order of the energy levels yields two different quantum-well types. 2D-O-EABr and 2D-S-EABr show a staggered arrangement with the VBM and CBM, respectively below the HOMO and the LUMO, respectively, resulting in a type II quantum-well. For 2D-Se-EABr the HOMO and LUMO lie outside of the bandgap, resulting in a type I

quantum-well (compare **Figure 6**). Therefore, the emission properties of the phases should change from 2D-O-EABr to 2D-Se-EABr. **Figure A46** shows the PL received upon excitation at 350 nm. All phases show emission at ~410 nm, which is attributed to radiative recombination of excited states in the semiconductor near the band edges.

Here it should be mentioned that in no case a bright visible emission can be observed. Since PL is **strongly quenched** for 2D-O-EABr and 2D-S-EABr, it can be assumed that **charge separation** occurs.

The excitation at 350 nm is enough to excite both the inorganic and organic species, so excited charge carriers are expected in both parts of the layered structure. Excited electrons from the heterocycle may migrate to the CBM and are accumulated in the semiconducting phase. Excited holes from the semiconductor can migrate to the heterocycle and accumulate in the organic phase. Therefore, no or a largely quenched radiative recombination should occur. For 2D-Se-EABr, on the other hand, it is difficult to make a concrete statement, since here impurities probably do not result in a clear signal. Here, visible emission from the semiconducting layers should be expected, since all generated charge carriers can accumulate and recombine there. In the future, further experiments such as time-resolved PL spectroscopy or transient absorption spectroscopy (TAS) should be carried out in order to make accurate statements about charge carrier mechanisms.

4.3.2 Halide variation in 2D layered hybrid perovskites with heterocycles

As mentioned earlier, preliminary work was done with the iodine-containing analog of hybrid perovskites $(\text{CH}_3\text{NH}_3)\text{PbI}_3$.^[118] Here, the thiophene ligand could not be incorporated into a layered material, probably due to the hexyl group, which was added to solubilize the ligand in non-polar solvents. The use of iodine-containing perovskites ensures the change of the band gap due to a halide exchange. To verify whether the thiophene ligand S-EABr can be incorporated into the iodine-containing analogue, it is first reacted with HI instead of HBr (see **chapter 6.1**). By using varying ratios of bromide and iodide in the DMF precursor, it is also tested if mixtures of the halide can be obtained via the antisolvent process and how this affects the band gap and the band alignment of the resulting particles. An experimental description is given in **chapter 6.2.3**. To verify that the ratio used in the precursor corresponds to the ratio obtained the exact composition of the particles is examined. For the exact evaluation of the iodine ratio, EDX spectra are recorded and shown in **Figure A50**. **Table 11** summarizes the experimentally found compositions.

Table 11 - Composition of the mixed halide LHPs with S-EAX ligand. Iodine ratio is determined with EDX, shown in **Figure A50**.

<i>Initial precursor</i>	<i>Experimental composition</i>	<i>Iodine ratio</i>
$(\text{S-EA})_2\text{PbBr}_4$	$(\text{S-EA})_2\text{PbBr}_4$	0 %
$(\text{S-EA})_2\text{PbBr}_3\text{I}$	$(\text{S-EA})_2\text{PbBr}_{3.52}\text{I}_{0.48}$	12 %
$(\text{S-EA})_2\text{PbBr}_2\text{I}_2$	$(\text{S-EA})_2\text{PbBr}_{2.8}\text{I}_{1.2}$	30 %
$(\text{S-EA})_2\text{PbBrI}_3$	$(\text{S-EA})_2\text{PbBr}_{1.6}\text{I}_{2.4}$	60 %
$(\text{S-EA})_2\text{PbI}_4$	$(\text{S-EA})_2\text{PbI}_4$	100 %

The iodine content found in EDX varies greatly from the concentration used in the precursor. Presumably, the smaller bromine anion is preferentially incorporated into the $[\text{PbX}_4]$ -layers. Therefore, the overall composition of a particle can be determined. However, it must be clarified whether phase separation occurs. This could be, for example, if individual layers would have a composition of $[\text{PbBr}_4]$ or $[\text{PbI}_4]$ solely. This would mean that a single particle, which is composed of several $n=1$ layers, is composed of different layers with respect to the halide. Whether the observed particles are a genuine mixture of crystalline $[\text{PbX}_4]$ -layers can be investigated by means of PXRD.

Iodine incorporation occurs without phase separation, which can be determined by PXRD, shown in **Figure 67a**. Considering the first reflection of the lattice plane (001) (see

Figure 67b), which is marked in green, the basal distance of the layers does not change significantly. This distance is given by the organic cation S-EA⁺, which packs similar for both phases. However, with respect to the (110) lattice plane (marked in grey; see **Figure 67c**), the distance $d_{(110)}$ increases significantly for increasing iodine content in the crystal phase. This lattice plane is much more dependent on the size of the anions, which is why it increases quasi-linearly, best seen in **Figure 67d**. Since a continuous diffraction pattern is obtained for all intermediate phases (12%, 30% and 60%) it can be assumed that no phase separation occurs.

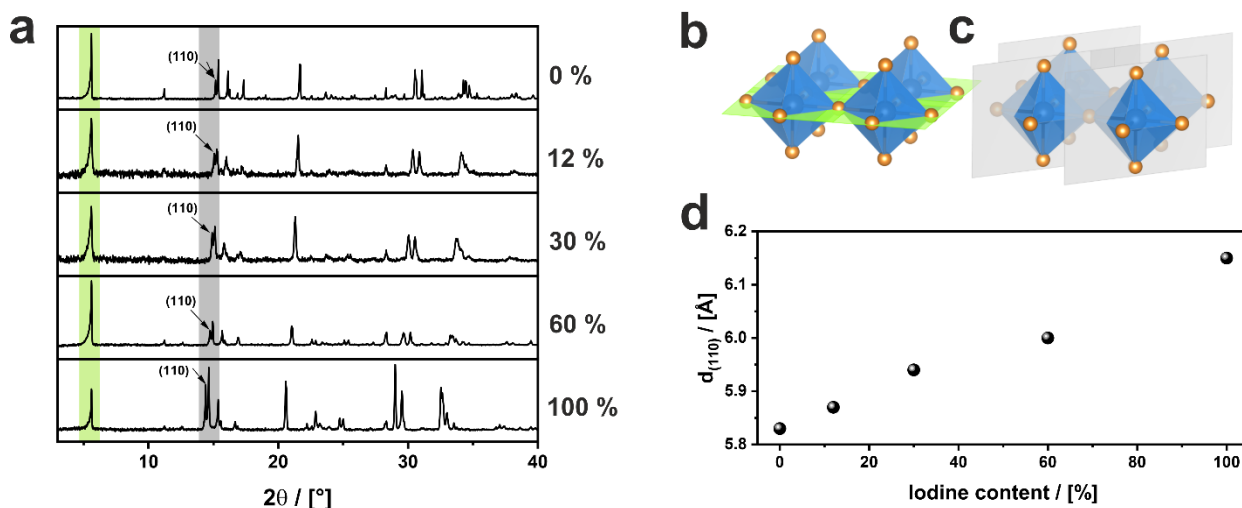


Figure 67 - a) PXRD of the particles with varying iodine content from 0 % (top) to 100 % (bottom). b) (001) lattice plane marked in green and c) (110) lattice plane marked in grey. (see also a)) d) Distance d of the (110) lattice plane in dependency of the iodine content.

In addition, the crystallographic analysis, the particles are also examined for their size and morphology in the SEM (see **Figure A51**). The size of the particles remains in a regime between 1 μm and 3 μm as observed before for 2D-S-EABr. However, particles with a high iodine content have less pronounced edges and corners, as previously observed for 2D-S-EABr (see **Figure 65c**). Deteriorated morphology indicates a slower growth mechanism of the particles during the antisolvent process. This confirms the previously established hypothesis that bromine is better incorporated into the $[\text{PbX}_4]$ -layers than iodine.

Beside to crystallographic changes of the lattice planes, a change in optical and electronical properties is expected as a result of halide exchange. This is already evident from the color of the particles after the synthesis, shown in a photograph in **Figure 68a**. The materials color ranges from white for the iodine-free composition $(\text{S-EA})_2\text{PbBr}_4$ to a bright orange for the bromide-free composition $(\text{S-EA})_2\text{PbI}_4$. UV/Vis absorption measurement confirm the altered band gap of the materials, displayed in **Figure 68b**.

All materials show a sharp absorption maximum ranging from 413 nm (3.02 eV) to 524 nm (2.37 eV). The values found are in good agreement with literature.^[265]

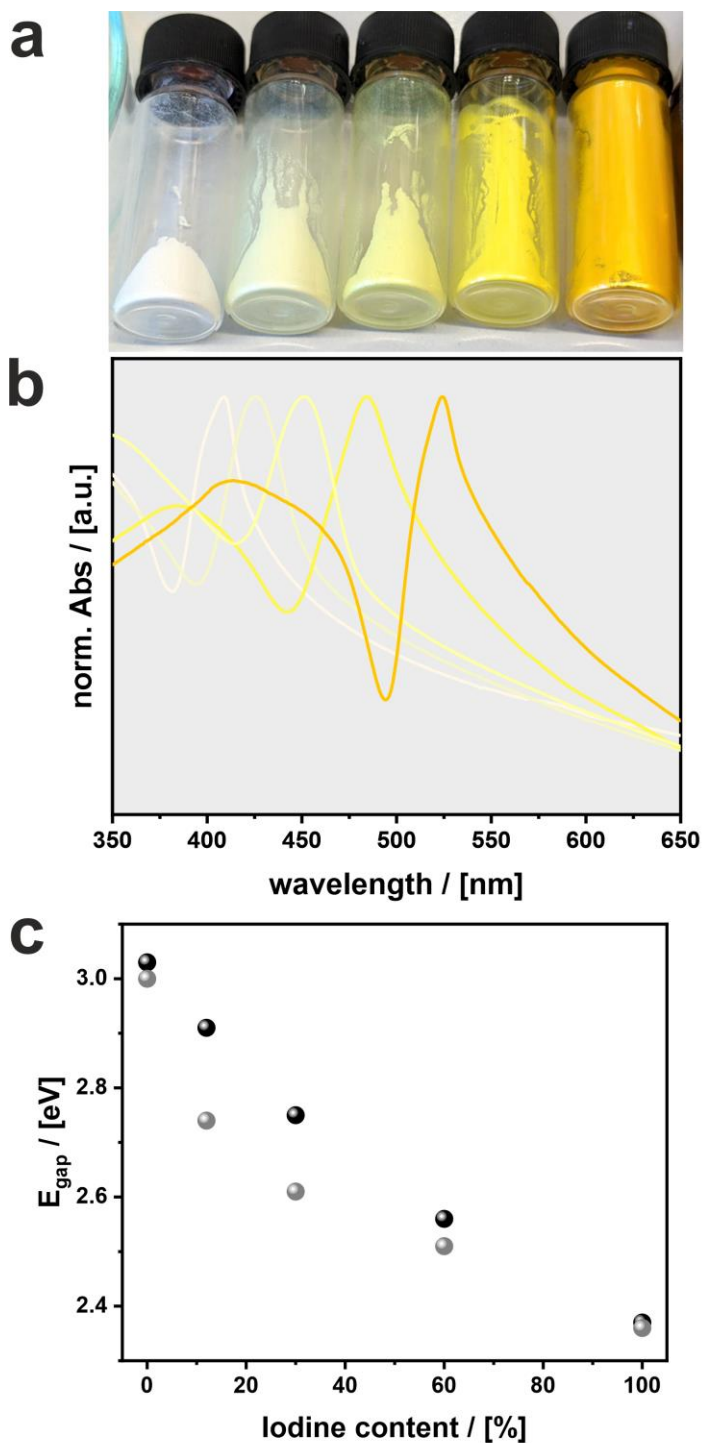


Figure 68 - a) Photograph of particles with varying iodine/Bromine ratio (increasing from left to right) b) UV/Vis of dispersed particles with iodine content of 0%, 12%, 30%, 60% and 100% (from left to right), and c) Band gap determined from absorption spectra (black) and PL spectra (grey) (see **Figure A52**). Iodine and bromine ratio are determined from EDX measurements shown in **Figure A50**.

For mixed bromine/iodine phases, the absorption maximum is slightly broader than for the pure phases. The broadening of the excitonic absorption peak indicates more constrained excitons. For mixed halide phases of the 3D perovskite, such an effect is due to lower rotational degrees of freedom for the CH_3NH_3^+ cation.^[43] H-bonds form preferentially with larger anions, since they show a greater polarizability. Therefore, the dielectric environment of the excitons is affected. Whether this effect can be extended to the H-bonding of larger ligands at the surface is yet not known. However, it could be indicative of the broadened absorption spectra observed above.

The much larger cation S-EAX may of course not rotate in the structure, but the head group could be more fixed to the inorganic $[\text{PbX}_4]$ -layers due to H-bonding. Since the organic part is strongly responsible for the dielectric confinement of excitons in the inorganic layers, halide exchange and thus an increased stiffness of the organic interlayer due to increased H-bonding can have an influence on the dielectric confinement and therefore on the width of the excitonic absorption band.

This hypothesis is confirmed when considering the PL and the excitonic band gap of the particles (see

Figure A52a). The excitonic band gap (black dots) is determined by the absorption maximum using UV/Vis absorption spectroscopy. As expected for the PL, the emissions (grey dots) are redshifted compared to the absorption bands (see **Figure 68c**). However, the redshift is more pronounced for mixed halide phases. A redshift is attributed to more strongly confined excitons.^[132] Therefore, the halide exchange does not only affect the band gap, but also the generated excitons in the inorganic lead halide layers.

To validate the relative energy landscape of the crystalline phases as a function of the halide composition, PESA measurements in combination with UV/Vis absorption spectroscopy provide information about the alteration of the energetic level of the band edges. The results are combined in **Figure 69**.

It is already known from the literature that the energetic composition of the VB has a strong halide character, which is why the relative energy of the band edge in particular is changed by the halide exchange.^[29] The relative energy of the CBM remains approximately at the same level. If the band edges are presented next to each other, the result is a step-like arrangement of the bands. This could be especially interesting for gradient materials, which could function as a kind of energy funnel. Charge carriers would be collected in the material

of the smallest band gap, similar to a diode, and recombine there, for example, in a radiative manner.

Considering the organic part of the structure, the energy levels of the MOs of the large organic cation S-EA⁺ remain the same. Therefore, a significant change of the quantum-well type occur, since the HOMO lies below the energy of the VBM, and the LUMO is above the energy of the CBM. This results in a quantum-well type I, meaning that all charge carriers can accumulate on the semiconducting bands of the perovskite phase.

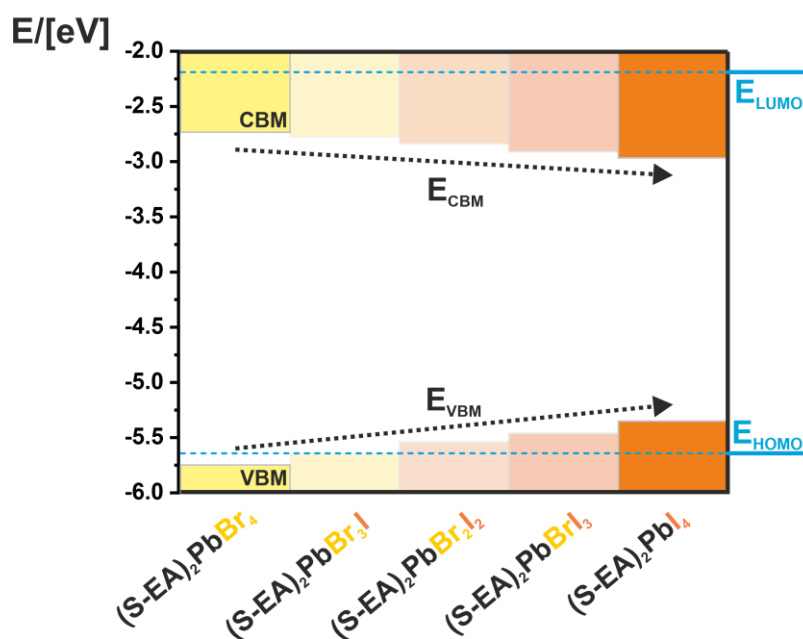


Figure 69 - Band alignment of VBM and CBM for (S-EA)₂PbBr₄ (left) and (S-EA)₂PbI₄ (right, PESA see **Figure A52b**). It is noted that the mixed halide phases are shown purely from the band gap calculation, but no experimental determination of the E_{VBM} using PESA was performed.

The adjustability of the band gap of the semiconducting inorganic phase becomes particularly interesting when the MOs of the organic chromophore are in the range of the band gap change due to halide exchange.

These initial studies show, that the **variation of the halide** anions (Br, I) is **continuous** for LHPs with S-EABr as ligand.

Thus, the composition seems to affect the quantum well type formed. Therefore, the type can be adjusted as needed via the halide concentration.

4.3.3 Ruddlesden-Popper phases with thiophen-based surfactants

Besides halide exchange, there is also the possibility of layer thickness adjustment. Again, starting from the same chromophore, different quantum well types can be obtained without changing the organic cation. Since the layer thicknesses differ in their arrangement of the bands and thus also in the band gap due to the quantum confinement, different charge carrier dynamics are expected.

In addition to LHPs with a single lead halide layer ($n=1$), the incorporation of MABr will induce the formation of quasi-2D RPPs ($n=2,3,4,5$) with altered band gap. As already investigated for AzoC_2Br and FcC_6Br , S-EABr will be used for the synthesis of RPPs. A general formula gives the composition of the phases with $(\text{S-EA})_2(\text{MA})_{n-1}\text{Pb}_n\text{Br}_{3n+1}$ (with $n=1,2,3,4,5$). In the scope of a Bachelor thesis different attempts were made to synthesize and characterize RPPs based on S-EABr. The goal was to understand the synthesis via antisolvent process to ultimately generate phase-pure RPPs. Not all experiments are summarized here, but the most insightful results are presented.

To obtain a first indication of the formation of RPPs with S-EABr, the synthesis of a supposed $n=2$ layer is investigated by UV/Vis kinetics measurement, displayed in **Figure 70a**. For this purpose, the conversion of the precursor is studied using a UV/Vis probe during synthesis. For the synthesis, the starting materials are dissolved in DMF in a specific ratio ($n=2 \rightarrow (1:2:2)$ for (MABr:PbBr₂:S-EABr)) and precipitated in an antisolvent. The exact experimental procedure is described in **chapter 6.2.3**.

Shortly after addition of the DMF precursor, two discrete absorption bands evolve at 409 nm (3.03 eV), attributed to a $n=1$ layer and 433 nm (2.86 eV), attributed to a $n=2$ layer. During the course of the reaction, another absorption band is formed at 456 nm (2.72 eV), which is attributed to a $n=3$ layer, and a band edge at 530 nm (2.33 eV), which is attributed to the 3D phase ($n \geq 5$). In principle, it is possible to prepare RPPs with layer thicknesses of $n > 1$, similar to that for FcC_6Br (see **chapter 4.2.5**). Nevertheless, UV/Vis absorption suggests, that there is more than one layer thickness present in the precipitation.

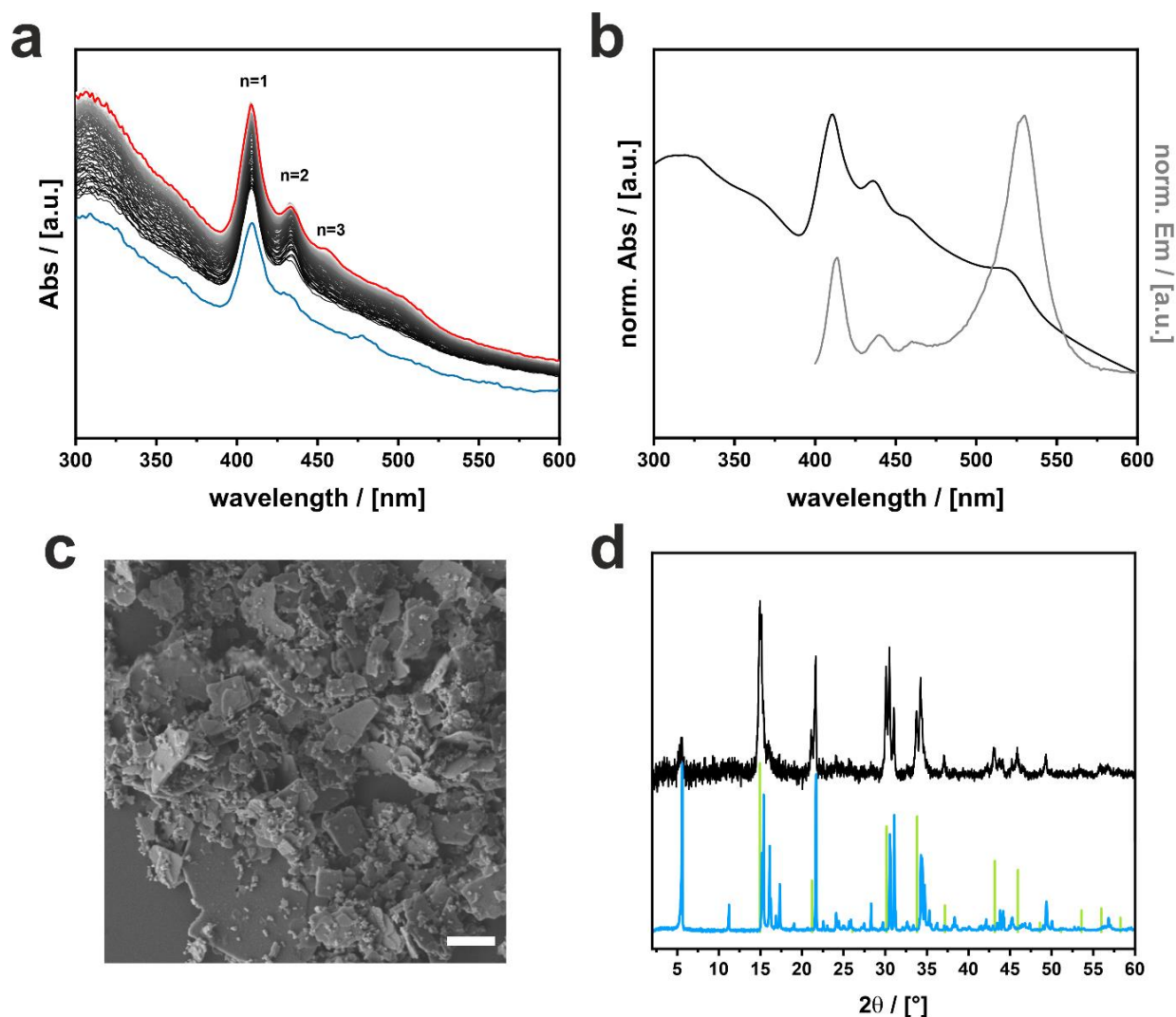


Figure 70 - a) UV/Vis kinetic measurement of DMF based precursor with specified ratio of starting materials for the precipitation an RPP with $n=2$. First measurement (blue) and last measurement (red) are colored. b) UV/Vis absorption (black) and PL spectra (grey) of particles after synthesis dispersed in toluene. Excitation occurred at 350 nm c) SEM image of particles. d) PXRD measurement of the particles (black, top) with reference of MAPbBr₃ (green) and (S-EA)₂PbBr₄ (blue).

After purification of the precipitated particles, a UV/Vis absorption spectrum and an emission spectrum are recorded to ensure that the composition of the particles remains unchanged during purification. Since it is a dynamic growth process, changes may occur during the washing processes. This is particularly the case if the ligand is highly soluble in the antisolvent, so that layers can partially dissolve again and form new layers. The normalized spectra are shown in **Figure 70b**. All three previously determined absorption bands of the $n=1,2$ and 3 layers and also the absorption edge are found, so it is assumed that the purification process has little or no effect on the phase of the particles. For the PL measurement, emission bands at 414 nm (2.99 eV), 440 nm (2.81 eV), 466 nm

(2.66 eV) and 530 nm (2.30 eV) are found, which are in good agreement with the absorption bands found previously. The values of the absorption and emission maxima for the RPPs established in **chapter 4.2.5** (RPPs with FcC₆Br), **Table 10**, can also be transferred for phases with S-EABr, since only the inorganic layers contribute to excitonic absorption/emission.

Investigating the precipitation in the SEM, as shown in **Figure 70c**, it is clear that different particles are generated during synthesis. There are larger, flat particles in the μm range and small particles in the range from 50 nm to 100 nm, which seem to grow on top of the large particles. Based on the crystal structure, large, flat particles are probably RPPs, which are formed at the beginning of precipitation. Due to a heterogeneous nucleation at the emerging surface of the large particles, smaller particles of the 3D phase grow on the surface. This hypothesis also explains a delayed appearance of the continuous band edge at 530 nm in the observation of the absorption during the precipitation (see **Figure 70a**).

From UV/Vis, PL and SEM it is already evident, that the precipitate contains mixed crystalline phases. Thus, PXRD is used to determine the crystal structures of the mixture to confirm these results, shown in **Figure 70d**. Reference diffraction patterns of an $n=1$ (S-EA)₂PbBr₄ (blue) layered structure and the 3D phase MAPbBr₃ (green) are given below. Reflections between 15° and 50° are a superposition of the two references given, confirming that two distinct phases are present. A reflection of the lattice plane (001), the basal distance at $2\Theta = 5.6^\circ$ (15.8 Å) indicates the presence of the $n=1$ layer. For layer thicknesses $n>1$, a larger distance is expected, i.e. reflections at smaller angles. By adding the height of a unit cell of the 3D perovskite MAPbBr₃ (~5.9 Å), approximately all of the following thicknesses ($n>1$) can be calculated theoretically from the $n=1$ layer. The calculations are summarized in **Table 12**.

Based on the optical characterization, a material with multiple layer thicknesses is expected. The absence of other reflections at low angles is probably due to the statistical distribution of layers in the material. If there are occasional layer thicknesses with $n>1$, these are not detected in the PXRD because there is no periodicity of the lattice. These can nevertheless be detected in UV/Vis and PL, since this is not a cooperative property of the layered phases.

Table 12 - Calculated layer thicknesses for $(S-EA)_2(MA)_{n-1}Pb_nBr_{3n+1}$.

Layer thickness n	1	2	3	4	5
distance d	15.8 Å	21.7 Å	27.6 Å	33.5 Å	39.4 Å
angle 2θ	5.60°	4.07°	3.20°	2.64°	2.24°

The studies show that it is indeed possible to obtain RPPs with S-EABr via the antisolvent route, but not phase-pure. The $n=1$ layer thickness, as well as the 3D phase, are very prominently present in the precipitate despite the adjustment of the composition of the precursor. To ensure precipitation of phase-pure materials, the conditions for crystal growth must be well understood and adjusted.

As a result of the previous investigations, further approaches of a similar kind (solvation of all starting materials as precursor in varying ratios) were attempted, but this did not lead to the desired phase-pure product. UV/Vis kinetic measurements showed that the 3D phase emerges late as they grow on large particles of the 2D phases. In addition, it can be assumed that nanoplatelets of individual layers are present in the synthesis at the beginning and that these arrange themselves into larger particles by stacking. Therefore, a new approach is developed in which the starting materials are added at different times (see **chapter 6.2.3**) and the reaction time is greatly reduced. Initially, the growth of the $n=1$ layer is induced specifically by adding $PbBr_2$ and S-EABr. Then MABr is added in the early stage of growth so that it can attach between two existing layers. Indeed, the approach shows the preparation of a phase-pure $n=2$ RPP with the composition $(S-EA)_2(MA)Pb_2Br_7$. **Figure 71** summarizes the results for the obtained particles.

The diffraction pattern (**Figure 71a**, top) of the obtained particles shows a reflection at 4.07°, which clearly confirms an $n=2$ layer (see **Table 12**). At the same time, no other reflection at low angles is found indicating the complete conversion of the $n=1$ layers produced in the nucleation phase. Particles produced with this approach are significantly smaller than particles of the $n=1$ RPP, which can be seen in SEM images (**Figure 71b+c**). This is due to the shortened reaction time, as presumably no Ostwald ripening or similar processes can take place. Furthermore, optical absorption and emission spectroscopy are recorded to characterize of $(S-EA)_2(MA)Pb_2Br_7$ exclusively, displayed in **Figure 71d**.

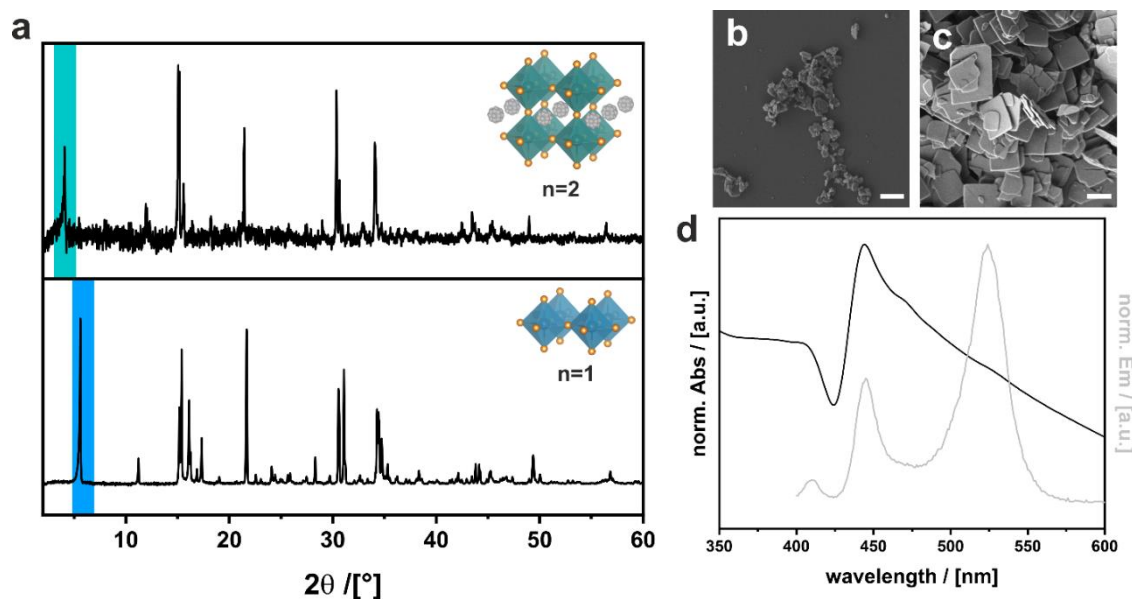


Figure 71 - a) PXRD of $(S-EA)_2(MA)Pb_2Br_7$ (top) and $(S-EA)_2PbBr_4$ (bottom). Reflection of the basal distance ($d_{(001)}$) are colored; SEM images of b) $(S-EA)_2(MA)Pb_2Br_7$ and c) $(S-EA)_2PbBr_4$ with scalebar = 1 μm and d) UV/Vis absorption (black) with $\lambda_{max} = 443$ nm (2.80 eV) and PL emission (grey) spectra with $\lambda_{max} = 445$ nm (2.79 eV) of $(S-EA)_2(MA)Pb_2Br_7$.

The absorption spectrum (black) shows an absorption peak at 443 nm (2.80 eV), which is in good agreement with the previously found values for the $n=2$ crystal phase. However, a shoulder at 470 nm (2.64 eV) and 526 nm (2.36 eV) indicate the presence of layers with $n>2$ and 3D phase. Considering the PL spectrum (grey), a weak emission band is found at 446 nm, which is attributed to the $n=2$ layer and an emission band at 525 nm, which is comparatively stronger and is attributed to the 3D phase. Although it is clear from PXRD and UV/Vis that the particles contain significantly more $n=2$ phase, the PL spectrum confounds the results. This phenomenon is best explained via energy transfer between the layers. In a multi-phase layered perovskite, excited charge carriers migrate across an inhomogeneous energy landscape. However, charge carriers are concentrated to the smallest band gap, where they recombine radiatively.^[248] Therefore, no quantitative statement of the film thickness distribution can be obtained via the PL spectrum.

In summary, it is clear that S-EABr is also **suitable for the preparation of RPPs**, but the synthesis of phase-pure particles via the antisolvent-process cannot yet be well guaranteed.

A new approach in which nucleation and growth are separated in time shows promising results, which still needs to be optimized and reproduced. To date, there is no antisolvent synthesis in the literature in which phase-pure RPPs can be selectively produced.

5 Conclusion and Outlook

The present work was devoted to the investigation of 2D layered hybrid perovskites (LHPs) and Ruddlesden-Popper phases (RPPs) with functional surfactants as an integral component of the periodically ordered layered materials and their dependence on external stimuli. The investigations were carried out on micrometer-sized particles obtained in an antisolvent process by precipitation of the desired phase. The synthesis and incorporation of functional molecules enables a variety of novel materials with the semiconducting properties of the inorganic perovskite phase and the functionality of organics. Different functionalities were selected which are, among other features, conductive, but also reversibly modifiable, such as photoswitches or redox-active organometallics (**Figure 72**).

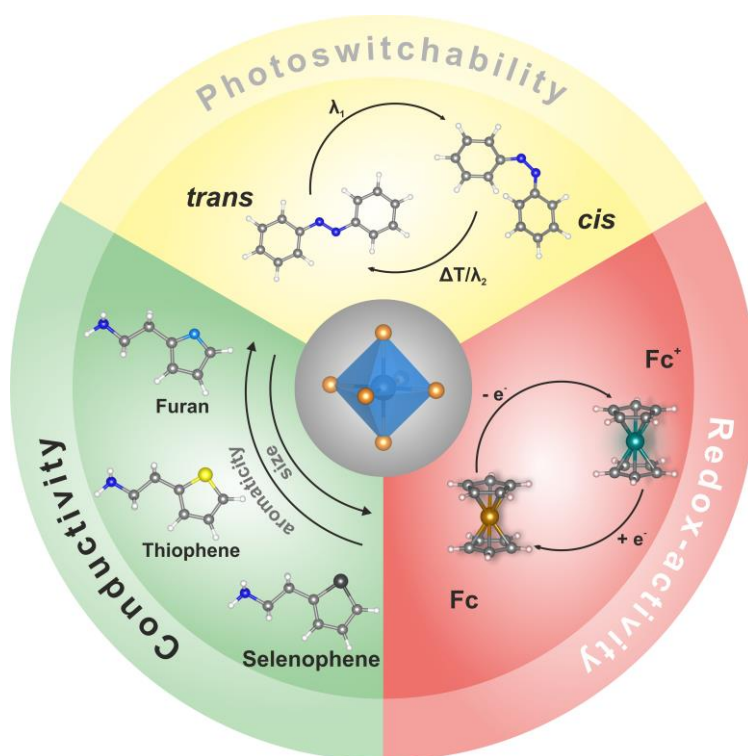


Figure 72 – Overview of the functional ligands used for the synthesis of 2D LHPs.

The first part of the thesis (**chapter 4.1**) was based on the synthesis and integration of photoswitchable azobenzene ligands into 2D LHPs, RPPs with thicker layers and the functionalization of 3D perovskite particles. The following points should be clarified:

- Is the incorporation of such ligands possible?
- How does the photoswitchability of the organic ligands behave in combination with a semiconductor? Does this enable control of transfer of energy between the layers?

Azobenzene, which undergoes a conformational change from *trans* to *cis* around the azo bond due to irradiation (see **Figure 72**, yellow), was equipped with four head groups of different lengths. These varied from a methyl and ethyl chain (AzoC₁, AzoC₂) providing

short distances between the azobenzene moiety and the coordinating head group, over a medium-length butoxy chain (AzoC₄), to a long dodecyloxy chain (AzoC₁₂). The different head group lengths are intended to provide variation in the distance of the azobenzene group from the semiconductor to **investigate distance dependent charge carrier dynamics**. The ligands were first characterized using standard chemical analysis, and later tested for their intrinsic photoswitchability yielding a degree of isomerization (DOI) between 20 % and 50 % depending on the length of the head group. The DOI here refers to the photoswitching reaction to the *cis*-isomer.

In an antisolvent synthesis using a DMF based precursor in which the corresponding azobenzene ligand and lead bromide (PbBr₂) were dissolved, particles in the micrometer range were precipitated. Powder X-ray diffraction (PXRD) revealed a layered character of the resulting phases, confirming the presence of 2D LHPs with integrated azobenzene ligand. The ligand with the shortest head group AzoC₁ could not be incorporated between the layers of the LHPs. This was attributed to an increased stiffness of the ligand and thus worse packing between the inorganic layers. All particles show a plate like morphology, confirming the layered character of the resulting crystal phase. The periodic layer spacing between the inorganic [PbBr₄]-layers increased with the length of the spacer between the azobenzene and the head group.

To verify the photoswitchability of the incorporated ligands, two approaches were used. On the one hand, the precursor was irradiated before precipitation, on the other hand, the synthesized particles were irradiated in dispersion. Due to the conformational change, a variation in the basal distance of the 2D LHPs was expected for the irradiated phases. For the first approach, ¹H-NMR measurements revealed a low DOI with a maximum of about 10 % for the irradiated precursor solution containing PbBr₂ and AzoC₂.

The phases precipitated after the irradiation and illustrated no significant changes in the basal distance between the [PbBr₄]-layers, which **disproves the assumption of the incorporation of ligands in *cis*-conformation**.

The second approach, in which the particles were dispersed and irradiated with 313 nm for up to 6 h did neither yield a changed basal distance.

It was now questionable whether the conformational change between the layers was suppressed due to a charge transfer from the photoexcited azobenzene ligand to the semiconductor, as Torres *et al.* found for a charge transfer complex with TiO₂ and an azobenzene dye,^[186] or due to steric hindrance between the perovskite layers. Indeed, a combination of UV/Vis spectroscopic investigations with subsequent ¹H-NMR of the dissolved particles revealed a low DOI (2.5 % to 12.3 %) for the photoswitchable

azobenzene ligands, confirming the conformational change for a small fraction of the ligands.

It was therefore assumed, that a **distinction** must be made **between surface bound** ligands, which are **not sterically hindered** and may therefore photoswitch from *trans*- to *cis*-conformation, and **incorporated ligands**, which were **not available** for **photoswitching**.

In order to detect a possible charge transfer between the organic and inorganic layers, the relative energy levels of the different species were determined. Using a combination of UV/Vis reflectance and PESA, the alignment of the VBM and CBM energy levels with respect to HOMO and LUMO were determined. Both VBM and HOMO, as well as CBM and LUMO each have almost the same energy level for all LHPs, allowing charge carrier or energy transfer. PL analysis of the 2D LHPs revealed the distance dependency of the charge carrier transfer from the azobenzene to the inorganic lead bromide phase. With a short and middle-ranged head group (AzoC₂ and AzoC₄), no fluorescence of the azobenzene ligands was observed. However, a long-chained head group (AzoC₁₂) showed fluorescence of the azobenzene moiety and confirmed only a partial charge carrier or energy transfer.

Since LHPs contain both integrated and surface coordinating ligands, 3D perovskite particles with the composition CH₃NH₃PbBr₃ (MAPbBr₃) were prepared to observe surface-effects alone. The particles were in the size regime of 100 nm to 300 nm, providing a high surface-to-volume ratio. Surface functionalization with the azobenzene ligands was confirmed using a combination of UV/Vis spectroscopic and IR measurements. With a combination of UV/Vis reflectance spectroscopy and PESA, the band level alignment (VBM/CBM) in comparison to the molecular orbitals (HOMO/LUMO) revealed a step-like arrangement of the energy levels. Thereby, the VBM and the HOMO have an almost similar energy level and the CBM is below the LUMO, allowing charge carrier migration between the two species. Irradiation experiments with 313 nm revealed that, due to the coordination of the azobenzene ligands to the perovskite, there was a significantly increased DOI compared to the free ligands. The improved photoswitching is attributed to an energy transfer from the perovskite particles to the azobenzene ligand.

The improved photoswitching is attributed to an **energy transfer from the perovskite** particles to the **azobenzene** ligand.

Lastly, by addition of MABr to the precursor, the synthesis of RPPs with layer thicknesses of $n > 1$ was attempted. Despite variation of parameters (composition, temperature,

conformation of the ligand), no RPPs were obtained, but only mixed phases of 3D perovskite particles and 2D LHPs. This was attributed to the nature of the ligands with strong π -interactions and poor solubility of the azobenzene ligands in the antisolvent. Thus, no MABr could be intercalated between the inorganic lead bromide layers.

After it was shown that no significant change in energy transfer between the organic and inorganic phase could be observed by photoswitching the azobenzene ligands, another switchable system, based on redox-active organometals was developed, described in **chapter 4.2**. Ferrocene (Fc) was chosen for this purpose, which is an excellent ligand due to its simple, fast redox chemistry and its high stability under various conditions (see **Figure 72**, red). With Fc as ligand the following points should be investigated:

- Is the integration into the perovskite phase possible?
- How do the optoelectronic properties behave depending on the distance between the Fc ligand and the semiconductor?
- Is oxidation of the Fc ligand possible and how does it affect the optoelectronic properties?

Starting from ferrocene carboxylic acid, five novel Fc ligands were synthesized by ester coupling. The ligands differed in the length of their head groups, which ranged from an ethylammonium (FcC₂Br) up to a hexylammonium (FcC₆Br) group, providing different distances between the inorganic perovskite phase and the Fc unit. The ligands were characterized using standard molecule analytical techniques (¹H-/¹³C-NMR, IR, UV/Vis). The oxidized state (Fc⁺) of the ligands was observed by UV/Vis spectroscopy, as oxidation causes a further optical absorption band and the color impression changes from red to blue.

In an antisolvent process, the ligands were incorporated as integral component into the hybrid lead bromide phases, yielding micrometer sized particles.

PXRD measurements suggested **complex crystal structures** for the precipitations formed with PbBr₂ and **FcC₂, FcC₃ and FcC₄**, respectively.

LHPs were obtained only with sufficiently long head group (FcC₅ and FcC₆), which was evident from the PXRD measurements by comparing to phases known in literature. Strong structure directing properties of the ligands were revealed by 3D electron diffraction (3D ED) with subsequent crystal structure refinement. This indicated that the ester group can interact with the ammonium head group and thus compete with the anionic lead bromide network. Moreover, the Fc units arrange similarly to the initial structure of non-substituted Fc, leading to the formation of two novel exotic lead bromide

phases with FcC_2 and $\text{FcC}_3/\text{FcC}_4$. All phases are characterized by their semiconducting abilities with band gaps between 3.51 eV and 3.06 eV and a staggered arrangement of energy levels, similar to a quantum well type II. Energy levels, as well as the band gap were determined using a combination of UV/Vis reflectance spectroscopy and PESA.

As representative system $(\text{FcC}_2)\text{PbBr}_3$ was used to study the redox activity using two different approaches. Cyclic voltammetry (CV) was performed to **verify the redox activity of the incorporated ligands** of the crystalline phase. A halfwave potential at 0.45 V, typical of Fcs, was found, implying that the ligands are accessible to redox processes. Permanent oxidation was achieved by applying a voltage at 0.65 V, after which the characterization of optical properties (UV/Vis and PL) was performed. On the one hand, the color of the material changed, and on the other hand, the emission of the oxidized Fc^+ ligand was detected. Radiative recombination was induced by electron and hole migration from the excited lead bromide phase to the Fc^+ ligand where the charge carriers recombine.

Therefore, it is assumed that the **previously staggered arrangement** of the **quantum well type II energy levels** has **changed** due to the emergence of a SOMO, that now lies above the VBM (similar to a quantum well type I).

Since only a small fraction of the ligands can be addressed by electrochemical oxidation, the approach of chemical oxidation using a perchlorate-containing oxidant ($\text{Fe}(\text{ClO}_4)_3$) was used. PXRD and SEM measurements showed that the phases are stable against the oxidant. Subsequent characterization of the optoelectronic properties using UV/Vis reflectance spectroscopy confirmed the effects found for electrochemical oxidation. X-ray photoelectron spectroscopy (XPS) allowed the determination of the exact degree of oxidation. Depending on the concentration of the oxidant, a degree of oxidation of up to 63.3 % could be achieved. Above 50 %, a cooperative effect was observed and a new band was formed from the periodically arranged SOMOs of the oxidized Fc ligands within the hybrid phase. This was evident in a decrease of 0.24 eV of the band gap. Theoretical calculations showed that electron spins are delocalized over several ligands, which is why a hopping process between the ligands could be concluded and a novel band inside the band gap emerged.

The **oxidation of the ligands** can therefore be seen as a **kind of active defect**, which can be specifically turned on by the oxidation to tune the electrooptical properties.

Lastly, the synthesis of RPPs with the ligand FcC₆ was tested, which showed the formation of periodically ordered LHPs (n=1) before. The addition of MABr resulted in different RPPs (n=2,3,4,5), but these did not have a uniform composition in terms of their layer thickness n. Optical properties of the particles were composed of different layer thicknesses randomly present in the particles. This effect is already known from synthesis of hybrid perovskite nanoparticles in literature, where alkyl ligands were used.^[67]

Finally, conductive ligands based on the heterocycles furan, thiophene, and selenophene were developed for the synthesis of LHPs and RPPs (see **Figure 72**, green), described in **chapter 4.3**. All ligands possessed an ethylammonium head group and differed only in the heteroatom they contained (O, S, Se). The following questions are identified:

- Is the formation of LHPs and RPPs with the heterocycles possible?
- How does the heteroatom affect the electronic processes in the materials?
- How does halide change and the layer thickness, respectively, affect the quantum well structure of the resulting materials?

Selenophene ethylammonium bromide (Se-EABr) was prepared in a three-step synthesis and verified by ¹H-NMR spectroscopy. The other ligands (furan and thiophene) were commercially available. In an antisolvent process, the formation of 2D LHPs (n=1) was observed and the emerging particles with the phase (X-EA)₂PbBr₄ (X = O, S, Se) were characterized using SEM and PXRD. Since in the final synthesis step for Se-EABr so far uninvestigated decomposition took place, only particles with low crystallinity and poorly pronounced morphology were obtained for this ligand.

Optical characterization by UV/Vis reflectance spectroscopy and PESA illustrated that the change in relative energies for the HOMO and LUMO depends on the heteroatom, which is due to a decreased aromaticity from furan to selenophene due to a lower overlap of the frontier MOs.

Therefore, **both a type I quantum well** (for Se) and **type II quantum wells** (for O and S) were obtained.

At the same time, VBM, CBM and the band gap at about 3.1 eV remained largely the same, which is consistent with known values from the literature.^[265]

Afterwards, the crystalline phases were adapted to tune the band gap using two different approaches. On the one hand, the continuous substitution of bromide with iodide was investigated, on the other hand RPPs with larger layer thicknesses were prepared. Here, **halide exchange proved to be a suitable method for tuning the optoelectronic properties**, namely the band gap, as continuous incorporation of the halides was

observed. RPPs ($n=2,3,4,5$) proved to be much more difficult to prepare, since, on the one hand, phase purity could not be achieved with respect to the layer thickness n and, on the other hand, predominantly the thermodynamically most stable form of the $n=1$ layer was obtained. The investigation of crystal formation during synthesis with UV/Vis kinetic measurements showed that layer thicknesses with $n>1$ were indeed formed, but these were only statistically present in the largest part of the material. RPPs of the composition $(S-EA)_2(MA)Pb_2Br_7$ ($n=2$) could only be obtained by an adapted synthesis.

This thesis provides insights into hybrid perovskite materials with a higher degree of functionality given by the organic species. Concluding, all surfactants, especially the redox-active Fc ligands, showed interesting results that should be pursued in future research. Azobenzene ligands proved to be suitable for surface functionalization of hybrid perovskites, however, integration suppressed the pronounced photoswitching process, unlike previously reported in literature. Photoswitching of surface-adherent ligands potential to be of particular interest for the controlled destabilization of hybrid perovskite nanoparticle dispersions. For example, self-assembly processes may be monitored, however, this was not relevant for this work. In addition, the conjugated molecule offers the possibility of charge transfer and could improve the conductivity at the surface of the particles, compared to typical alkyl-based ligands. In the future, conductivity measurements (e.g. photodiode tests^[118]) should be conducted for clarity.

Fc ligands proved to yield redox-active semiconductors, which is a completely new field of functional hybrid perovskites and opens a variety of applications for the materials. The presence of the paramagnetic spin of the Fe^{3+} nuclei after the oxidation can result in unusual effects in the magnetic field. Magnetic semiconductors may especially be interesting for spintronics. Therefore, in the future, the focus should be on magnetic measurements of the materials, before and after oxidation. Furthermore, it would be interesting to investigate, whether single molecules are addressable to create point defects. Therefore, thin-films should be prepared on a substrate, which is on the one hand suitable for crystal growth and on the other hand non-magnetic, to investigate possible magnetic properties of the material. Alternatively, the particle synthesis could be improved and self-assembly of the particles could be performed. This would allow the production of particle-based thin films.

Finally, the heterocyclic compounds must also be considered in more detail. In particular, problems in the synthesis of Se-EABr and the subsequent particle synthesis should be solved in order to be able to make exact statements about these systems. Furthermore, first results show, that the synthesis of RPPs is possible with thicker layers ($n>1$). However, synthesis parameters need to be improved (e.g. reaction time, concentration of the precursor, addition of salts) to obtain phase pure particles reliably.

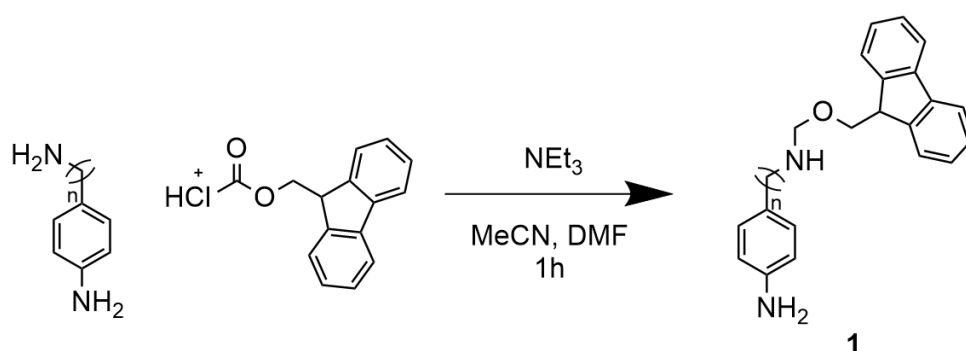
6 Experimental Section

6.1 Synthesis of functional ligands

This chapter describes experimental details of the synthesis of the functional ligands AzoC_nBr (with $n=1,2,4,12$), FcC_nBr ($n=2,3,4,5,6$) and X-EABr (with $\text{X} = \text{O}, \text{S}, \text{Se}$) used for the material synthesis of hybrid perovskites.

Synthesis of AzoC_1Br and AzoC_2Br

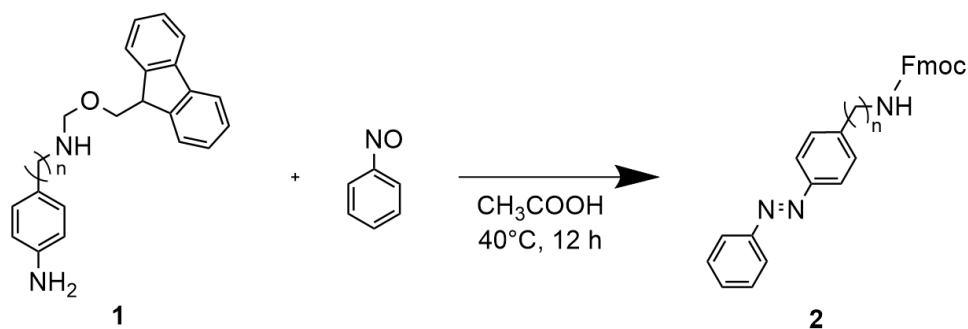
Step 1:



The azobenzene based ligands AzoC_1Br ($n=1$) and AzoC_2Br ($n=1$) are produced via the same synthesis route. For the synthesis of compound **1**, 30 mmol (4-aminomethyl) aniline ($n=1$) respectively 2-(4-aminoethyl) aniline ($n=2$) was dissolved in 250 mL dichloromethane (DCM). After adding 36 mmol Fmoc-Cl, trimethylamine (NEt_3) was added dropwise under stirring. The suspension was stirred for 4 h at ambient temperature. The solvent was removed and the remaining the residue solved in ethyl acetate (EtOAc) and methanol (MeOH) (5:1) and filtered over silica gel. The solvent was removed and a yellow powder was obtained.^[267]

$^1\text{H-NMR}$ (400 MHz, DMSO) $n=1$: δ (ppm) = 7.88 (d, 2H, CH Fmoc-Cl), 7.69 (d, 2H, CH Fmoc-Cl), 7.41 (t, 2H, CH, Fmoc-Cl), 7.32 (t, 3H, CH, Fmoc-Cl), 6.89 (d, 2H, CH, 2-(4-aminophenyl) methylamin), 6.50 (d, 2H, CH, 2-(4-aminophenyl) methylamin), 4.31 (d, 2H, CH_2 , Fmoc-Cl), 4.21 (t, 1H, CH, Fmoc-Cl), 4.00 (t, 2H, CH_2); $n=2$ δ (ppm) = 7.89 (d, 2H, CH Fmoc-Cl), 7.69 (d, 2H, CH Fmoc-Cl), 7.41 (t, 2H, CH Fmoc-Cl), 7.33 (t, 3H, CH, Fmoc-Cl), 6.83 (d, 2H, CH, 2-(4-aminoethyl) aniline), 6.49 (d, 2H, CH, 2-(4-aminoethyl) aniline), 4.29 (d, 2H, CH_2 , Fmoc-Cl), 4.20 (t, 1H, CH, Fmoc-Cl) 3.11 (t, 2H, CH_2), 2.52 (t, 2H, CH_2)

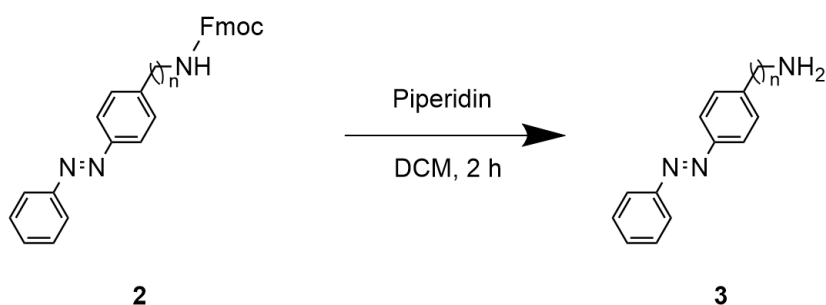
Step 2:



For the azo coupling, compound **1** was then added to a solution of nitroso benzene (1.25 eq) in glacial acetic acid. After stirring at 80°C for 24 h about 100 mL purified water was added and a brown precipitate was obtained. The solid was solved in DCM and separated from the glacial acetic acid. After washing the organic phase once with purified water and two times with brine, the organic solvent was removed.^[268] Chromatographic purification with EtOAc and pentane (PE), (1:2) gave an orange solid. The product was characterized with $^1\text{H-NMR}$ spectroscopy.

$^1\text{H-NMR}$ (400 MHz, DMSO) $n=1$: δ (ppm) = 7.90-7.84 (m, 6H), 7.71 (d, 2H), 7.60 (d, 2H), 7.42 (t, 4H), 7.34 (m, 3H) 4.39 (d, 2H, CH_2 , Fmoc-Cl), 4.28 (t, 1H, CH, Fmoc-Cl), 4.03 (d, 2H, CH_2); $n=2$: δ (ppm) = 7.89-7.86 (m, 4H), 7.81 (d, 2H), 7.67-7.56 (m, 5H), 7.43-7.30 (m, 6H), 4.31 (d, 2H, CH_2 , Fmoc-Cl), 4.20 (t, 1H, CH, Fmoc-Cl), 3.28 (t, 2H, CH_2), 2.83 (t, 2H, CH_2)

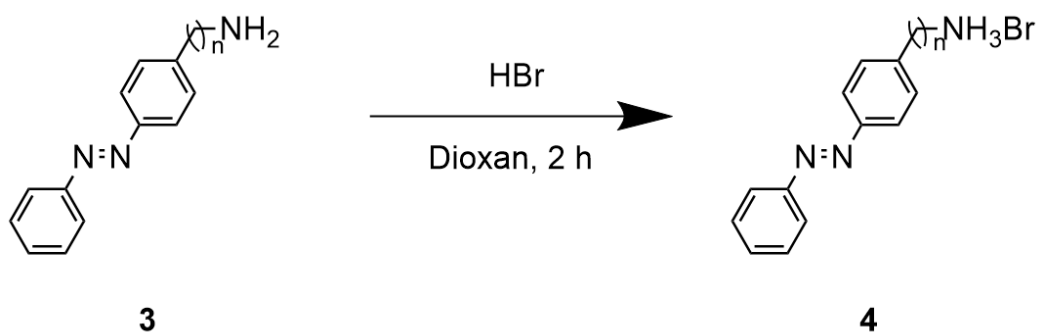
Step 3:



For the alkaline deprotection of compound **2** the orange solid was solved in DCM. Under stirring, piperidine was added dropwise. After 2 h at ambient temperature the solvent was removed. The product was purified chromatographically with EtOAc:PE (1:1) and NEt_3 (5.0 %). The product was characterized with $^1\text{H-NMR}$.

$^1\text{H-NMR}$ (400 MHz, DMSO) $n=1$: δ (ppm) = 7.90-7.82 (m, 4H), 7.63-7.51 (m, 5H), 3.82 (s, 2H, $\text{C-CH}_2\text{-NH}_3^+$); $n=2$: δ (ppm) = 8.04 (s, 3H, NH_3^+), 7.89-7.86 (m, 4H), 7.63-7.49 (m, 5H), 3.10 (m, 2H, $\text{CH}_2\text{-CH}_2\text{-NH}_3^+$), 3.01 (t, 2H, $\text{CH}_2\text{-CH}_2\text{-C}$)

Step 4:

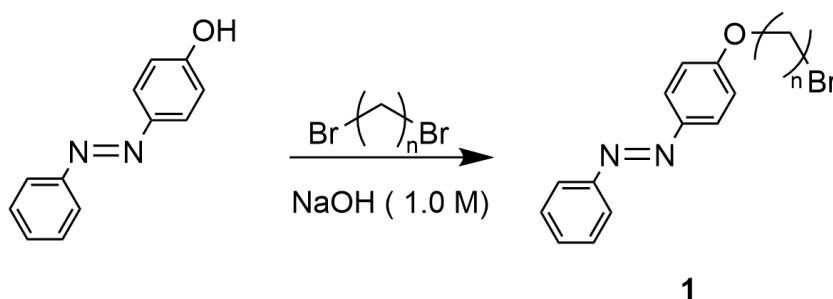


Compound **3** was then dissolved in 1,4-dioxane and treated with HBr (1.5 eq) to obtain the ammonium bromide salt. The solvent was removed in vacuum and an orange to brown solid is obtained. The salt is then solved in sufficient EtOH and reprecipitated with diethyl ether (Et₂O). The powder was filtrated, washed with Et₂O and dried in vacuum. All products were stored under inert gas and characterized with ¹H-NMR, ¹³C-NMR and ESI-MS (see **Figure A1+Figure A2**).

¹H-NMR (400 MHz, DMSO) *n=1*: δ (ppm) = 7.90-7.82 (m, 4H, CN=CH-CH), 7.63-7.51 (m, 5H), 3.82 (s, 2H, C-CH₂-NH₃⁺); *n=2*: δ (ppm) = 7.90-7.82 (m, 4H, CN=CH-CH), 7.63-7.51 (m, 5H), 3.82 (s, 2H, C-CH₂-NH₃⁺)

Synthesis of AzoC₄Br and AzoC₁₂Br

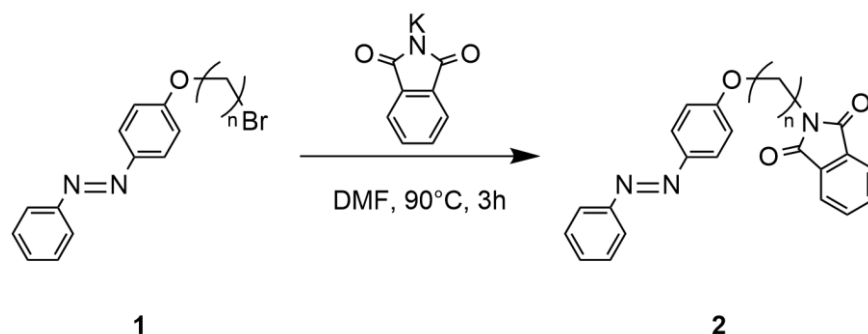
Step 1:



The azobenzene based ligands AzoC₄Br (*n*=4) and AzoC₁₂Br (*n*=12) were prepared according to the synthesis of Sasai *et al.*^[120] For the synthesis of compound **1**, 60 mmol of 1,4-dibromobutane (*n*=4) respectively 1,12-dibromododecane (*n*=12) and 30 mmol 4-phenylazophenol were solved in 30 mL of aqueous NaOH (1.0 M) and heated under reflux over night. After cooling a brown solid precipitated which is filtered, solved in DCM and washed with purified water for three times. The organic phase is dried over MgSO₄ and the solvent is removed. To remove excess dibromo alkane the solid was washed with *n*-hexane and dried under reduced pressure. Compound **1** was further characterized with ¹H-NMR.

¹H-NMR (400 MHz, DMSO) **n=4**: δ (ppm) = 7.90-7.83 (m, 4H, CN=CH-CH), 7.59-7.52 (m, 3H, CH-CH=CH), 7.13 (d, 2H, CH-CH=CO), 4.12 (t, 2H, O-CH₂-CH₂) 3.62 (t, 2H, CH₂-CH₂-Br), 1.99 (p, 2H, CH₂-CH₂-CH₂), 1.88 (p, 2H, CH₂-CH₂-CH₂); **n=12** (400 MHz, CDCl₃) δ (ppm) = 7.93-7.87 (m, 4H, CN=CH-CH), 7.52-7.41 (m, 3H, CH-CH=CH), 7.00 (d, 2H, CH-CH=CO), 4.04 (t, 2H, O-CH₂-CH₂), 3.41 (t, 2H, CH₂-CH₂-Br), 1.89-1.79 (m, 4H), 1.42 (m, 2H), 1.29 (s, 14H)

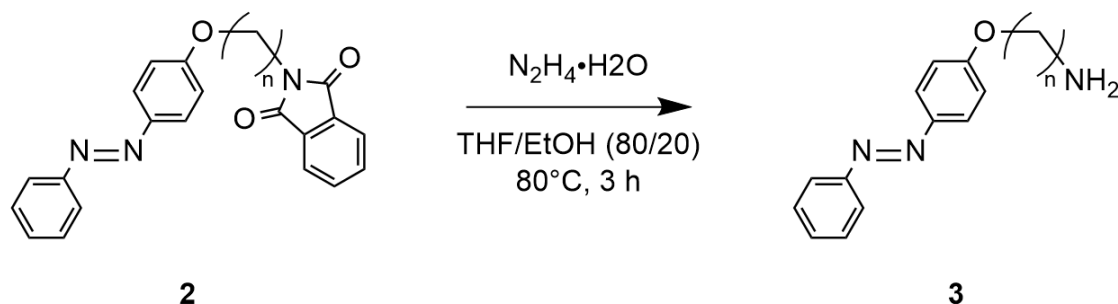
Step 2:



Compound **1** was then dissolved in dimethyl formamide (DMF) and potassium phthalimide (1.2 eq) was added. The solution was stirred and heated to 95 °C for 3 h. After cooling the solvent was removed and the obtained solid was solved in DCM, washed three times with purified water and dried over MgSO₄. An orange powder was obtained, which was further purified chromatographically from PE:EtOAc E (9:1) to pure EtOAc, but only for n=12. Compound **2** was then characterized with ¹H-NMR.

¹H-NMR (400 MHz, DMSO) **n=4**: δ (ppm) = 7.86-7.82 (8H, m), 7.58-7.49 (m, 3H, CH-CH=CH), 7.09 (d, 2H, CH-CH=CO), 4.10 (t, 2H, O-CH₂-CH₂), 3.65 (t, 2H, CH₂-CH₂-N), 1.81-1.76 (m, 4H, CH₂-CH₂-CH₂); **n=12**: (400 MHz, CDCl₃) δ (ppm) = 7.92-7.87 (m, 8H), 7.51-7.42 (m, 3H, CH-CH=CH), 7.00 (d, 2H, CH-CH=CO), 4.04 (t, 2H, O-CH₂-CH₂), 3.40 (t, 2H, CH₂-CH₂-N), 1.88-1.82 (m, 4H), 1.48 (m, 2H), 1.29 (s, 14H)

Step 3:

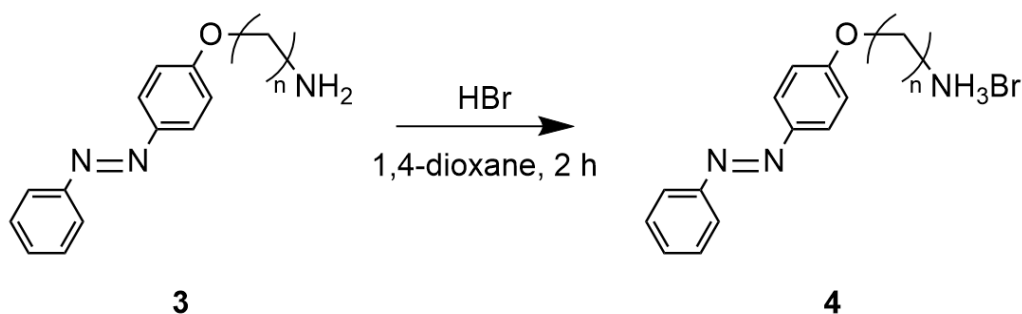


Compound **2** was dissolved in tetrahydro furan (THF)/EtOH (8:2) and hydrazine monohydrate (50.0 eq) was added dropwise. The reaction was stirred for 3 h at 80°. After

cooling, the solvent was removed and yielded an orange powder and excessive N_2H_4 . The product was then solved in DCM and washed with purified water three times. The DCM was dried over $MgSO_4$ and reduced. The product for $n=12$ was chromatographically purified in EtOAc/ NEt_3 (95:5). Compound **3** was characterized with 1H -NMR.

1H -NMR (400 MHz, $CDCl_3$) $n=4$: δ (ppm) = 7.93-7.87 (m, 4H, $CN=CH-CH$), 7.52-7.41 (m, 3H, $CH-CH=CH$), 7.00 (d, 2H, $CH-CH=CO$), 4.06 (t, 2H, $O-CH_2-CH_2$), 2.79 (t, 2H, $CH_2-CH_2-NH_2$), 1.87 (p, 2H, $CH_2-CH_2-CH_2$), 1.65 (p, 2H, $CH_2-CH_2-CH_2$); $n=12$: δ (ppm) = 7.91-7.86 (m, 4H, $CN=CH-CH$), 7.51-7.40 (m, 3H, $CH-CH=CH$), 7.00 (d, 2H, $CH-CH=CO$), 4.03 (t, 2H, $O-CH_2-CH_2$), 2.75 (t, 2H, $CH_2-CH_2-NH_2$), 1.81 (m, 2H), 1.57-1.43 (m, 4H), 1.28 (s, 14H)

Step 4:

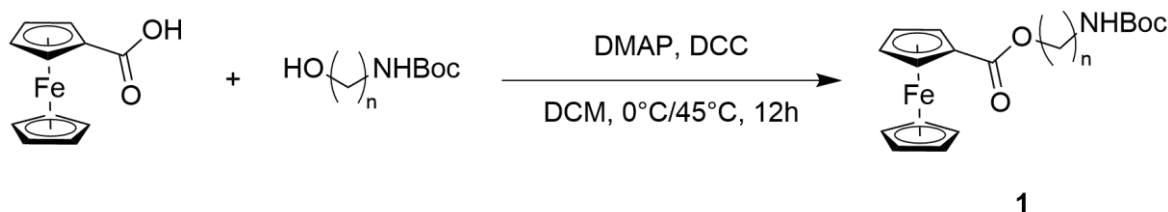


Compound **3** is then dissolved in in 1,4-dioxane and treated with HBr (1.5 eq) to obtain the ammonium bromide salt. The solvent was removed in vacuum and an orange to brown solid is obtained. The salt is then solved in sufficient EtOH and reprecipitated with diethyl ether (Et_2O). The powder was filtrated, washed with Et_2O and dried in vacuum. All products were stored under inert gas and characterized with 1H -NMR, ^{13}C -NMR and ESI-MS (see **Figure A3+Figure A4**).

1H -NMR (400 MHz, $DMSO-d_6$) $n=4$: δ (ppm) = 7.90-7.83 (m, 4H, $CN=CH-CH$), 7.59-7.50 (m, 3H, $CH-CH=CH$), 7.14 (d, 2H, $CH-CH=CO$), 4.21 (t, 2H, $O-CH_2-CH_2$), 2.89 (m, 2H, $CH_2-CH_2-NH_3^+$), 1.84-1.71 (m, 4H, $CH_2-CH_2-CH_2$); $n=12$: δ (ppm) = 7.89-7.83 (m, 4H, $CN=CH-CH$), 7.59-7.52 (m, 3H, $CH-CH=CH$), 7.12 (d, 2H, $CH-CH=CO$), 4.08 (t, 2H, $O-CH_2-CH_2$), 2.77 (m, 2H, $CH_2-CH_2-NH_3^+$), 1.75 (m, 2H), 1.52-1.43 (m, 4H), 1.25 (s, 14H)

Synthesis of FcC_nBr

Step 1:



All Fc based ligands FcC_nBr (with n=2,3,4,5,6) were synthesized with the same synthesis strategy. 0.5 g (2.2 mmol) ferrocene carboxylic acid is dissolved in 50 mL DCM and treated with ultrasound. With stirring, 2.2 mmol N-Boc alkylamine, 2.6 mmol dimethylamino pyridine (DMAP) and 2.6 mmol 1-ethyl-3(3'-dimethylaminopropyl)carbodiimide hydrochloride (EDC·HCl) were added to the mixture. After addition of all reactants, any remaining solids should have dissolved. The mixture is then heated under reflux at 50 °C for 12 h over night. The solvent is removed in vacuum and a brown solid was filtered with EtOAc over ~4 cm of silica gel to give a yellow solution. The solvent was removed giving a yellow to orange solid. The product is then characterized with ¹H-NMR.

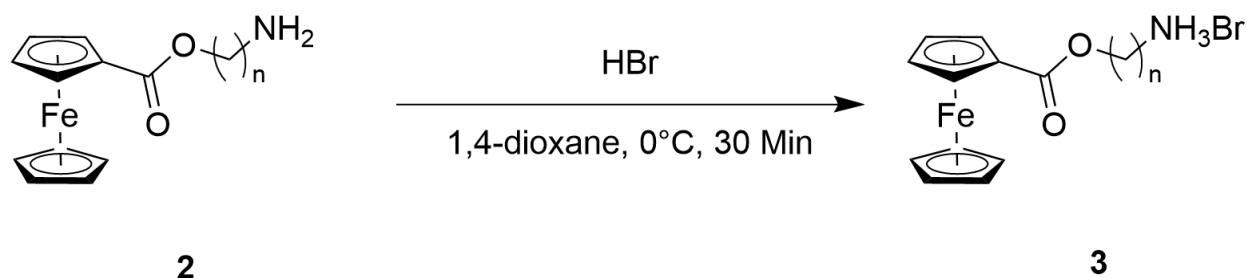
¹H-NMR: (400 MHz, CDCl₃) **n=2:** δ (ppm) = 4.81 (s, 2H, CH), 4.41 (s, 2H, CH), 4.29 (t, 2H, CH₂), 4.23 (s, 5H, CH), 3.48 (s, 2H, CH₂), 1.45 (s, 9H, CH₃); **n=3:** δ (ppm) = 4.89 (s, 2H, CH), 4.47 (s, 2H, CH), 4.31 (s, 5H, CH), 4.26 (s, 2H, CH₂), 3.29 (s, 2H, CH₂), 1.90 (s, 2H, CH₂), 1.46 (s, 9H, CH₃); **n=4:** δ (ppm) = 4.85 (s, 2H, CH), 4.44 (s, 2H, CH), 4.26 (s, 5H, CH), 4.20 (m, 2H, CH₂), 3.20 (s, 2H, CH₂), 1.74 (s, 2H, CH₂), 1.62 (s, 2H, CH₂), 1.44 (s, 9H, CH₃); **n=5:** δ (ppm) = 4.87 (s, 2H, CH), 4.45 (s, 2H, CH), 4.28 (s, 5H, CH), 4.18 (m, 2H, CH₂), 3.17 (s, 2H, CH₂), 1.73 (s, 2H, CH₂), 1.56 (m, 2H, CH₂), 1.44 (s, 9H, CH₃); **n=6:** δ (ppm) = 4.81 (s, 2H, CH), 4.39 (s, 2H, CH), 4.20 (m, 7H), 3.13 (s, 2H, CH₂), 1.72 (s, 2H, CH₂), 1.44 (m, 15H)

Step 2:



To remove the Boc protecting group, compound **1** was then dissolved in DCM and deprotected with 30.0 eq trifluoroacetic acid (TFA) for 30 min (up to 1 h) at 50 °C under reflux. Thin-layer chromatography is used to determine the end of the reaction, which is quantitative for all compounds. After deprotection, compound **2** was immediately used for step 3 without further purification or characterization.

Step 3:



Compound **2** was further solved in 1,4-dioxane and treated with HBr (1.5 eq) to obtain the ammonium salt. The solvent was removed, the obtained brown solid was solved in sufficient EtOH and reprecipitated with diethyl ether (Et₂O). The powder was filtrated, washed with Et₂O and dried under reduced pressure. All products were characterized with ¹H-NMR and ¹³C-NMR (see **Figure A22+Figure A23**).

¹H-NMR (400 MHz, DMSO-d₆) ***n*=2**: δ (ppm) = 7.95 (s, 3H, NH₃), 4.87 (t, 2H, CH), 4.50 (t, 2H, CH), 4.29 (t, 2H, CH₂), 4.23 (s, 5H, cp-ring) 3.16 (t, 2H, CH₂); ***n*=3**: δ (ppm) = 7.90 (s, 3H, NH₃), 4.97 (s, 2H), 4.45-4.29 (m, 9H), 3.47 (s, 2H, CH₂), 2.54 (s, 2H, CH₂); ***n*=4**: δ (ppm) = 4.73 (t, 2H, CH), 4.48 (t, 2H, CH), 4.22 (s, 5H, cp-ring), 4.16 (t, 2H, CH₂), 2.85 (s, 2H, CH₂), 1.69 (m, 4H, CH₂); ***n*=5**: δ (ppm) = 7.59 (s, 3H, NH₃), 4.89 (s, 2H, CH), 4.47 (s, 2H, CH), 4.31 (s, 7H), 3.43 (s, 2H, CH₂), 2.36 (s, 2H, CH₂), 1.99 (m, 4H, CH₂) ***n*=6**: δ (ppm) = 4.72 (t, 2H, CH), 4.47 (t, 2H, CH), 4.20 (s, 5H, cp-ring), 4.14 (t, 2H, CH₂), 2.78 (s, 2H, CH₂), 1.64 (p, 2H, CH₂), 1.55 (m, 2H, CH₂), 1.39 (m, 6H, CH₂)

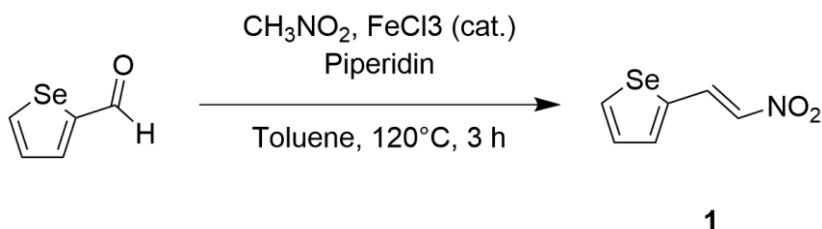
¹³C-NMR (400 MHz, DMSO-d₆) ***n*=2** δ (ppm) = 170.14 (O=C-O), 71.09 (2C, CH-cp), 69.68 (CH₂) 69.66 (2C, CH-cp) 69.27 (5C, CH-cp), 65.93 (CH₂); ***n*=3** δ (ppm) = 171.05, 71.91, 71.05, 70.22, 70.05 ***n*=4** δ (ppm) = 170.08 (O=C-O), 70.85 (2C, CH-cp), 70.27 (1C, CH-cp) 69.19 (2C, CH-cp), 69.07 (5C, CH-cp), 62.61 (CH₂), 38.04 (CH₂), 24.93 (CH₂), 23.35 (CH₂); ***n*=5** δ (ppm) = 170.04, 70.78, 70.40, 68.97, 27.65, 24.45 ***n*=6** δ (ppm) = 170.04 (O=C-O), 70.78 (2C, CH-cp), 70.40 (1C, CH-cp) 69.14 (2C, CH-cp), 68.97 (5C, CH-cp), 62.63 (CH₂), 39.73 (CH₂), 27.65 (CH₂), 24.44 (CH₂)

ESI-MS of ***n*=2** Expected 275.05 Observed 275.13; ***n*=4** Expected 302.08 Observed 302.20; ***n*=6** Expected 331.12 Observed 331.16

Synthesis of X-EABr

The starting materials 2-thiophenethylamine and 2-furanethylamine were obtained commercially and reacted as shown in the last step. Selenophene was prepared starting from 2-selenophenecarboxaldehyde.

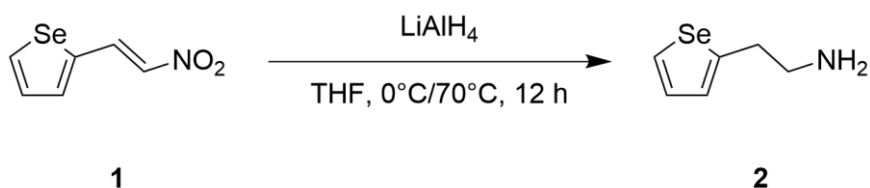
Step 1:



1 g (6.3 mmol) 2-selenophenecarboxaldehyde was shipped from the supplier with a stabilizer (hydroquinone, HQ), which is why it was filtered with 300 mL EtOAc over ~4 cm of silica gel to give a colorless solution. The solvent was then removed and the resulting liquid was dissolved in 10 mL toluene. 2 mL (37.8 mmol) nitromethane, 0.1 mL (6.3 mmol) piperidine and 0.1 g (6.3 mmol) FeCl_3 are added to the mixture. The reaction is then stirred and heated to 120°C for 3 h under reflux. The end of the reaction is determined by thin layer chromatography. The solvent is removed and the product was chromatographically purified in DCM/PE (1:1). After removing the solvent, a yellow liquid was obtained. Compound **1** was characterized with $^1\text{H-NMR}$. *Yield: 62.8 %*

$^1\text{H-NMR}$: (400 MHz, CDCl_3) δ (ppm) = 7.86 (d, 1H, $\text{CH}=\text{CH}-\text{NO}_2$), 7.79 (d, 1H, $\text{C}-\text{CH}=\text{CH}$), 7.70 (d, 1H, $\text{Se}-\text{CH}=\text{CH}$), 7.14 (d, 1H, $\text{HC}-\text{CH}=\text{C}$) 7.12 (q, 1H, $\text{CH}=\text{CH}-\text{CH}$)

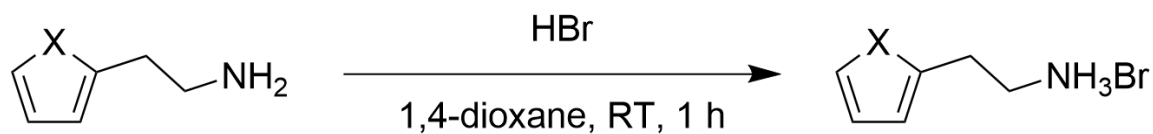
Step 2:



Compound **1** (4.0 mmol) was dissolved 20 mL dry tetrahydro furan (THF) in a 100 mL flask and cooled to 0°C for 10 min. 15.8 mL (16.0 mmol) LiAlH_4 (1.0 M in Et_2O) was dissolved in 60 mL dry THF in a separate flask. The mixture is then slowly dropped to compound **1**. After addition, the reaction is heated to 70°C under reflux for 4 h and stirred over night for another 8 h. The solvent is removed and the product is chromatographically purified with EtOAc/ NEt_3 (95:5). After removing the solvent, a brownish liquid is obtained. Compound **2** was characterized with $^1\text{H-NMR}$. *Yield: 30.5 %*

$^1\text{H-NMR}$: (400 MHz, CDCl_3) δ (ppm) = 7.70 (d, 1H, CH), 7.12 (d, 1H, CH), 6.90 (s, 1H, CH), 2.69 (t, 2H, CH_2), 2.22 (t, 2H, CH_2)

Step 3:



The corresponding amine is dissolved in 1,4-dioxane and cooled to 0 °C. Then, 1.5 eq HBr (47 wt% in H₂O) was dropped slowly to the reaction under stirring. The reaction was stirred for 1 h and allowed to warm up to RT. The solvent was removed to obtain the ammonium salt.

Since Se-EABr showed a low stability, the salt was directly dissolved in DMF to give a 0.2 M solution. The solution was kept under inert gas.

6.2 Particle synthesis

6.2.1 Particles with AzoC_nBr

Synthesis of 2D AzoC_nBr perovskite phases

For the synthesis of 2D perovskite phases with azobenzene-based ligands, a 0.1 M stock solution of PbBr₂ was prepared in DMF. Then, 2.0 eq of the appropriate AzoC_nBr ligand was added to the solution. Under vigorous stirring 0.2 mL of the precursor solution was added quickly into 30 mL antisolvent (DCM for n=2 and acetone for n=4, 12). The suspension was stirred for 1 h, then the precipitation was centrifuged, transferred to a small 3 mL vial and washed three times with the antisolvent. The sample was then dried under reduced pressure and kept under inert gas atmosphere to prevent decomposition.

Synthesis of 2D-AzoC₂ with irradiation

For the synthesis of 2D-AzoC₂ with irradiation, the precursor was prepared as described above and filled into a cuvette. The precursor was then irradiated under stirring for a defined time period. The particle synthesis is performed as described above.

Synthesis of functionalized 3D-AzoC_n perovskite phases

For the synthesis of functionalized 3D perovskite phases, a 0.1 M stock solution of PbBr₂ in triethylene glycol (TEG) was prepared. For the preparation of the precursor MABr (1.3 eq) and the appropriate AzoC_nBr ligand (0.1 eq) were dissolved. Under vigorous stirring 0.2 mL of the precursor solution was added quickly into 30 mL DCM. The suspension was stirred for 1 h, then the precipitation was centrifuged, transferred to a small 3 mL vial and washed three times with the antisolvent. The sample was then dried under reduced pressure and kept under inert gas atmosphere to prevent decomposition.

Synthesis of RPP with AzoC₂Br ligand

For the preparation of RPPs with AzoC₂Br, different precursor solutions in TEG were prepared with 0.1 M regarding PbBr₂, see **Table 13**. The particle synthesis then followed the same synthesis protocol as for the 2D-phases with AzoC_nBr.

For the preparation at different temperatures, the antisolvent was cooled using a thermostat.

Table 13 - Precursor concentrations used for the synthesis of RPPs with AzoC₂Br.

	MABr		PbBr₂		AzoC₂Br		V(TEG)
	m/[mg]	n/[μmol]	m/[mg]	n/[μmol]	m/[mg]	n/[μmol]	V/[mL]
RPP_{0.3}	17.5	156	44.0	120	11.0	36	1.2
RPP_{0.5}	17.5	156	44.0	120	18.4	60	1.2
RPP_{0.7}	17.5	156	44.0	120	25.7	84	1.2

6.2.2 Particles with FcC_nBr

Synthesis of (FcC₂)PbBr₃ phase

For the material synthesis of (FcC₂)PbBr₃ a precursor solution with a concentration of 0.1 M in DMF was produced. 1 eq of PbBr₂ and 1 eq of FcC₂Br were dissolved in dried DMF. Under vigorous stirring 0.2 mL of the precursor solution was added quickly into 30 mL DCM. The suspension was stirred for 1 h, then the precipitation was centrifuged, washed three times with 3 mL DCM and dried under reduced pressure. The samples were kept under nitrogen atmosphere to prevent decomposition.

Synthesis of (FcC₃)₄Pb₃Br₁₀ and (FcC₄)₄Pb₃Br₁₀ phase

For the material synthesis of (FcC₃)₄Pb₃Br₁₀ and (FcC₄)₄Pb₃Br₁₀ a precursor solution with a concentration of 0.1 M in DMF was produced. Therefore, 3.0 eq of PbBr₂ and 4.0 eq of FcC₃Br or FcC₄Br, respectively were dissolved in dried DMF. Under vigorous stirring 0.2 mL of the precursor solution was added quickly into 30 mL DCM. The suspension was stirred for 1 h, then the precipitation was centrifuged, washed three times with 3 mL DCM and dried under reduced pressure. The sample was kept under inert gas atmosphere to prevent decomposition.

Synthesis of (FcC₅)₂PbBr₄ and (FcC₆)₂PbBr₄ phases

For the material synthesis of (FcC₆)₂PbBr₄ a precursor solution with a concentration of 0.1 M in DMF was produced. Therefore, 1.0 eq of PbBr₂ and 2.0 eq of FcC₆Br were dissolved in dried DMF. Under vigorous stirring 0.2 mL of the precursor solution was

added quickly into 30 mL toluene or Et₂O. The suspension was stirred for 1 h, then the precipitation was centrifuged, washed three times with 3 mL DCM and dried under reduced pressure. The sample was kept under nitrogen atmosphere to prevent decomposition.

Synthesis of RPPs with FcC₆Br

For the synthesis of RPPs with FcC₆Br, three different precursors in DMF were prepared, see **Table 14**. For the particle synthesis 0.2 mL of the appropriate precursor was then added to 30 mL toluene under vigorous stirring. The suspension was stirred for 1 h, then the precipitation was centrifuged, transferred to a 3 mL vial and washed three times with 3 mL DCM. The particles were dried under reduced pressure and stored under inert gas atmosphere to prevent decomposition.

Table 14 - Precursor concentrations used for the synthesis of RPPs with AzoC₂Br.

	MABr		PbBr₂		FcC₆Br		V(DMF)
	m/[mg]	n/[μmol]	m/[mg]	n/[μmol]	m/[mg]	n/[μmol]	V/[mL]
RPP _{0.5}	1.4	12.5	18.4	50	20.5	50	2.0
RPP _{1.0}	11.2	100	73.4	200	54.7	200	0.5
RPP _{2.0}	14.9	133	73.4	200	82.0	133	2.0

Synthesis of surface functionalized FcC₆@MAPbBr₃

For the synthesis of functionalized FcC₆@MAPbBr₃, a 0.1 M stock solution of PbBr₂ in DMF was prepared. For the preparation of the precursor MABr (1.3 eq) and the FcC₆Br ligand (0.1 eq) were dissolved. Under vigorous stirring 0.2 mL of the precursor solution was added quickly into 30 mL toluene. The suspension was stirred for 1 h, then the precipitation was centrifuged, transferred to a small 3 mL vial and washed three times with the antisolvent. The sample was then dried under reduced pressure and kept under inert gas atmosphere to prevent decomposition.

6.2.3 Particles with X-EABr

Synthesis of 2D-X-EABr perovskite phases

For the synthesis of 2D-X-EABr, a 0.1 M precursor solution in DMF was prepared by solving 1.0 eq PbBr₂ and 2.0 eq X-EABr. Under vigorous stirring 0.2 mL of the precursor solution was added to 30 mL antisolvent (DCM, toluene or CHCl₃, for detailed description see Bachelor thesis Katja Meyer). After 1 h of stirring, the precipitation was centrifuged, transferred to a 3 mL vial and washed three times with 3 mL DCM. The sample was dried under reduced pressure and kept under inert gas to prevent decomposition.

For the mixed halide perovskite phases with bromide and iodide, precursor solutions with mixed halide salts were prepared, shown in **Table 15**.

Table 15 - Precursor concentrations used for the synthesis of mixed halide 2D-S-EAX phases.

	PbBr₂		PbI₂		S-EABr		S-EAI	
	m/[mg]	n/[mmol]	m/[g]	n/[mmol]	m/[g]	n/[mmol]	m/[g]	n/[mmol]
(S-EA)₂PbBr₄	36.7	1.0			41.6	2.0		
(S-EA)₂PbBr₃I	36.7	1.0			20.8	1.0	25.4	1.0
(S-EA)₂PbBr₂I₂	36.7	1.0					50.8	2.0
(S-EA)₂PbBrI₃			46.1	1.0	20.8	1.0	25.4	1.0
(S-EA)₂PbI₄			46.1	1.0			50.8	2.0

Synthesis of RPP with S-EABr

For the first approach, a 0.1 M stock solution of PbBr₂ in DMF was prepared. Then, 1.0 eq of S-EABr and 0.5 eq of MABr were added to the solution. 0.2 mL of the precursor was then added quickly to DCM, which was stirred vigorously. The suspension was stirred for 1 h, then the precipitation was centrifuged, transferred to a 3 mL vial and washed three times with 3 mL DCM. The particles were then dried under reduced pressure and stored under inert gas to prevent decomposition.

For the second approach, a 0.1 M stock solution of PbBr₂ in DMF was prepared. Then 2.0 eq S-EABr were added to the solution. Another precursor solution with 0.05 M was prepared, by adding MABr. For the particle synthesis, first 0.2 mL of the PbBr₂-containing precursor solution was added to vigorously stirred 30 mL DCM. After 30 sec, 0.2 mL of the MABr-containing solution was added. The particles were then stirred for 5 min and then centrifuged. The precipitation was transferred to a 3 mL vial, washed three times with DCM and then dried under reduced pressure. They were kept under inert gas to prevent decomposition.

6.3 Methodology and analytical techniques

Results presented in **chapter 4.1** were exclusively produced at the University of Konstanz and results presented in **chapter 4.2** and **4.3** were exclusively produced at the Wilhelm Leibniz University of Hannover (the instrument in Konstanz was used for PESA measurements for all chapters). Therefore, the analytical instruments are listed according to their location.

University of Konstanz:

- PXRD measurements were recorded with a Bruker AXS D8 Advance Powder X-ray diffractometer with Bragg-Brentanon setup and $\text{CuK}\alpha$ source ($\lambda = 1.54059 \text{ \AA}$), equipped with a Lynxeye detector
- SAXS measurements were recorded with a Bruker Nanostar
- SEM measurements were taken with a Zeiss Crossbeam 1540XB and a Zeiss Auriga Crossbeam electron microscope
- UV/Vis kinetic measurements were recorded with a Varian Cary 50 equipped with a submersible probe for light-guiding with 1 mm slit
- UV/Vis measurements of solid samples were collected with an Agilent Cary 5000 with integration sphere for reflectance measurements
- UV/Vis measurements of liquid (solution and dispersion) samples were obtained with a Varian Cary 100
- PL measurements (stationary and time-dependent) were recorded with a FluoTime 300 from PicoQuant equipped with an Xe-lamp and a 405 nm Laser
- IR spectra were recorded using a PerkinElmer Spectrum 100 equipped with an attenuated total reflection (ATR) unit
- ^1H - and ^{13}C -NMR were recorded with a Bruker Avance III 400 and a Bruker Avance III 600
- TAS measurements were recorded with a self-build setup from the AG Schmidt-Mende
- PESA measurements were acquired with a Riken Keiki AC-2

Wilhelm Leibniz University of Hannover:

- PXRD measurements were obtained using an X-ray diffractometer StadiP from Stoe with Debye-Scherrer setup and $\text{CuK}\alpha$ radiation ($\lambda = 1.54059 \text{ \AA}$), equipped with a Mythen 1K detector (Dectris) with angular range of 12.5° .
- PXRD measurements of dropcasted particles were obtained using a ThetaTheta from Stoe with Bragg-Brentano setup and $\text{CuK}\alpha$ radiation ($\lambda = 1.54059 \text{ \AA}$)

- SEM images were taken with a Jeol JSM-6700F, equipped with an Oxford INCA 300 EDX detector
- UV/Vis measurements of solid samples were collected with an Agilent Cary 5000 with integration sphere for reflectance measurements and an Agilent Cary 4000 with Praying Mantis setup
- UV/Vis measurements of liquid (solution and dispersion) samples were obtained with a Varian Cary 4000
- XPS measurements were obtained with a Versaprobe III from Physical Electronics GmbH
- PL measurements were obtained with a Cary Eclipse from Agilent
- CV measurements were obtained with a potentiostat Autolab, PGSTAT101 from Metrohm
- IR spectra were recorded with a Bruker Tensor 27
- ^1H - and ^{13}C -NMR spectra were collected with a Bruker Ascend 400 MHz

UV/Vis measurements

For the investigation of optical absorption, different methodologies were used.

UV/Vis spectroscopy from liquid samples

Absorption of liquid samples (solution and dispersion) was measured in a region from 250 nm to 800 nm. Solutions were diluted to a concentration of about 10^{-5} M for optimal measurement conditions. Solid samples were dispersed in toluene by ultra-sonification for 1 to 10 minutes (depending on the sample). Baseline measurements were collected before every measurement session. All samples were measured in a Quartz cuvette.

UV/Vis spectroscopy for recording reaction kinetics

By using an external probe which is immersed into the reaction medium, absorption during a particle synthesis can be recorded. The absorbance of the solution is measured within a slit with 1 mm width. Spectra from 200 nm to 900 nm can be recorded at a defined speed and time period.

UV/Vis spectroscopy from solid samples

For the measurement, particles were dispersed in toluene using ultra-sonification and applied to a glass substrate which was heated to 40 °C with a heat-plate via drop-coating. For high-quality measurements, the film should be optically dense. The plates with sample were stored in a glovebox under inert gas atmosphere to prevent decomposition.

For the measurement in the integration sphere, the substrates were mounted on an opening of the integration sphere (direct irradiation of the light-beam). For the measurement in the Praying Mantis, the substrate was placed in the middle of the setup, aligned between two mirrors. Spectra were recorded in reflectance mode (R%).

Band gaps were determined using the Kubelka-Munk analysis. Therefore, reflectance spectra were adapted and linear regression lines from the baseline and the slope were fitted using OriginPro.

Photoluminescence

Sample preparation of liquid and solid samples occurred identically as for UV/Vis measurements. PL spectra of liquid samples were collected in a Quartz cuvette with four transparent sides. With the FluoTime 300, additional filters were used to filter excitation wavelengths and scattering.

Photoelectron spectroscopy on air

For PESA measurements, particle preparation followed the same procedure as UV/Vis reflectance spectroscopy.

Powder X-Ray Diffractogram

For the measurement of PXRD pattern in a Bragg-Brentano setup, particles were dispersed in toluene and applied to a silicon substrate at 40 °C on a heat-plate. The silicon substrates were previously purified with soap-water, acetone and ethanol. They were stored in ethanol and dried with compressed air before use.

For the measurement of PXRD pattern in a Debye-Scherrer setup, particles were applied in a sample holder between two foils which show no scattering. In order to avoid obtaining a preferred direction, the sample holder was rotated during measurement.

SEM measurements

For the investigation of samples in SEM, particles were applied to a silicon substrate, similar as for samples measured in the PXRD with Bragg-Brentano setup. However, dispersions are diluted to reduce the load of particles on the substrate.

¹H-NMR

¹H-NMR spectroscopy of precursor solution was recorded using a capillary with deuterated benzene as reference. For ¹H-NMR measurement of irradiated particles, the particles were first centrifuged, separated from the initial dispersion medium and then dissolved in MeOD. Residual PbBr₂ was centrifuged to record distinct spectra.

Irradiation experiments

For irradiation experiments, the liquid sample (solution and dispersion) was put into a self-build setup, equipped with a water-cooled sample holder, a water-cooled mercury lamp and an optical filter at 313 nm. A shutter guaranteed the time of irradiation. The sample was measured in a Quartz cuvette and stirred for the time of irradiation.

Chemical Oxidation of (FcC₂)PbBr₃

For the chemical oxidation of the (FcC₂)PbBr₃ particles, iron (III) perchlorate (Fe(ClO₄)₃) was dried for 24 h at 60 °C under reduced pressure. A stock solution of Fe(ClO₄)₃ in CHCl₃ (10⁻³ M) was prepared. 1 mg of (FcC₂)PbBr₃ (1.4 μmol) were dispersed in 3 mL diluted solution of Fe(ClO₄)₃ with varying equivalents (0.1 eq, 0.2 eq, 0.5 eq, 1.0 eq and 2.0 eq) of oxidant and treated with ultrasound for 10 minutes. The particles were centrifuged, washed three times with 3 mL CHCl₃ and dried under reduced pressure. The samples were kept under nitrogen atmosphere to prevent decomposition.

Cyclic voltammetry measurements

For CV measurements, 1.44 g Lithiumbis(trifluoromethylsulfonyl)amid LiTFSI (5 mmol; salt was stored in a glovebox) were solved in 48.5 mL HFE and 1.5 mL diethyl carbonate (DEC). To remove dissolved oxygen, the solution was flushed with nitrogen for 10 minutes. ITO substrates were ultrasonically cleaned in a soap solution, ethanol and then acetone, 20 minutes each. The substrates were dried under a N₂-stream. The coated ITO substrate was prepared by drop-casting a concentrated dispersion of the particles in toluene onto an area of about 1 cm x 1 cm. The solvent was evaporated on a heat-plate at 40 °C. The counter electrode, a Pt-plate, was cleaned in H₂SO₄/H₂O₂, washed with deionized water, ethanol and acetone. Before use, the Pt-plate was dried under a N₂-stream. For the measurement, all electrodes were contacted with alligator clips and the electrodes were immersed in 30 mL of the electrolyte in a beaker. An Ag/AgCl electrode was used as reference electrode. For oxidation experiments (30 minutes at 0.65 V) the electrolyte was slightly stirred.

Purification of 2D-Se-EABr

For the separation of 2D-Se-EABr particles from the amorphous impurities, electrodeposition was used. Therefore, two cleaned ITO substrates were aligned parallel into the particle dispersion (typically toluene), directly after precipitation of the precursor. Then, a voltage of 136 V was applied for 2 h. PXRD and SEM of the particles was measured directly on the substrate.

The same approach was used to obtain an increased layer order of (FcC₆)₂PbBr₄.

7 Literature

- [1] J. Daly, <https://www.ibm.com/blogs/industries/global-semiconductor-shortage-solutions/>, **2021**.
- [2] J. Fallows, “The 50 Greatest Breakthroughs Since the Wheel,” can be found under <https://www.theatlantic.com/magazine/archive/2013/11/innovations-list/309536/>, **2013**.
- [3] “Enabling the Hyperconnected Age: The role of semiconductors,” can be found under <https://www.oxfordeconomics.com/recent-releases/enabling-the-hyperconnected-age-the-role-of-semiconductors>, **2014**.
- [4] “A Connected and Smart Future - The Internet of Things - Taiwan Semiconductor Manufacturing Company Limited,” can be found under https://www.tsmc.com/english/dedicatedFoundry/technology/platform_loT_connectedFuture, **2021**.
- [5] “Global silicon prices hit record highs amid Chinese shortage | Metal Bulletin.com,” can be found under <https://www.metalbulletin.com/Article/4009219/Global-silicon-prices-hit-record-highs-amid-Chinese-shortage.html>, **2021**.
- [6] A. Kojima, K. Teshima, Y. Shirai, T. Miyasaka, *J. Am. Chem. Soc.*, **2009**, *131*, 2.
- [7] Z. K. Tan, R. S. Moghaddam, M. L. Lai, P. Docampo, R. Higler, F. Deschler, M. Price, A. Sadhanala, L. M. Pazos, D. Credgington, F. Hanusch, T. Bein, H. J. Snaith, R. H. Friend, *Nat. Nanotechnol.* **2014**, *9*, 687–692.
- [8] G. S. Kumar, R. R. Sumukam, R. K. Rajaboina, R. N. Savu, M. Srinivas, M. Banavoth, *ACS Appl. Energy Mater.*, **2022**.
- [9] A. Dey, J. Ye, A. De, E. Debroye, S. K. Ha, E. Bladt, A. S. Kshirsagar, Z. Wang, J. Yin, Y. Wang, L. N. Quan, F. Yan, M. Gao, X. Li, J. Shamsi, T. Debnath, M. Cao, M. A. Scheel, S. Kumar, J. A. Steele, M. Gerhard, L. Chouhan, K. Xu, X. Wu, Y. Li, Y. Zhang, A. Dutta, C. Han, I. Vincon, A. L. Rogach, A. Nag, A. Samanta, B. A. Korgel, C.-J. Shih, D. R. Gamelin, D. H. Son, H. Zeng, H. Zhong, H. Sun, H. V. Demir, I. G. Scheblykin, I. Mora-Seró, J. K. Stolarczyk, J. Z. Zhang, J. Feldmann, J. Hofkens, J. M. Luther, J. Pérez-Prieto, L. Li, L. Manna, M. I. Bodnarchuk, M. V. Kovalenko, M. B. J. Roelofs, N. Pradhan, O. F. Mohammed, O. M. Bakr, P. Yang, P. Müller-Buschbaum, P. V. Kamat, Q. Bao, Q. Zhang, R. Krahne, R. E. Galian, S. D. Stranks, S. Bals, V. Biju, W. A. Tisdale, Y. Yan, R. L. Z. Hoyer, L. Polavarapu, *ACS Nano* **2021**, *15*, 10775–10981.
- [10] J. V. Milić, *J. Mater. Chem. C*, **2021**, *9* (35), 11428–11443.
- [11] D. B. Mitzi, *Prog. Inorg. Chem.* **1999**, 1–121.
- [12] D. B. Mitzi, *Dalton Trans.* **2001**, 1–12.
- [13] V. M. Goldschmidt, *Naturwissenschaften* **1926**, *14*, 477–485.
- [14] B. Saparov, D. B. Mitzi, *Chem. Rev.* **2016**, *116* (7), 4558–4596.
- [15] G. Kieslich, S. Sun, A. K. Cheetham, *Chem. Sci.* **2015**, *6*, 3430–3433.

- [16] J. Berry, T. Buonassisi, D. A. Egger, G. Hodes, L. Kronik, Y. L. Loo, I. Lubomirsky, S. R. Marder, Y. Mastai, J. S. Miller, D. B. Mitzi, Y. Paz, A. M. Rappe, I. Riess, B. Rybtchinski, O. Stafsudd, V. Stevanovic, M. F. Toney, D. Zitoun, A. Kahn, D. Ginley, D. Cahen, *Adv. Mater.*, **2015**, *27*, 5102–5112.
- [17] H. L. Wells, *Z. anorg. allg. Chem.*, **1893**, *3*, 195–210.
- [18] D. Weber, *Z. Naturforsch.*, **1978**, *33b*, 3.
- [19] D. Weber, *Z. Naturforsch. B: J. Chem. Sci.*, **1979**, *34*, 939–941.
- [20] C. C. Stoumpos, C. D. Malliakas, M. G. Kanatzidis, *Inorg. Chem.*, **2013**, *52*, 9019–9038.
- [21] G. A. Elbaz, D. B. Straus, O. E. Semonin, T. D. Hull, D. W. Paley, P. Kim, J. S. Owen, C. R. Kagan, X. Roy, *Nano Lett.*, **2017**, *17*, 1727–1732.
- [22] S. Govinda, B. P. Kore, D. Swain, A. Hossain, C. De, T. N. Guru Row, D. Sarma, *J. Phys. Chem. C*, **2018**, *122*, 13758–13766.
- [23] T. M. Brenner, D. A. Egger, L. Kronik, G. Hodes, D. Cahen, *Nat. Rev. Mater.*, **2016**, *1*, 1–16.
- [24] L. Protesescu, S. Yakunin, M. I. Bodnarchuk, F. Krieg, R. Caputo, C. H. Hendon, R. X. Yang, A. Walsh, M. V. Kovalenko, *Nano Lett.*, **2015**, *15*, 3692–6.
- [25] J. H. Noh, S. H. Im, J. H. Heo, T. N. Mandal, S. I. Seok, *Nano Lett.*, **2013**, *13*, 1764–1769.
- [26] A. Sadhanala, F. Deschler, T. H. Thomas, S. E. Dutton, K. C. Goedel, F. C. Hanusch, M. L. Lai, U. Steiner, T. Bein, P. Docampo, D. Cahen, R. H. Friend, *J. Phys. Chem. Lett.*, **2014**, *5*, 2501–2505.
- [27] N. K. Kumawat, A. Dey, A. Kumar, S. P. Gopinathan, K. Narasimhan, D. Kabra, *ACS Appl. Mater. Interfaces*, **2015**, *7*, 13119–13124.
- [28] D. M. Jang, K. Park, D. H. Kim, J. Park, F. Shojaei, H. S. Kang, J. P. Ahn, J. W. Lee, J. K. Song, *Nano Lett.*, **2015**, *15*, 5191–5199.
- [29] K. T. Butler, J. M. Frost, A. Walsh, *Mater. Horiz.*, **2015**, *2*, 228–231.
- [30] J. Even, L. Pedesseau, C. Katan, *ChemPhysChem*, **2014**, *15*, 3733–41.
- [31] M. R. Filip, G. E. Eperon, H. J. Snaith, F. Giustino, *Nat. Commun.* **2014**, *5*, 5757.
- [32] A. Amat, E. Mosconi, E. Ronca, C. Quarti, P. Umari, Md. K. Nazeeruddin, M. Grätzel, F. De Angelis, *Nano Lett.* **2014**, *14*, 3608–3616.
- [33] M. C. Gélvez-Rueda, D. H. Cao, S. Patwardhan, N. Renaud, C. C. Stoumpos, G. C. Schatz, J. T. Hupp, O. K. Farha, T. J. Savenije, M. G. Kanatzidis, F. C. Grozema, *J. Phys. Chem. C* **2016**, *120*, 16577–16585.
- [34] C. Motta, F. El-Mellouhi, S. Kais, N. Tabet, F. Alharbi, S. Sanvito, *Nat. Comm.*, **2015**, *6*, 1–7.
- [35] Y. Zhou, L. You, S. Wang, Z. Ku, H. Fan, D. Schmidt, A. Rusydi, L. Chang, L. Wang, P. Ren, *Nat. Comm.*, **2016**, *7*, 1–8.
- [36] D. A. Egger, A. M. Rappe, L. Kronik, *Acc. Chem. Res.*, **2016**, *49*, 573–581.

- [37] O. Knop, R. E. Wasylishen, M. A. White, T. S. Cameron, M. J. V. Oort, *Can. J. Chem.* **1990**, *68*, 412–422.
- [38] N. Onoda-Yamamuro, T. Matsuo, H. Suga, *J. Phys. Chem. Solids*, **1992**, *53*, 935–939.
- [39] F. Zheng, H. Takenaka, F. Wang, N. Z. Koocher, A. M. Rappe, *J. Phys. Chem. Lett.*, **2015**, *6*, 31–37.
- [40] Y. Kutes, L. Ye, Y. Zhou, S. Pang, B. D. Huey, N. P. Padture, *J. Phys. Chem. Lett.*, **2014**, *5*, 3335–3339.
- [41] A. Baumann, K. Tvingstedt, M. Heiber, S. V  th, C. Momblona, H. Bolink, V. Dyakonov, *APL Mater.*, **2014**, *2*, 081501.
- [42] H. J. Snaith, A. Abate, J. M. Ball, G. E. Eperon, T. Leijtens, N. K. Noel, S. D. Stranks, J. T.-W. Wang, K. Wojciechowski, W. Zhang, *J. Phys. Chem. Lett.*, **2014**, *5*, 1511–1515.
- [43] O. Selig, A. Sadhanala, C. M  ller, R. Lovrincic, Z. Chen, Y. L. A. Rezus, J. M. Frost, T. L. C. Jansen, A. A. Bakulin, *J. Am. Chem. Soc.*, **2017**, *139*, 4068–4074.
- [44] C. Eames, J. M. Frost, P. R. Barnes, B. C. O’regan, A. Walsh, M. S. Islam, *Nat. Comm.*, **2015**, *6*, 1–8.
- [45] J. M. Frost, A. Walsh, *Acc. Chem. Res.*, **2016**, *49*, 528–535.
- [46] V. Nandal, P. R. Nair, *ACS Nano* **2017**, *11*, 11505–11512.
- [47] L. McGovern, M. H. Futscher, L. A. Muscarella, B. Ehrler, *J. Phys. Chem. Lett.*, **2020**, *11*, 7127–7132.
- [48] D. Cahen, L. Kronik, G. Hodes, *ACS Energy Lett.* **2021**, *6*, 4108–4114.
- [49] A. Musiienko, D. R. Ceratti, J. Pipek, M. Brynza, H. Elhadidy, E. Belas, M. Betu  iak, G. Delport, P. Praus, *Adv. Funct. Mater.*, **2021**, *31*, 2104467.
- [50] R. Frei, R. McWilliam, B. Derrick, A. Purvis, A. Tiwari, G. D. M. Serugendo, *Int. J. Adv. Manuf. Technol.*, **2013**, *69*, 1033–1061.
- [51] D. Ceratti, A. Cohen, R. Tenne, Y. Rakita, L. Snarski, N. Jasti, L. Cremonesi, R. Cohen, M. Weitman, I. Rosenhek-Goldian, I. Kaplan-Ashiri, T. Bendikov, V. Kalchenko, M. Elbaum, M. A. C. Potenza, L. Kronik, G. Hodes, D. Cahen, *Mater. Horiz.*, **2021**, *8*, 1570–1586.
- [52] J. Siekmann, S. Ravishankar, T. Kirchartz, *ACS Energy Lett.* **2021**, *6*, 3244–3251.
- [53] J. S. Manser, J. A. Christians, P. V. Kamat, *Chem. Rev.* **2016**, *116*, 12956–13008.
- [54] N. Droseros, G. Longo, J. C. Brauer, M. Sessolo, H. J. Bolink, N. Banerji, *ACS Energy Lett.*, **2018**, *3*, 1458–1466.
- [55] L. M. Herz, *ACS Energy Lett.*, **2017**, *2*, 1539–1548.
- [56] L. M. Pazos-Out  n, M. Szumilo, R. Lamboll, J. M. Richter, M. Crespo-Quesada, M. Abdi-Jalebi, H. J. Beeson, M. Vru  cini  , M. Alsari, H. J. Snaith, *Science*, **2016**, *351*, 1430–1433.

- [57] J. M. Richter, M. Abdi-Jalebi, A. Sadhanala, M. Tabachnyk, J. P. Rivett, L. M. Pazos-Outón, K. C. Gödel, M. Price, F. Deschler, R. H. Friend, *Nat. Comm.*, **2016**, 7, 1–8.
- [58] D. Giovanni, M. Righetto, Q. Zhang, J. W. M. Lim, S. Ramesh, T. C. Sum, *Light: Science & Applications*, **2021**, 10, 1–9.
- [59] M. L. Steigerwald, L. E. Brus, *Acc. Chem. Res.*, **1990**, 23, 183–188.
- [60] J. E. Murphy, M. C. Beard, A. G. Norman, S. P. Ahrenkiel, J. C. Johnson, P. Yu, O. I. Mičić, R. J. Ellingson, A. J. Nozik, *J. Am. Chem. Soc.*, **2006**, 128, 3241–3247.
- [61] Z. Li, X. Peng, *J. Am. Chem. Soc.*, **2011**, 133, 6578–6586.
- [62] M.-R. Gao, Y.-F. Xu, J. Jiang, S.-H. Yu, *Chem. Soc. Rev.* **2013**, 42, 2986–3017.
- [63] J. Chen, C. Dong, H. Idriss, O. F. Mohammed, O. M. Bakr, *Adv. Energy Mater.*, **2020**, 10, 1902433.
- [64] J. Chen, W. Du, J. Shi, M. Li, Y. Wang, Q. Zhang, X. Liu, *InfoMat* **2020**, 2, 170–183.
- [65] M. Lu, Y. Zhang, S. Wang, J. Guo, W. W. Yu, A. L. Rogach, *Adv. Funct. Mater.*, **2019**, 29, 1902008.
- [66] J.-H. Im, C.-R. Lee, J.-W. Lee, S.-W. Park, N.-G. Park, *Nanoscale*, **2011**, 3, 4088–4093.
- [67] L. C. Schmidt, A. Pertegas, S. Gonzalez-Carrero, O. Malinkiewicz, S. Agouram, G. Minguez Espallargas, H. J. Bolink, R. E. Galian, J. Perez-Prieto, *J. Am. Chem. Soc.*, **2014**, 136, 850–853.
- [68] S. Gonzalez-Carrero, R. E. Galian, J. Pérez-Prieto, *J. Mater. Chem. A*, **2015**, 3, 9187–9193.
- [69] J. A. Sichert, Y. Tong, N. Mutz, M. Vollmer, S. Fischer, K. Z. Milowska, R. Garcia Cortadella, B. Nickel, C. Cardenas-Daw, J. K. Stolarczyk, A. S. Urban, J. Feldmann, *Nano Lett.*, **2015**, 15, 6521–6527.
- [70] F. ; Z. Zhang H. ;. Chen, C. ;. Wu, X. ;. Hu, X. ;. Huang, H. ;. Han, J. ;. Zou, B. ;. Dong, Y., *ACS Nano*, **2015**, 9, 10.
- [71] L. Protesescu, S. Yakunin, M. I. Bodnarchuk, F. Bertolotti, N. Masciocchi, A. Guagliardi, M. V. Kovalenko, *J. Am. Chem. Soc.*, **2016**, 138, 14202–14205.
- [72] H. Huang, A. S. Susha, S. V. Kershaw, T. F. Hung, A. L. Rogach, *Adv. Sci.*, **2015**, 2, 1500194.
- [73] M. Imran, V. Caligiuri, M. Wang, L. Goldoni, M. Prato, R. Krahne, L. De Trizio, L. Manna, *J. Am. Chem. Soc.*, **2018**, 140, 2656–2664.
- [74] V. A. Hintermayr, A. F. Richter, F. Ehrat, M. Doblinger, W. Vanderlinden, J. A. Sichert, Y. Tong, L. Polavarapu, J. Feldmann, A. S. Urban, *Adv. Mater.*, **2016**, 28, 9478–9485.
- [75] L. Protesescu, S. Yakunin, O. Nazarenko, D. N. Dirin, M. V. Kovalenko, *ACS Appl. Nano Mater.*, **2018**, 1, 1300–1308.

- [76] P. Tyagi, S. M. Arveson, W. A. Tisdale, *J. Phys. Chem. Lett.*, **2015**, *6*, 1911–1916.
- [77] C. C. Stoumpos, D. H. Cao, D. J. Clark, J. Young, J. M. Rondinelli, J. I. Jang, J. T. Hupp, M. G. Kanatzidis, *Chem. Mater.*, **2016**, *28*, 2852–2867.
- [78] T. Ishihara, X. Hong, J. Ding, A. Nurmikko, *Surf. Sci.*, **1992**, *267*, 323–326.
- [79] D. B. Mitzi, C. A. Feild, W. T. A. Harrison, A. M. Guloy, *Nature*, **1994**, *369*, 3.
- [80] S. Ruddlesden, P. Popper, *Acta Crystallogr.*, **1958**, *11*, 54–55.
- [81] D. B. ; W. Mitzi S. ; Feild, C. A. ; Chess, C. A. ; Guloy, A. M., *Science*, **1994**, *267*, 5.
- [82] Y. Y. ; L. Li C. K. ; Zheng, G. L. ; Cheng, Z. Y. ; You, H. ; Wang, W. D. ; Lin, J., *Chem. Mater.*, **2006**, *18*, 7.
- [83] L. Mao, Y. Wu, C. C. Stoumpos, M. R. Wasielewski, M. G. Kanatzidis, *J. Am. Chem. Soc.*, **2017**, *139*, 11956–11963.
- [84] E. R. Dohner, A. Jaffe, L. R. Bradshaw, H. I. Karunadasa, *J. Am. Chem. Soc.*, **2014**, *136*, 13154–13157.
- [85] E. R. Dohner, E. T. Hoke, H. I. Karunadasa, *J. Am. Chem. Soc.*, **2014**, *136*, 1718–1721.
- [86] B. Vargas, R. Torres-Cadena, J. Rodriguez-Hernandez, M. Gembicky, H. Xie, J. Jimenez-Mier, Y.-S. Liu, E. Menendez-Proupin, K. R. Dunbar, N. Lopez, *Chem. Mater.*, **2018**, *30*, 5315–5321.
- [87] L. Mao, P. Guo, M. Kepenekian, I. Hadar, C. Katan, J. Even, R. D. Schaller, C. C. Stoumpos, M. G. Kanatzidis, *J. Am. Chem. Soc.*, **2018**, *140*, 13078–13088.
- [88] Y. Bekenstein, B. A. Koscher, S. W. Eaton, P. Yang, A. P. Alivisatos, *J. Am. Chem. Soc.*, **2015**, *137*, 16008–16011.
- [89] Q. A. Akkerman, V. D’Innocenzo, S. Accornero, A. Scarpellini, A. Petrozza, M. Prato, L. Manna, *J. Am. Chem. Soc.*, **2015**, *137*, 10276–10281.
- [90] O. Vybornyi, S. Yakunin, M. V. Kovalenko, *Nanoscale*, **2016**, *8*, 6278–6283.
- [91] M. C. Weidman, M. Seitz, S. D. Stranks, W. A. Tisdale, *ACS Nano*, **2016**, *10*, 7830–7839.
- [92] W. Paritmongkol, N. S. Dahod, A. Stollmann, N. Mao, C. Settens, S.-L. Zheng, W. A. Tisdale, *Chem. Mater.*, **2019**, *31*, 5592–5607.
- [93] M. C. Weidman, A. J. Goodman, W. A. Tisdale, *Chem. Mater.* **2017**, *12*, 5019–5030.
- [94] C. M. M. Soe, G. Nagabhushana, R. Shivaramaiah, H. Tsai, W. Nie, J.-C. Blancon, F. Melkonyan, D. H. Cao, B. Traoré, L. Pedesseau, *Proc. Natl. Acad. Sci.*, **2019**, *116*, 58–66.
- [95] A. Ciccioli, A. Latini, *J. Phys. Chem. Lett.*, **2018**, *9*, 3756–3765.
- [96] C. C. Stoumpos, L. Mao, C. D. Malliakas, M. G. Kanatzidis, *Inorg. Chem.*, **2017**, *56*, 56–73.

- [97] D. H. Cao, C. C. Stoumpos, T. Yokoyama, J. L. Logsdon, T.-B. Song, O. K. Farha, M. R. Wasielewski, J. T. Hupp, M. G. Kanatzidis, *ACS Energy Lett.*, **2017**, *2*, 982–990.
- [98] E. Hanamura, N. Nagaosa, M. Kumagai, T. Takagahara, *Mater. Sci. Eng. B*, **1988**, *1*, 255–258.
- [99] J. Jagielski, S. Kumar, W.-Y. Yu, C.-J. Shih, *J. Mater. Chem. C*, **2017**, *5*, 5610–5627.
- [100] M. I. Saidaminov, O. F. Mohammed, O. M. Bakr, *ACS Energy Lett.*, **2017**, *2*, 889–896.
- [101] T. Ishihara, J. Takahashi, T. Goto, *Solid State Comm.*, **1989**, *69*, 933–936.
- [102] T. Ishihara, J. Takahashi, T. Goto, *Phys. Rev. B*, **1990**, *42*, 11099.
- [103] K. Chondroudis, C. R. Kagan, D. B. Mitzi, **2001**, *45*, 17.
- [104] J. L. Knutson, J. D. Martin, D. B. Mitzi, *Inorg Chem* **2005**, *44*, 7.
- [105] D. B. Mitzi, C. D. Dimitrakopoulos, L. L. Kosbar, *Chem. Mater.*, **2001**, *13*, 3728–3740.
- [106] Z. Xu, D. B. Mitzi, C. D. Dimitrakopoulos, K. R. Maxcy, *Inorg. Chem.* **2003**, *42*, 2031–2039.
- [107] K. Z. Du, Q. Tu, X. Zhang, Q. Han, J. Liu, S. Zauscher, D. B. Mitzi, *Inorg. Chem.*, **2017**, *56*, 9291–9302.
- [108] X. Hong, T. Ishihara, A. Nurmikko, *Physical Review B* **1992**, *45*, 6961.
- [109] J. V. Passarelli, C. M. Mauck, S. W. Winslow, C. F. Perkinson, J. C. Bard, H. Sai, K. W. Williams, A. Narayanan, D. J. Fairfield, M. P. Hendricks, *Nat. Chem.*, **2020**, *12*, 672–682.
- [110] A. Raja, A. Chaves, J. Yu, G. Arefe, H. M. Hill, A. F. Rigosi, T. C. Berkelbach, P. Nagler, C. Schüller, T. Korn, *Nat. Comm.*, **2017**, *8*, 1–7.
- [111] Z. Xu, D. B. Mitzi, *Chem. Mater.* **2003**, *15*, 3632–3637.
- [112] D. B. Mitzi, K. Chondroudis, C. R. Kagan, *ACS Inorg. Chem.* **1999**, *38*, 11.
- [113] L. Mao, H. Tsai, W. Nie, L. Ma, J. Im, C. C. Stoumpos, C. D. Malliakas, F. Hao, M. R. Wasielewski, A. D. Mohite, *Chem. Mater.*, **2016**, *28*, 7781–7792.
- [114] M. Braun, W. Tuffentsammer, H. Wachtel, H. C. Wolf, *Chem. Phys. Lett.*, **1999**, *303*, 8.
- [115] Y. Gao, E. Shi, S. Deng, S. B. Shiring, J. M. Snaider, C. Liang, B. Yuan, R. Song, S. M. Janke, A. Liebman-Peláez, P. Yoo, M. Zeller, B. W. Boudouris, P. Liao, C. Zhu, V. Blum, Y. Yu, B. M. Savoie, L. Huang, L. Dou, *Nat. Chem.*, **2019**, *11*, 1151–1157.
- [116] M. Era, K. Maeda, T. Tsutsui, *Chem. Phys. Lett.*, **1998**, *296*, 4.
- [117] J. V. Passarelli, D. J. Fairfield, N. A. Sather, M. P. Hendricks, H. Sai, C. L. Stern, S. I. Stupp, *J. Am. Chem. Soc.*, **2018**, *140*, 7313–7323.

- [118] T. Kollek, D. Wurmbrand, S. T. Birkhold, E. Zimmermann, J. Kalb, L. Schmidt-Mende, S. Polarz, *ACS Appl. Mater. Interfaces*, **2017**, *9*, 1077–1085.
- [119] M. Era, K. Miyake, Y. Yoshida, K. Yase, *Thin Solid Films*, **2001**, *393*, 4.
- [120] R. Sasai, H. Shinomura, *J. Solid State Chem.*, **2013**, *198*, 452–458.
- [121] B. Tieke, G. Chapuis, *J. Polym. Sci., Polym. Chem. Ed.*, **1984**, *22*, 2895–2921.
- [122] W. Chen, Y. Shi, J. Chen, P. Ma, Z. Fang, D. Ye, Y. Lu, Y. Yuan, J. Zhao, Z. Xiao, *Adv. Mater.*, **2021**, *33*, 2104842.
- [123] H. Duim, M. A. Loi, *Matter*, **2021**, *4*, 3835–3851.
- [124] G. Long, C. Jiang, R. Sabatini, Z. Yang, M. Wei, L. N. Quan, Q. Liang, A. Rasmita, M. Askerka, G. Walters, *Nat. Photonics*, **2018**, *12*, 528–533.
- [125] T. Kataoka, T. Kondo, R. Ito, S. Sasaki, K. Uchida, N. Miura, *Phys. B: Condens. Matter*, **1993**, *184*, 132–136.
- [126] M. Hirasawa, T. Ishihara, T. Goto, *J. Phys. Soc. Jpn.*, **1994**, *63*, 3870–3879.
- [127] C. Xu, H. Sakakura, T. Kondo, S. Takeyama, N. Miura, Y. Takahashi, K. Kumata, R. Ito, *Solid State Comm.*, **1991**, *79*, 249–253.
- [128] D. Liang, Y. Peng, Y. Fu, M. J. Shearer, J. Zhang, J. Zhai, Y. Zhang, R. J. Hamers, T. L. Andrew, S. Jin, *ACS Nano*, **2016**, *10*, 6897–6904.
- [129] T. Hattori, T. Taira, M. Era, T. Tsutsui, S. Saito, *Chem. Phys. Lett.*, **1996**, *254*, 103–108.
- [130] D. B. Mitzi, *Chem. Mater.*, **1996**, *8*, 791–800.
- [131] D. Umeyama, Y. Lin, H. I. Karunadasa, *Chem. Mater.*, **2016**, *28*, 3241–3244.
- [132] M. D. Smith, B. A. Connor, H. I. Karunadasa, *Chem. Rev.* **2019**, *119*, 3104–3139.
- [133] D. Cortecchia, J. Yin, A. Bruno, S.-Z. A. Lo, G. G. Gurzadyan, S. Mhaisalkar, J.-L. Bredas, C. Soci, *J. Mater. Chem. C*, **2017**, *5*, 2771–2780.
- [134] R. Williams, K. Song, *J. Phys. Chem. Solids*, **1990**, *51*, 679–716.
- [135] D. B. Straus, C. R. Kagan, *J. Phys. Chem. Lett.*, **2018**, *9*, 1434–1447.
- [136] Y. Chen, X. Liu, T. Wang, Y. Zhao, *Acc. Chem. Res.*, **2021**, *54*, 3452–3461.
- [137] National Renewable Energy Laboratory, *Best Research-Cell Efficiency Chart 2021*.
- [138] W. Yin, T. Shi, Y. Yan, *Adv. Mater.*, **2014**, *26*, 4653–4658.
- [139] K. Wang, G. Xing, Q. Song, S. Xiao, *Adv. Mater.*, **2021**, *33*, 2000306.
- [140] G. Grancini, C. Roldan-Carmona, I. Zimmermann, E. Mosconi, X. Lee, D. Martineau, S. Narbey, F. Oswald, F. De Angelis, M. Grätzel, M. K. Nazeeruddin, *Nat. Commun.*, **2017**, *8*, 15684.
- [141] C. C. Stoumpos, C. M. M. Soe, H. Tsai, W. Nie, J.-C. Blancon, D. H. Cao, F. Liu, B. Traoré, C. Katan, J. Even, *Chem.*, **2017**, *2*, 427–440.
- [142] H. Tsai, W. Nie, J. C. Blancon, C. C. Stoumpos, R. Asadpour, B. Harutyunyan, A. J. Neukirch, R. Verduzco, J. J. Crochet, S. Tretiak, L. Pedesseau, J. Even, M. A.

- Alam, G. Gupta, J. Lou, P. M. Ajayan, M. J. Bedzyk, M. G. Kanatzidis, *Nature*, **2016**, 536, 312–316.
- [143] Y.-H. Kim, S. Kim, A. Kakekhani, J. Park, J. Park, Y.-H. Lee, H. Xu, S. Nagane, R. B. Wexler, D.-H. Kim, *Nat. Photonics*, **2021**, 15, 148–155.
- [144] Y. J. Yoon, J. Y. Kim, *J. Semicond.*, **2021**, 42, 101608.
- [145] D. N. Dirin, L. Protesescu, D. Trummer, I. V. Kochetygov, S. Yakunin, F. Krumeich, N. P. Stadie, M. V. Kovalenko, *Nano Lett.*, **2016**, 16, 5866–5874.
- [146] G. C. Papavassiliou, G. Pagona, N. Karousis, G. A. Mousdis, I. Koutselas, A. Vassilakopoulou, *J. Mater. Sci.*, **2012**, 22, 8271.
- [147] Y. Tong, E. Bladt, M. F. Ayguler, A. Manzi, K. Z. Milowska, V. A. Hintermayr, P. Docampo, S. Bals, A. S. Urban, L. Polavarapu, J. Feldmann, *Angew. Chem. Int. Ed. Engl.*, **2016**, 55, 13887–13892.
- [148] Y. Wang, X. Li, J. Song, L. Xiao, H. Zeng, H. Sun, *Adv. Mater.*, **2015**, 27, 7101–7108.
- [149] S. Yakunin, L. Protesescu, F. Krieg, M. I. Bodnarchuk, G. Nedelcu, M. Humer, G. De Luca, M. Fiebig, W. Heiss, M. V. Kovalenko, *Nat. Comm.* **2015**, 6, 1–9.
- [150] T. J. Evans, A. Schlaus, Y. Fu, X. Zhong, T. L. Atallah, M. S. Spencer, L. E. Brus, S. Jin, X. Zhu, *Adv. Opt. Mater.*, **2018**, 6, 1700982.
- [151] P. Ramasamy, D.-H. Lim, B. Kim, S.-H. Lee, M.-S. Lee, J.-S. Lee, *Chem. Commun.*, **2016**, 52, 2067–2070.
- [152] H. Wang, D. H. Kim, *Chem. Soc. Rev.* **2017**, 46, 5204–5236.
- [153] X. Qi, Y. Zhang, Q. Ou, S. T. Ha, C. Qiu, H. Zhang, Y. Cheng, Q. Xiong, Q. Bao, *Small*, **2018**, 14, 1800682.
- [154] H. Kim, J. S. Han, J. Choi, S. Y. Kim, H. W. Jang, *Small Methods* **2018**, 2, 1700310.
- [155] H. Bouas-Laurent, H. Dürr, *Pure Appl. Chem.* **2001**, 73, 27.
- [156] K. G. Yager, C. J. Barrett, *J. Photochem. Photobiol. A* **2006**, 182, 250–261.
- [157] H. Hayashi, J. Rabek, *Photochemistry and Photophysics*, CRC Press, Boca Raton, Florida, **1990**.
- [158] L. Brzozowski, E. H. Sargent, *J. Mater. Sci.*, **2001**, 12.
- [159] M. J. Hansen, M. M. Lerch, W. Szymanski, B. L. Feringa, *Angew. Chem. Int. Ed.*, **2016**, 55, 13514–13518.
- [160] L. W. Giles, C. F. Faul, R. F. Tabor, *Mater. Adv.*, **2021**, 13, 4152–4164.
- [161] P. Bortolus, S. Monti, *J. Phys. Chem.*, **1979**, 83, 648–652.
- [162] H. M. Bandara, S. C. Burdette, *Chem. Soc. Rev.*, **2012**, 41, 1809–1825.
- [163] H. Rau, E. Lueddecke, *J. Am. Chem. Soc.* **1982**, 104, 1616–1620.
- [164] C. J. Brown, *Acta Cryst.*, **1966**, 21, 1.
- [165] P. Cattaneo, M. Persico, *Phys. Chem. Chem. Phys.* **1999**, 1, 4739–4743.
- [166] G. Tiberio, L. Muccioli, R. Berardi, C. Zannoni, *ChemPhysChem*. **2010**, 11, 1018.

- [167] L. Gagliardi, G. Orlandi, F. Bernardi, A. Cembran, M. Garavelli, *Theor. Chem. Acc.*, **2004**, *111*, 363–372.
- [168] E. Bergmann, L. Engel, S. Sándor, *Eur. J. In. Chem.*, **1930**, 63.
- [169] Y. Shirota, K. Moriwaki, S. Yoshikawa, T. Ujike, H. Nakano, *J. Mater. Chem.*, **1998**, *8*, 2579–2581.
- [170] G. S. Hartley, *J. Chem. Soc.*, **1938**, *0*, 10.
- [171] M. Poutanen, O. Ikkala, A. Priimagi, *Macromolecules* **2016**, *49*, 4095–4101.
- [172] S. W. Magennis, F. S. Mackay, A. C. Jones, K. M. Tait, P. J. Sadler, *Chem. Mater.*, **2005**, *17*, 4.
- [173] E. Merino, *Chem. Soc. Rev.*, **2011**, *40*, 3835–3853.
- [174] T. Hugel, N. B. Holland, A. Cattani, L. Moroder, M. Seitz, H. E. Gaub, *Science*, **2002**, *296*, 5.
- [175] C. J. Barrett, J. Mamiya, K. G. Yager, T. Ikeda, *Soft Matter*, **2007**, *3*, 1249.
- [176] P. Zhou, Y. Li, X. Li, S. Liu, Y. Su, *Liq. Cryst. Rev.*, **2016**, *4*, 83–100.
- [177] L. Dong, Y. Zhao, *Mater. Chem. Front.*, **2018**, *2*, 1932–1943.
- [178] X. Huang, T. Li, *J. Mater. Chem. C*, **2020**, *8*, 821–848.
- [179] T. Ikeda, O. Tsutsumi, *Science*, **1995**, *268*, 4.
- [180] X. Chi, X. Ji, D. Xia, F. Huang, *J. Am. Chem. Soc.* **2015**, *137*, 1440–1443.
- [181] Y. Kim, A. Garcia-Lekue, D. Sysoiev, T. Frederiksen, U. Groth, E. Scheer, *Phys. Rev. Lett.*, **2012**, *109*, 226801.
- [182] J. M. Mativetsky, G. Pace, M. Elbing, M. A. Rampi, M. Mayor, P. Samori, *J. Am. Chem. Soc.*, **2008**, *130*, 9192–9193.
- [183] S.-C. Lee, S.-H. Lee, O. P. Kwon, *J. Mater. Chem. C*, **2016**, *4*, 1935–1944.
- [184] A. Natansohn, P. Rochon, *Chem. Rev.*, **2002**, *102*, 4139–4176.
- [185] J. Wen, Z. Tian, J. Ma, *J. Phys. Chem. C*, **2013**, *117*, 19934–19944.
- [186] A. Torres, L. R. Prado, G. Bortolini, L. G. C. Rego, *J. Phys. Chem. Lett.*, **2018**, *9*, 5926–5933.
- [187] G. Wilkinson, M. Rosenblum, M. Whiting, R. Woodward, *J. Am. Chem. Soc.*, **1952**, *74*, 2125–2126.
- [188] R. Woodward, M. Rosenblum, M. Whiting, *J. Am. Chem. Soc.*, **1952**, *74*, 3458–3459.
- [189] D. Astruc, *Eur. J. Inorg. Chem.*, **2017**, *2017*, 6–29.
- [190] L. Fabbrizzi, *ChemTexts*, **2020**, *6*, 22.
- [191] N. G. Connelly, W. E. Geiger, *Chem. Rev.*, **1996**, *96*, 877–910.
- [192] A. Paul, R. Borrelli, H. Bouyanfif, S. Gottis, F. Sauvage, *ACS Omega*, **2019**, *4*, 14780–14789.
- [193] D. W. Macomber, W. P. Hart, M. D. Rausch, *Adv. Organomet. Chem.* **1982**, *21*, 1–55.
- [194] D. Astruc, *Acc. Chem. Res.*, **1997**, *30*, 383–391.

- [195] S. Fery-Forgues, B. Delavaux-Nicot, *J. Photochem. Photobiol.*, **2000**, *132*, 137–159.
- [196] S. Bitter, M. Schlötter, M. Schilling, M. Krumova, S. Polarz, R. F. Winter, *Chem. Sci.*, **2021**, *12*, 270–281.
- [197] M. Hmyene, A. Yassar, M. Escorne, A. Percheron-Guegan, F. Garnier, *Adv. Mater.*, **1994**, *6*, 564–568.
- [198] S. Bitter, M. Kunkel, L. Burkart, A. Mang, R. F. Winter, S. Polarz, *ACS Omega*, **2018**, *3*, 8854–8864.
- [199] R. Deschenaux, M. Schweissguth, A.-M. Levelut, *Chem. Comm.*, **1996**, 1275–1276.
- [200] R. Deschenaux, M. Schweissguth, M.-T. Vilches, A.-M. Levelut, D. Hautot, G. J. Long, D. Luneau, *Organometallics*, **1999**, *18*, 5553–5559.
- [201] M. Hadadpour, J. Gwyther, I. Manners, P. J. Ragogna, *Chem. Mater.*, **2015**, *27*, 3430–3440.
- [202] R. D. Hudson, *J. Organomet. Chem.*, **2001**, *637*, 47–69.
- [203] R. H. Staff, M. Gallei, M. Mazurowski, M. Rehahn, R. Berger, K. Landfester, D. Crespy, *ACS Nano*, **2012**, *6*, 9042–9049.
- [204] J. Elbert, M. Gallei, C. Rüttiger, A. Brunsen, H. Didzoleit, B. Stühn, M. Rehahn, *Organometallics*, **2013**, *32*, 5873–5878.
- [205] S. M. Beladi-Mousavi, S. Sadaf, L. Walder, M. Gallei, C. Rüttiger, S. Eigler, C. E. Halbig, *Adv. Energy Mater.*, **2016**, *6*, 1600108.
- [206] Z. Huang, H. Yu, L. Wang, X. Liu, T. Lin, F. Haq, S. Z. Vatsadze, D. A. Lemenovskiy, *Coord. Chem. Rev.*, **2021**, *430*, 213737.
- [207] G. S. Mohammad-Pour, K. O. Hatfield, D. C. Fairchild, K. Hernandez-Burgos, J. Rodríguez-López, F. J. Uribe-Romo, *J. Am. Chem. Soc.*, **2019**, *141*, 19978–19982.
- [208] T. J. Farrugia, D. C. Magri, *New Journal of Chemistry* **2013**, *37*, 148–151.
- [209] Y. Cai, Y. Gao, Q. Luo, M. Li, J. Zhang, H. Tian, W.-H. Zhu, *Adv. Opt. Mater.*, **2016**, *4*, 1410–1416.
- [210] X. Li, Z. Guo, J. Li, Y. Zhang, H. Ma, X. Pang, B. Du, Q. Wei, *Analytica Chimica Acta*, **2015**, *854*, 40–46.
- [211] D. Dorokhin, N. Tomczak, A. H. Velders, D. N. Reinhoudt, G. J. Vancso, *J. Phys. Chem. C*, **2009**, *113*, 18676–18680.
- [212] D. Jańczewski, J. Song, G. Julius Vancso, *Eur. Polym. J.*, **2014**, *54*, 87–94.
- [213] J. T. DuBose, P. V. Kamat, *J. Phys. Chem. Lett.*, **2019**, *10*, 6074–6080.
- [214] T. Qin, Q. Chang, F. Wang, W. Xu, A. Wang, Y. Liu, J. Wang, Y. Yun, S. Gao, K. Xiao, L. Zhang, L. Wang, J. Wang, W. Huang, *Angew. Chem. Int. Ed.*, **2021**, *60* (48), 25567–25574.
- [215] Z.-X. Zhang, H.-Y. Zhang, W. Zhang, X.-G. Chen, H. Wang, R.-G. Xiong, *J. Am. Chem. Soc.*, **2020**, *142*, 17787–17794.

- [216] T. Kollek, D. Gruber, J. Gehring, E. Zimmermann, L. Schmidt-Mende, S. Polarz, *Angew. Chem. Int. Ed. Engl.*, **2015**, *54*, 1341–1346.
- [217] T. Kollek, C. Fischer, I. Göttker-Schnetmann, S. Polarz, *Chem. Mat.* **2016**, *28*, 4134–4138.
- [218] T. Kollek, S. Polarz, *CrystEngComm* **2017**, *19*, 4615–4621.
- [219] C. C. Stoumpos, M. G. Kanatzidis, *Acc. Chem. Res.* **2015**, *48*, 2791–2802.
- [220] N. Fillafer, Anisotrope Hybride Perowskit-Nanopartikel, Bachelorthesis, Universität Konstanz, **2015**.
- [221] S. T. Birkhold, E. Zimmermann, T. Kollek, D. Wurmbrand, S. Polarz, L. Schmidt-Mende, *Adv. Funct. Mat.*, **2017**, *27*, 1604995.
- [222] M. I. Saidaminov, A. L. Abdelhady, B. Murali, E. Alarousu, V. M. Burlakov, W. Peng, I. Dursun, L. Wang, Y. He, G. Maculan, A. Goriely, T. Wu, O. F. Mohammed, O. M. Bakr, *Nat. Commun.*, **2015**, *6*, 7586.
- [223] U. J. Bahnmüller, H. Kuper, T. Seewald, Y. Yalçinkaya, J. A. Becker, L. Schmidt-Mende, S. A. Weber, S. Polarz, *Nanomaterials*, **2021**, *11*, 3057.
- [224] L. Schmidt-Mende, J. Weickert, *Organic and Hybrid Solar Cells*, De Gruyter, **2016**.
- [225] P. Kubelka, *Zeitschrift für technische Physik* **1931**, *12*, 593–601.
- [226] A. Murphy, *Sol. Energ. Mat. Sol. Cells.* **2007**, *91*, 1326–1337.
- [227] P. Makuła, M. Pacia, W. Macyk, *J. Phys. Chem. Lett.* **2018**, *9*, 6814–6817.
- [228] J. R. Lakowicz, *Principles of Fluorescence Spectroscopy*, Baltimore, Maryland USA, **2010**.
- [229] S. Hüfner, *Photoelectron Spectroscopy: Principles and Applications*, Springer Science & Business Media, **2003**.
- [230] J. Heinze, *Angew. Chem.* **1984**, *96*, 823–840.
- [231] M. Hasan, S. Venkatesan, D. Lyashenko, J. D. Slinker, A. Zakhidov, *Anal. Chem.* **2017**, *89*, 9649–9653.
- [232] N. Fillafer, Herstellung von Mikrokristallinen Perowskit Kristallen Mit Funktionellen Grenzflächenadditiven, Masterthesis, Universität Konstanz, **2017**.
- [233] N. Fillafer, T. Seewald, L. Schmidt-Mende, S. Polarz, *Beilstein J. Nanotechnol.*, **2020**, *11*, 466–479.
- [234] N. Fillafer, H. Kuper, A. Schaate, S. Locmelis, J. A. Becker, Y. Krysiak, S. Polarz, *Adv. Funct. Mater.*, **2022**, 2201126.
- [235] A. A. Beharry, G. A. Woolley, *Chem. Soc. Rev.*, **2011**, *40*, 4422–4437.
- [236] T. Cusati, G. Granucci, M. Persico, *J. Am. Chem. Soc.* **2011**, *133*, 5109–5123.
- [237] H. Mashiyama, Y. Kawamura, *JKPS*, **2007**, *51*, 4.
- [238] A. Kumar, S. Mandal, P. Selvakannan, R. Pasricha, A. Mandale, M. Sastry, *Langmuir*, **2003**, *19*, 6277–6282.
- [239] S. Saeed, J. Yin, M. A. Khalid, P. A. Channar, G. Shabir, A. Saeed, M. A. Nadeem, C. Soci, A. Iqbal, *J. Photochem. Photobio. A: Chem.*, **2019**, *375*, 48–53.

- [240] Q. M. Zhang, X. Li, M. R. Islam, M. Wei, M. J. Serpe, *J. Mater. Chem. C* **2014**, *2*, 6961–6965.
- [241] M. L. Rahman, T. K. Biswas, S. M. Sarkar, M. M. Yusoff, A. Yuvaraj, S. Kumar, *J. Colloid Interface Sci.*, **2016**, *478*, 384–393.
- [242] B. Wu, H. T. Nguyen, Z. Ku, G. Han, D. Giovanni, N. Mathews, H. J. Fan, T. C. Sum, *Adv. Energy Mater.*, **2016**, *6*, 1600551.
- [243] M. B. Price, J. Butkus, T. C. Jellicoe, A. Sadhanala, A. Briane, J. E. Halpert, K. Broch, J. M. Hodgkiss, R. H. Friend, F. Deschler, *Nat. Commun.*, **2015**, *6*, 8420.
- [244] B. Murali, E. Yengel, C. Yang, W. Peng, E. Alarousu, O. M. Bakr, O. F. Mohammed, *ACS Energy Lett.*, **2017**, 846–856.
- [245] K. Tanaka, T. Takahashi, T. Kondo, T. Umebayashi, K. Asai, K. Ema, *Phys. Rev. B*, **2005**, *71*, 045312.
- [246] L. N. Quan, M. Yuan, R. Comin, O. Voznyy, E. M. Beaugard, S. Hoogland, A. Buin, A. R. Kirmani, K. Zhao, A. Amassian, D. H. Kim, E. H. Sargent, *J. Am. Chem. Soc.*, **2016**, *138*, 2649–2655.
- [247] Z. Chen, Y. Guo, E. Wertz, J. Shi, *Adv. Mater.* **2019**, *31*, 1803514.
- [248] M. Yuan, L. N. Quan, R. Comin, G. Walters, R. Sabatini, O. Voznyy, S. Hoogland, Y. Zhao, E. M. Beaugard, P. Kanjanaboos, Z. Lu, D. H. Kim, E. H. Sargent, *Nat. Nanotechnol.*, **2016**, *11*, 872–877.
- [249] M. Rowe, A. McCaffery, *J. Chem. Phys.*, **1973**, *59*, 3786–3794.
- [250] E. Mugnaioli, T. Gorelik, U. Kolb, *Ultramicroscopy*, **2009**, *109*, 758–765.
- [251] U. Kolb, Y. Krysiak, S. Plana-Ruiz, *Acta. Crystallogr. B. Struct.*, **2019**, *75*, 463–474.
- [252] S. Plana-Ruiz, Y. Krysiak, J. Portillo, E. Alig, S. Estradé, F. Peiró, U. Kolb, *Ultramicroscopy*, **2020**, *211*, 112951.
- [253] L. Palatinus, P. Brázda, P. Boullay, O. Perez, M. Klementová, S. Petit, V. Eigner, M. Zaarour, S. Mintova, *Science*, **2017**, *355*, 166–169.
- [254] D. Bowden, Y. Krysiak, L. Palatinus, D. Tsivoulas, S. Plana-Ruiz, E. Sarakinou, U. Kolb, D. Stewart, M. Preuss, *Nat. Commun.*, **2018**, *9*, 1–10.
- [255] C. Mac Gillavry, H. Nijveld, S. Dierdorp, J. Karsten, *Rec. Trav. Chim. Pays Bas*, **1939**, *58*, 193–200.
- [256] C. P. Brock, Y. Fu, *Acta. Crystallogr. B. Struct.*, **1997**, *53*, 928–938.
- [257] H. Steinfink, G. D. Brunton, *Inorg. Chem.*, **1969**, *8*, 1665–1668.
- [258] T. Wiest, R. Blachnik, H. Reuter, *Z. Naturforsch.*, **1999**, *54b*, 1099–1102.
- [259] M. D. Smith, B. L. Watson, R. H. Dauskardt, H. I. Karunadasa, *Chem. Mater.*, **2017**, *29*, 7083–7087.
- [260] N. Kitazawa, *Mater. Sci. Eng., B* **1997**, *49*, 233–238.
- [261] R. H. Palmer, J. Liu, C.-W. Kung, I. Hod, O. K. Farha, J. T. Hupp, *Langmuir*, **2018**, *34*, 4707–4714.

- [262] A. L. Abdelhady, M. I. Saidaminov, B. Murali, V. Adinolfi, O. Voznyy, K. Katsiev, E. Alarousu, R. Comin, I. Dursun, L. Sinatra, E. H. Sargent, O. F. Mohammed, O. M. Bakr, *J. Phys. Chem. Lett.*, **2016**, 7, 295–301.
- [263] K.-F. Berggren, B. E. Sernelius, *Phys. Rev. B*, **1981**, 24, 1971.
- [264] V. Palankovski, G. Kaiblinger-Grujin, S. Selberherr, *Mater. Sci. Eng. B*, **1999**, 66, 46–49.
- [265] A. Zanetta, Z. Andaji-Garmaroudi, V. Pirota, G. Pica, F. U. Kosasih, L. Gouda, K. Frohna, C. Ducati, F. Doria, S. D. Stranks, G. Grancini, *Adv. Mater.*, **2021**, 2105942.
- [266] J. Clayden, N. Greeves, S. Warren, *Organische Chemie*, Springer Spektrum, Berlin, **2013**
- [267] A. Walia, S. Kang, R. B. Silverman, *J. Org. Chem.*, **2013**, 78, 10931–20937.
- [268] Matthew Volgraf, Pau Gorostiza, Stephanie Szobota, Max R. Helix, Ehud Y. Isacoff, D. Trauner, *J. Am. Chem. Soc.*, **2007**, 129, 2.

8 List of figures

Figure 1 - Polyhedral representation of a cubic AMX_3 perovskite. (A^+ =green, M^{2+} =orange (center of octahedron), X^- =grey).....	3
Figure 2 - $MAPbX_3$ perovskite materials with varying anions ($X=Cl, Br, I$). Taken from ref. [28].	4
Figure 3 - Typical defects in $MAPbI_3$; taken from ref. [49].....	5
Figure 4 - Scheme of the layered perovskites structures, that can emerge through a cut of the perovskite structure in a certain crystal direction. a) layered perovskite in (100) direction with a layer thickness of $n=1$ having the general formula $(R-NH_3)_2A_{n-1}M_nX_{3n+1}$, b) layered perovskite structure in (110) crystal direction with a layer thickness of $m=2$ having the general formula $(R-NH_3)_2A_{m-1}M_mX_{3m+2}$ and c) layered perovskite structure in (111) crystal direction with a layer thickness of $q=2$ having the general formula $(R-NH_3)_2A_{q-1}M_qX_{3q+3}$	8
Figure 5 - LHPs of the Ruddlesden-Popper type with the general formula $(R-NH_3)_2A_{n-1}M_nX_{3n+1}$ with $n=1,2,3,4,\dots \infty$. The quantum confinement increases with decreasing layer thickness.	9
Figure 6 - Type I and Type II quantum-well (QW) electronic structures based on the energy alignment of the valence band maximum (VBM), conduction band minimum (CBM), highest occupied (HOMO) and lowest unoccupied molecular orbitals (LUMO) in hybrid LHPs. a)+b) Type I QW with one component (blue = inorganic MX_6 octahedra, green = organic cation) serving as quantum well. c)+d) Type II QW with a step-like arrangement allowing charge carrier separation.....	12
Figure 7 - a) Crystal structure of the $n=1$ LHP for $(R-NH_3)_2PbI_4$ and b) the used functional cations. Taken from ref. [109]......	12
Figure 8 - a) Absorption and emission spectra with photograph and b) crystal structure of $(n-MPDA)PbBr_4$. c) absorption and emission spectra with photograph and d) crystal structure of $(N-MEDA)PbBr_4$. Taken from ref. [132]......	13
Figure 9 – Various applications of hybrid perovskites.....	14
Figure 10 - Subclasses of azobenzene (a) azobenzene, (b) aminoazobenzene and (c) pseudostilbene.	16

Figure 11 - UV/Vis absorption spectra of the thermally induced isomerisation from <i>cis</i> (red) to <i>trans</i> (purple) isomer. Taken from ref. [171].	17
Figure 12 - Schematic model structure of azo based LHPs before (left) and after (right) UV irradiation according to Sasai <i>et al.</i> [120].	18
Figure 13 - Redox reaction of the ferrocene (Fc) / ferrocenium (Fc ⁺) couple.	19
Figure 14 – MOF thin-film electrode containing redox active mediators (=RAM; Fc) enabling fast redox conductivity via hopping. Taken from ref. [207].	20
Figure 15 - Crystal structure of ferrocene containing 1D perovskites of a) (FMTMA)PbI ₃ b) (FMTMA)PbBr ₂ I and c) (FMTMA)PbCl ₂ I. Taken from ref. [205].	21
Figure 16 - a) Crystal structure of (TEG) ₂ (CH ₃ NH ₃)PbBr ₃ (structure can be found at CCSD, number 1538521). Hydrogen atoms have been removed for clarity. b) Two TEG molecules chelating the MA ⁺ cation.	22
Figure 17 - a) chemical structure of DAI (top) and the thiophene derivative, b) micrometersized MAPbI ₃ particles applied on a sensor, c) conductivity measurements of MAPbI ₃ with surface functionalized particles (D = DAI, C0+C4 = thiophene copper with low (C0) and high (C4) concentration).	23
Figure 18 - Crystals obtained via a) a microwave assisted (scalebar = 5 μm) and b) aerosol assisted (scalebar = 1 μm) inverse temperature crystallization.	24
Figure 19 - a) Schematic experimental setup for transient absorption spectroscopy experiments. b) Example for the most common TA signals, which are <i>ground-state bleach</i> (GSB), <i>stimulated emission</i> (SE) and <i>photoinduced absorption</i> (PIA). Figures taken from ref. [224].	26
Figure 20 - a) Setup of a typical CV measurement with a reference electrode (RE), a counter electrode (CE) and the working electrode (WE) which are placed in an electrolyte. b) Current signal of a reversible single electron process.	30
Figure 21 – Schematic representation of the architecture of the energy levels in layered hybrid perovskite with functional organic molecules. Different scenarios for energy transfers from the perovskite phase to the functional molecule: a) no energy transfer due to closed valves, b) partial energy transfer with one valve opened and c) full energy transfer from the perovskite to the organic moiety due to both valves opened. Note that the energy levels are not to be considered quantitatively.	31
Figure 22 - Systematic series of azobenzene derivatives for the synthesis of hybrid perovskites.	35

Figure 23 – a) Scheme of the photoswitching reaction the azobenzene ligands, when irradiating with UV-light (λ_1) a conformational change from *trans*- to *cis*-conformation occurs. Blue light (λ_2) or heat (ΔT) cause the reverse reaction, b) UV/Vis kinetic measurement of AzoC₂ in purified H₂O. The solution was irradiated with 313 nm, black: beginning of the reaction, light-grey: ending of the reaction, c) absorption at 325 nm during a time period of 2600 sec. d) Energy scheme of azobenzene with the singlets S₀ (HOMO), S₁ (LUMO) and S₂ and possible transitions, responsible for the absorption bands at 425 nm and 325 nm in b).....36

Figure 24 – a) ¹H-NMR of AzoC₂ in MeOD before (top) and after (bottom) irradiation at 313 nm for 4 h. b) DOI of AzoC_n determined from ¹H-NMR.....37

Figure 25 - DFT calculated structure of AzoC₂ in a) *trans* conformation and b) *cis* conformation.....38

Figure 26 –SEM images of a) 2D-AzoC₂ b) 2D-AzoC₄ and c) 2D-AzoC₁₂ with scalebar = 1 μ m. d) PXRD patterns of the obtained precipitates. e) Scheme of the resulting 2D LHPs.41

Figure 27 - a) ¹H-NMR of the precursor during the irradiation with 313 nm measured with a capillary with benzene. The DOI after 530 minutes is 9.9 %. b) PXRD patterns of the resulting particles after irradiation with 313 nm of the precursor.....43

Figure 28 - PXRD of 2D-AzoC₂ before (black) and after (grey) 6 hours of irradiation at 313 nm.....44

Figure 29 – a) UV/Vis absorption measurement of dispersed particles of 2D-AzoC₂ during the irradiation with 313 nm. b) Intensity of absorbance maximum of AzoC₂ (328 nm) referenced to the absorption of the PbBr₄ layers (409 nm). c) ¹H-NMR of 2D-AzoC₂ (top), 2D-AzoC₄ (middle) and 2D-AzoC₁₂ (bottom) after irradiation dissolved in MeOD. DOI is 2.5 %, 12.3 % and 7.8 % respectively. d) Schematic representation of the crystal phase during irradiation at 313 nm.45

Figure 30 – Energy level diagram of 2D-AzoC₂, 2D-AzoOC₄ and 2D-AzoOC₁₂ in dependency to the distance between the perovskite layer and the azobenzene moiety. UV/Vis and PESA measurements are provided in **Figure A13**.47

Figure 31 – PL spectra of a) 2D-AzoC₂, b) 2D-AzoC₄ and c) 2D-AzoC₁₂ excited with an Xe-lamp at 350 nm.48

Figure 32 - Schematic overview of the observed PL in LHPs based on azobezene ligands. The excited state of the ligand is quenched by an electron (or energy) transfer to

the PbBr₄ layers, when the spacer length is short (AzoC₂ and AzoC₄). A long spacer suppresses the quenching event and emission of the azobenzene is observed (AzoC₁₂).

.....	49
Figure 33 - SEM images of MAPbBr ₃ NPs from the antisolvent synthesis with a) AzoC ₁ , b) AzoC ₂ , c) AzoC ₄ and d) AzoC ₁₂ . Scalebar = 1 μm.....	51
Figure 34 - a) PXRD measurements of 3D-AzoC ₂ (black) with reference taken from [237]. b) Fourier transform infrared (FT-IR) spectra of non-functionalized MAPbBr ₃ phase (black), AzoC ₂ (red) and 3D-AzoC ₂ (blue). Wavenumbers at 2991 cm ⁻¹ , 832 cm ⁻¹ , 765 cm ⁻¹ , 727 cm ⁻¹ and 685 cm ⁻¹ are highlighted in grey as significant vibrations for the azobenzene. c) Schematic representation of surface functionalized 3D-AzoC ₂ and d) normalized UV/Vis absorption spectrum of 3D-AzoC ₂ dispersed in toluene (black) and AzoC ₂ in H ₂ O (grey, dashed). Signals of azobenzene (yellow) and MAPbBr ₃ (blue) are highlighted.	52
Figure 35 – Energy level diagram of 3D-AzoC ₁ , 3D-AzoC ₂ , 3D-AzoOC ₄ and 3D-AzoOC ₁₂ in dependency to the distance between the perovskite phase and the azobenzene moiety. UV/Vis and PESA measurements are provided in Figure A16	54
Figure 36 - a) UV/Vis absorption spectra of 3D-AzoC ₂ during the irradiation at 313 nm. b) Absorption maximum at 328 nm of AzoC ₂ at the surface of MAPbBr ₃ particles (black) and in solution (grey) c) ¹ H-NMR spectra of dissolved 3D-AzoC ₂ before (top) and after irradiation at 313 nm for 600 sec (bottom).....	55
Figure 37 - DOI of the azobenzene ligands attached to the MAPbBr ₃ particles (blue) and in solution (orange).....	56
Figure 38 – Time-resolved PL decay of dispersed particles in toluene of 3D-AzoC ₁ (black), 3D-AzoC ₂ (dark-grey), 3D-AzoC ₄ (grey) and 3D-AzoC ₁₂ (light-grey). Radiative recombination at 530 nm of the semiconductor phase is observed. Photographs of dispersed particles under UV-irradiation with AzoC ₂ (left) and dodecylammonium bromide (DABr) at the surface.	57
Figure 39 – TA spectra with excitation at 398 nm of a) 3D-AzoC ₁ , b) 3D-AzoC ₂ and c) 3D-AzoC ₁₂ . d) Decay of the ground-state bleach after the excitation at 398 nm for 3D-AzoC ₁ (at 533.5 nm, in black), 3D-AzoC ₂ (at 500 nm, in dark grey) and 3D-AzoC ₁₂ (at 515 nm, in light grey).	58
Figure 40 – Schematically overview of the photoinduced isomerization of the synthesized Azo ligands between the perovskite layers (left, 2D phase) and on the surface of hybrid perovskite particles (right, 3D phase). When integrated into the semiconductor phase, no	

photoswitching is available due to steric hindrance. However, surface bound ligands show an improved photoswitching reaction due to a charge carrier transfer from the perovskite to the ligands.60

Figure 41 – SEM images of precipitates with a) 0.7 eq AzoC₂, b) 0.5 eq AzoC₂ and c) 0.3 eq AzoC₂. Scalebar = 1 μm d) PXRD patterns of the precipitates with 0.7 eq AzoC₂ (top), 0.5 eq AzoC₂ (middle) and 0.3 eq AzoC₂ (bottom). e) Overview of the found band gaps determined with UV/Vis reflectance spectroscopy using the Kubelka-Munk analysis (see **Figure A20**).....61

Figure 42 - a) PXRD patterns of RPP^{RT}_{0.5}-AzoC₂ (top, black), RPP^{-10 °C}_{0.5}-AzoC₂ (middle, dark green) and RPP^{-20 °C}_{0.5}-AzoC₂ (bottom, light blue). SEM images of b) RPP^{RT}_{0.5}-AzoC₂, c) RPP^{-10 °C}_{0.5}-AzoC₂ and d) RPP^{-20 °C}_{0.5}-AzoC₂.62

Figure 43 - a) Overview of the band gaps for the particles obtained at varying temperature. Determination occurs with UV/Vis reflection spectroscopy with subsequent Kubelka-Munk analysis (see **Figure A21**). b) PL spectra of the dispersed particles in toluene obtained at varying temperature. Excitation occurred with an Xe-lamp at 380 nm.63

Figure 44 - Chemical structure of Fc ligands with n=2,3,4,5,665

Figure 45 – a) UV/Vis spectrum of FcC₂Br in H₂O with energy scheme of the MO alignment. The HOMO-LUMO transition at ~450 nm occurs from the a_{1g} MO to the e*_{1g} MO. b) Schematic representation of the oxidation/reduction process of Fc derivatives and c) UV/Vis spectrum of FcC₂Br in H₂O after oxidation with Ce(SO₄)₂. A new absorption band is found which is attributed to a transition from a deeper lying MO into the emerging SOMO e_{2g}, which now lies above the initial HOMO a_{1g}.66

Figure 46 – SEM images of precipitations with PbBr₂ and a) FcC₂Br, b) FcC₃Br, c) FcC₄Br, d) FcC₅Br and e) FcC₆Br. Scalebar = 1 μm.....67

Figure 47 – Experimental PXRD patterns of precipitation products with PbBr₂ and FcC₂Br (bottom, blue), FcC₄Br (middle, dark green) and FcC₆Br (top, light green). Reflections were indicated based on the crystal structure analysis, which will be described in the following.....68

Figure 48 – a) Crystal structure of Fe(C₃H₇NO)₆Pb₂Br₆ viewed from the b-direction. Hydrogen atoms were removed for clarity. b) Fe²⁺ cation which is coordinated octahedrally by six dimethylformamide (C₃H₇NO = DMF) solvent molecules. In solution, a ligand exchange takes place due to an excess of DMF.....69

Figure 49 – Crystal structure of $(\text{FcC}_2)\text{PbBr}_3$ viewed from the a) b-direction, b) c-direction and c) a-direction (without Fc	71
Figure 50 – Crystal structure of $(\text{FcC}_4)_4\text{Pb}_3\text{Br}_{10}$ viewed from the a) a-direction, b) b-direction and c) c-direction (without Fc ligands). Hydrogen atoms are removed for clarity.	72
Figure 51 – Crystal structure of $(\text{FcC}_6)_2\text{PbBr}_4$ viewed from the a) a-direction, b) b-direction and c) c-direction (without Fc ligands). Hydrogen atoms are removed for clarity.	73
Figure 52 - a) Energy level alignment of the obtained particles with FcC_nBr ($n=2,3,4,5,6$). UV/Vis reflectance spectroscopy with Kubelka-Munk analysis and PESA measurements are provided in Figure A31 and Figure A32 . b) UV/Vis absorption spectra of the particles dispersed in toluene. The color coding corresponds to that from a).	76
Figure 53 - Quantum well structures of the obtained materials for $(\text{FcC}_2)\text{PbBr}_3$, $(\text{FcC}_4)_4\text{Pb}_3\text{Br}_{10}$ and $(\text{FcC}_6)_2\text{PbBr}_4$ (left to right). VBM, CBM, HOMO and LUMO levels were calculated using a combination of UV/Vis reflectance spectroscopy and PESA.	79
Figure 54 - a) Cyclic voltammogram (CV) of $(\text{FcC}_2)\text{PbBr}_3$ (black) on ITO (lightblue) at scan speed of 10 mV/sec in 0.1 M LiTFSI in HFE:DEC=(97:3). (b) Current vs. time for sixth cycle (10 cycles see Figure A35).	81
Figure 55 - a) Normalized UV/Vis reflectance spectra of the particles before (red) and after (blue) oxidation. Inset: Photographs of the ITO substrates coated with $(\text{FcC}_2)\text{PbBr}_3$. b) PL spectra of $(\text{FcC}_2)\text{PbBr}_3$ on ITO before (red) and after (blue) oxidation with emission maximum at 494 nm. Excitation at 310 nm with an Xe-lamp.	82
Figure 56 - SEM images of the particles a) before oxidation and after oxidation with b) 0.1 eq c) 0.2 eq, d) 0.5 eq, e) 1.0 eq and f) 2.0 eq of the oxidant. a)-e) scalebar = 1 μm , f) scalebar = 2 μm	84
Figure 57 - a) Photographs of glass substrates with a film of dried particles. b) UV/Vis absorption spectra of the dispersed particles in toluene with varying Fe^{3+} content. The color coding of the varying Fe^{3+} contents is used for further diagrams and is no longer specified there. c) PL emission spectra of dispersed particles with 0.0 % (orange) and 63.3 % (green) Fe^{3+} with excitation at 310 nm.	85
Figure 58 - a) Normed Kubelka-Munk plots of the (oxidized) particles with evaluation of the band gap. Two linear regression lines are fitted to the slope and the baseline. b) Band gap vs. Fe^{3+} content in the particles determined with XPS.	86

Figure 59 - Representation of the *ab initio* calculations using the BAND code for a) the intrinsic (FcC₂)PbBr₃, b) with 25% of the ligands oxidized with (ClO₄)⁻, c) with 50% of the ligands oxidized with (ClO₄)⁻. The location of the unpaired paramagnetic spin was calculated and made visible with spin density calculations (blue isosurface). Hydrogen atoms were removed for clarity; Experimentally determined band structure of (FcC₂)PbBr₃ d) in the intrinsic state showing why PET occurs upon excitation (Exc) at 310 nm, e) after the oxidation with (ClO₄)⁻ at low oxidation degrees (radiative recombination/emission (Em) occurs due to the new energy alignment of the single occupied molecular orbital (SOMO) and f) at high oxidation degrees with the emergence of the new SOMO_{band}.....88

Figure 60 - Schematic overview of the observed effects in (FcC₂)PbBr₃. In the ground state, no radiative recombination is observed, similar to an indirect semiconductor. When oxidized, however, radiative recombination is possible.89

Figure 61 - a) UV/Vis absorption spectra recorded during the reaction of RPP_{0.5} in DCM. Baseline before addition of the precursor = yellow, final measurement = red. Temporal sequence of the spectra is from black to white. b) Normed absorption at 402 nm (blue) and 434 nm (green) over the timescale of 2100 sec.....91

Figure 62 - SEM images of a) RPP_{0.5} with scalebar = 1 μm and b) RPP_{1.0} with scalebar = 2 μm and TEM images of c) RPP_{2.0} with scalebar = 100 nm.93

Figure 63 - a) Normed PL spectra of RPP_{0.5} (blue), RPP_{1.0} (dark green) and RPP_{2.0} (light green) with excitation at 310 nm. b) Band gap alignment of the RPPs based on UV/Vis absorption measurements and PESA measurements shown in **Figure A44a-c**. HOMO and LUMO levels of FcC₆Br are calculated from PESA measurements shown in **Figure A44d** and UV/Vis absorption measurement shown in **Figure A28a**.....94

Figure 64 - Structural formula and designation of the three surfactants based on heterocycles with varying hetero atom. Atomic radii of the heteroatoms suggest that there is little change in the size of the functional group.97

Figure 65 - a) PXRDs of 2D-O-EABr (top), 2D-S-EABr (middle) and 2D-Se-EABr (bottom). The basal distance of the n=1 LHP is colored. SEM images of b) 2D-O-EABr, c) 2D-S-EABr and d) 2D-Se-EABr with scalebar = 5 μm.98

Figure 66 - Alignment of energy levels of 2D-O-EABr (left, blue), 2D-S-EABr (middle, yellow) and 2D-Se-EABr (right, black) determined from UV/Vis absorption spectroscopy and PESA given in **Figure A46-Figure A49**..... 100

Figure 67 - a) PXRD of the particles with varying Iodine content from 0 % (top) to 100 % (bottom). b) (001) lattice plane marked in green and c) (110) lattice plane marked in grey. (see also a)) d) Distance d of the (110) lattice plane in dependency of the iodine content. 103

Figure 68 - a) Photograph of particles with varying Iodine/Bromine ratio (increasing from left to right) b) UV/Vis of dispersed particles with iodine content of 0%, 12%, 30%, 60% and 100% (from left to right), and c) Band gap determined from absorption spectra (black) and PL spectra (grey) (see **Figure A52**). Iodine and bromine ratio are determined from EDX measurements shown in **Figure A50**. 104

Figure 69 - Band alignment of VBM and CBM for (S-EA)₂PbBr₄ (left) and (S-EA)₂PbI₄ (right, PESA see **Figure A52b**). It is noted that the mixed halide phases are shown purely from the band gap calculation, but no experimental determination of the E_{VBM} using PESA was performed. 105

Figure 70 - a) UV/Vis kinetic measurement of DMF based precursor with specified ratio of starting materials for the precipitation an RPP with n=2. First measurement (blue) and last measurement (red) are colored. b) UV/Vis absorption (black) and PL spectra (grey) of particles after synthesis dispersed in toluene. Excitation occurred at 350 nm c) SEM image of particles. d) PXRD measurement of the particles (black, top) with reference of MAPbBr₃ (green) and (S-EA)₂PbBr₄ (blue). 107

Figure 71 - a) PXRD of (S-EA)₂(MA)Pb₂Br₇ (top) and (S-EA)₂PbBr₄ (bottom). Reflection of the basal distance (d₍₀₀₁₎) are colored; SEM images of b) (S-EA)₂(MA)Pb₂Br₇ and c) (S-EA)₂PbBr₄ with scalebar = 1 μm and d) UV/Vis absorption (black) with λ_{max} = 443 nm (2.80 eV) and PL emission (grey) spectra with λ_{max} = 445 nm (2.79 eV) of (S-EA)₂(MA)Pb₂Br₇. 110

Figure 72 – Overview of the functional ligands used for the synthesis of 2D LHPs. 111

9 List of tables

Table 1 - DFT calculated distances from the ammonium head group ($-NH_3^+$) to the terminal carbon group (C_4) of the azobenzene moiety.	38
Table 2 – Relative energy of molecular orbitals of the azobenzene ligands determined and calculated using PESA and UV/Vis measurement.....	39
Table 3 - Basal distances of 2D-AzoC _n (n = 2,4,12) phases determined with PXRD and SAXS.....	42
Table 4 - Summary of relative energies of the VBM and CVM, determined with a combination of UV/Vis reflection with Kubelka-Munk analysis and PESA of all 2D LHPs with AzoC _n . Spectra are found in Figure A13	47
Table 5 – Summary of relative energies of the VBM and CBM, determined with a combination of UV/Vis reflection with Kubelka-Munk analysis and PESA of all functionalized particles. Spectra are found in Figure A16	54
Table 6 - Crystal structure data determined for precipitates with FcC _n Br and PbBr ₂ . Crystal structures for n=2,4 were determined with 3D ED. Crystal structure of n=6 was modelled using DFT calculations.....	75
Table 7 - Content of Fe ³⁺ of the particles after oxidation.....	84
Table 8 - Ratios of the precursors used for the formation of RPPs.	90
Table 9 - Calculated layer thicknesses for (FcC ₆) ₂ (MA) _{n-1} Pb _n Br _{3n+1}	92
Table 10 - Band gap found from UV/Vis and PL for varying layer thicknesses.	94
Table 11 - Composition of the mixed halide LHPs with S-EAX ligand. Iodine ratio is determined with EDX, shown in Figure A50	102
Table 12 - Calculated layer thicknesses for (S-EA) ₂ (MA) _{n-1} Pb _n Br _{3n+1}	109
Table 13 - Precursor concentrations used for the synthesis of RPPs with AzoC ₂ Br. ..	127
Table 14 - Precursor concentrations used for the synthesis of RPPs with AzoC ₂ Br. ..	128
Table 15 - Precursor concentrations used for the synthesis of mixed halide 2D-S-EAX phases.....	129
Table 16 – Crystal data for hybrid lead bromide phase with Fe(C ₃ H ₇ NO) ₆ ²⁺ complex obtained from SCXRD.	176
Table 17 – Fractional coordinates of crystal structure of Fe(C ₃ H ₇ NO) ₆ Pb ₂ Br ₆	177
Table 18 - Elemental composition of the particles after oxidation with 2.0 eq of oxidant according to EDX. The Si signal stems from the substrate.....	182
Table 19 - Elemental composition of (Se-EA) ₂ PbBr ₄ evaluated from EDX. The ratio between Se (~2), Br (~4) and Pb (~1) corresponds to the chemical composition. However, a high C-proportion suggests organic impurities.....	186

10 List of abbreviations

1D	one dimensional
2D	two dimensional
2D-AzoC _n	layered hybrid perovskite with azobenzene ligands
3D	three dimensional
3D ED	three dimensional electron diffraction
3D-AzoC _n	surface functionalized hybrid perovskite particles with azobenzene ligand
ARPES	angle resolved photoelectron spectroscopy
ATR	attenuated total reflection
Azo	azobenzene
AzoC ₁	1-(4-(phenyldiazenyl) phenyl)methyl-1-ammonium bromide
AzoC ₁₂	12-(4-(phenyl-diazenyl)phenoxy)dodecyl-1-ammonium bromide
AzoC ₂	2-(4-(phenyldiazenyl)phenyl)ethyl-1-ammonium bromide
AzoC ₄	4-(4-(phenyldiazenyl)phenoxy)butyl-1-ammonium bromide
Boc	tert-butyloxycarbonyl
CB(M)	conduction band (minimum)
CE	counter electrode
cp	cyclopentadienyl
CV	cyclic voltammetry
DABr	C ₁₂ H ₂₅ NH ₃ Br; dodecylammonium bromide
DAI	C ₁₂ H ₂₅ NH ₃ I; dodecylammonium iodide
DCM	dichloromethane
DEC	Diethyl carbonate
DMAP	dimethylamino pyridine
DMF	dimethyl formamide
DMSO	dimethylsulfoxide
DOI	degree of isomerization
EDC-HCl	1-ethyl-3(3'-dimethylaminopropyl)carbodi-imide hydrochloride
EDX	energy dispersive X-ray
eq	equivalent
ESI-MS	electron spray ionization mass spectroscopy
Et ₂ O	diethylether

EtOAc	ethyl acetate
EtOH	ethanol
FAX	CH(NH ₂) ₂ X (with X=Br,I); formamidinium halide
Fc	ferrocene
Fc ⁺	ferrocenium
FcC ₂ Br	2-(ferrocene carboxyl)ethyl-1-ammonium bromide
FcC ₃ Br	3-(ferrocene carboxyl)propyl-1-ammonium bromide
FcC ₄ Br	4-(ferrocene carboxyl)butyl-1-ammonium bromide
FcC ₅ Br	5-(ferrocene carboxyl)pentyl-1-ammonium bromide
FcC ₆ Br	6-(ferrocene carboxyl)hexyl-1-ammonium bromide
Fmoc	Fluorenylmethylcarbonyl protecting group
FMTMA	(ferrocenylmethyl) trimethylammonium
FT-IR	Fourier-transform infrared
FWHM	full-width half-maximum
GSB	groundstate bleach
HFE	hydrofluoroether
HOMO	highest occupied molecular orbital
IR	infrared
ITO	indium tin oxide
LARP	ligand-assisted reprecipitation
LED	light emitting diode
LHP	layered hybrid perovskite
LiTFSI	Lithiumbis(trifluoromethylsulfonyl)amide
LUMO	lowest unoccupied molecular orbital
MAPbX ₃	(CH ₃ NH ₃)PbX ₃ (with X=Cl,Br,I); Methylammonium lead halide
MAX	CH ₃ NH ₃ X (with X=Br ,I); Methylammonium halide
MeOD	CD ₃ OD; methanol (deuterated)
MeOH	methanol
MO	molecular orbital
MOF	metal organic framework
NC	nanocrystal
NEt ₃	triethylamine
NMR	nuclear magnetic resonance
OA	oleylamine
O-EABr	2-furane ethylammonium bromide

OLABr	oleylammonium bromide
PE	pentane
PEA	phenylethyl ammonium
PES(A)	photoelectron spectroscopy (on air)
PET	photoinduced electron/energy transfer
PIA	photoinduced absorption
PL	photoluminescence
PLQY	photoluminescence quantum yield
PXRD	powder X-ray diffraction
QW	quantum-well
RE	reference electrode
RPP	Ruddlesden-Popper phases
SAM	self-assembled monolayer
SAXS	small angle X-ray scattering
SCE	saturated Calomel electrode
SCXRD	single crystal X-ray diffraction
SE	stimulated emission
S-EABr	2-thiophene ethylammonium bromide
sec	second
Se-EABr	2-selenophene ethylammonium bromide
SEM	scanning electron microscopy
SHG	second harmonic generator
SOMO	single occupied molecular orbital
TA(S)	transient absorption (spectroscopy)
TEG	triethylene glycole
TEM	transmission electron microscopy
TFA	trifluoroacetic acid
THF	tetrahydrofurane
UPS	UV photoelectron spectroscopy
UV	Ultraviolet
UV/Vis	Ultraviolet/Visible
VB(M)	valence band (maximum)
WE	working electrode
XPS	X-ray photoelectron spectroscopy

11 Appendix

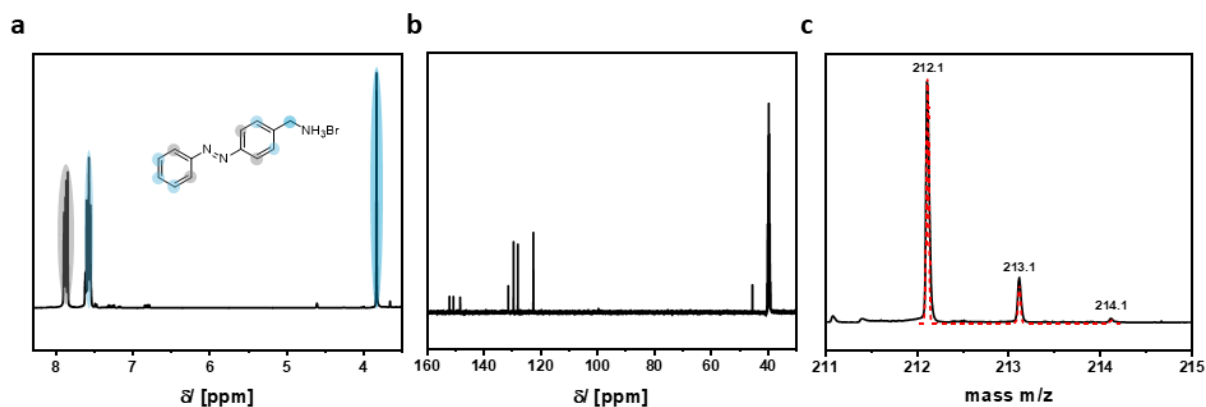


Figure A1 – a) ¹H-NMR spectrum of AzoC₁ in DMSO-d₆, H-atoms are marked. b) ¹³C-NMR spectrum of AzoC₁ in DMSO-d₆, c) ESI-MS spectrum of AzoC₁, black line: experimental, red dashed line: calculated. For a quantitative evaluation of the spectra refer to the experimental section in **chapter 6.1**.

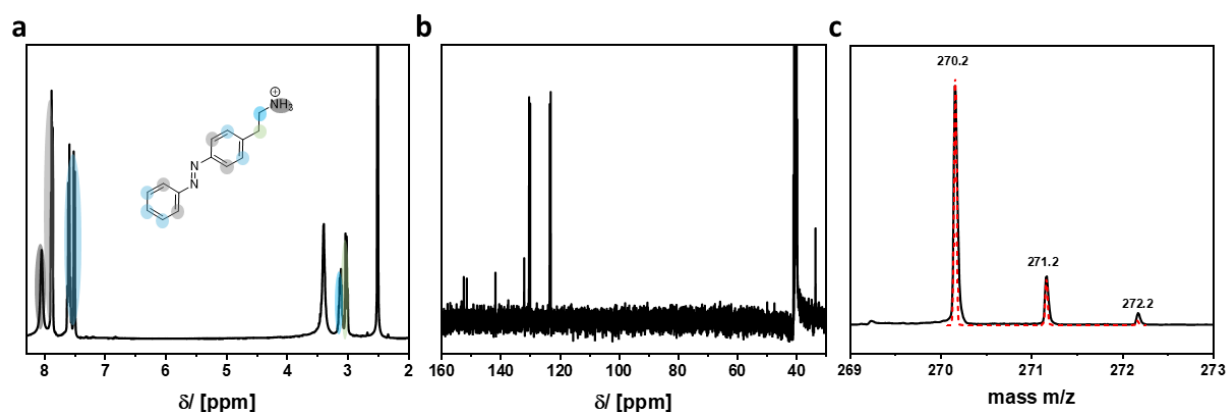


Figure A2 – a) ¹H-NMR spectrum of AzoC₂ in DMSO-d₆, H-atoms are marked. b) ¹³C-NMR spectrum of AzoC₂ in DMSO-d₆, c) ESI-MS spectrum of AzoC₂, black line: experimental, red dashed line: calculated. For a quantitative evaluation of the spectra refer to the experimental section in **chapter 6.1**.

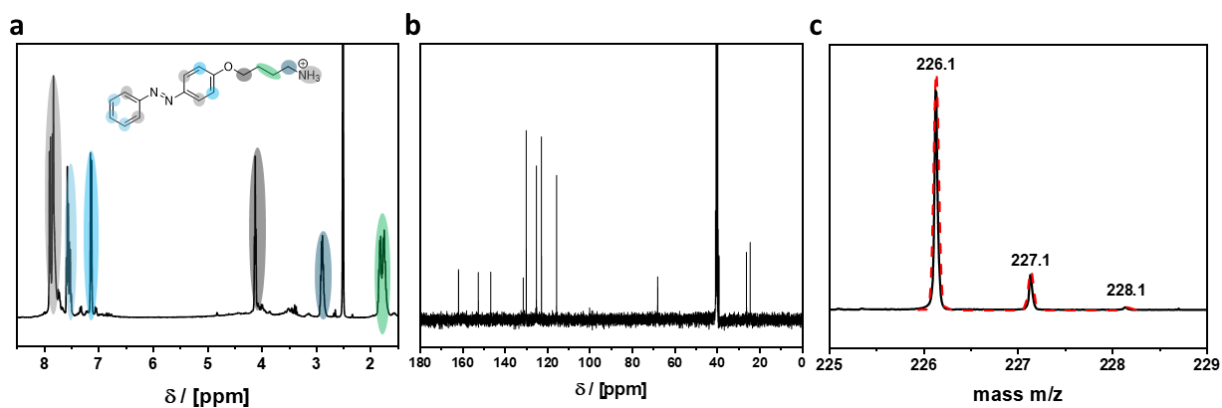


Figure A3 – a) ¹H-NMR spectrum of AzoC₄ in DMSO-d₆, H-atoms are marked. b) ¹³C-NMR spectrum of AzoC₄ in DMSO-d₆, c) ESI-MS spectrum of AzoC₄, black line: experimental, red dashed line: calculated. For a quantitative evaluation of the spectra refer to the experimental section in **chapter 6.1**.

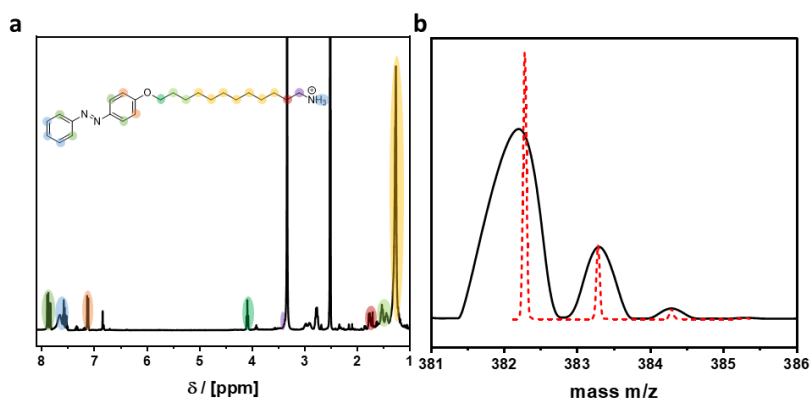


Figure A4 – a) ¹H-NMR spectrum of AzoC₄ in DMSO-d₆, H-atoms are marked. b) ESI-MS spectrum of AzoC₁₂, black line: experimental, red dashed line: calculated. For a quantitative evaluation of the spectra refer to the experimental section in **chapter 6.1**.

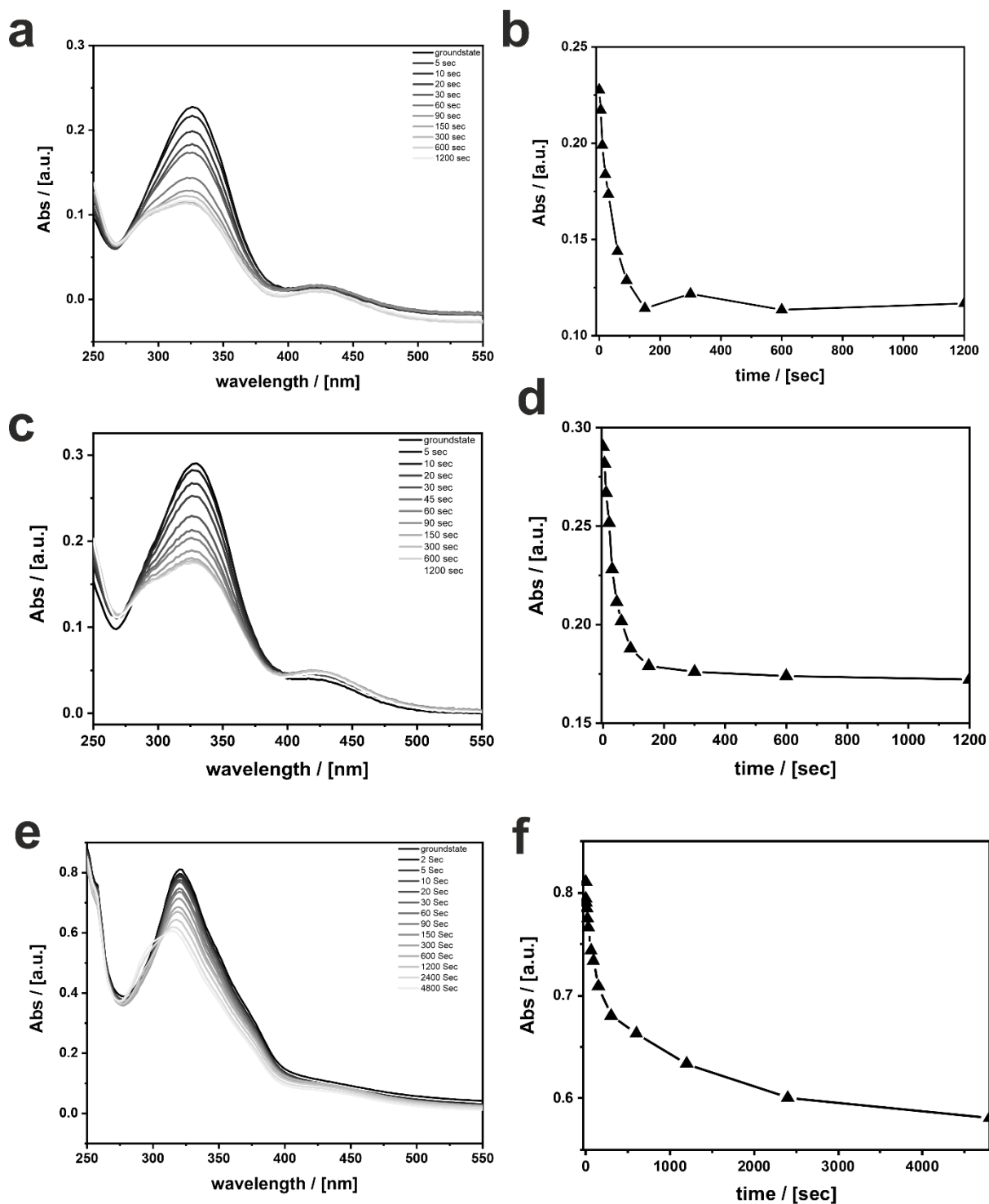


Figure A5 – UV/Vis absorption spectra during irradiation with 313 nm of a) AzoC₁, c) AzoC₄ and e) AzoC₁₂. The groundstate is marked in black, the spectrum at the end of the irradiation in light grey. Absorption of the maximum between 309 nm and 325 nm during the irradiation with 313 nm of b) AzoC₁, d) AzoC₄ and f) AzoC₁₂.

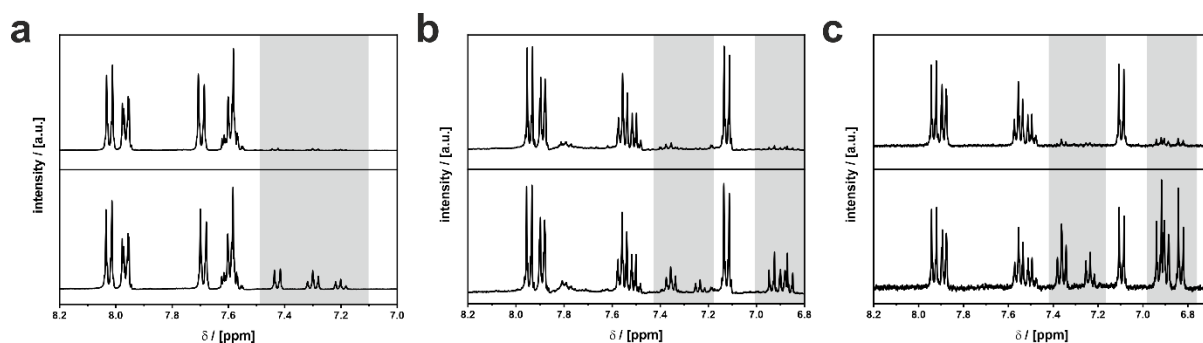


Figure A6 - a) $^1\text{H-NMR}$ from AzoC₁ in MeOD from 8.0 ppm to 7.2 ppm, before (top) and after irradiation (bottom) at 313 nm for 1 h. Highlighted in grey is the signal of the *cis*-isomer. DOI is 21.7%. b) $^1\text{H-NMR}$ from AzoC₄ in MeOD from 8.0 ppm to 7.2 ppm, before (top) and after irradiation (bottom) at 313 nm for 1 h. Highlighted in grey is the signal of the *cis*-isomer. DOI is 25.1%. and c) $^1\text{H-NMR}$ from AzoC₁₂ in MeOD from 8.0 ppm to 7.2 ppm, before (top) and after irradiation (bottom) at 313 nm for 1 h. Highlighted in grey is the signal of the *cis*-isomer. DOI is 50.7%.

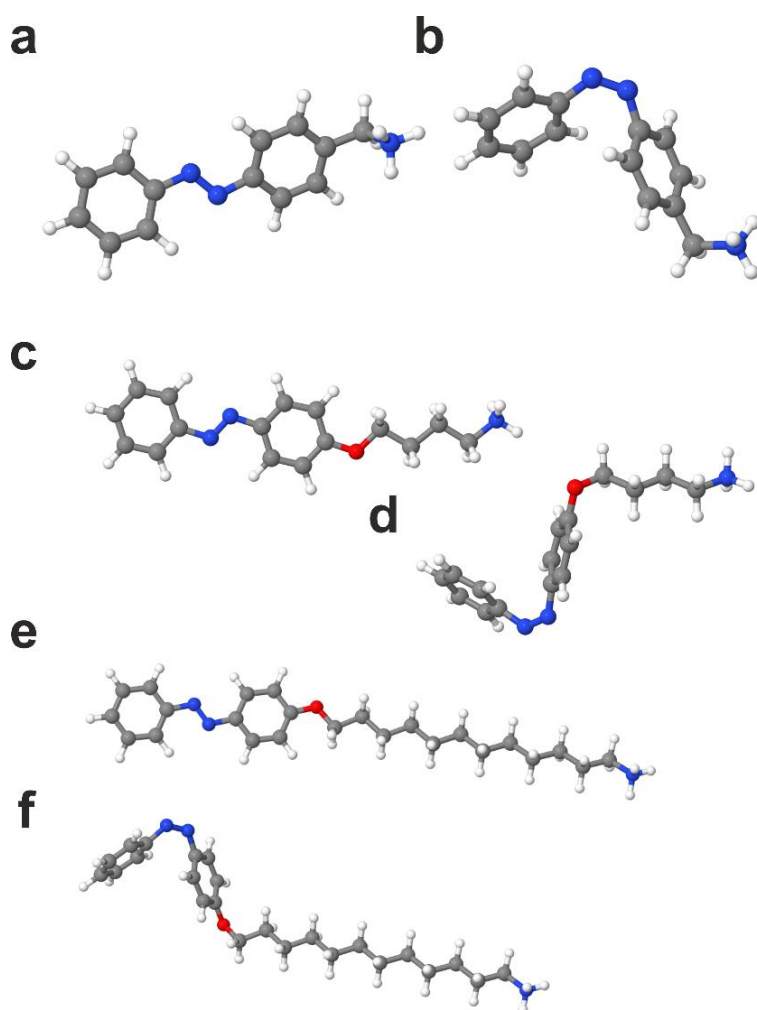


Figure A7 - DFT calculations of AzoC₁ in a) *trans* and b) *cis* conformation, AzoC₄ in c) *trans* and d) *cis* conformation and AzoC₁₂ in e) *trans* and f) *cis* conformation. All structures were created and measured with Jmol.

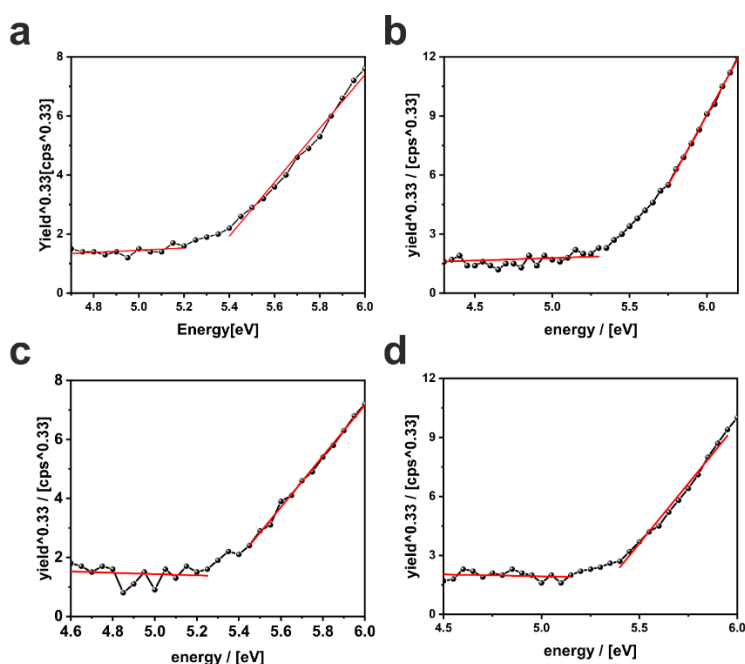


Figure A8 - PESA measurements of a) AzoC₁ b) AzoC₂, c) AzoC₄ and d) AzoC₁₂ measured as solid film on a glass substrate. Linear regression lines are fitted to the baseline and slope. The intersection of the linear regression lines gives the relative energy of the HOMO. Results are listed in **Table 2**.

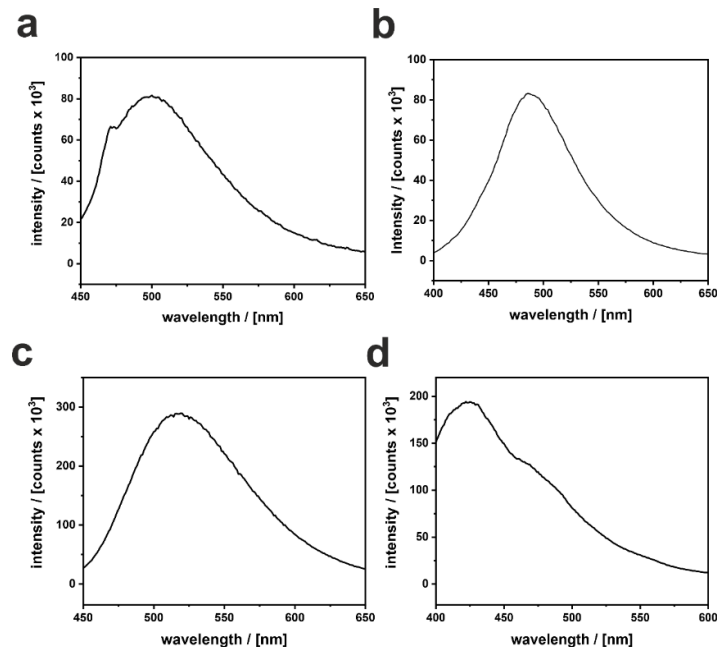


Figure A9 - PL spectra of a) AzoC₁ excited at 405 nm (laser) with a filter at 420 nm. An absorption maximum at 500 nm is found. b) AzoC₂ excited at 405 nm (laser) with a filter at 420 nm. An absorption maximum at 485 nm is found. c) AzoC₄ excited at 405 nm (laser) with a filter at 420 nm. An absorption maximum at 517 nm is found d) AzoC₁₂ excited at 405 nm (laser) with a filter at 420 nm. An absorption maximum at

430 nm and a shoulder at 502 nm is found, respectively. Presumably, the maximum at 430 nm is attributed to the initial excitation wavelength.

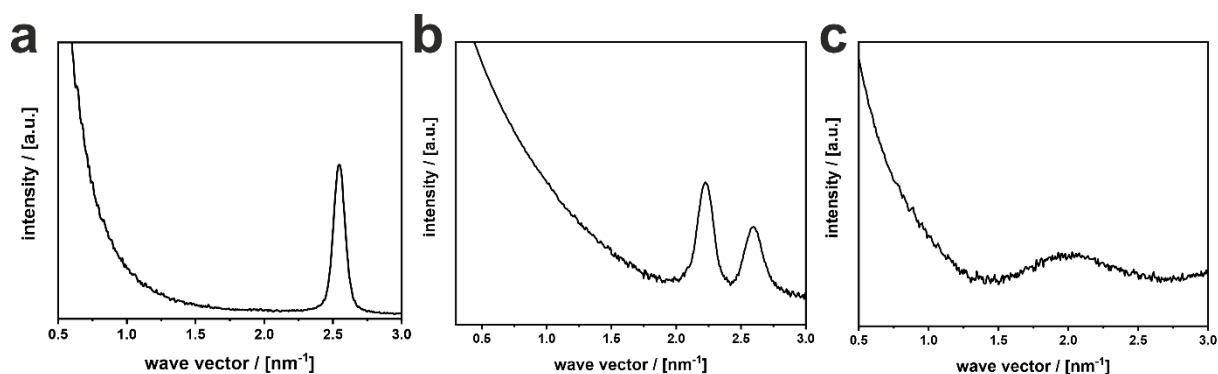


Figure A10 - Small angle X-ray scattering (SAXS) patterns of a) 2D-AzoC₂ with $q = 2.55 \text{ nm}^{-1}$ ($d_{(001)} = 2.47 \text{ nm}$), b) 2D-AzoC₄ with $q_1 = 2.23 \text{ nm}^{-1}$ ($d_{(001)} = 2.82 \text{ nm}$) and $q_2 = 2.60 \text{ nm}^{-1}$ ($d_{(001)} = 2.42 \text{ nm}$) and c) 2D-AzoC₁₂ with $q = 2.03 \text{ nm}^{-1}$ ($d_{(001)} = 3.10 \text{ nm}$)

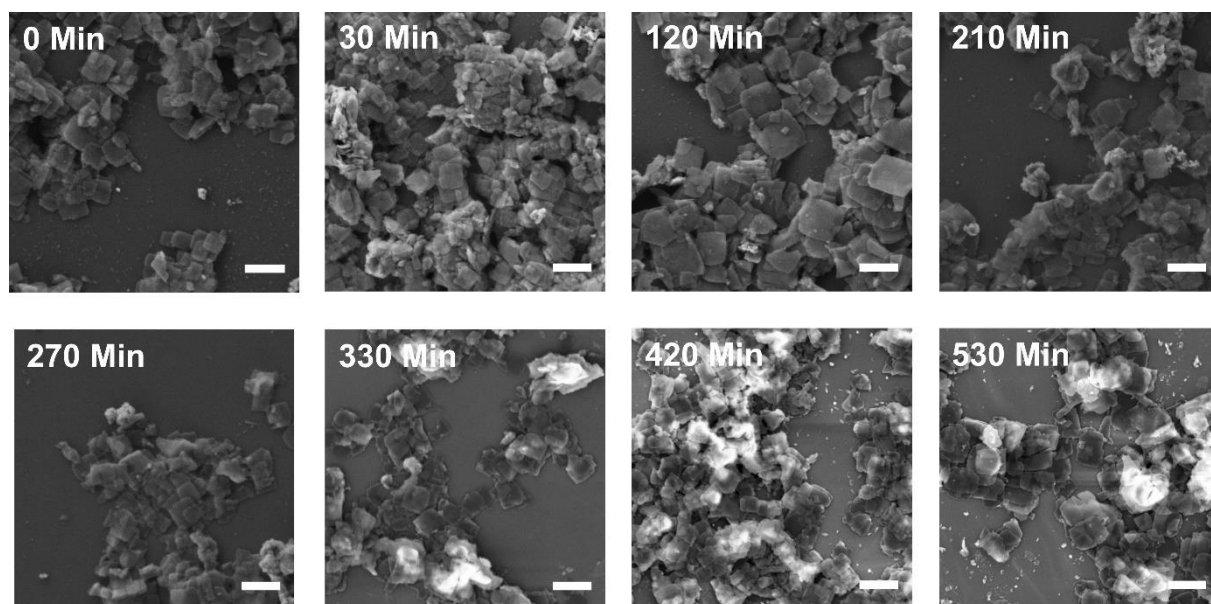


Figure A11 - SEM images of the particles which were synthesized with irradiated precursor. Irradiation occurred at 313 nm for the marked time. Scalebar = 1 μm

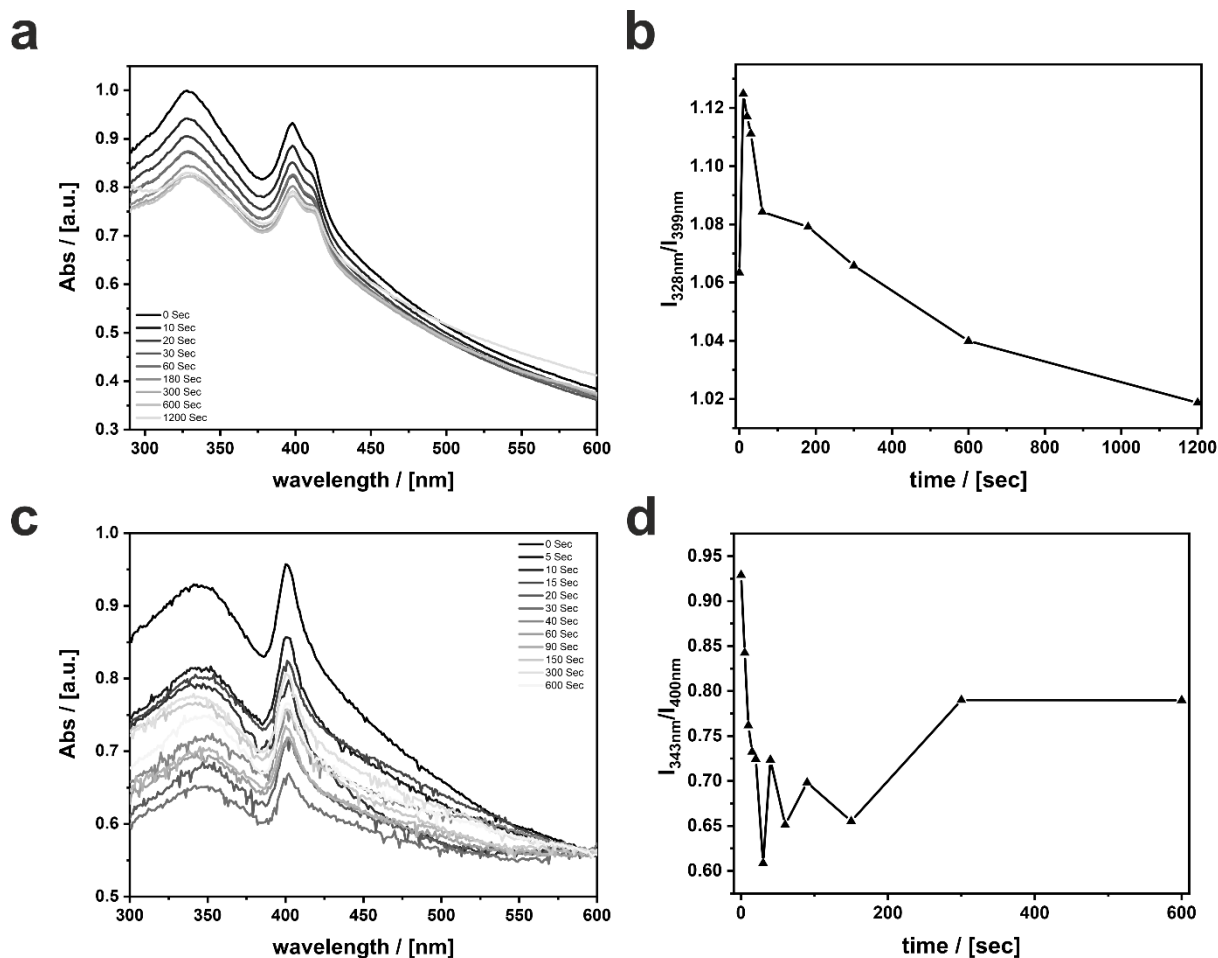


Figure A12 – a) UV/Vis absorption measurement of dispersed particles of 2D-AzoC₄ during the irradiation with 313 nm. b) Intensity of absorbance maximum of AzoC₄ (328 nm) referenced to the absorption of the PbBr₄ layers (399 nm). c) UV/Vis absorption measurement of dispersed particles of 2D-AzoC₁₂ during the irradiation with 313 nm. b) Intensity of absorbance maximum of AzoC₁₂ (343 nm) referenced to the absorption of the PbBr₄ layers (400 nm).

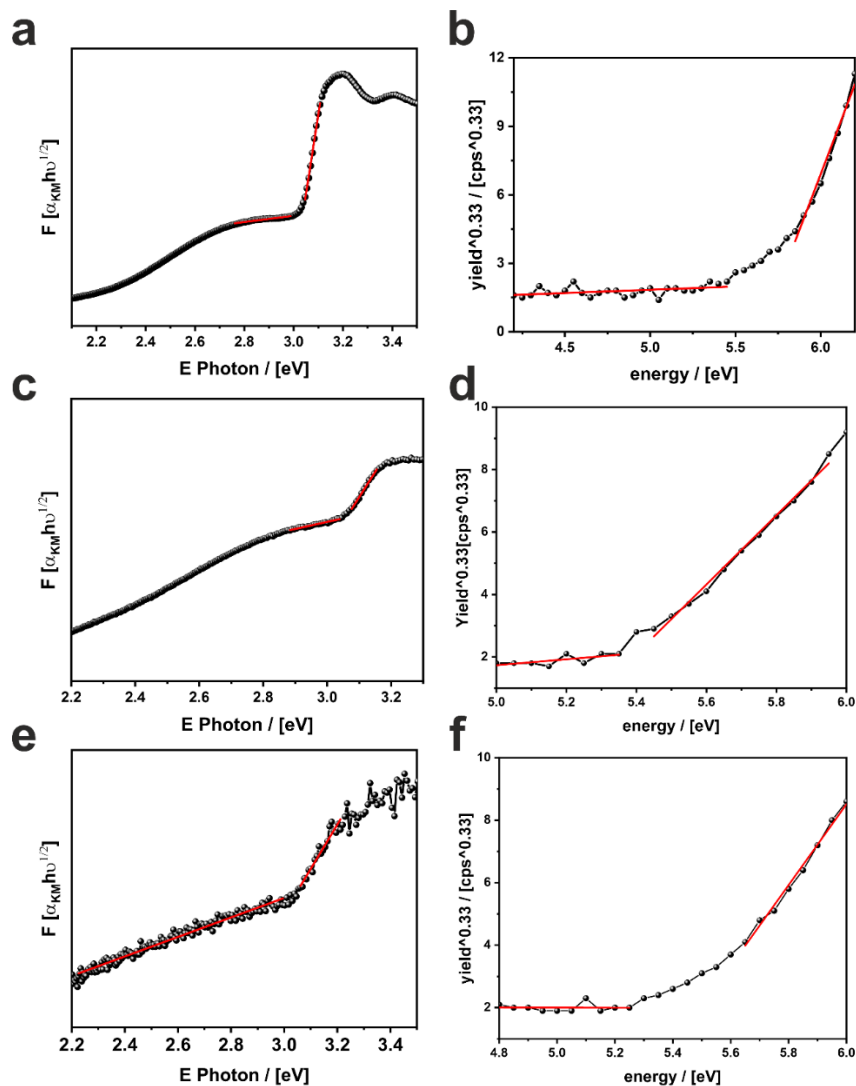


Figure A13 - a) UV/Vis and b) PESA measurement of 2D-AzoC₂ with $E_g = 3.10$ eV and $E_{\text{VBM}} = -5.57$ eV. c) UV/Vis and d) PESA measurement of 2D-AzoC₄ with $E_g = 3.06$ eV and $E_{\text{VBM}} = -5.42$ eV. e) UV/Vis and f) PESA measurement of 2D-AzoC₁₂ with $E_g = 3.04$ eV and $E_{\text{VBM}} = -5.52$ eV. The results are summarized in **Figure 30** and **Table 4**.

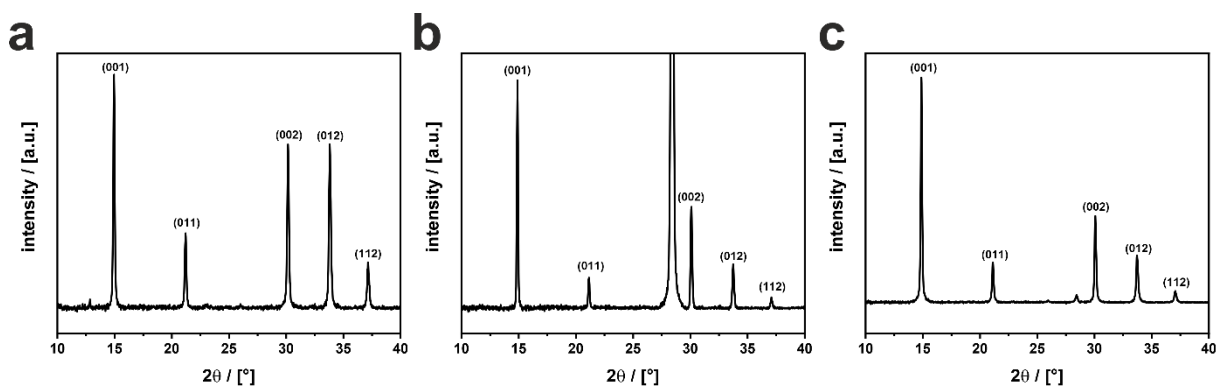


Figure A14 – a) PXRD of 3D-AzoC₂, b) PXRD of 3D-AzoOC₄, c) PXRD of 3D-AzoOC₁₂, all reflexes stem from the $\text{CH}_3\text{NH}_3\text{PbBr}_3$ (see **Figure 34a**), reflexes at $2\theta = 28^\circ$ stem from the Si-substrate.

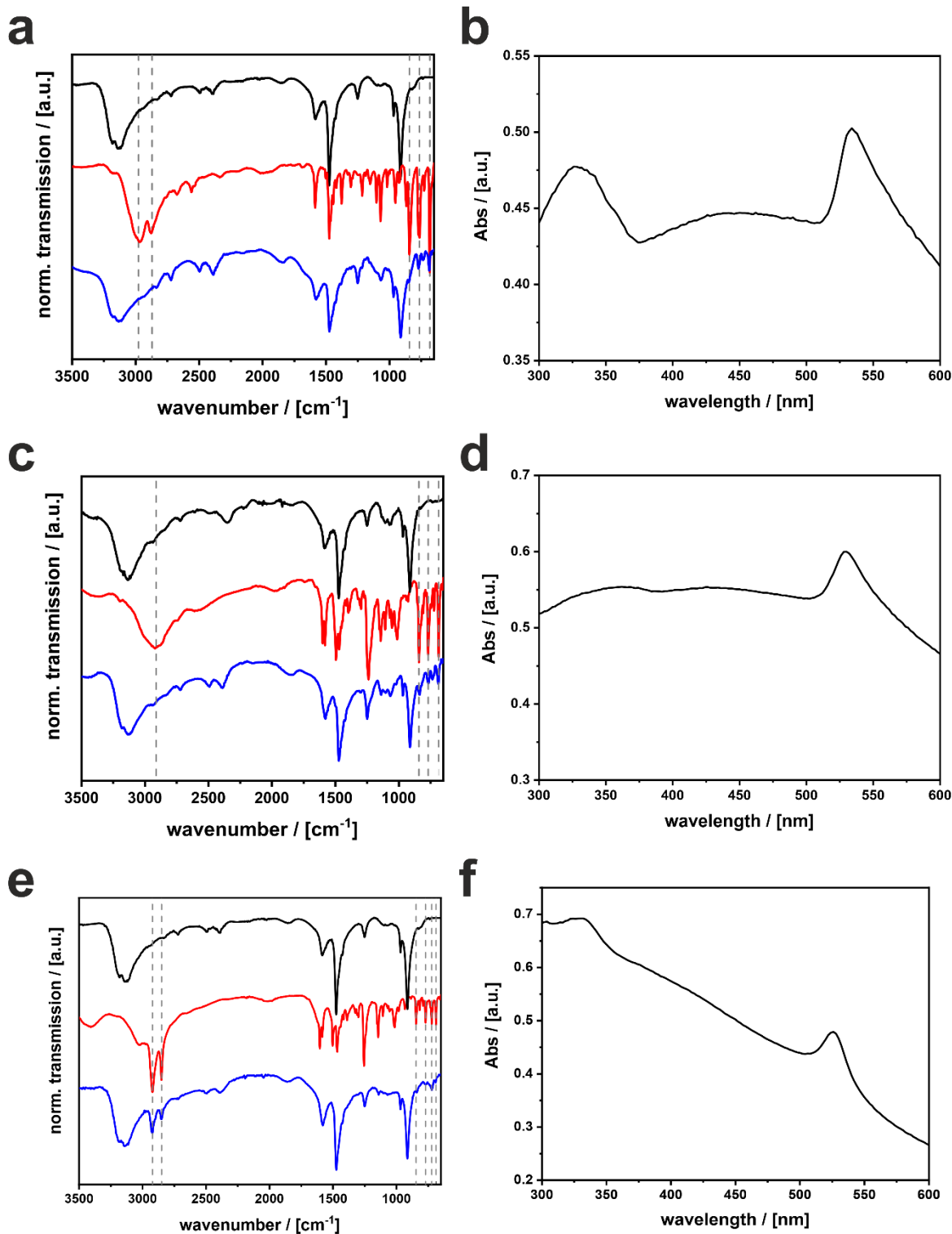


Figure A15 – a) IR spectrum of AzoC₁ (red), CH₃NH₃PbBr₃ (black) and 3D-AzoC₁ (blue) b) UV/Vis absorption of 3D-AzoC₁ in toluene, c) IR spectrum of AzoOC₄ (red), CH₃NH₃PbBr₃ (black) and 3D-AzoOC₄ (blue) d) UV/Vis absorption of 3D-AzoOC₄ in toluene, e) IR spectrum of AzoOC₁₂ (red), CH₃NH₃PbBr₃ (black) and 3D-AzoOC₁₂ (blue) f) UV/Vis absorption of 3D-AzoOC₁₂ in toluene.

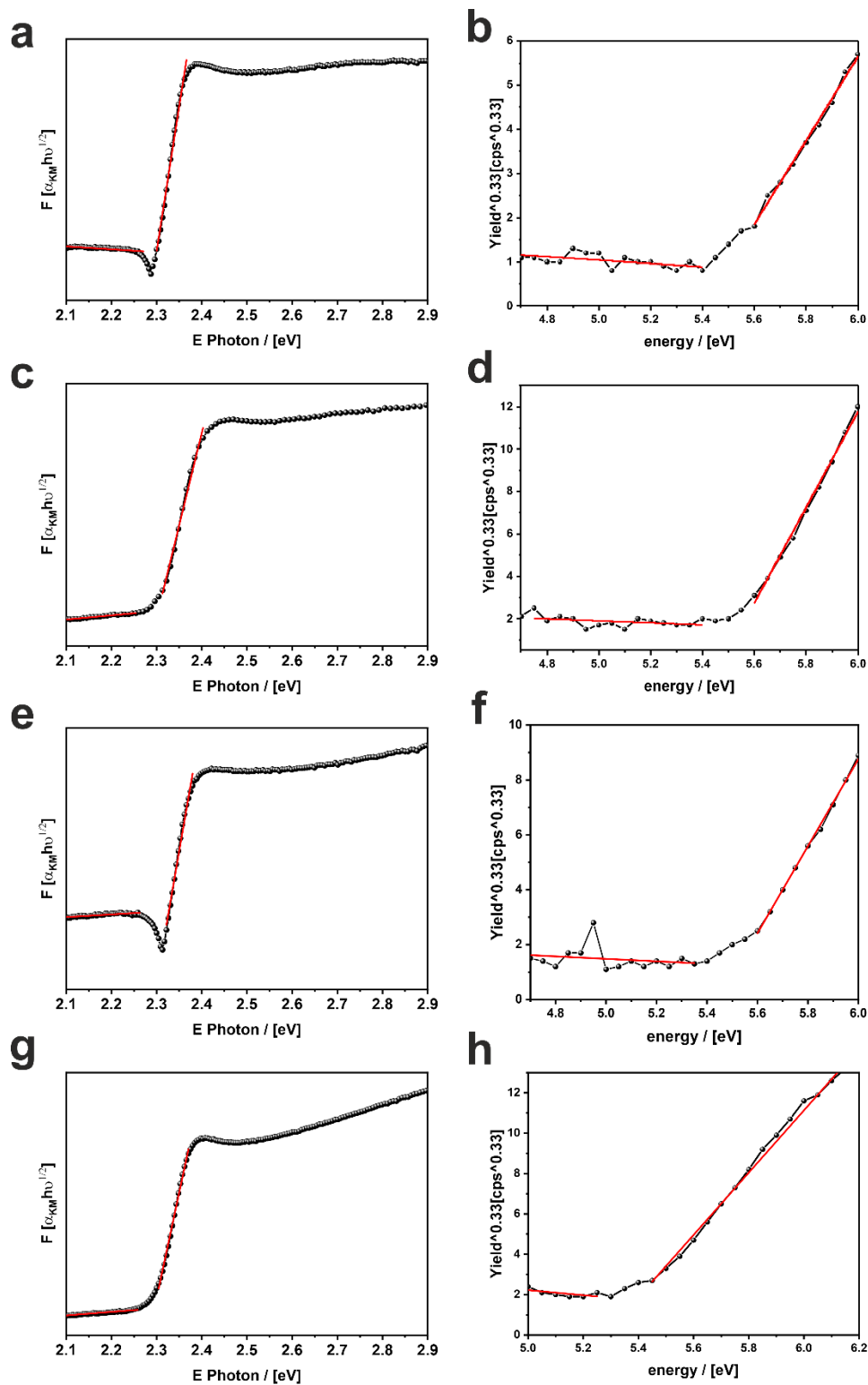


Figure A16 – a)+b) UV/Vis reflection with Kubelka-Munk analysis and PESA of 3D-AzoC₁, c)+d) UV/Vis reflection with Kubelka-Munk analysis and PESA of 3D-AzoC₂, e)+f) UV/Vis reflection with Kubelka-Munk analysis and PESA of 3D-AzoOC₄, g)+h) UV/Vis reflection with Kubelka-Munk analysis and PESA of 3D-AzoOC₁₂; intersection of baseline fit and slope fit give the band gap E_g respectively the relative energy E_{VBM} of the valence band maximum. All values are listed in **Table 5**.

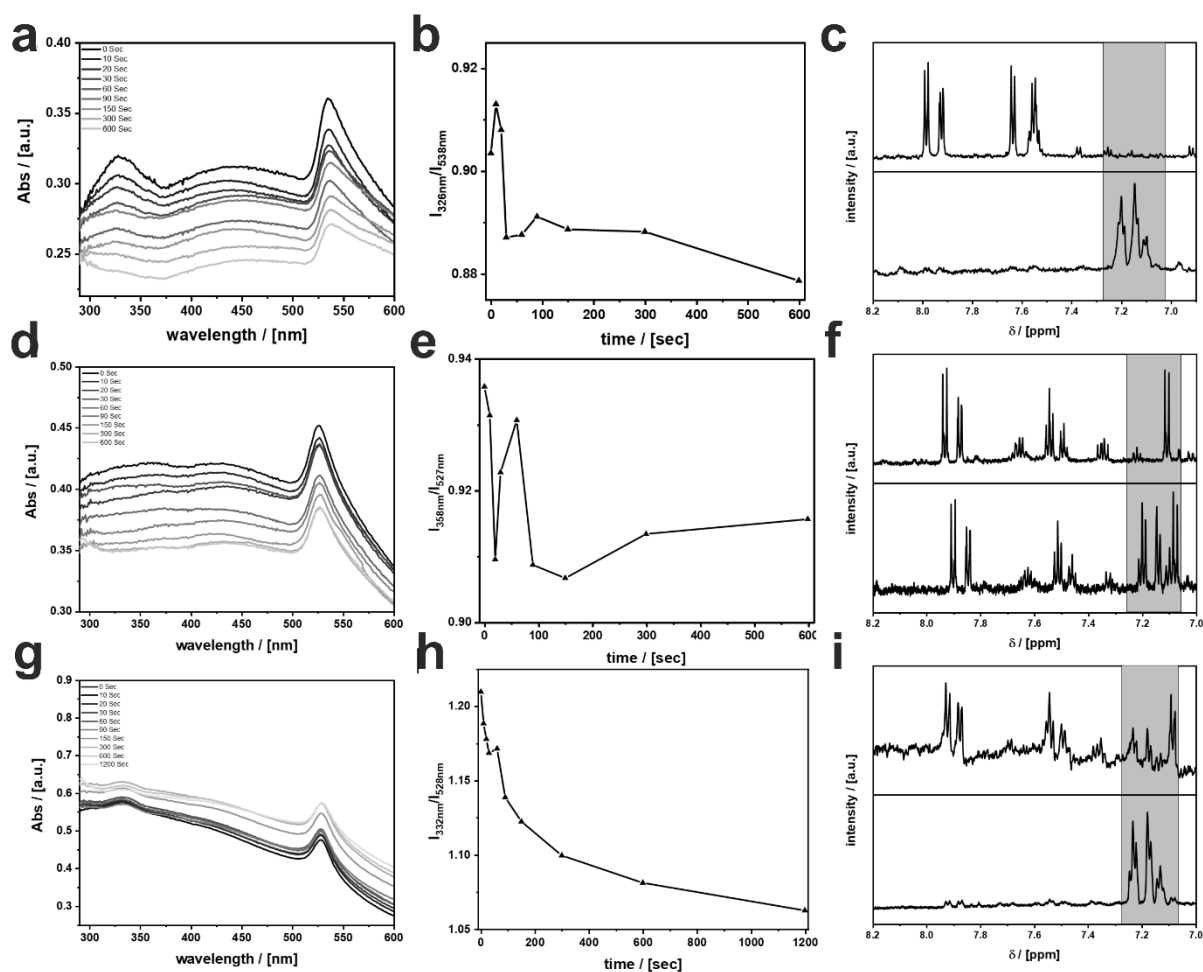


Figure A17 – a)+b) UV/Vis kinetic measurement of 3D-AzoC₁ in toluene over a timescale of 600 seconds. Because the dispersion is not stable, the absorbance of AzoC₁ at 326 nm is referenced to the absorbance of the excitonic band gap at 538 nm and plotted against the time, c) ¹H-NMR spectrum of dissolved 3D-AzoC₁ before (top) and after irradiation with 313 nm for 600 seconds (bottom), d)+e) UV/Vis kinetic measurement of 3D-AzoOC₄ in toluene over a timescale of 600 seconds. Because the dispersion is not stable, the absorbance of AzoOC₄ at 358 nm is referenced to the absorbance of the excitonic band gap at 527 nm and plotted against the time, f) ¹H-NMR spectrum of dissolved 3D-AzoOC₄ before (top) and after irradiation with 313 nm for 600 seconds (bottom), g)+h) UV/Vis kinetic measurement of 3D-AzoOC₁₂ in toluene over a timescale of 1200 seconds. Because the dispersion is not stable, the absorbance of AzoOC₁₂ at 332 nm is referenced to the absorbance of the excitonic band gap at 528 nm and plotted against the time, i) ¹H-NMR spectrum of dissolved 3D-AzoOC₁₂ before (top) and after irradiation with 313 nm for 1200 seconds (bottom).

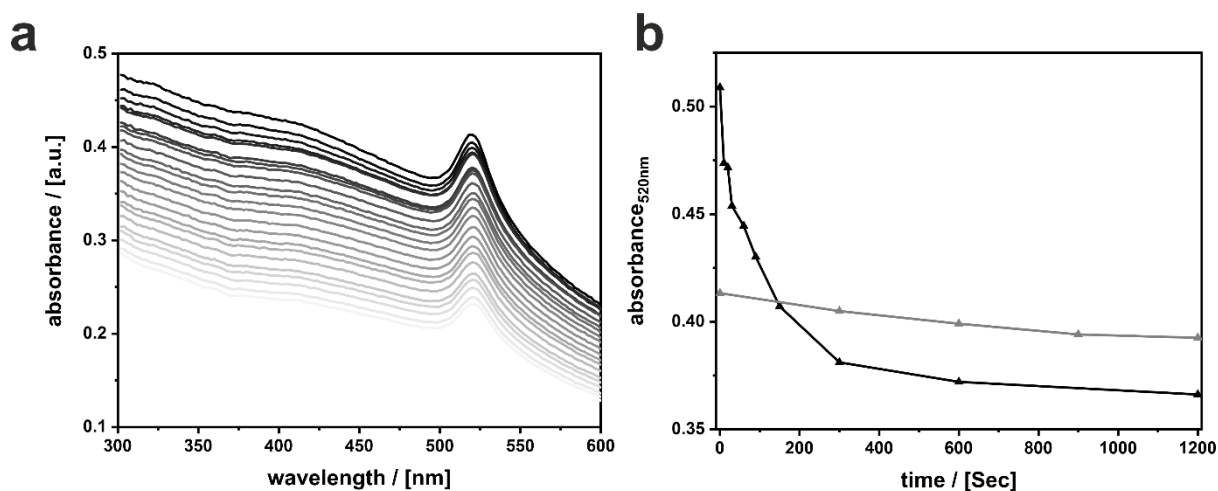


Figure A18 – a) UV/Vis absorption kinetic of the particle dispersion without irradiation every 300 seconds. b) absorbance against the time of dispersed particles without irradiation (grey) and with irradiation (black, spectrum see **Figure 36b**). The dispersion is not stable over the time, which is why we refer the azobenzene signal to the signal of the bandgap.

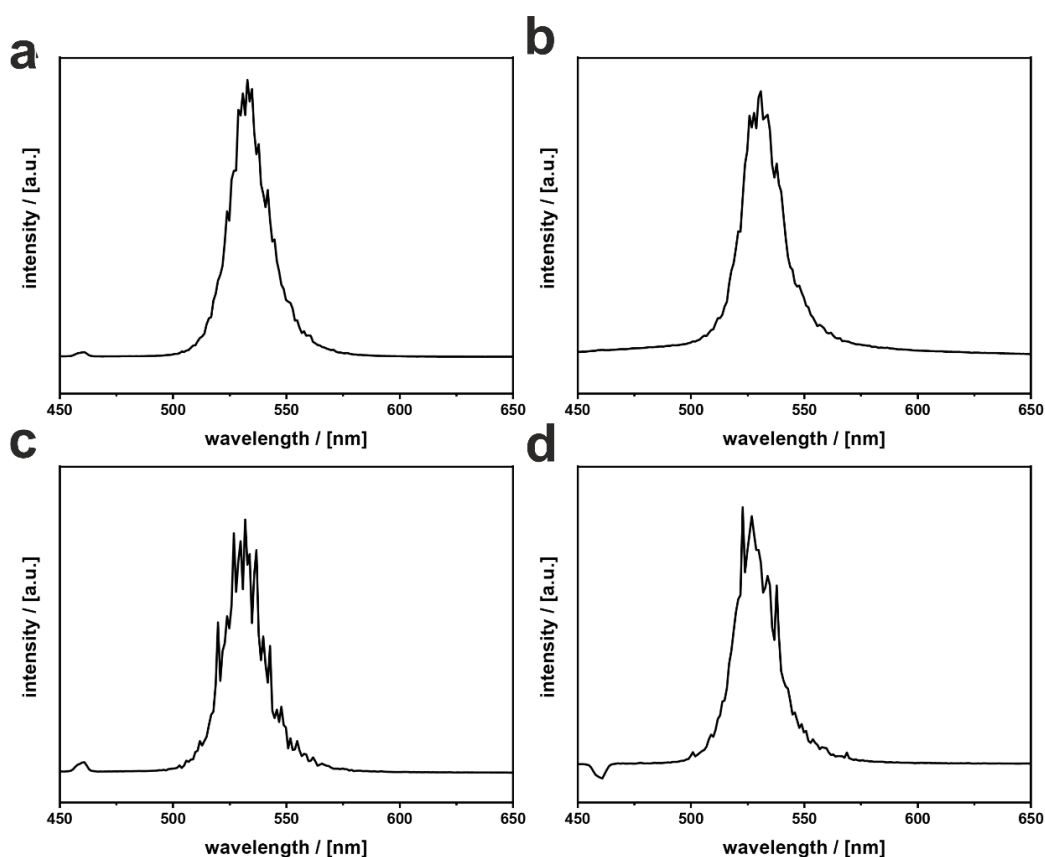


Figure A19 – PL spectra of dispersed particles in toluene of a) 3D-AzoC₁, b) 3D-AzoC₂, c) 3D-AzoC₄ and d) 3D-AzoC₁₂ with excitation at $\lambda_{exc}=405$ nm. A cutoff filter at 420 nm was used to filter the excitation wavelength. Signals at 460 nm stem from toluene.

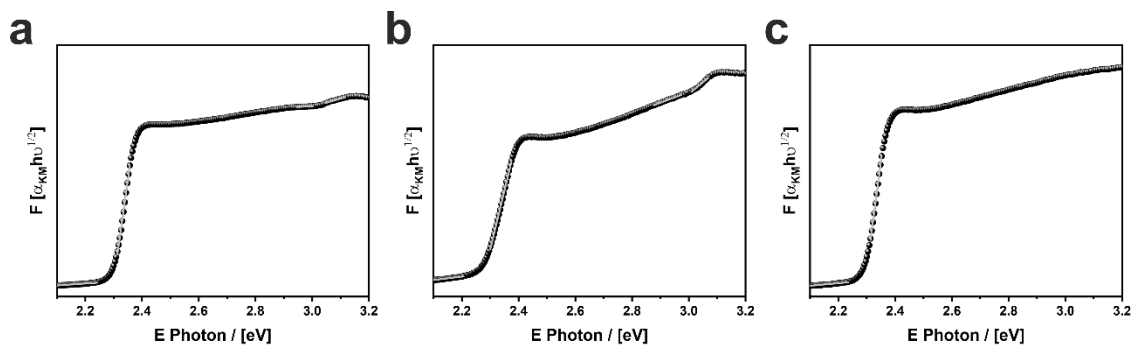


Figure A20 - UV/Vis reflectance spectra with Kubelka-Munk analysis for a) RPP^{RT}_{0.7}-AzoC₂ with $E_{g,1} = 3.02$ eV and $E_{g,2} = 2.29$ eV, b) RPP^{RT}_{0.5}-AzoC₂ with $E_{g,1} = 3.01$ eV and $E_{g,2} = 2.28$ eV and c) RPP^{RT}_{0.3}-AzoC₂ with $E_g = 2.30$ eV.

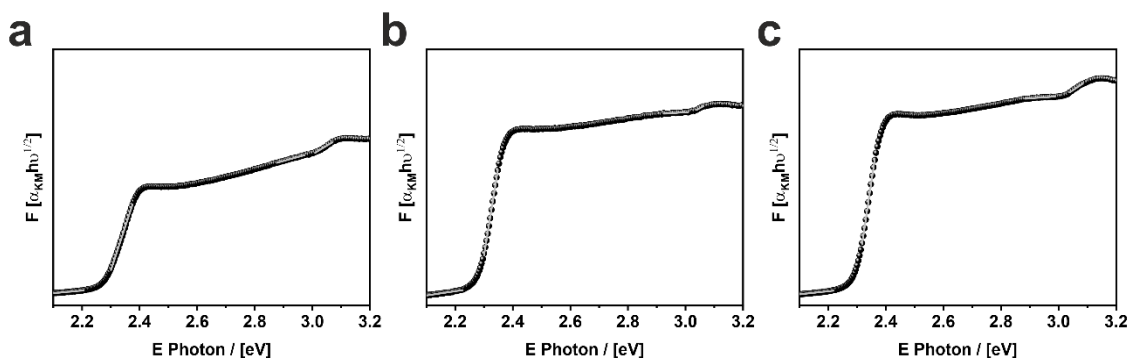


Figure A21 – UV/Vis reflectance spectra with Kubelka-Munk analysis for a) RPP^{RT}_{0.5}-AzoC₂ with $E_{g,1} = 3.01$ eV and $E_{g,2} = 2.30$ eV, b) RPP^{-10 °C}_{0.5}-AzoC₂ with $E_{g,1} = 3.03$ eV and $E_{g,2} = 2.28$ eV and c) RPP^{-20 °C}_{0.5}-AzoC₂ with $E_{g,1} = 3.02$ eV and $E_{g,2} = 2.27$ eV.

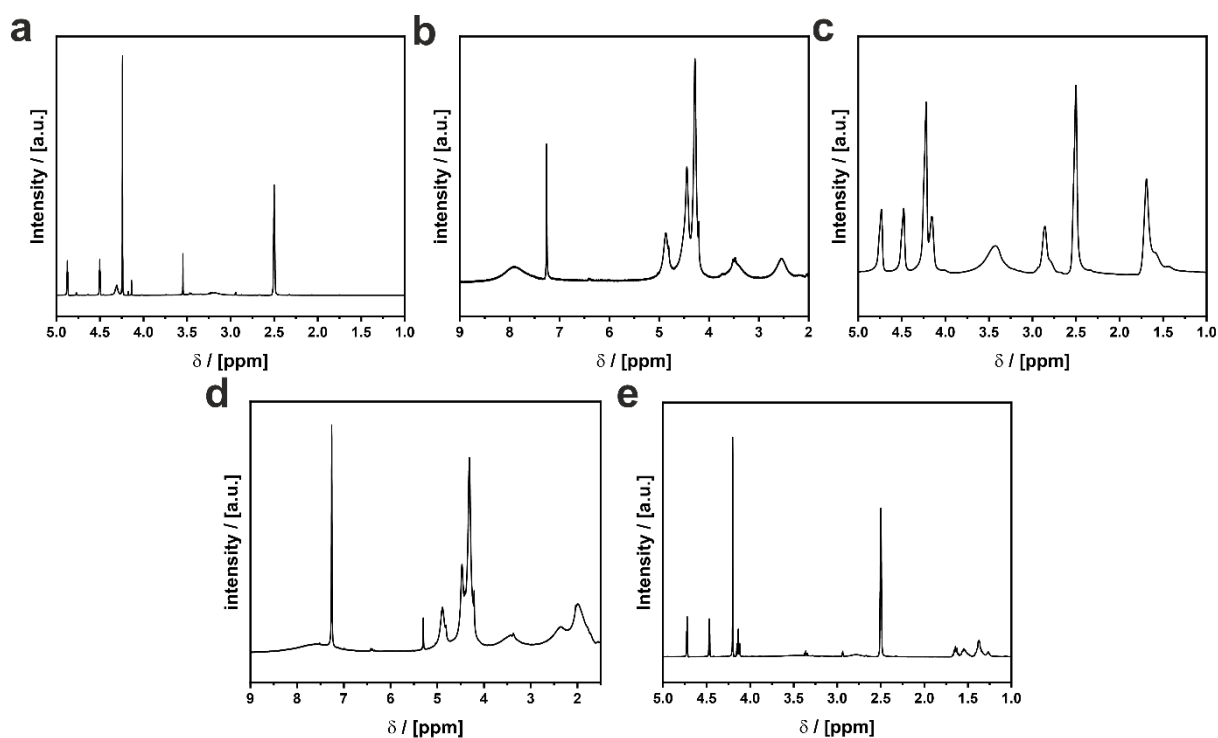


Figure A22 – ^1H -NMR of a) $\text{C}_{13}\text{H}_{16}\text{BrFeNO}_2$ (= FcC₂Br), b) $\text{C}_{14}\text{H}_{18}\text{BrFeNO}_2$ (= FcC₃Br) c) $\text{C}_{15}\text{H}_{20}\text{BrFeNO}_2$ (= FcC₄Br), d) $\text{C}_{16}\text{H}_{22}\text{BrFeNO}_2$ (= FcC₅Br) and e) $\text{C}_{17}\text{H}_{24}\text{BrFeNO}_2$ (= FcC₆Br) in CDCl_3 . For a quantitative evaluation of the spectra refer to the experimental section in **chapter 6.1**.

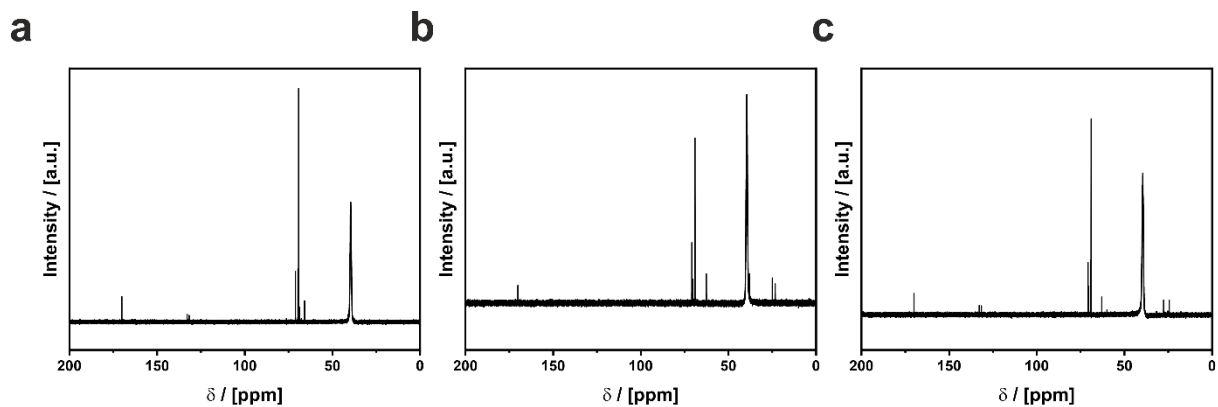


Figure A23 – ^{13}C -NMR of a) $\text{C}_{13}\text{H}_{16}\text{BrFeNO}_2$ (= FcC₂Br), b) $\text{C}_{15}\text{H}_{20}\text{BrFeNO}_2$ (= FcC₄Br), c) $\text{C}_{17}\text{H}_{24}\text{BrFeNO}_2$ (= FcC₆Br) in CDCl_3 . For a quantitative evaluation of the spectra refer to the experimental section in **chapter 6.1**.

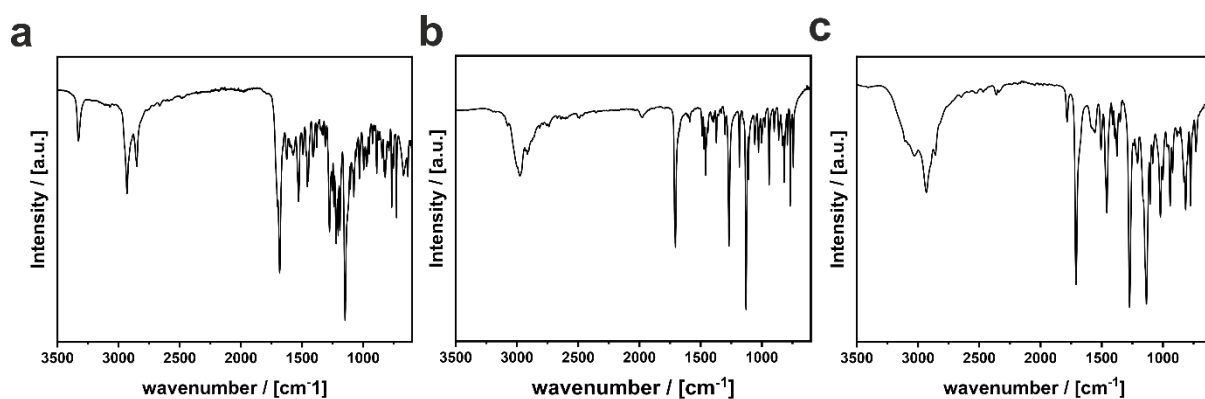


Figure A24 – IR transmission spectra of a) FcC_2Br with significant vibrations at $2930\text{--}2850\text{ cm}^{-1}$ (NH_3 stretching vibration), 1683 cm^{-1} ($\text{C}=\text{O}$ stretching vibration), 1526 cm^{-1} (O-CH_2 deformation vibration), 1273 cm^{-1} (O-C=O stretching vibration), 1144 cm^{-1} (O-C=O stretching vibration), 767 cm^{-1} + 728 cm^{-1} (cp C-H out-of-plane vibration), b) FcC_4Br with significant vibrations at 2970 cm^{-1} (NH_3 stretching vibration), 1706 cm^{-1} ($\text{C}=\text{O}$ stretching vibration), 1459 cm^{-1} (O-CH_2 deformation vibration), 1269 cm^{-1} (O-C=O stretching vibration), 1129 cm^{-1} (O-C=O stretching vibration), 769 cm^{-1} (cp C-H out-of-plane vibration) and c) FcC_6Br with significant vibrations at 2931 cm^{-1} (NH_3 stretching vibration), 1711 cm^{-1} ($\text{C}=\text{O}$ stretching vibration), 1458 cm^{-1} (O-CH_2 deformation vibration) 1273 cm^{-1} (O-C=O stretching vibration), 1134 cm^{-1} (O-C=O stretching vibration), 773 cm^{-1} (cp C-H out-of-plane vibration).

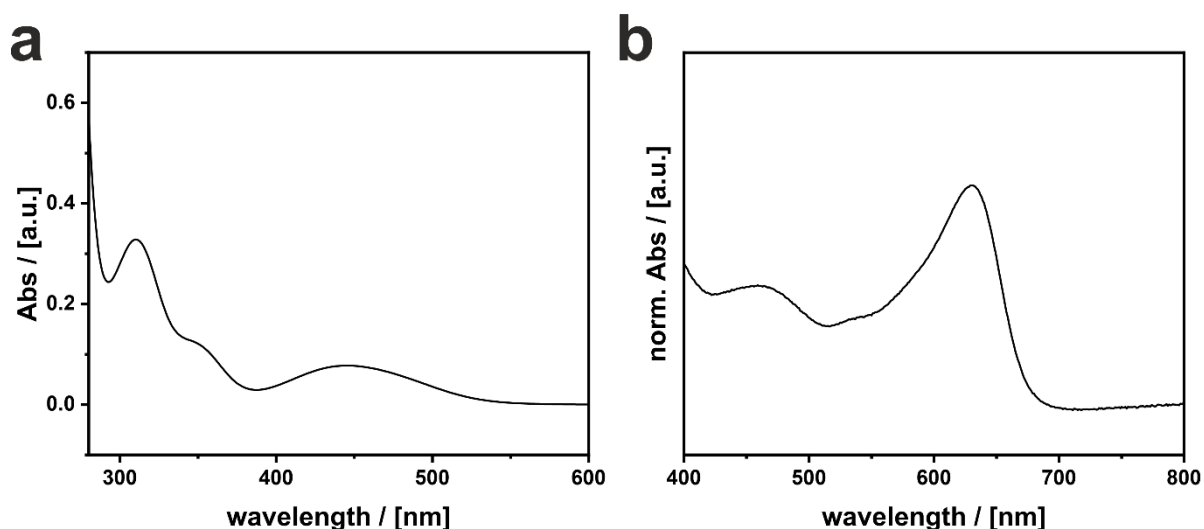


Figure A25 – a) UV/Vis spectrum of FcC_3Br in H_2O . Absorption bands at 446 nm (2.78 eV), 359 nm (3.55 eV) and 311 nm (3.98 eV) are found. b) UV/Vis spectrum of FcC_3Br in H_2O after oxidation with $\text{Ce}(\text{SO}_4)_2$. A new absorption band at 631 nm (1.97 eV) is found which is attributed to a transition from a deeper lying MO into the emerging SOMO e_{2g} , which now lies above the initial HOMO a_{1g} (see **Figure 45**).

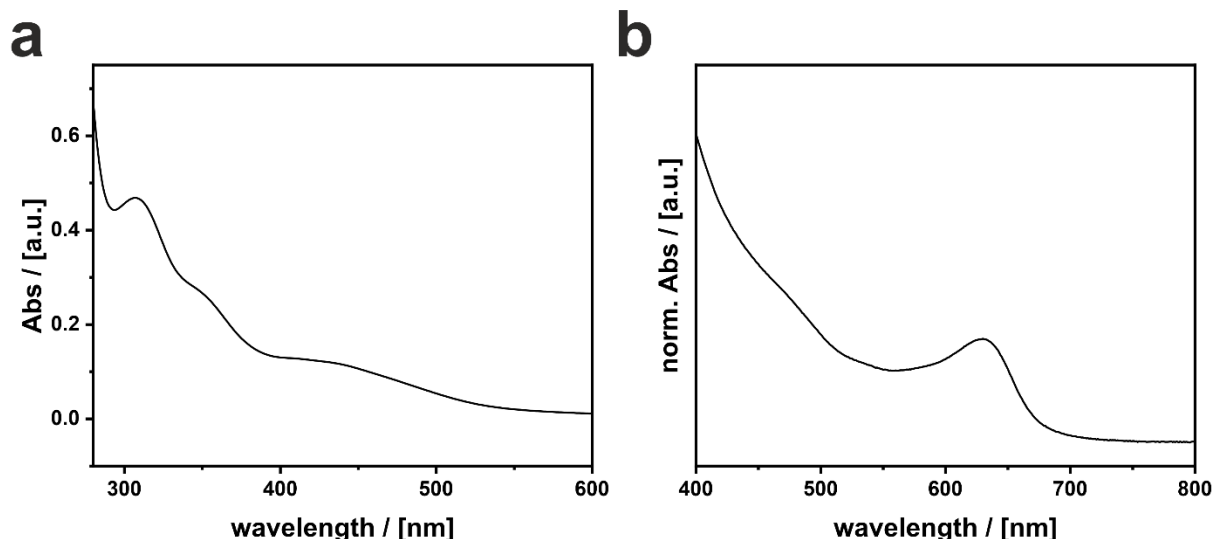


Figure A26 – a) UV/Vis spectrum of FcC₄Br in H₂O. Absorption bands at 431 nm (2.87 eV), 350 nm (3.54 eV) and 307 nm (4.04 eV) are found. b) UV/Vis spectrum of FcC₄Br in H₂O after oxidation with Ce(SO₄)₂. A new absorption band at 630 nm (1.97 eV) is found which is attributed to a transition from a deeper lying MO into the emerging SOMO e_{2g}, which now lies above the initial HOMO a_{1g} (see **Figure 45**).

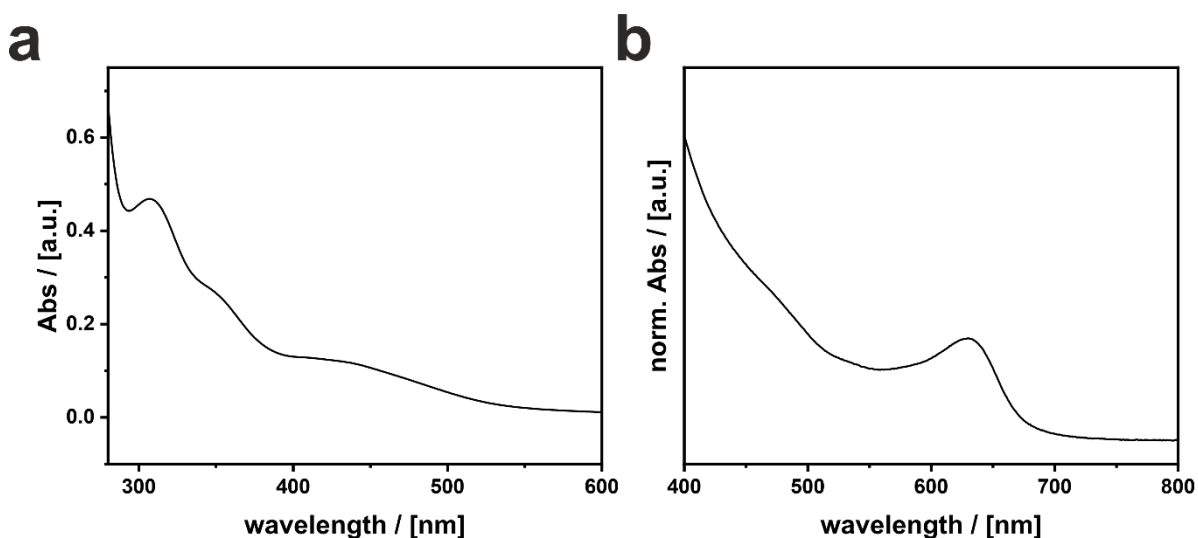


Figure A27 – a) UV/Vis spectrum of FcC₅Br in H₂O. Absorption bands at 430 nm (2.88 eV), 350 nm (3.54 eV) and 306 nm (4.05 eV) are found. b) UV/Vis spectrum of FcC₅Br in H₂O after oxidation with Ce(SO₄)₂. A new absorption band at 631 nm (1.97 eV) is found which is attributed to a transition from a deeper lying MO into the emerging SOMO e_{2g}, which now lies above the initial HOMO a_{1g} (see **Figure 45**).

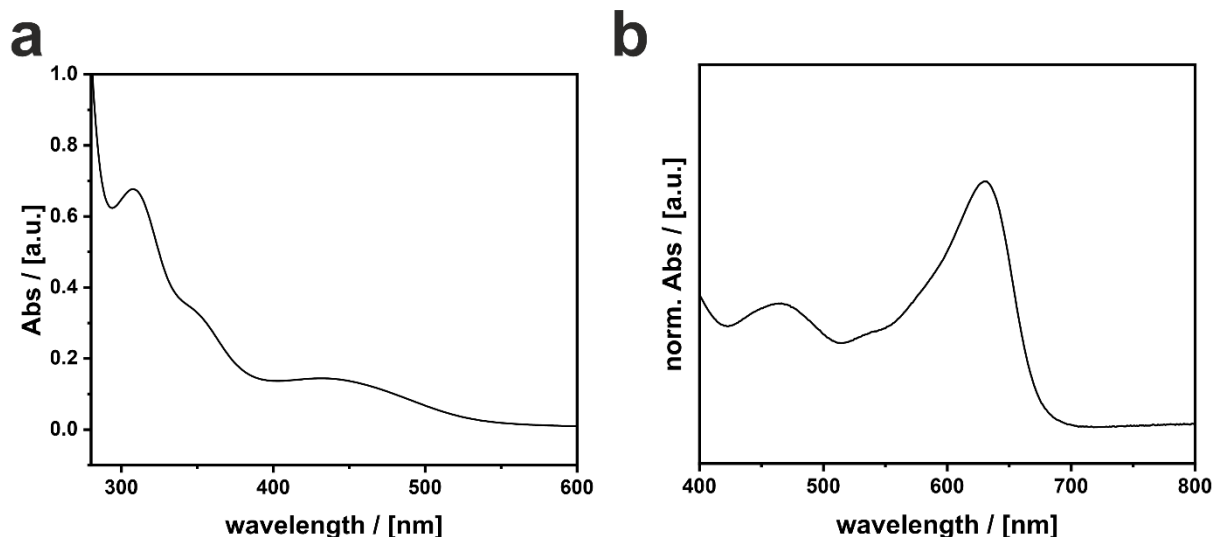


Figure A28 – a) UV/Vis spectrum of FcC₆Br in H₂O. Absorption bands at 431 nm (2.88 eV), 350 nm (3.54 eV) and 308 nm (4.02 eV) are found. b) UV/Vis spectrum of FcC₆Br in H₂O after oxidation with Ce(SO₄)₂. A new absorption band at 631 nm (1.97 eV) is found which is attributed to a transition from a deeper lying MO into the emerging SOMO e_{2g}, which now lies above the initial HOMO a_{1g} (see **Figure 45**).

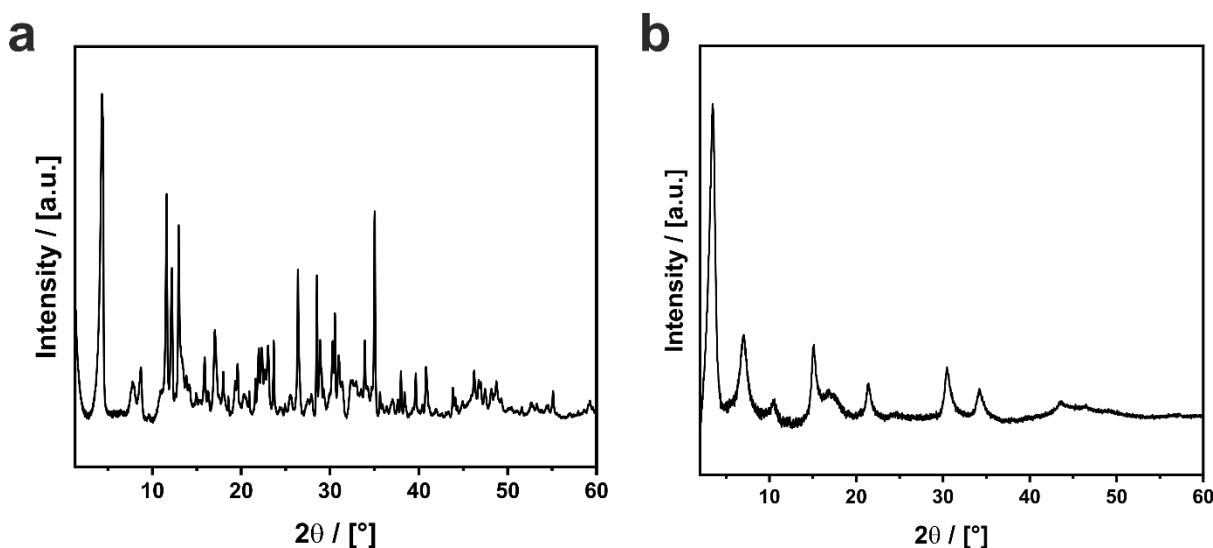


Figure A29 – Experimental PXRD pattern of precipitations with PbBr₂ and a) FcC₃Br, having a similar crystal structure as FcC₄Br and b) FcC₅Br, having a similar crystal structure as FcC₆Br (a true Ruddlesden-Popper phase).

Table 16 – Crystal data for hybrid lead bromide phase with $\text{Fe}(\text{C}_3\text{H}_7\text{NO})_6^{2+}$ complex obtained from SCXRD.

empirical formula	$\text{Fe}(\text{C}_3\text{H}_7\text{NO})_6\text{Pb}_2\text{Br}_6$
<i>formula weight (g/mol)</i>	1388.23
<i>crystal system</i>	triclinic
<i>space group</i>	P-1
<i>a [Å]</i>	8.6723
<i>b [Å]</i>	9.9748
<i>c [Å]</i>	11.9205
<i>V [Å³]</i>	978.3621
<i>α, β, γ [°]</i>	93.67(5), 105.89(7), 97.31(4)

Table 17 – Fractional coordinates of crystal structure of $\text{Fe}(\text{C}_3\text{H}_7\text{NO})_6\text{Pb}_2\text{Br}_6$.

Atom type	Site label	x	y	z	$U_{\text{iso}} [\text{\AA}^2]$
Pb	Pb01	0.75768	0.98339	0.02910	0.033
Br	Br02	0.56798	1.17524	0.12561	0.048
Br	Br03	1.07288	1.17166	0.11742	0.048
Fe	Fe04	0.50000	0.50000	0.50000	0.025
Br	Br05	0.80549	0.83068	0.21100	0.091
O	O006	0.39870	0.54960	0.32820	0.044
O	O007	0.68580	0.42200	0.44670	0.039
O	O008	0.63550	0.69860	0.53430	0.042
N	N009	0.67870	0.92330	0.58900	0.045
N	N00A	0.88570	0.42290	0.36000	0.033
N	N00B	0.31490	0.54530	0.13240	0.040
C	C00C	0.37600	0.49330	0.22910	0.035
H	H00C	0.40472	0.40704	0.22277	0.043
C	C00D	0.76790	0.47460	0.38620	0.032
H	H00D	0.74368	0.55631	0.35756	0.038
C	C00E	0.66090	1.03400	0.66670	0.071
H	H00A	0.58129	1.00300	0.70527	0.107
H	H00B	0.62653	1.10707	0.62203	0.107
H	H00E	0.76296	1.06536	0.72422	0.107
C	C00F	0.61440	0.79820	0.59190	0.038
H	H00F	0.54806	0.78329	0.64078	0.046
C	C00G	0.78570	0.95470	0.51750	0.081
H	H00G	0.75260	1.02802	0.47276	0.122
H	H00H	0.78100	0.87601	0.46512	0.122
H	H00I	0.89475	0.98086	0.56689	0.122
C	C00H	0.97690	0.48870	0.28900	0.061
H	H00J	0.94767	0.43865	0.21283	0.092
H	H00K	1.09074	0.49164	0.32575	0.092
H	H00L	0.95300	0.57958	0.28116	0.092
C	C00I	0.92810	0.29400	0.40000	0.052
H	H00M	0.88798	0.27592	0.46587	0.078
H	H00N	1.04392	0.29856	0.42296	0.078
H	H00O	0.88046	0.22246	0.33763	0.078
C	C00J	0.26260	0.67510	0.13480	0.099
H	H00P	0.23730	0.69424	0.20716	0.149
H	H00Q	0.16772	0.67470	0.07018	0.149
H	H00R	0.34740	0.74360	0.12870	0.149
C	C00K	0.28880	0.47240	0.01820	0.069
H	H00S	0.32879	0.38719	0.02756	0.104
H	H00T	0.34525	0.52552	-0.02670	0.104
H	H00U	0.17483	0.45612	-0.02192	0.104

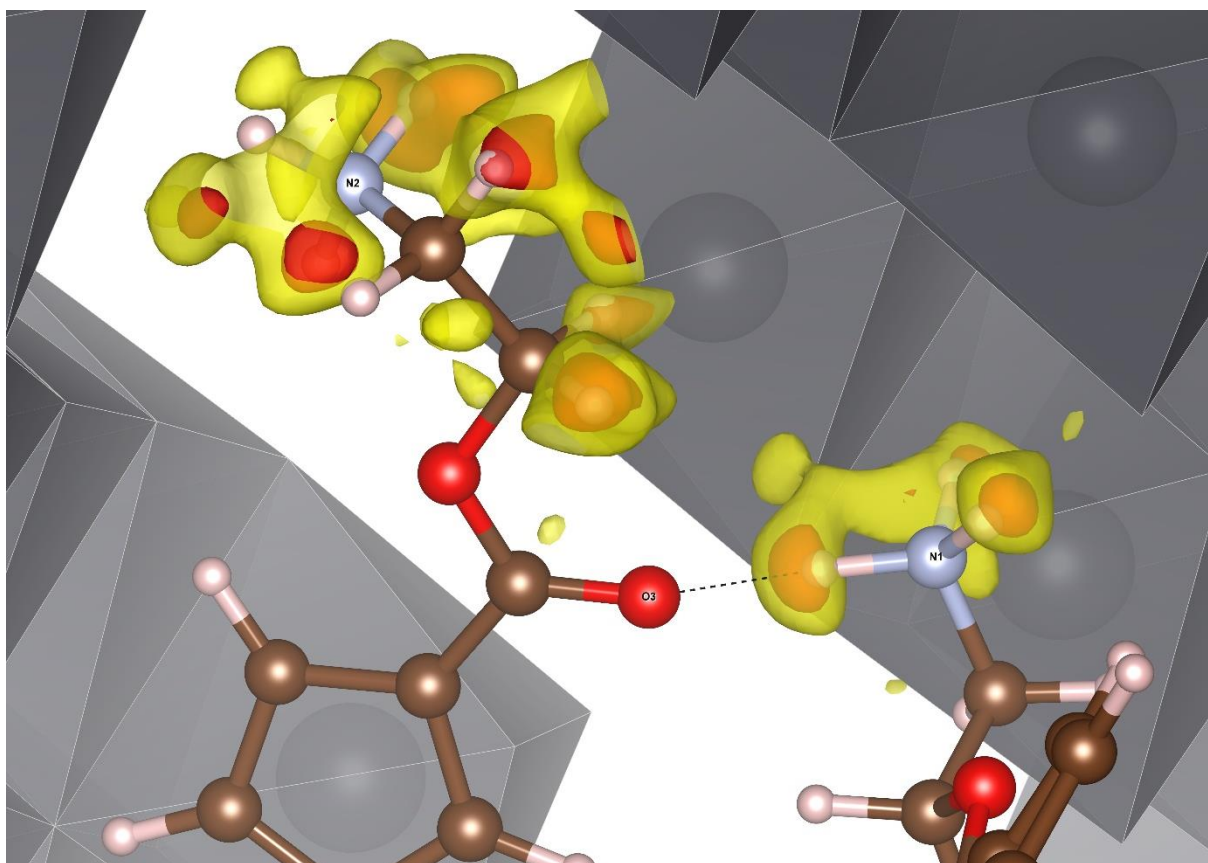


Figure A30 - Difference potential map of $(\text{FcC}_2)\text{PbBr}_3$ based on the final model. Yellow isosurfaces correspond to the expected locations of some hydrogen sites.

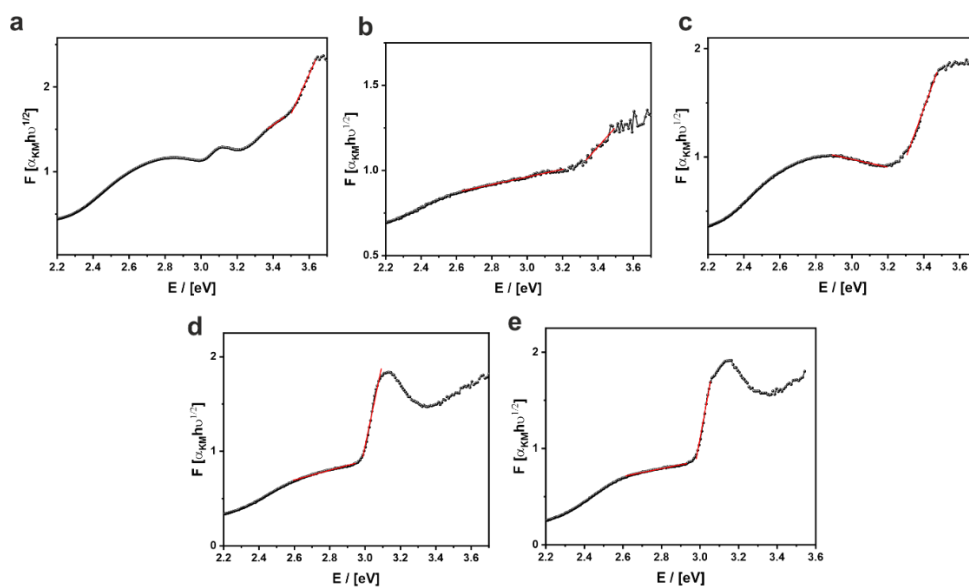


Figure A31 - Kubelka-Munk analysis of reflectance measurements of a) $(\text{FcC}_2)\text{PbBr}_3$ with $E_g = 3.51$ eV, b) $(\text{FcC}_3)_4\text{Pb}_3\text{Br}_{10}$ with $E_g = 3.32$ eV, c) $(\text{FcC}_4)_4\text{Pb}_3\text{Br}_{10}$ with $E_g = 3.27$ eV, d) $(\text{FcC}_5)_2\text{PbBr}_4$ with $E_g = 3.11$ eV and e) $(\text{FcC}_6)_2\text{PbBr}_4$ with $E_g = 3.06$ eV.

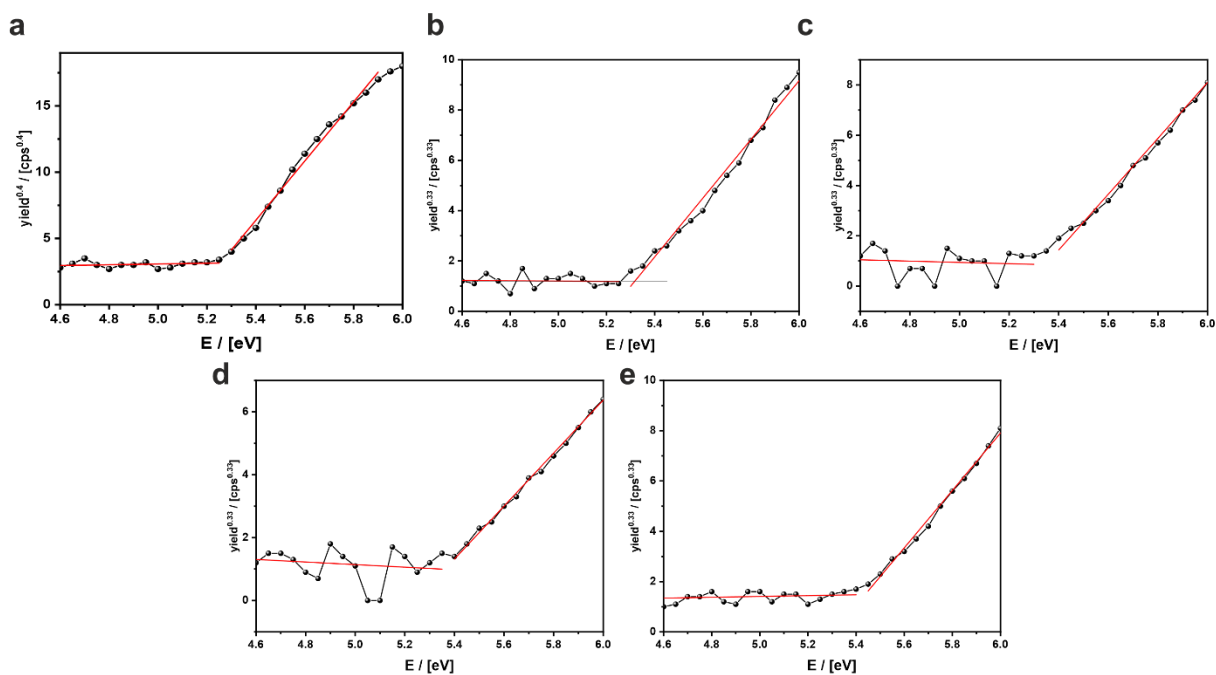


Figure A32 - Photoelectron spectroscopy in air (PESA) of a) $(\text{FcC}_2)\text{PbBr}_3$ with $E_{\text{VBM}} = -5.27$ eV, b) $(\text{FcC}_3)_4\text{Pb}_3\text{Br}_{10}$ with $E_{\text{VBM}} = -5.32$ eV, c) $(\text{FcC}_4)_4\text{Pb}_3\text{Br}_{10}$ with $E_{\text{VBM}} = -5.35$ eV, d) $(\text{FcC}_5)_2\text{PbBr}_4$ with $E_{\text{VBM}} = -5.37$ eV and e) $(\text{FcC}_6)_2\text{PbBr}_4$ with $E_{\text{VBM}} = -5.45$ eV.

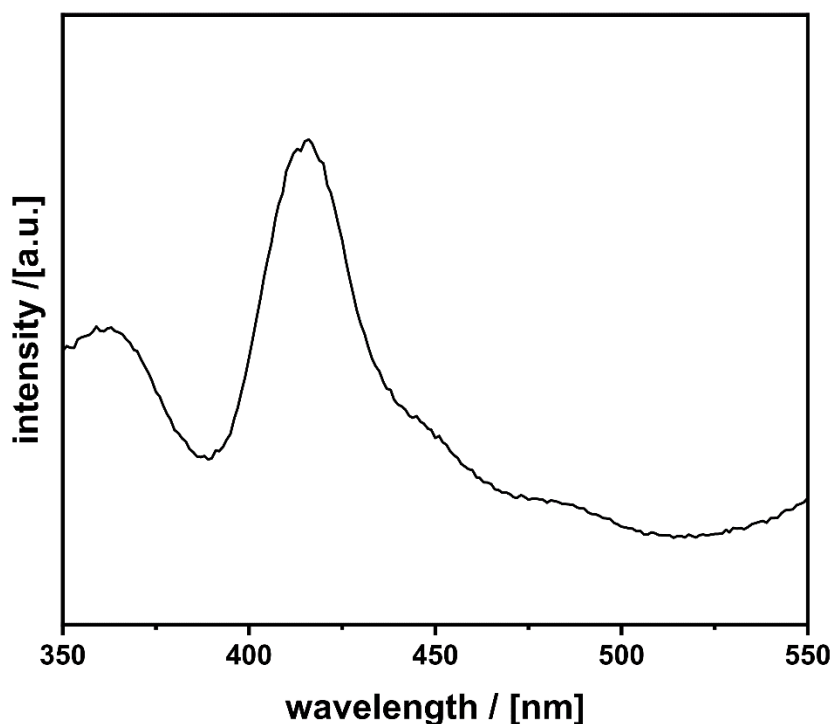


Figure A33 - PL emission spectrum of $(\text{FcC}_6)_2\text{PbBr}_4$ excited at 300 nm with an Xe-lamp. Emission maximum is found at 416 nm (2.98 eV).

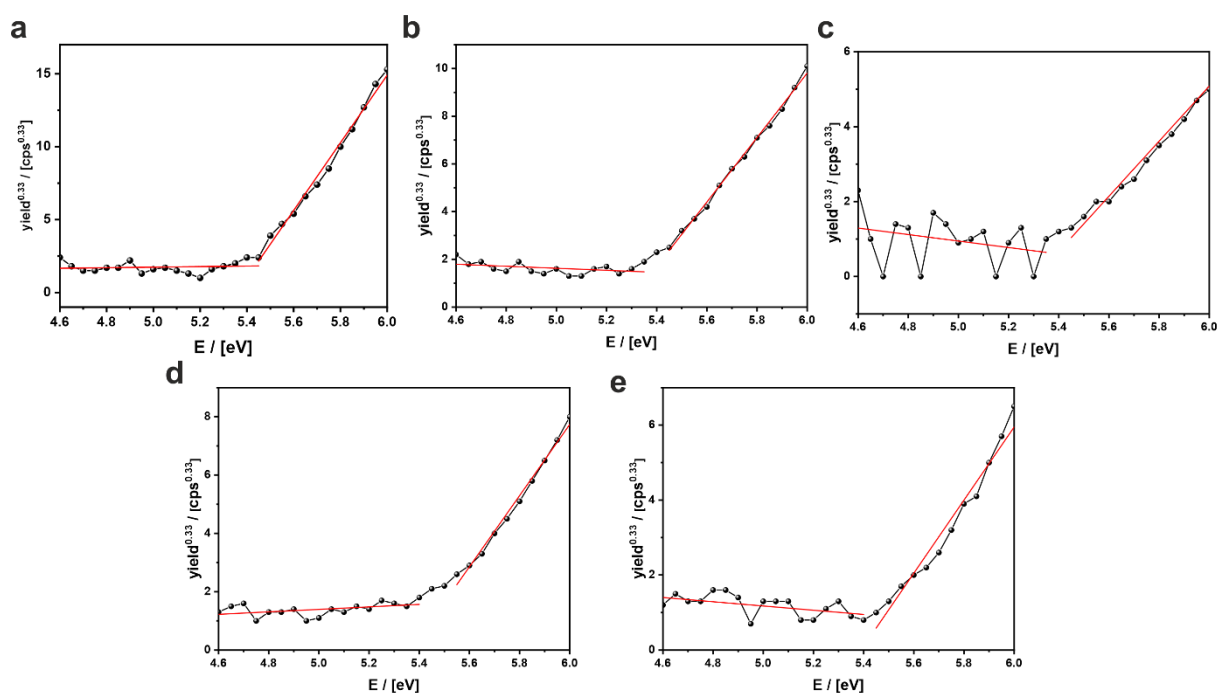


Figure A34 - Photon electron spectroscopy in air (PESA) of (a) FcC₂Br with $E_{\text{HOMO}} = -5.44$ eV, (b) FcC₃Br with $E_{\text{HOMO}} = -5.40$ eV, (c) FcC₄Br with $E_{\text{HOMO}} = -5.39$ eV, (d) FcC₅Br with $E_{\text{HOMO}} = -5.50$ eV, (e) FcC₆Br with $E_{\text{HOMO}} = -5.48$ eV.

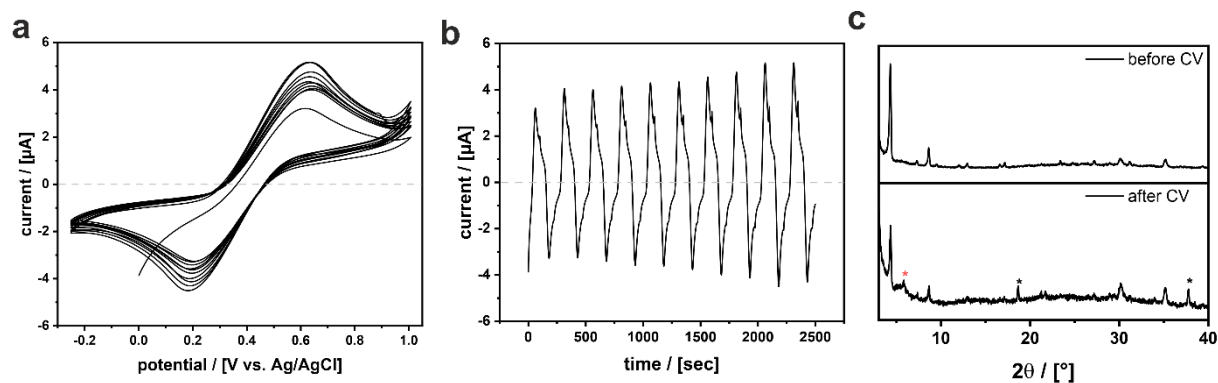


Figure A35 - a) 10 CV scans of a (FcC₂)PbBr₃ film on ITO at a speed scan of 10 mV/s in 0.1 M LiTFSI in HFE/DEC (97:3), b) current vs. time of the 10 CV scans. The consumed current increases over the time of the measurement, c) PXR patterns of the (FcC₂)PbBr₃ film on ITO before (top) and after (bottom) 10 CV scans. Reflexes marked with (*) show a small degradation of the material (black = PbBr₂, red = FcC₂Br).

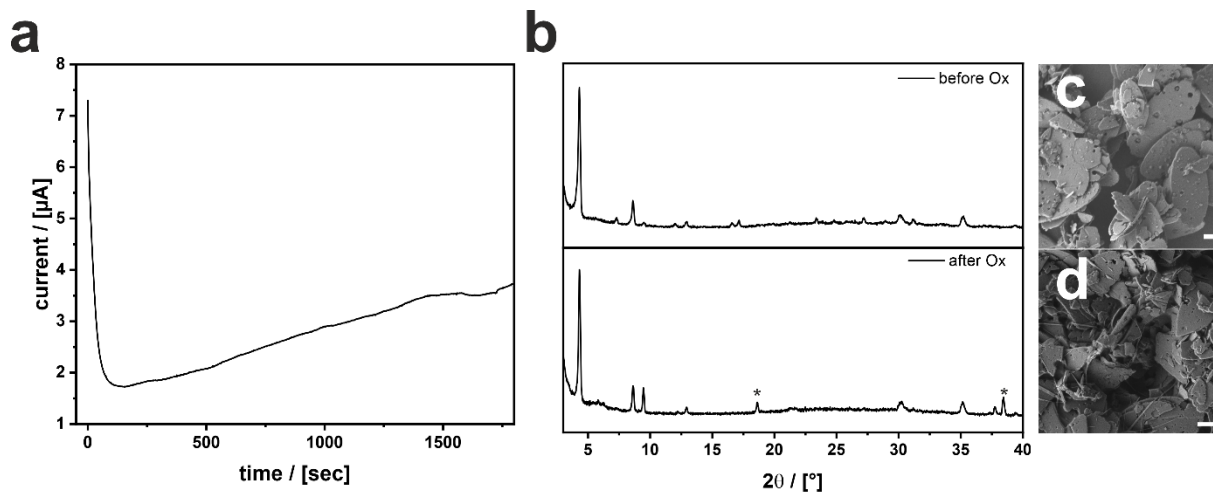


Figure A36 - a) Current flow during the oxidation of $(\text{FcC}_2)\text{PbBr}_3$ for 1800 sec. b) PXRD of $(\text{FcC}_2)\text{PbBr}_3$ on ITO before (top) and after (bottom) oxidation. Realignment of the particles lead to changed intensities of the reflexes. In addition, typical reflections of PbBr_2 are found after oxidation, which are marked with (*). SEM image of $(\text{FcC}_2)\text{PbBr}_3$ on ITO c) before oxidation and d) after oxidation.; Scalebar = 1 μm .

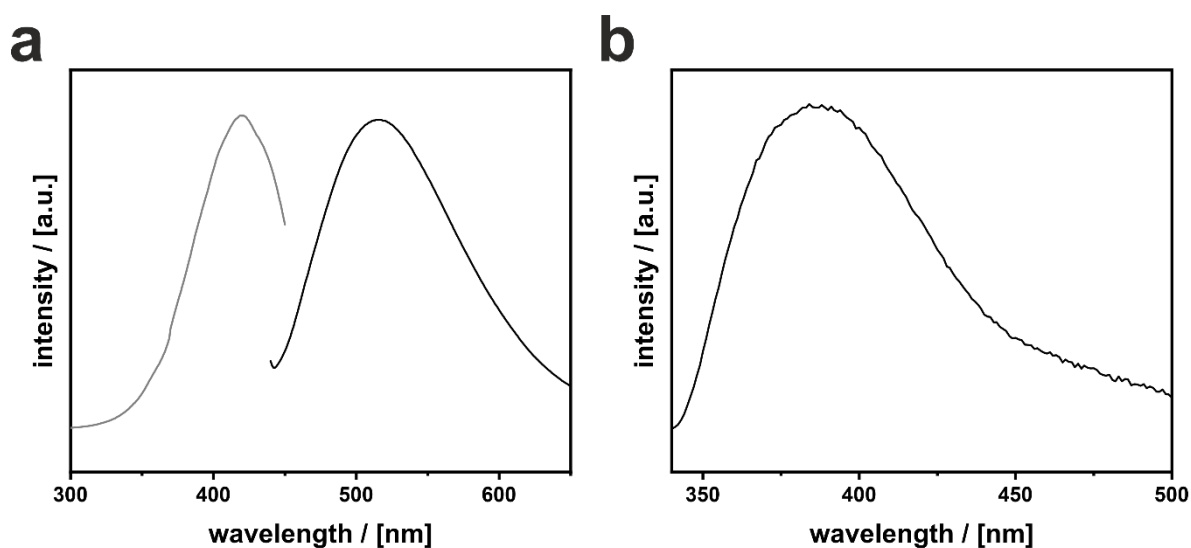


Figure A37 - a) Excitation (grey) and emission (black) spectra of $[\text{FcC}_2\text{Br}]^+$ in water, oxidized with $\text{Ce}(\text{SO}_4)_2$. b) Emission of ITO upon excitation at 310 nm.

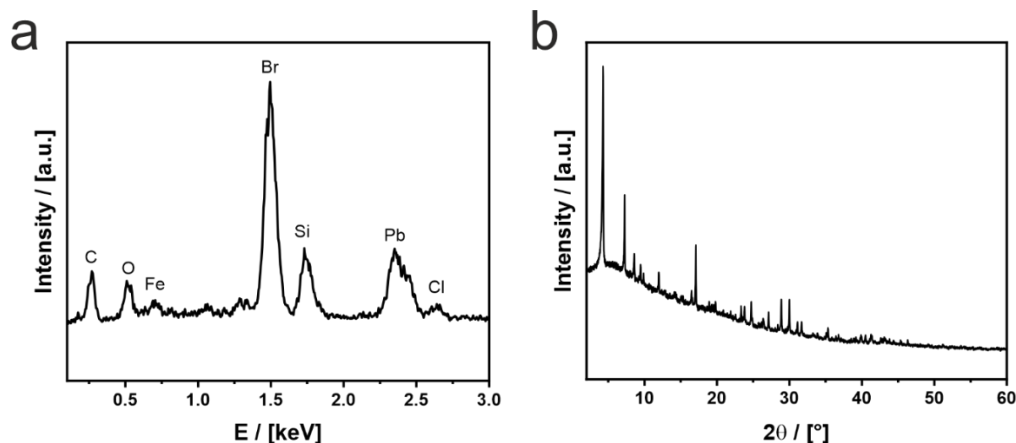


Figure A38 - a) Energy dispersive X-ray (EDX) spectrum of the particles after oxidation with 2.0 eq of oxidant. Elemental analysis of the EDX spectrum is given in **Table 18**. b) PXRD spectrum of the particles after oxidation with 2.0 eq of oxidant. The crystal phase remains even after rearrangement of the particles (see **Figure 47**).

Table 18 - Elemental composition of the particles after oxidation with 2.0 eq of oxidant according to EDX. The Si signal stems from the substrate.

Atom	C	O	Si	Cl	Fe	Br	Pb
[at%]	51.0	15.6	7.6	1.7	3.8	15.4	4.7

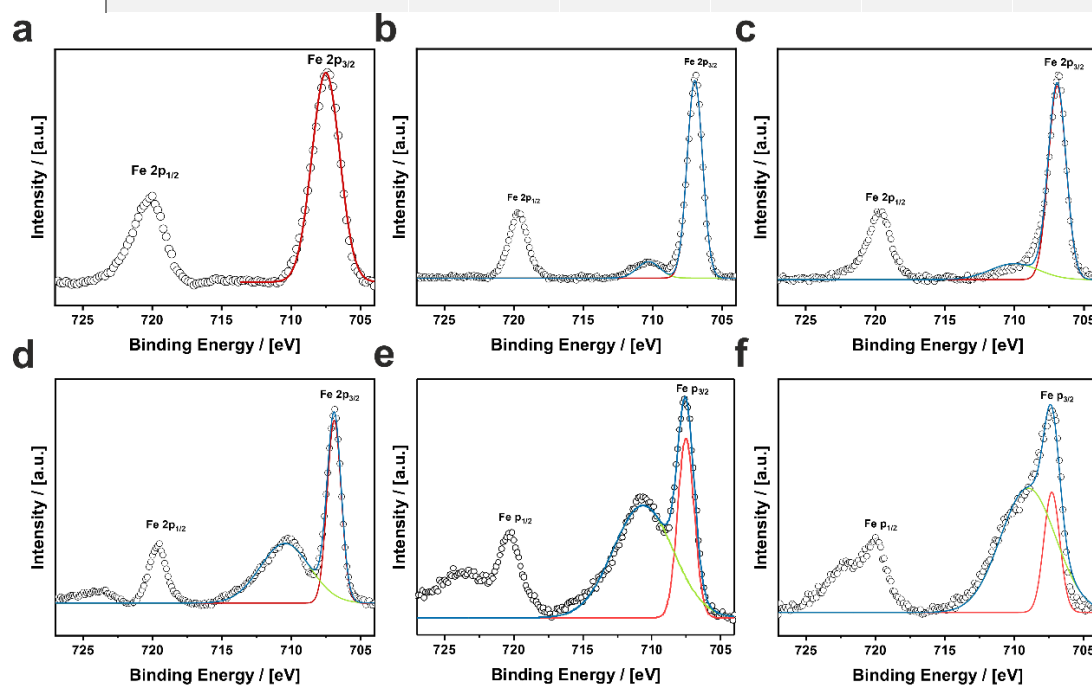


Figure A39 - X-ray photon spectroscopy (XPS) fits of particles oxidized with a) 0 eq, b) 0.1 eq c) 0.2 eq, d) 0.5 eq e) 1.0 eq and f) 2.0 eq of $\text{Fe}(\text{ClO}_4)_3$. A detailed experimental procedure of the oxidation is provided in **chapter 6.3**. Evaluation of the XPS-spectra is provided in **Table 7**.

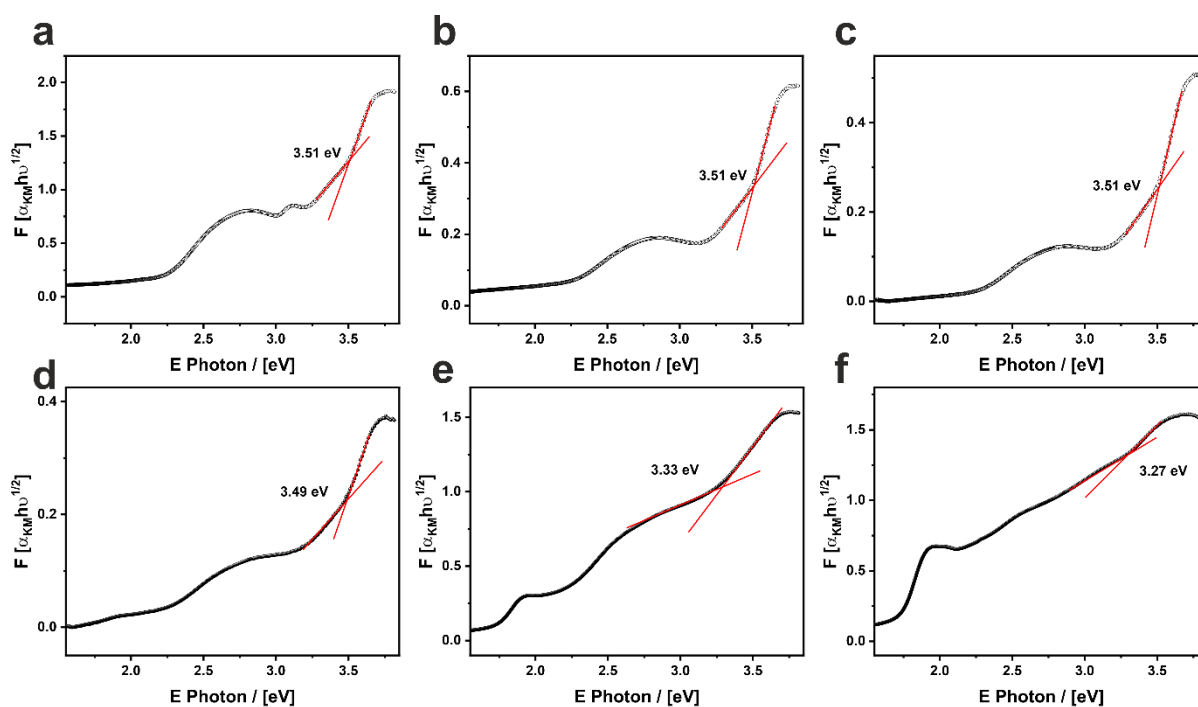


Figure A40 - Kubelka-Munk plots of $(\text{FcC}_2)\text{PbBr}_3$ oxidized with a) 0.0 % Fe^{3+} with $E_g = 3.51$ eV , b) 10.8 % Fe^{3+} with $E_g = 3.51$ eV, c) 18.2 % Fe^{3+} with $E_g = 3.51$ eV, d) 46.4 % Fe^{3+} with $E_g = 3.49$ eV, e) 57.8 % Fe^{3+} with $E_g = 3.33$ eV and f) 63.3 % Fe^{3+} with $E_g = 3.27$ eV.

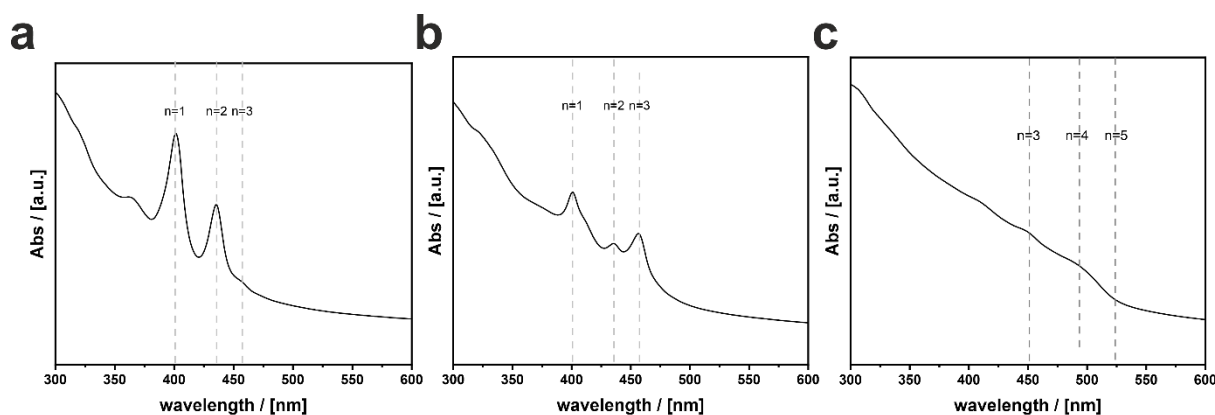


Figure A41 - UV/vis absorption spectra of a) $\text{RPP}_{0.5}$ with absorption maxima 402 nm (3.08 eV), 436 nm (2.84 eV) and a shoulder at 456 nm (2.72 eV) b) $\text{RPP}_{1.0}$ with absorption maxima at 401 nm (3.09 eV), 436 nm (2.84 eV) and 457 nm (2.71 eV) and c) $\text{RPP}_{2.0}$ with shoulders at 449 nm (2.76 eV), 493 nm (2.51 eV) and a band edge at 527 nm (2.35 eV) dispersed in toluene. Absorption of different layers are marked.

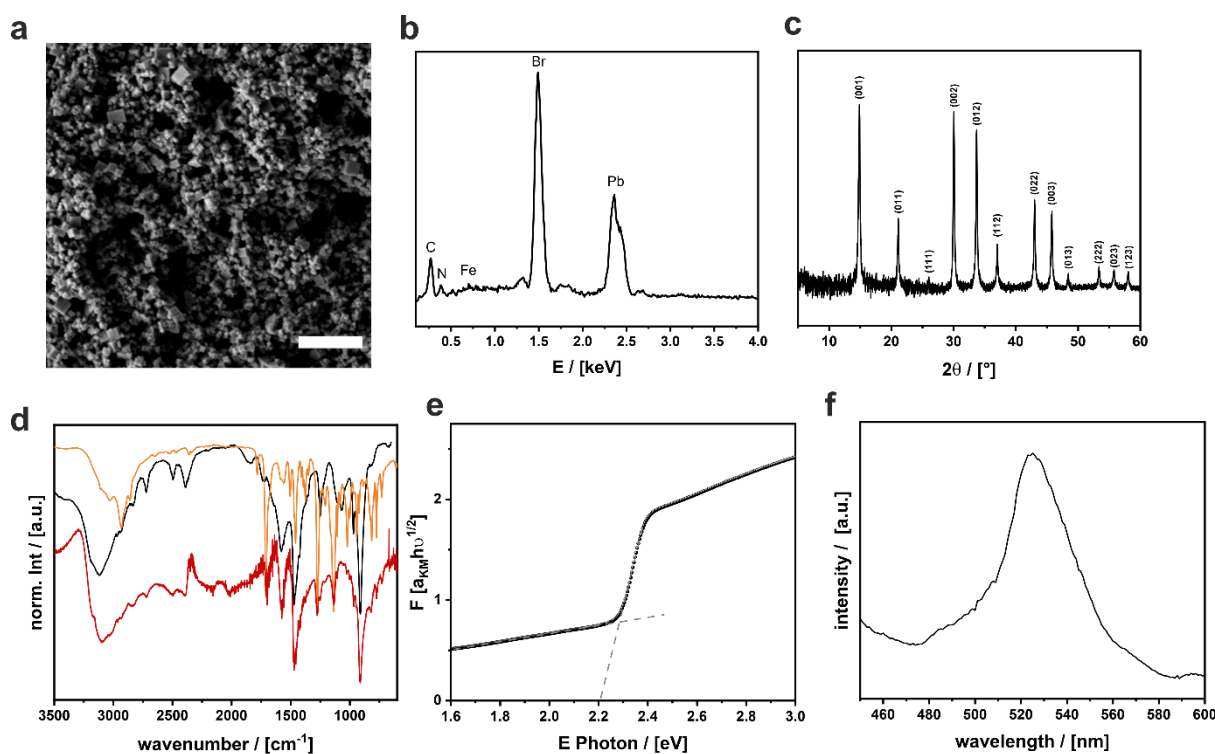


Figure A42 - a) SEM image of the surface-functionalized particles $\text{FcC}_6\text{@MAPbBr}_3$, scalebar = 1 μm . b) energy dispersive X-ray (EDX) spectrum of the particles with Fe (1.6%), Pb (9.1%), Br (20.0%), O (2.0%), N (19.4%) and C (47.8%) c) PXRD of the particles. All reflexes agree with the literature reflexes. No additional reflections can be detected, which shows that no phase impurities are present. d) normalized IR transmission spectra of the particles (red), unfunctionalized MAPbBr_3 (black) and the ferrocene-ligand (orange). Significant vibrations of the ferrocene-ligand at 1700 cm^{-1} (C=O stretching vibration), 1275 cm^{-1} (O-C=O stretching vibration), 1134 cm^{-1} (O-C=O stretching vibration), 820 cm^{-1} , 774 cm^{-1} and 730 cm^{-1} are found for the surface functionalized particles. e) UV/Vis reflection spectra with Kubelka-Munk analysis giving a band gap of $E_g = 2.29\text{ eV}$ f) PL spectrum of $\text{FcC}_6\text{@MAPbBr}_3$ with excitation at 350 nm and emission maximum at 525 nm (2.36 eV).

The experimental details of the preparation of the particles $\text{FcC}_6\text{@MAPbBr}_3$ is described in **chapter 6.2.2**.

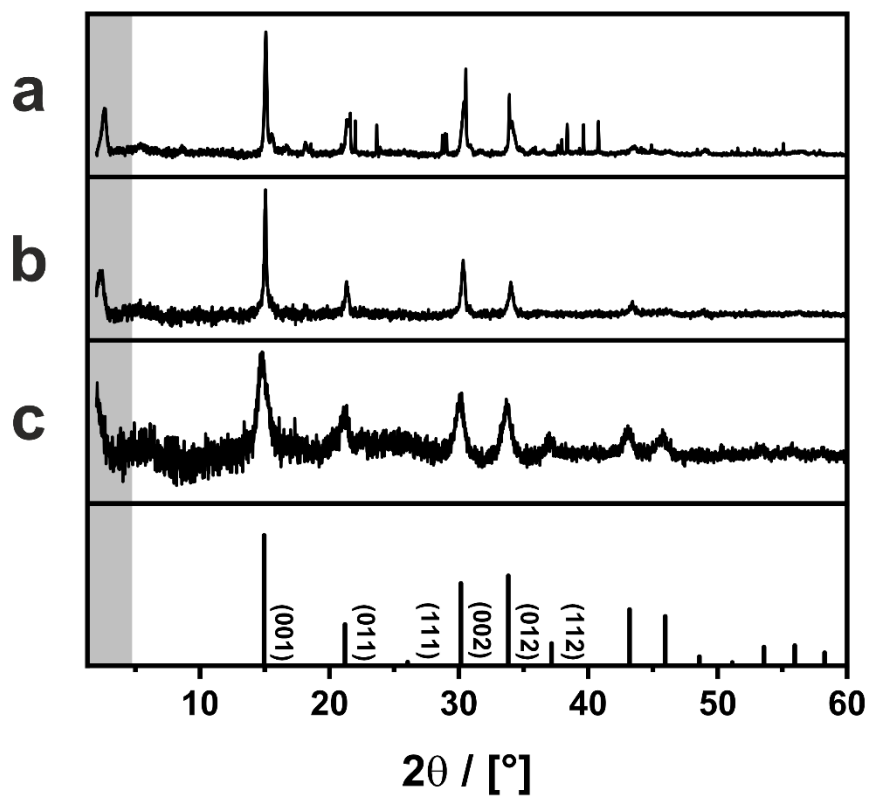


Figure A43 - PXRD measurements of a) RPP_{0.5}, b) RPP_{1.0} and c) RPP_{2.0}. Reference of MAPbBr₃ is given at the bottom. The region marked in grey highlights the average basal distance of the particles.

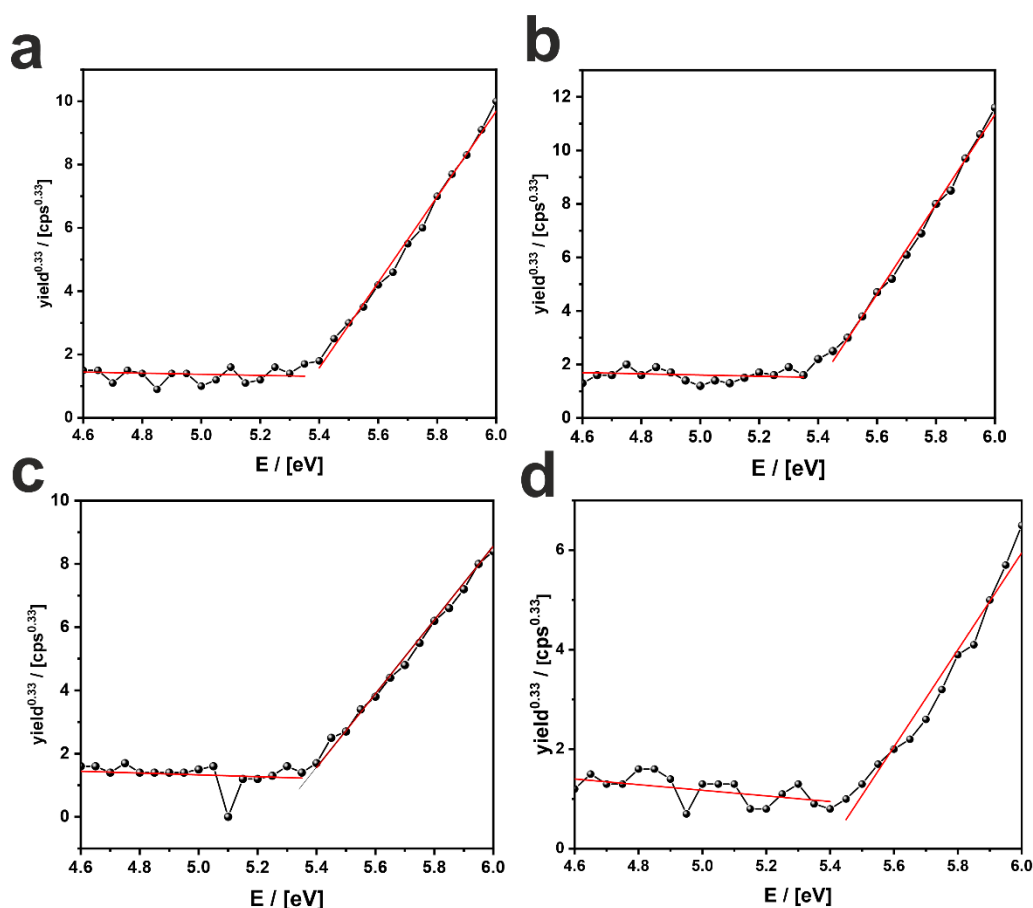


Figure A44 - PESA measurements of drop casted particles on a glass substrate of a) $RPP_{0.5}$ with $E_{VBM} = -5.41$ eV b) $RPP_{1.0}$ with $E_{VBM} = -5.38$ eV and c) $RPP_{2.0}$ with $E_{VBM} = -5.37$ eV. d) PESA measurement of dried FcC_6Br on a glass substrate with $E_{HOMO} = -5.48$ eV.

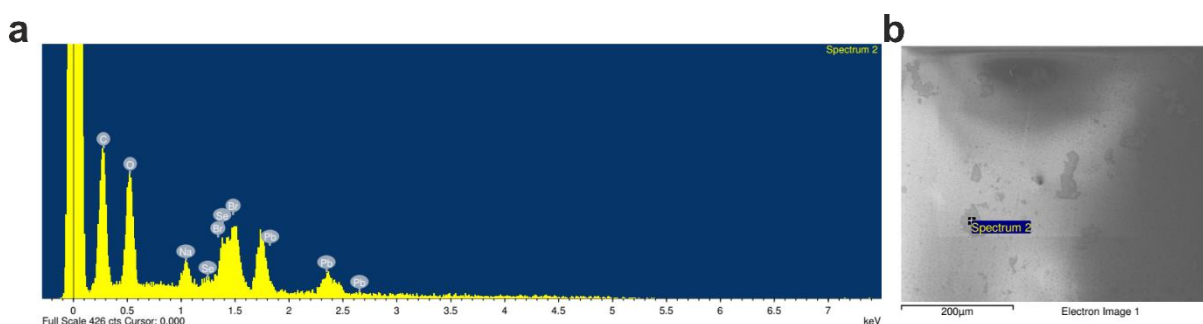


Figure A45 - a) EDX measurement of $(Se-EA)_2PbBr_4$ with b) SEM image of the particle used for the EDX measurement. Evaluation of the EDX data is given in **Table 19**.

Table 19 - Elemental composition of $(Se-EA)_2PbBr_4$ evaluated from EDX. The ratio between Se (~2), Br (~4) and Pb (~1) corresponds to the chemical composition. However, a high C-proportion suggests organic impurities.

Atom	C	O	Na	Se	Br	Pb
[at%]	59.0	32.3	2.0	2.2	3.7	0.8

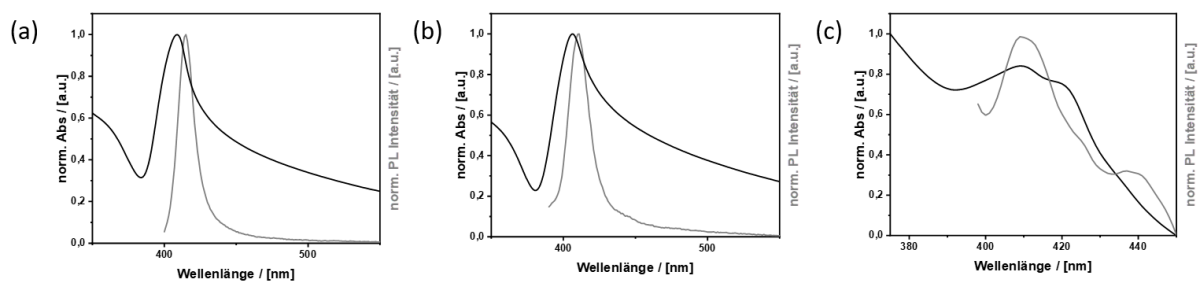


Figure A46 - UV Vis absorption spectra (black) and PL measurements (grey) with excitation at 350 nm of dispersed particles of a) 2D-S-EABr with $\lambda_{\max, \text{abs}} = 408$ nm (3.04 eV) and $\lambda_{\max, \text{PL}} = 413$ nm (3.00 eV), b) 2D-O-EABr with $\lambda_{\max, \text{abs}} = 408$ nm (3.04 eV) and $\lambda_{\max, \text{PL}} = 413$ nm (3.00 eV) and b) 2D-Se-EABr with $\lambda_{\max, \text{abs}} = 409$ nm (3.03 eV) and $\lambda_{\max, \text{PL}} = 410$ nm (3.02 eV).

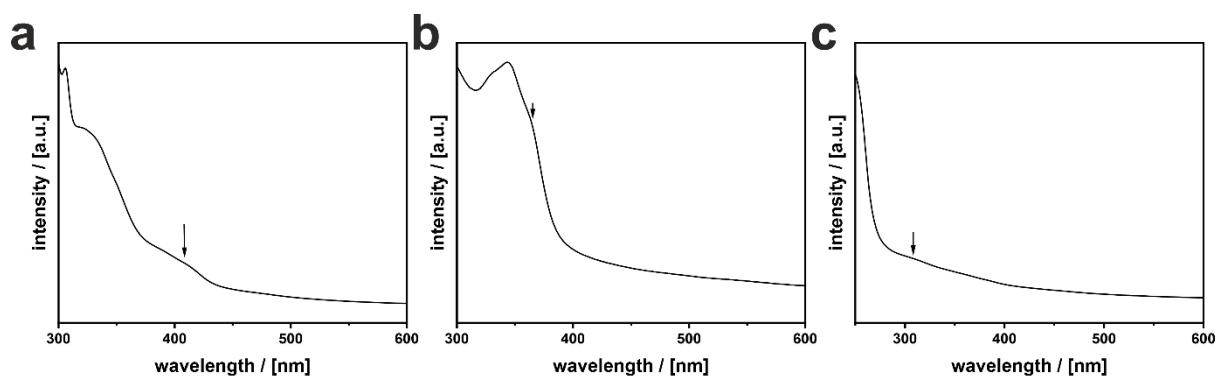


Figure A47 - UV/Vis absorption measurement of a) O-EABr with $\lambda_{\text{abs}} = 408$ nm (3.04 eV), b) S-EABr with $\lambda_{\text{abs}} = 364$ nm (3.41 eV) and c) Se-EABr with a shoulder at $\lambda_{\text{abs}} = 308$ nm (4.03 eV) dissolved in MeOH.

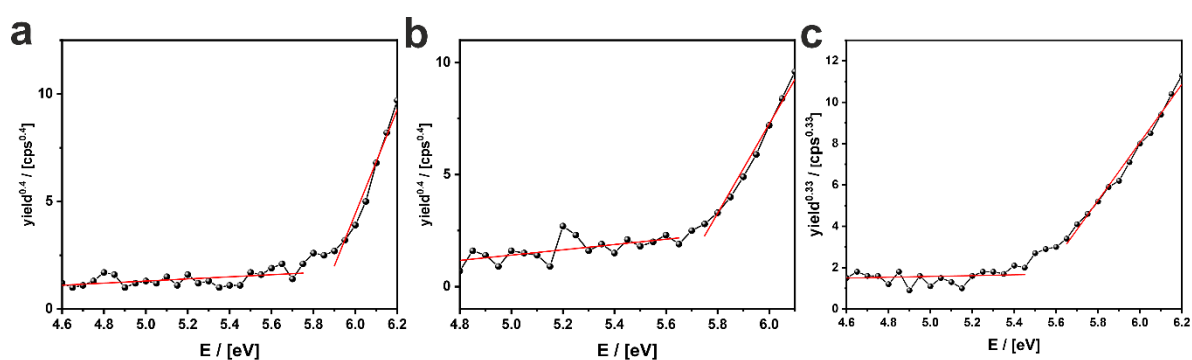


Figure A48 - PESA measurements of a) 2D-O-EABr with $E_{\text{VBM}} = -5.87$ eV, b) 2D-S-EABr with $E_{\text{VBM}} = -5.75$ eV and c) 2D-Se-EABr with $E_{\text{VBM}} = -5.54$ eV.

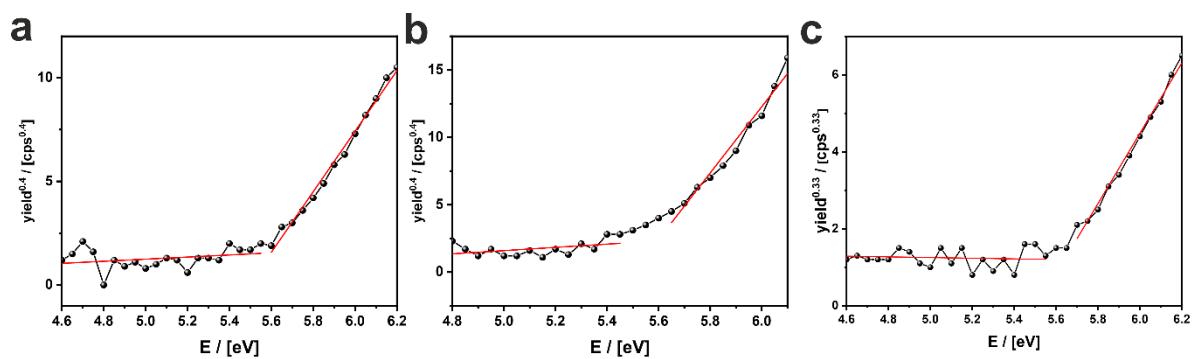


Figure A49 - PESA measurements on a glass substrate of a) O-EABr with $E_{\text{HOMO}} = -5.60$ eV, b) S-EABr with $E_{\text{HOMO}} = -5.60$ eV and c) Se-EABr with $E_{\text{HOMO}} = -5.64$ eV.

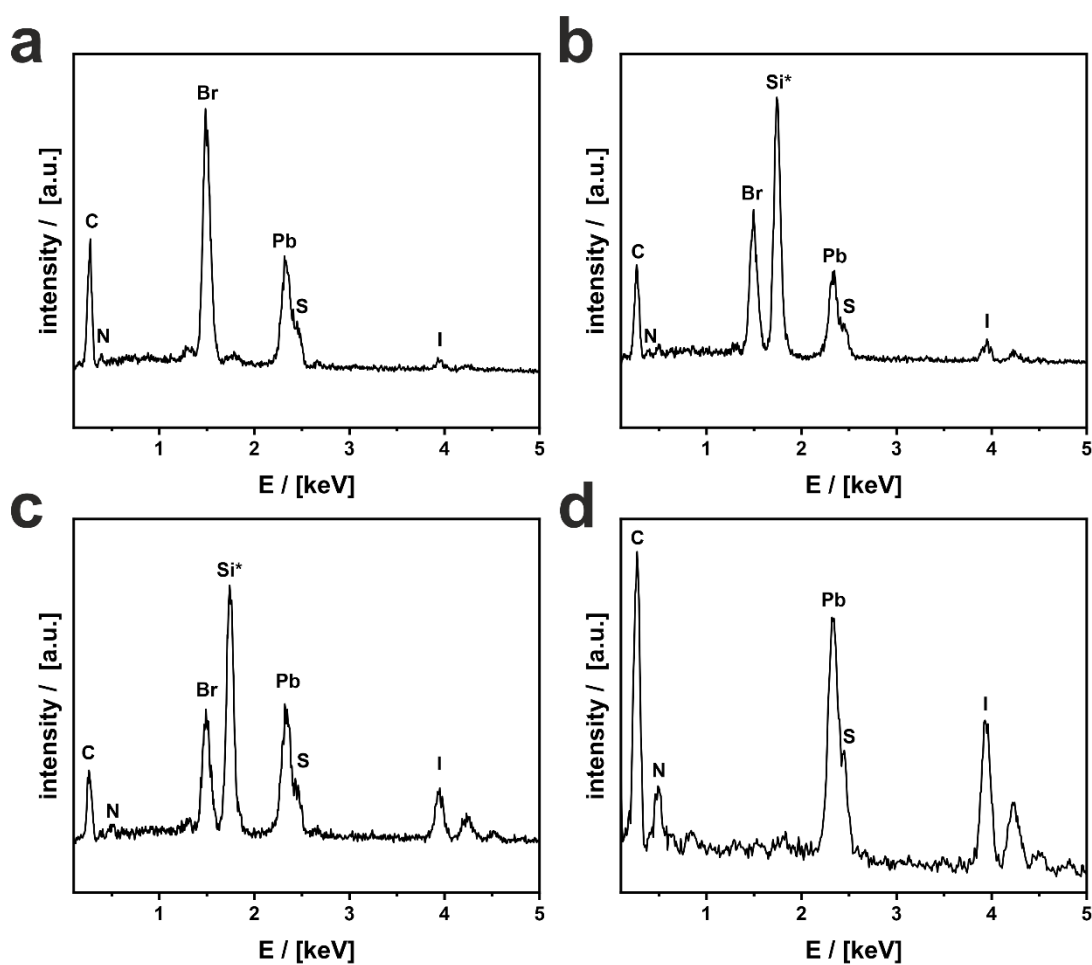


Figure A50 - EDX spectra for particles with a) 12 %, b) 30 %, c) 60 % and d) 100 % iodine content. A peak at 1.74 keV is attributed to the $K\alpha$ absorption of the silicon substrate.

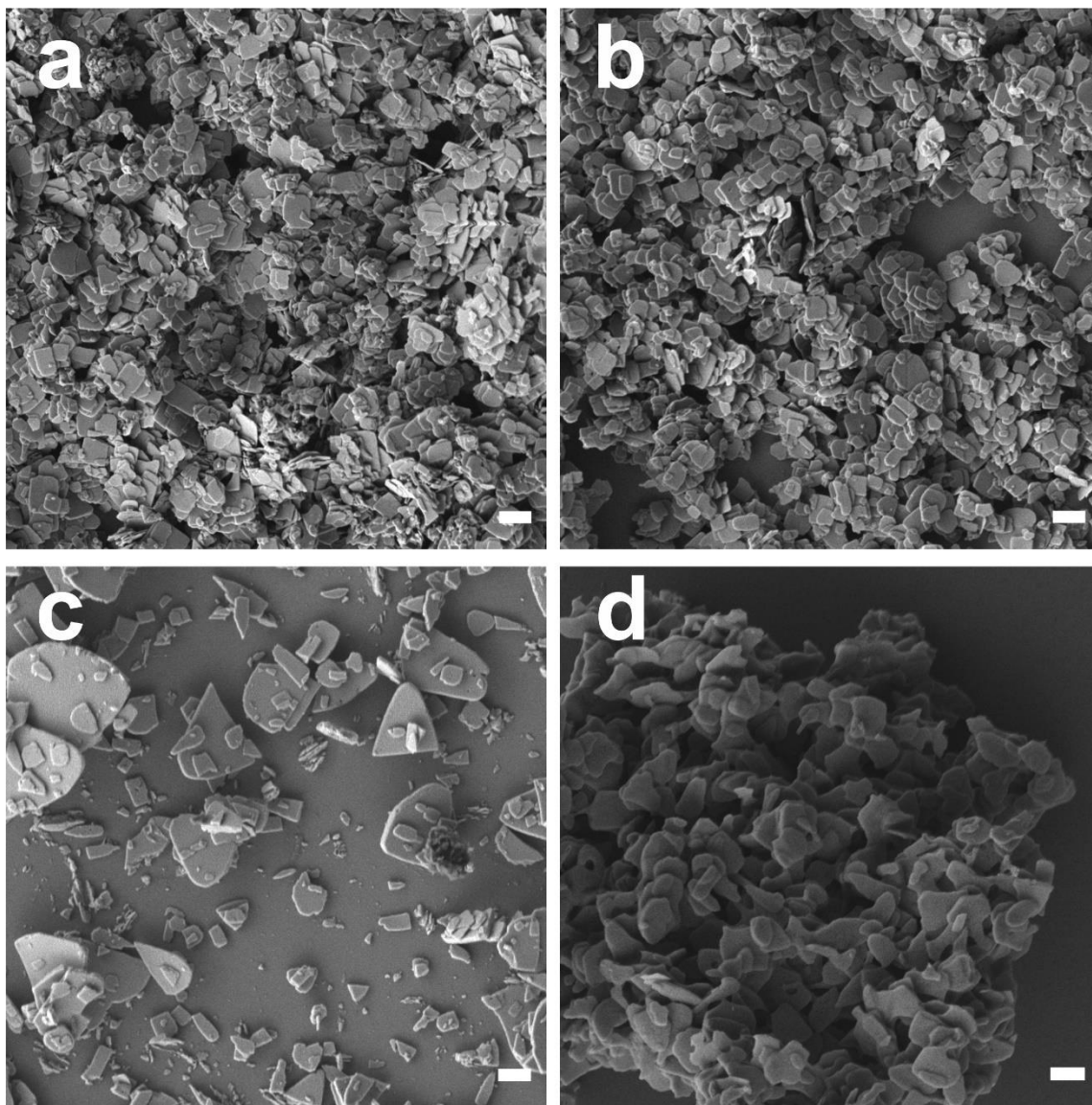


Figure A51 - SEM images of particles with a) 12 %, b) 30 %, c) 60 % and d) 100 % iodine content. Scalebar = 1 μm .

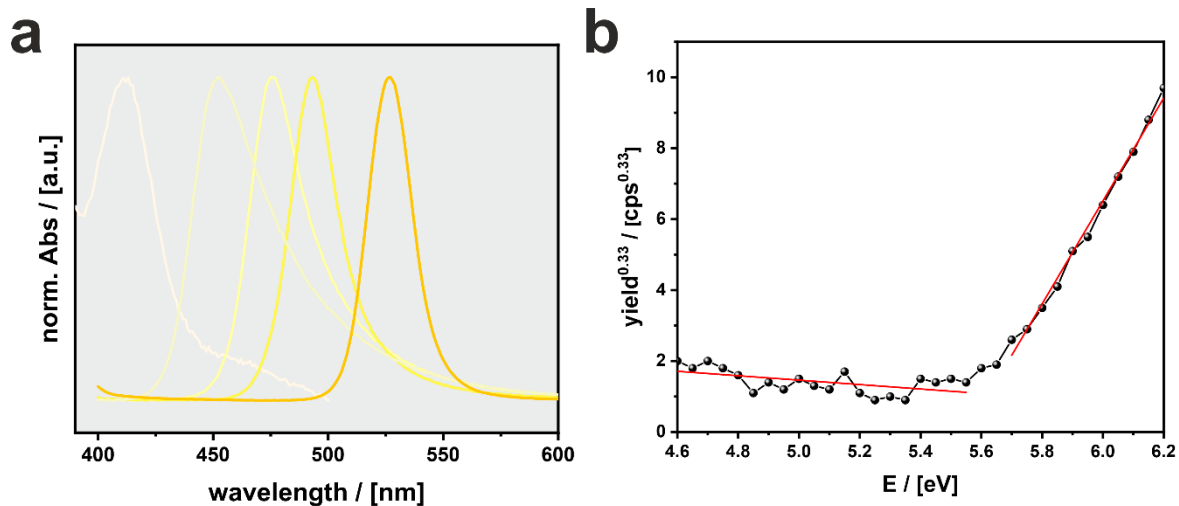


Figure A52 – a) PL of mixed halide phases with $(S-EA)_2PbX_4$ ($X=Br,I$) with Iodine ratio of 0 % ($\lambda_{max} = 413$ nm; $E_g = 3.00$ eV), 12 % ($\lambda_{max} = 452$ nm; $E_g = 2.74$ eV), 30 % ($\lambda_{max} = 475$ nm; $E_g = 2.61$ eV), 60 % ($\lambda_{max} = 493$ nm; $E_g = 2.51$ eV), and 100 % ($\lambda_{max} = 527$ nm; $E_g = 2.35$ eV) from left to right. b) PESA of $(S-EA)_2PbI_4$ with $E_{VBM} = -5.36$ eV).

Lebenslauf

Persönliche Daten

Name	Nicole Denise Fillafer
Geburtsdaten	06.10.1993 in Weingarten
Staatsangehörigkeit	deutsch
Adresse	78462 Konstanz

Ausbildung

Seit 04/2020	Promotionsvorhaben im Fachbereich Chemie an der Leibniz Universität Hannover (AG Polarz)
02/2018 – 03/2020	Promotionsvorhaben im Fachbereich Chemie an der Universität Konstanz (AG Polarz)
10/2015 – 12/2017	Master of Science (Nanoscience) an der Universität Konstanz - Abschlussnote: 1,3
10/2012 – 09/2015	Bachelor of Science (Nanoscience) an der Universität Konstanz - Abschlussnote: 2,0
10/2003 – 07/2012	Abitur am Gymnasium Weingarten - Abschlussnote: 1,6

Karriere

01/2017 – 04/2017	Betriebspraktikum bei ZF Friedrichshafen
-------------------	--

Kenntnisse

Fremdsprachen	Englisch (Fließend) Französisch (Grundkenntnisse) Spanisch (Grundkenntnisse)
---------------	--

Publications

The following publication and manuscript contributed to this thesis:

1. **N. Fillafer**, T. Seewald, L. Schmidt-Mende, S. Polarz, Fillafer, Nicole, et al. "Interfacial charge transfer processes in 2D and 3D semiconducting hybrid perovskites: azobenzene as photoswitchable ligand." *Beilstein J. Nanotechnol.* **2020**, 11, 466-479.
2. **N. Fillafer**, H. Kuper, A. Schaate, S. Locmelis, J. A. Becker, Y. Krysiak, S. Polarz, "Design of Active Defects in Semiconductors: 3D Electron Diffraction Revealed Novel Organometallic Lead Bromide Phases Containing Ferrocene as Redox Switches." *Adv. Funct. Mater.* **2022**, 22011.